The star formation & chemical evolution timescales of two nearby dwarf spheroidal galaxies

Boer, Thomas Jacobus Laurens de

rijksuniversiteit
groningen

The Star Formation & Chemical Evolution timescales of two nearby dwarf spheroidal galaxies

Proefschrift

ter verkrijging van het doctoraat in de
Wiskunde en Natuurwetenschappen
aan de Rijksuniversiteit Groningen
op gezag van de
Rector Magnificus, dr. E. Sterken,
in het openbaar te verdedigen op
vrijdag 20 april 2012
om 11:00 uur

door

Thomas Jacobus Laurens de Boer

geboren op 9 september 1983
te Edam-Volendam

Promotor:	Prof. dr. E. Tolstoy
Copromotor:	Prof. dr. A. Saha

Beoordelingscommissie:	Prof. dr. P.C. van der Kruit
	Prof. dr. R.F. Peletier
	Prof. dr. E.D. Skillman

ISBN: 978-90-367-5422-4 Printed version
ISBN: 978-90-367-5423-1 Electronic version

"To know that we know what we know, and to know that we do not know what we do not know, that is true knowledge."
– Nicolaus Copernicus

COVER: The front cover shows a combination of synthetic images of the Fornax dwarf spheroidal galaxy, illustrating the effect of the increased central concentration of stellar populations with higher metallicity and younger age. The back cover shows a colour-composite image of the Sculptor and Fornax dwarf spheroidal galaxies. Credit: T. de Boer & DART.

PRINTED BY: Ipskamp Drukkers, Enschede

Contents

CHAPTER ONE

INTRODUCTION

Ever since the discovery that there are galaxies other than our own (Hubble, 1926, 1936), astronomers have sought to explain how galaxies form, and what processes are responsible for their diversity.

The evolution of galaxies is usually studied by looking at the properties of the stars and gas within them. The lifetime of low mass stars can be very long, and can even exceed the current age of the Universe. This means that some stars which were formed when the Universe was very young, may still be around today. Stars contribute metals[1] to their surroundings through stellar winds and supernova explosions, which increase the metal content of the interstellar gas within a galaxy over time. Subsequent generations of stars that form from this enriched gas all carry distinct imprints or chemical abundance patterns from the time when the star formed. Therefore, by studying different generations of stars, we can determine how chemical abundances have changed over time.

In distant galaxies, the integrated light of the entire galaxy is the only way of studying their properties, using integrated spectra or colours. In this way, the mean age and metallicity of a galaxy can be determined.

For the more nearby galaxies, it is possible to identify individual stars. For these “resolved" galaxies, the properties of their individual stars can be determined through photometric and spectroscopic observations, giving the brightness, colour, metallicity, radial velocity and the chemical abundance pattern (the abundances of different elements compared to those of the Sun) of each star. By obtaining such information for a large sample of individual stars, we can disentangle different stellar populations and determine their characteristics as a function of age, metallicity and/or position within the galaxy.

From photometric observations, the stars in these galaxies can be plotted in a Colour-Magnitude Diagram (CMD), which allows us to obtain the metallicity and age of the stellar populations in the galaxy. By modelling the CMD using stellar evolution models (e.g., isochrones), it is possible to obtain the Star Formation History (SFH) and Chemical Evolution History (CEH) of the galaxy, which give the strength of star forma-

[1] metals: all elements heavier than Helium

tion at different age and metallicity respectively (e.g., Harris and Zaritsky, 2001; Dolphin, 2002; Aparicio and Gallart, 2004). The SFH shows on which timescale the majority of stars in a galaxy were formed, and with which metallicity, and indicates how star formation proceeded over time. Furthermore, by determining the SFH at different position in the galaxy, the change in stellar populations can be studied as a function of radius.

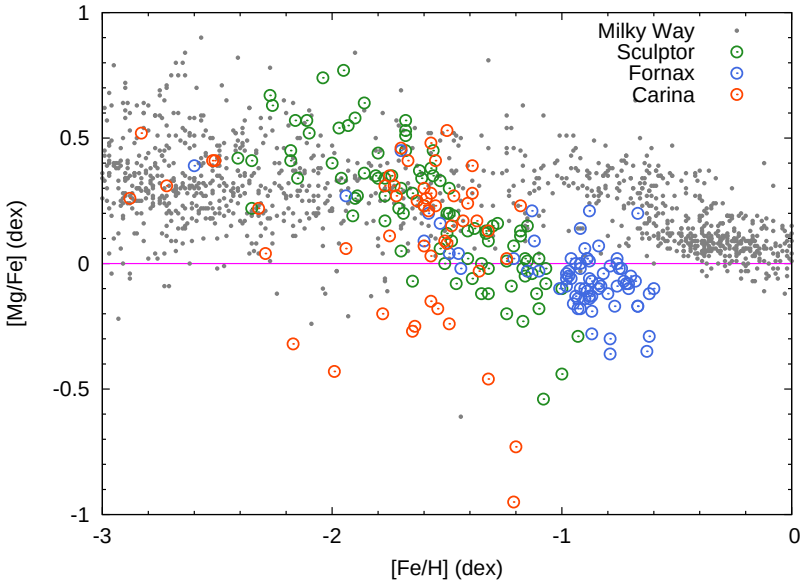

Figure 1.1: *The abundances of the α-element magnesium (Mg/Fe) as a function of metallicity (Fe/H) in three nearby dwarf spheroidal galaxies, as obtained from medium and high resolution spectroscopy of individual RGB stars. The abundances are shown as green points for Sculptor (Hill et al., in prep, see Tolstoy et al., 2009), blue points for Fornax (Letarte et al., 2010) and red points for Carina (Shetrone et al., 2003; Koch et al., 2008; Lemasle et al., 2011, Venn et al., 2012, in press). The abundance of magnesium measured for Milky Way disk and halo stars is shown for comparison (as grey dots), from Venn et al. (2004).*

From spectroscopic observations we can directly determine the abundances of many chemical elements in individual stars (e.g., Bonifacio et al., 2009; Letarte et al., 2010, Hill et al., in prep). In this way, we can investigate the enrichment history of different elements (see Figure 1.1) as a function of metallicity. By obtaining chemical abundances for a large sample of stars, we can also study the effect of different stellar populations on the abundance pattern of the galaxy. Furthermore, spectroscopic observations also allow us to derive the stellar velocity distribution of the galaxy, and hence study its kinematics and dynamics (e.g., Tolstoy et al., 2004; Battaglia et al., 2008a).
The sample of galaxies that can be resolved into individual stars consists mostly of dwarf galaxies within the Local Group. A wide variety of different properties have been found within these dwarf galaxies (see Tolstoy et al. (2009) for a recent overview), with

some experiencing continuous star formation and others discrete bursts. Furthermore, there are galaxies which have very similar overall properties (such as total mass and luminosity), but contain very different stellar populations. To determine what is responsible for the differences seen in galaxies, their properties need to be carefully quantified.
In this thesis, I will present a new method of determining the SFH, that directly combines photometric and spectroscopic information. In this way, a very accurate SFH is obtained, which is used to define the detailed star formation and chemical properties of individual galaxies. Furthermore, by coupling the accurate SFH directly to the spectroscopic abundances, it is possible to measure the evolution of abundances as a function of age, and directly determine the timescale for the evolution of different chemical elements in different galaxies.

1.1 The Local Group

The Local Group is dominated by two large spiral galaxies (the Milky Way and Andromeda), but also contains numerous smaller satellites of different types (see Mateo (1998)). The dwarf galaxies in the Local Group can be divided into different classes, based on properties such as surface brightness, absolute magnitude and physical size and morphology. The majority of Local Group dwarf galaxies fall into one of two classes, dwarf spheroidal or dwarf irregular. The dwarf spheroidal galaxies (dSph) are typically dominated by old populations, with no HI gas or current star formation, and are most commonly found close to the main spiral galaxies. Conversely, dwarf irregular galaxies have current star formation, contain significant amounts of HI gas and are typically found farther away from the large spirals.
Besides these two dominant galaxy types, the Local Group contains a single dwarf elliptical galaxy (M32), and a single dwarf spiral galaxy (M33), although the Large Magellanic Cloud also appears to be a low-luminosity spiral galaxy, which has been disturbed by an encounter with the Small Magellanic Cloud and the Milky Way (Besla et al., 2012). The Sloan Digital Sky Survey discovered an ultra-faint class of dwarf galaxies in and around the Milky Way. These small, diffuse galaxies are thought to be made up of ancient stars, and appear to be the extension of the dwarf galaxies to lower luminosity (e.g., Belokurov et al., 2006, 2007; Simon and Geha, 2007; Martin et al., 2008; Salvadori and Ferrara, 2009).

The Local Group galaxies have revealed complex behaviour, with spatially varying population gradients, distinct bursts of star formation and galactic interactions. The distribution of stars in individual galaxies has revealed substructures within and around galaxies (e.g., Olszewski and Aaronson, 1985; Coleman et al., 2004), such as tidal tails and shells, over-dense regions within galaxies and merging events, such as the merger of the Sagittarius dwarf with the Milky Way (Ibata et al., 1994; Majewski et al., 2003).
By obtaining the detailed SFH and CEH of a sample of galaxies in the Local Group, it will be possible to study how factors such as environment and total mass influence the evolution of a galaxy. We can also determine the timescale over which the internal processes (such as metal enrichment and changes in the abundance pattern through

supernovae explosions) take place in different galaxies. In particular, the SFH of dSph galaxies can be obtained with great accuracy, since they show no current star formation (e.g., Tolstoy et al., 2009), which means there are no overlying young populations in the CMD that obscures the old stars.

1.2 Photometry

Photometry of individual stars is the measurement of their luminosity, expressed in terms of magnitudes. The distribution of light is modelled using a predicted stellar profile (point spread function), using the photometry package DoPHOT (Schechter et al., 1993). By determining the luminosity of stars in different filters it is also possible to obtain the colour of a star. Since many thousands of stars are observed on a single image, the colours and magnitudes of millions of individual stars within a galaxy can be obtained relatively easily.
The colours and magnitudes determined from the images need to be calibrated to a standard photometric system, to allow accurate comparison with stellar evolution models and other photometric datasets. To this end, many observations of standard star fields are made throughout the observing nights. For these fields, the luminosity and colour of the standard stars are known with great accuracy, in several standard photometric systems (e.g., Landolt, 1992, 2007). Comparison between the observed and known magnitudes and colours allows us to determine the calibration to the standard system, as a function of magnitude, colour and position of the observed field on the sky (airmass).
To couple together stars in different filters, the positions of stars need to be determined with great accuracy across each wide-field image. A comparison of observed stellar positions to a known, accurate astrometric catalog allows us to determine how the position of stars on an observed image (in X,Y coordinates) compares to positions on the sky (in Right Ascension and Declination). In particular, great care needs to be taken to achieve a uniform astrometric calibration across each image, since the pixel scale is not constant across the images due to radial distortions in the large field of view.
In this way, a final photometric catalog can be obtained which is accurately calibrated to a standard photometric system, across a wide field-of-view (e.g., Saha et al., 2010). It is only with these precise photometric measurements and careful calibrations that an accurate comparison of data and theory can be obtained.

1.3 CMD analysis

In the early 1900s, Ejnar Hertzsprung and Henry Norris Russell independently found that stars occupy distinct positions when plotted in a temperature-luminosity diagram (later named the Hertzsprung-Russell Diagram). The positions of the stars in the diagram were found to be linked to the mass and evolutionary state of these stars. The observed form of the diagram is a CMD, an example of which is shown in Figure 1.2.
Everything else being equal (e.g., distance), the positions of stars in a CMD are sensitive to age and metallicity, and can be used to study the properties of stellar populations (e.g., Harris and Zaritsky, 2001; Dolphin, 2002; Aparicio and Gallart, 2004; Gallart et al., 2005b). Large numbers of stellar systems have been observed and analysed

using CMDs (see Sandage (1986) for an overview of early CMD observations). In particular, observations that resolved individual stars in the Sculptor and Fornax dwarf spheroidal galaxies played a key role in the development of the concept of stellar populations (e.g., Baade and Hubble, 1939; Baade, 1944; Sandage, 1986). Very early on, globular clusters were found to occupy very thin sequences in a CMD, which was inferred to be the sign of a single age stellar population (e.g., Arp et al., 1952; Sandage, 1957; Harris et al., 1983). The CMDs of different galaxies were found to show different, more spread out features, indicating a variety of different evolutionary histories for different galaxies (e.g., Olszewski and Aaronson, 1985; Gallart et al., 1999; Monelli et al., 2010). Some galaxies display a relatively smooth CMD suggesting continuous star formation, while others show distinct bursty episodes of star formation (such as the Carina dSph, see Bono et al. (2010)).

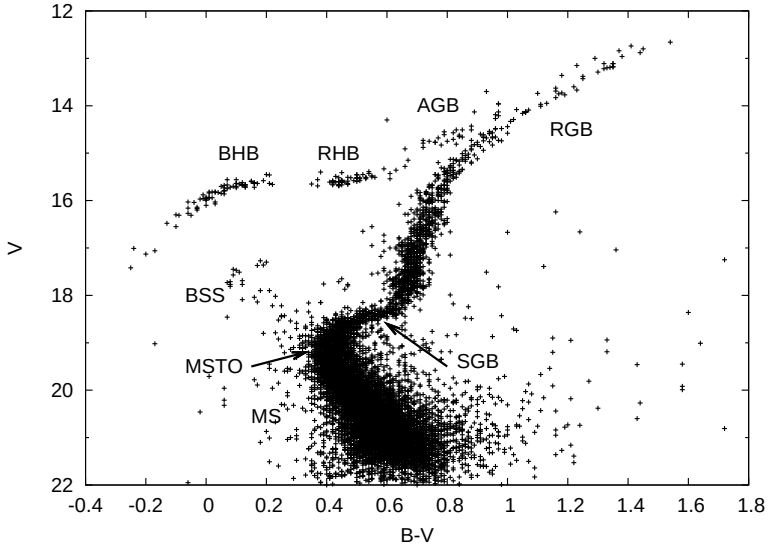

Figure 1.2: *The Colour-Magnitude Diagram of the globular cluster M3, as obtained from Buonanno et al. (1994). Labels indicate the evolutionary phases present in the CMD: Main Sequence (MS), Main Sequence Turn-Off (MSTO), Blue Stragglers (BSS), Sub-Giant Branch (SGB), Red Giant Branch (RGB), Asymptotic Giant Branch (AGB), Blue Horizontal Branch (BHB) and Red Horizontal Branch (RHB).*

In practice, some CMD features are more sensitive to certain parameters than others (e.g., Gallart et al., 2005b). For instance, the Main Sequence (when a star is powered by hydrogen fusion in its core) is mostly sensitive to age and less to metallicity. The Main Sequence Turn-Off (MSTO) marks the point at which stars have exhausted the hydrogen fuel in their core and move towards the Subgiant Branch (see Figure 1.2). The positions of the MSTOs in the CMD are excellent indicators of age, with older stellar populations displaying fainter and redder MSTOs.

After the Main Sequence, stars move to the Red Giant Branch (RGB) (see Figure 1.2), where they fuse hydrogen in a shell around an inert Helium core. The position occupied by the RGB in a CMD is dependant primarily on the age and metallicity, but also weakly on the α-element (O, Mg, Ca, Si, Ti) abundances (e.g., Salaris and Girardi, 2002). The overall colour of the RGB becomes redder (higher B−V colour) both with increasing age and metallicity. Therefore, the RGB can often be reproduced by multiple combinations of age and metallicity, which is the so-called “age-metallicity degeneracy". Therefore, the RGB alone is usually not sufficient to obtain a unique age and metallicity for the stellar populations within a galaxy.
Later evolutionary stages can also be used to obtain information about the age and metallicity of stellar populations. For instance, the presence of RR Lyrae stars indicates that a system contains populations with ages ≥10 Gyr (e.g., Bersier and Wood, 2002). However, the colour and luminosity of evolved stars such as RR Lyrae, Cepheid variables, Asymptotic Giant Branch and Horizontal Branch is dependant on several parameters, which are not obviously related. For example, the poorly constrained mass-loss fraction when moving from the tip of the RGB to the horizontal branch makes the position and number of these stars in the CMD hard to interpret in terms of age or metallicity.

1.4 Determining accurate star formation histories

The position of individual stars in the CMD of a galaxy can be compared with predictions from theoretical stellar evolution models (e.g., Dotter et al., 2008; Pietrinferni et al., 2004, 2006; Yi et al., 2001; Kim et al., 2002). Theoretical isochrones give the positions in a CMD of populations of stars with a single age and metallicity. Therefore, by matching an isochrone to a CMD it is possible to determine the range of ages and metallicities of the stars. This technique works best in simple stellar systems such as globular clusters, since they are well approximated by a single isochrone (e.g., Sandage, 1982; Vandenberg, 1983; Kravtsov et al., 1997). However, if there are multiple overlapping stellar populations, it can be hard to uniquely distinguish them. Therefore, galaxies must be studied using a different approach, the synthetic CMD method (e.g., Tosi et al., 1991; Tolstoy and Saha, 1996; Gallart et al., 1996a; Dolphin, 1997; Aparicio et al., 1997; Aparicio and Gallart, 2004). This method has been shown to be very effective, and is in common use.
This method makes use of synthetic CMDs of single stellar populations, by generating synthetic stars along an isochrone. An Initial Mass Function (IMF) is assumed, to determine the relative number of stars at each stellar mass. The model CMD is convolved with the observed error distribution, to take into account the photometric errors and incompleteness of the observed CMD. Furthermore, the synthetic stars are given a systematic offset in magnitude and colour to match the distance and reddening of the galaxy. In this way a synthetic CMD is obtained which can be directly compared to the observed CMD.
A set of synthetic CMDs can be generated, which correspond to single stellar populations of different ages and metallicities (and α-element abundances). Subsequently, the combination of these model CMDs is found, which best matches the observed

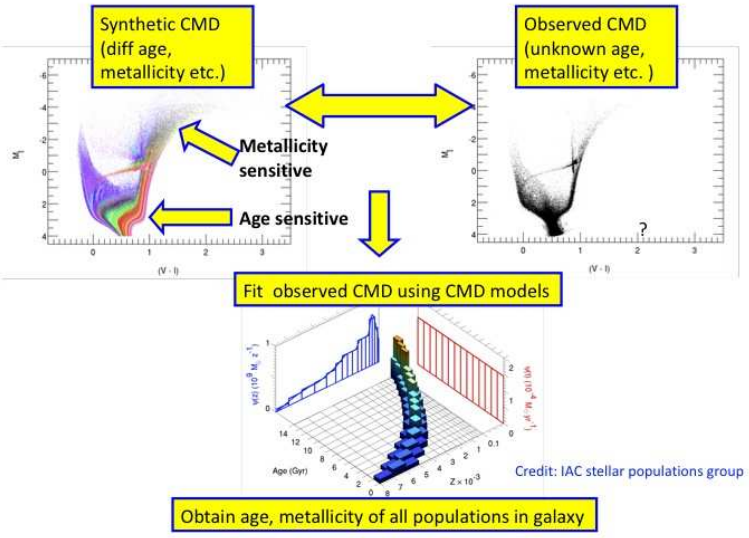

Figure 1.3: *A schematic picture of the steps involved in determining the star formation history of a galaxy from an observed CMD, using the synthetic CMD method. First, a set of synthetic CMD models are generated, with known age and metallicity (upper left). These models are then compared to the observed CMD of a galaxy (upper right). By finding the set of models that best match the observed CMD it is possible to determine the star formation history, as shown in the bottom panel.*

CMD (see Figure 1.3). In this way, the SFH and CEH of the observed galaxy are determined, as shown in Figure 1.3.

The accuracy with which the SFH can be determined depends strongly on the photometric depth of the observed CMD (e.g., Harris and Zaritsky, 2001; Dolphin, 2002; Gallart et al., 2005b). To obtain accurate age estimates of the stellar populations it is necessary to determine precise colours and magnitudes of stars on the MSTO. However, due to its relative faintness, the MSTO feature is not always observable in distant galaxies. Conversely, the brighter evolutionary features (such as the RGB) are more accessible, even in galaxies outside the Local Group (e.g., Dalcanton et al., 2012). The SFH can be determined from CMDs based solely on the RGB, but an accurate estimate of the metallicity of the stellar population is needed, to break the age-metallicity degeneracy.

The accuracy of a SFH is also dependant on the stellar populations of the observed system. The changes in the CMD due to age become less obvious for increasing ages and decreasing redshift, z. Therefore, the age of a young population ($\leq$5 Gyr) can be determined with greater accuracy than the age of ancient populations ($\geq$10 Gyr) (e.g., Gallart et al., 2005b). Furthermore, the MSTOs are also more luminous and more spread out in

luminosity for younger populations, which reduces the photometric uncertainty and increases the age accuracy. As a result, the ages of old stellar populations are often determined with limited accuracy. A single number is often adopted for the star formation rate at ages ≥10 Gyr (e.g., Gallart et al., 2005a; Coleman and de Jong, 2008).
The oldest ages are often the most relevant, especially in the context of understanding galaxy formation. For example, the effect of the first generations of stars on the abundance patterns of the stars in a galaxy occurs at ancient ages. Furthermore, the Epoch of Reionisation (EoR), which re-ionised the neutral hydrogen gas in the Universe between redshifts z≈20 and z≈6 (or between 12.7 and 13.55 Gyr ago), may also have influenced the star formation at these times in dwarf galaxies. The ability to distinguish any effect due to early cosmological events requires an increased accuracy of the SFH determined at the earliest epochs.

1.5 Spectroscopy

Absorption lines formed in the photosphere of stars contain the abundance pattern of the interstellar gas from which the star was formed. From the spectrum of a star, the chemical properties of this gas can be quantified. Spectroscopic observations typically target only a fraction of the stars in a CMD (at most, several hundred stars can be observed at once using a multi-object spectrograph). Nevertheless, detailed information can be obtained about kinematics, metallicity and chemical abundances. Two broad types of spectroscopic studies are performed: low-resolution studies and high-resolution studies.

Low-resolution spectroscopy is relatively straightforward, usually measuring few strong absorption lines, and requiring relatively short amounts of telescope time. When using multi-object spectrographs, large numbers of RGB stars (several hundreds) can be studied in individual galaxies (e.g., Battaglia et al., 2006; Walker et al., 2009; Kirby et al., 2010). Low-resolution spectroscopy of individual stars in Local Group dwarf galaxies usually focusses on the relatively strong Ca II triplet or Mg b lines. By measuring the strength of the individual spectral lines, the metallicity ([Fe/H]) and radial velocity of the stars can be obtained (e.g., Suntzeff et al., 1993; Tolstoy et al., 2001; Pont et al., 2004; Tolstoy et al., 2004; Battaglia et al., 2006; Simon and Geha, 2007; Starkenburg et al., 2010).
In this way, the detailed Metallicity Distribution Function (MDF) of a galaxy can be obtained, which shows the relative number of stars of different metallicities. The spectroscopic metallicities and velocities can be used to study the chemical and kinematical properties of a galaxy. By measuring the MDF at different positions within a galaxy, radial trends with metallicity can be identified (e.g., Tolstoy et al., 2004; Koch et al., 2006; Battaglia et al., 2006, 2008a).

High resolution spectroscopy of extragalactic stars requires a significant investment in telescope time, to obtain a spectrum in which weaker spectral features are detected. The high-resolution spectroscopic samples are thus usually relatively small (<100 stars), but allow the accurate determination of abundances of many chemical elements, such

as C, Mg, Si, Ca, Sc, Ti, Cr, Mn, Co, Ni, Zn, Sr, and Ba (e.g., Bonifacio et al., 2009; Letarte et al., 2010, Hill et al., in prep).
Thus, the detailed abundance pattern of Local Group galaxies can be determined, as a function of metallicity. These patterns can be used by chemical evolution models, to constrain the chemical evolution models of individual galaxies. Furthermore, effects of supernovae on the abundance pattern can be investigated by looking at the abundance ratios of elements synthesised by supernovae of different types.
For instance, the "knee" in the α-element distribution indicates the time when supernovae type Ia start to contribute to the chemical enrichment of the galaxy (Matteucci and Brocato, 1990; Matteucci, 2003). The analysis of α-elements in dwarf galaxies reveals that the "knee" in the α-element distribution takes place at a different metallicity in different galaxies (Tolstoy et al. (2009), and see Figure 1.1). In this thesis I show that the timescale for this process is $\approx 2 \pm 1$ Gyr in the Sculptor dSph galaxy (see Chapter 3).

1.6 Galaxy modelling

Numerous theoretical models have been developed, to simulate the formation and evolution of galaxies, concentrating on different aspects. Cosmological N-body simulations follow the formation of structure using dark matter alone. They can reproduce the number and distribution of large galaxies and galaxy clusters, as well as the filamentary structure of the Universe (e.g., Springel et al., 2005; Boylan-Kolchin et al., 2009). Semi-analytic models can be used in combination with these models, to simulate the stars within these haloes in a simple way (e.g., De Lucia and Helmi, 2008). Full hydrodynamical simulations can also be used to follow in detail the evolution of gas and stars within individual haloes, predicting the observable properties of individual galaxies, such as the luminosity, stellar mass and distribution, star formation timescales and chemical abundances (e.g., Stinson et al., 2007; Governato et al., 2010; Revaz and Jablonka, 2012). The computationally less intensive semi-analytic models treat the physics of baryons in a simple way, through a set of "recipes" for different processes (e.g., Baugh, 2006; Salvadori et al., 2007, 2008; Benson, 2010). Some chemical evolution models can take into account the detailed evolution of individual stars within galaxies, and their effect on the surrounding interstellar gas, through outflows and feedback due to supernova explosions (e.g., Lanfranchi and Matteucci, 2003; Romano et al., 2007, Romano & Starkenburg, in prep). The predicted detailed abundance pattern of stars is followed over time, allowing a detailed comparison with chemical abundances of individual stars.
Some models can reproduce the overall properties of the Milky Way as well as the global physical properties of satellite galaxies, such as their mean age and metallicity, luminosity, relative number and colours (e.g., Salvadori et al., 2008; De Lucia and Helmi, 2008; Li et al., 2010). The internal properties of dwarf galaxies, such as star formation histories and metallicity distributions are also reproduced fairly well (e.g., Revaz et al., 2009; Revaz and Jablonka, 2012, Starkenburg et al., 2012, in prep). However, some physics in the simulations is not well constrained, such as mechanical feedback due to supernovae, star formation efficiency, supernovae yields, re-ionization etc. This prevents us from accurately modelling the details of galaxy formation, and obtaining

exact analogous of Local Group dwarfs. However, some models can do quite well in reproducing the global properties of nearby galaxies, as I show in Chapter 5.

1.7 This thesis

In this thesis, I determine the SFH and CEH of two Local Group dwarf spheroidal galaxies (Sculptor and Fornax), by self-consistently combining all available observational information (both photometric and spectroscopic). In this way, I determine their star formation and chemical evolution timescales and investigate their abundance evolution directly as a function of time. I also compare the results for Sculptor with the outcome of four different galaxy simulations, to test the ability of models to reproduce the detailed properties of dwarf galaxies in the Local Group.

The first object of study is the relatively simple case of the Sculptor dwarf spheroidal galaxy, shown in Figure 1.4. Sculptor is dominated by old stars (≥10 Gyr), and therefore allows an unobscured view of the ancient star formation. In Chapter 2, I present a new wide-field photometric dataset obtained using the CTIO/MOSAIC camera. The new photometry goes down to the oldest MSTO, covering ≈80% of the tidal radius area of the galaxy. Great care was taken to accurately calibrate the photometric data, to ensure an accurate well defined CMD.

Figure 1.4: *An image of the central 0.4×0.4 square degrees of the Sculptor dSph galaxy, composed from photometric observations in the B (blue), V (green) and I (red) bands. East is up, and North is to the right.*

Chapter 2 describes the photometric and structural properties of Sculptor, and a qualitative analysis of the observed CMD. I show that the gradients seen in the velocity dispersion (Battaglia et al., 2008a), metallicity (Tolstoy et al., 2004) and horizontal branch morphology (Majewski et al., 1999; Hurley-Keller et al., 1999; Harbeck et al., 2001) are also matched by an age gradient, as seen by the variation of the properties of the MSTO with radius in the galaxy.

In Chapter 3, I present a new method of determining the SFH of resolved stellar populations (Talos) and apply it to Sculptor. This method directly combines spectroscopic

metallicities of individual stars with a classical CMD analysis. By simultaneously modelling the observed CMD and the spectroscopic MDF, greater constraints are placed on the properties of the stellar populations, which results in a more accurate SFH compared to standard methods, especially at the oldest ages.
The detailed SFH of Sculptor confirms and quantifies the radial age and metallicity gradient seen in Chapter 2. The SFH is also used to determine accurate age estimates for individual RGB stars, which have high-resolution spectroscopy (Hill et al., in prep, see Tolstoy et al., 2009). I have, for the first time, coupled ages to the chemical abundances, and determined the evolution of individual elements with time. The resulting, detailed Age-Metallicity Relation (AMR) shows a clear trend, with the most metal-poor stars being old and the more metal-rich stars being progressively younger. In this way, I am also able to determine the evolution timescale of α-elements, and specifically determine the time at which the "knee" in the [Fe/H] vs [Mg/Fe] plot of Sculptor occurs. This shows that supernovae type Ia started contributing to the chemical enrichment of Sculptor 2 ± 1 Gyr after star formation started.

In Chapter 4, I apply Talos to new wide-field CTIO/MOSAIC data of the Fornax dwarf spheroidal galaxy, which is known to have a more complex evolutionary history than Sculptor (e.g., Stetson et al., 1998; Buonanno et al., 1999; Saviane et al., 2000; Gallart et al., 2005a; Coleman and de Jong, 2008). The new SFH I determined confirms that Fornax has experienced star formation over all ages, from ancient ($\approx$14 Gyr) to very recent ($\leq$1 Gyr). Accurate age estimates are determined for the individual RGB stars in the spectroscopic samples of Fornax. The detailed AMR shows the presence of different populations, with different properties at different times. The time evolution of [Mg/Fe] shows a clear gradient with age for metal-rich stars, and a varying slope related to the strength of different star formation episodes in Fornax. Unfortunately, the "knee" in the α-element distribution is not well defined in the spectroscopic sample. A comparison between the detailed chemical evolution timescales of Sculptor and Fornax shows that the initial properties are very similar during the first few Gyr, but that star formation and metal enrichment in Fornax continued for a much longer period of time.

Finally, in Chapter 5 the detailed SFH of the Sculptor dwarf galaxy (as determined in Chapter 3) is compared to four different simulations of Sculptor-like galaxies. By comparing the model properties to the observations, the simulations and their input physics are tested. The comparison is done by generating the predicted CMD, MDF, SFH and abundance pattern of the models (accurately matching the observational limitations) and comparing these to the observations. Most models can reproduce the general properties of Sculptor to a greater or lesser extent. The accurate observed properties of Sculptor and the careful comparison to the model outputs can be used to give feedback to the simulations, to understand how to better reproduce the properties of a Sculptor-like dwarf galaxy.

For each chapter in my this thesis I have collaborated with many people, as part of the Dwarf Abundances and Radial velocities Team (DART) and through observing pro-

posals and papers. All these collaborators have provided valuable contributions to the chapters and resulting papers, through providing data, as well as advice and comments on the writing of the manuscript. However, the leadership of the work for each chapter is my own.

1.7.1 Future outlook

The detailed analysis of the Sculptor and Fornax dwarf spheroidals have shown the power of combining photometric and spectroscopic information to obtain a complete picture of the star formation and metallicity evolution of a resolved galaxy. The comparison of these two systems has shown the similarities and differences between both galaxies. However, to determine which parameters (total mass, size, Milky Way proximity, etc.) drive the differences observed in galaxies, a larger sample needs to be studied. By studying several more Local Group dwarfs, I can determine the effects of these parameters on the evolutionary history. Several Local Group galaxies have been observed in detail, in photometric and spectroscopic studies, such as Carina (e.g., Bono et al., 2010; Lemasle et al., 2011), Tucana (e.g., Monelli et al., 2010), Sextans (e.g., Battaglia et al., 2011) and the LMC (e.g., Carrera et al., 2011). For these galaxies, the accurate SFH and timescale of chemical evolution can be determined, using my approach.

The comparison between four different simulations of the Sculptor dwarf spheroidal has shown the value of using accurate observational properties to constrain simulations. In particular, the assumed timescale of star formation processes can be tested against the accurate observational timescales. This can be developed further by using the detailed evolutionary history of different galaxies, to provide even more elaborate ways to test the sensitivity of parameters used in models in more detail.

The detailed analyses of Local Group galaxies can also be used as templates to study the integrated properties of more distant galaxies. Using the detailed evolution history of Local Group dwarfs, unresolved spectral energy distribution can be created, to compare to observed integrated spectra of more distant galaxies. In this way, it is possible to look for analogues of Local Group galaxies in the more distant Universe. Furthermore, applying standard unresolved techniques to the generated unresolved spectrum can be a useful tool to determine what information can or cannot be accurately extracted from an unresolved spectrum with realistic properties.
In addition, combining the techniques used in resolved and unresolved stellar population analysis will be useful in preparing for the next generation of large telescopes. The future plans for E-ELT and TMT extremely large telescopes will only be able to semi-resolve many galaxies far beyond the Local Group. Thus, a combination of resolved and unresolved techniques will be necessary to obtain the most information for these data.

In conclusion, the careful, detailed study of individual galaxies, both near and far, provides invaluable insights into galactic formation and evolution.

CHAPTER TWO

DEEP WIDE-FIELD IMAGING DOWN TO THE OLDEST MAIN SEQUENCE TURNOFFS IN THE SCULPTOR DWARF SPHEROIDAL GALAXY

T.J.L. de Boer, E. Tolstoy, A. Saha, et al.

Based on: A&A, 2011, 528, A119

Abstract

We present wide-field photometry of resolved stars in the Sculptor dwarf spheroidal galaxy using CTIO/MOSAIC, going down to the oldest Main Sequence Turn-Off. The accurately flux calibrated wide field Colour-Magnitude Diagrams can be used to constrain the ages of different stellar populations, and also their spatial distribution. The Sculptor dSph contains a predominantly ancient stellar population (>10 Gyr old) which can be easily resolved into individual stars. A galaxy dominated by an old population provides a clear view of ancient processes of galaxy formation unimpeded by overlying younger populations. By using spectroscopic metallicities of RGB stars in combination with our deep Main Sequence Turn-Off photometry we can constrain the ages of different stellar populations with particular accuracy. We find that the known metallicity gradient in Sculptor is well matched to an age gradient. This is the first time that this link with age has been directly quantified. This gradient has been previously observed as a variation in Horizontal Branch properties and is now confirmed to exist for Main Sequence Turn-Offs as well. It is likely the Sculptor dSph first formed an extended metal-poor population at the oldest times, and subsequent more metal-rich, younger stars were formed more towards the centre

until the gas was depleted or lost roughly 7 Gyr ago. The fact that these clear radial gradients have been preserved up to the present day is consistent with the apparent lack of signs of recent tidal interactions.

2.1 Introduction

The Sculptor dwarf spheroidal galaxy is a faint ($M_V \approx -11.2$), well studied system in the Local Group. It has a tidal radius of 76.5 arcmin on the sky (Irwin and Hatzidimitriou, 1995), which corresponds to 1.9 kpc at a distance of 86±5 kpc (Pietrzyński et al., 2008). It is located at high galactic latitude (b=-83°) with a systemic velocity of $V_{hel} = +110.6 \pm 0.5$ km/s (Battaglia et al., 2008b) and suffers from relatively low amounts of reddening, E(B−V)=0.018 (Schlegel et al., 1998). Sculptor was the first early-type dwarf galaxy discovered around the Milky Way (Shapley, 1938a). Since then it has been the target of numerous studies of its resolved stellar populations.

Early work on the radial and two-dimensional structure of the Sculptor dSph (Demers et al., 1980; Eskridge, 1988c,c; Irwin and Hatzidimitriou, 1995) uncovered a complex spatial structure, with a radially increasing eccentricity. The presence of a spatial asymmetry was suggested in the East/West direction, of the order 30% above the level expected for a symmetric profile (Eskridge, 1988d). Using Colour-Magnitude Diagrams (CMD), Norris and Bessell (1978), interpreting photometric data from Hodge (1965) and Kunkel and Demers (1977), argued that the Red Giant Branch (RGB) is wider than can be explained by photometric uncertainties, suggesting the presence of internal age and/or abundance variations. The first CMDs using CCDs in a field just outside the core radius confirmed the large RGB spread and extended down to the Main Sequence Turn-Off (MSTO) region, determining an age range of 13±2 Gyr (Da Costa, 1984). A very deep HST CMD of a small field of view (~2′) well outside the centre of Sculptor, going down 3 magnitudes below the oldest MSTO, accurately confirmed the ancient age (15±2 Gyr) of the bulk of the stars in Sculptor. This is similar to the age of globular clusters (Monkiewicz et al., 1999). From the same HST data set it was shown using CMD synthesis analysis that Sculptor displays an extended Star Formation History (Dolphin, 2002), with most of the stars having formed 8−15 Gyr ago, but with a small (and highly uncertain) tail reaching down to more recent times. Ground based wide-field imaging studies, covering a larger fraction ($\approx 30' \times 30'$) of Sculptor, including the centre, found that the Horizontal Branch (HB) morphology changes significantly with distance from the centre (Majewski et al., 1999; Hurley-Keller et al., 1999).

On the RGB the presence of the age-metallicity degeneracy is a problem for the accurate analysis of the properties of the Sculptor dSph. The age-metallicity degeneracy on the RGB results in two populations displaying nearly identical RGB, if the second population has an age a factor of 3 higher and a metallicity a factor of 2 lower than that of population 1. Therefore, spectroscopic observations are needed to remove the degeneracy on the RGB and allow an accurate analysis of Sculptor properties.

Wide-field medium resolution Ca II triplet spectroscopy of RGB stars in Sculptor have independently confirmed the presence of two distinct stellar components (Tolstoy et al., 2004; Coleman et al., 2005a; Westfall et al., 2006), with different spatial distributions,

kinematics and metallicities. A metal-poor ($-2.8<$[Fe/H]<-1.7 dex), spatially extended component is present, as well as a metal-rich ($-1.7<$[Fe/H]<-0.9 dex) more concentrated component ,which also has a lower velocity dispersion than the metal-poor component (Battaglia, 2007; Battaglia et al., 2008b).

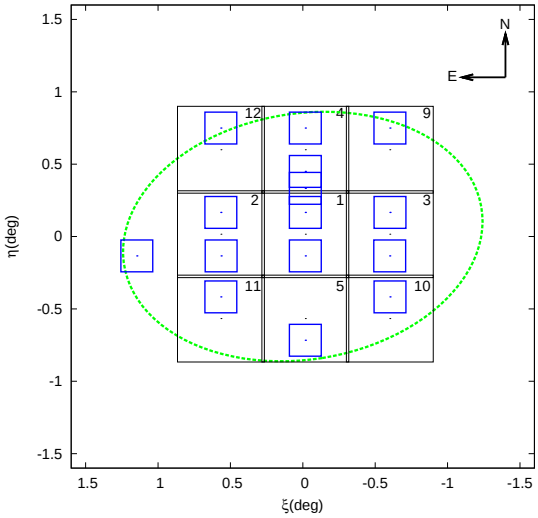

Figure 2.1: *Coverage of the photometric data across the Sculptor dwarf spheroidal. Big squares (no. 1-5,9-12) denote the CTIO 4m fields observed. The 15 smaller squares show the CTIO 0.9m calibration fields that were observed. The dashed ellipse is the tidal radius of Sculptor, as determined by Irwin and Hatzidimitriou (1995).*

High resolution spectroscopic studies in Sculptor have been carried out to determine detailed abundances of a range of chemical elements for small numbers of individual RGB stars (Shetrone et al., 2003 [5 stars]; Geisler et al., 2005 [4 stars]) using VLT/UVES and more recently with wide-field multi-fibre spectrograph VLT/FLAMES in high resolution mode (Hill et al., in prep; see Tolstoy et al. (2009)) for a sample of 93 stars. These studies are able to constrain the chemical evolution of Sculptor. This can then be compared to the other Local Group galaxies, including the Milky Way. For example, the [α/Fe] abundances are sensitive to the relative rates of SNe II and SNe Ia and can thus be used to trace the star formation timescale. Thus, the [Fe/H] and [α/Fe] abundances obtained from spectroscopic studies can be combined with deep photometry to accurately determine the ages of the Sculptor stellar populations, and the relation between Star Formation Rate and the chemical enrichment processes. Obtaining accurate time scales for star formation and the build up of abundance patterns in Sculptor also allows us to determine the early history of Sculptor, and also until which time Sculptor could contribute to the build-up of the Milky Way.
In this work we present deep wide-field carefully calibrated photometry of the Sculptor dSph galaxy, carried out with MOSAIC on the CTIO 4m/Blanco telescope. These CMDs reach down to the oldest MSTO, for an area covering ≈80% of the tidal radius of Sculptor. Accurately calibrated photometry is essential in determining ages, since the position of the MSTO directly correlates with the age of the stellar population. From

deep MSTO photometry over a large region we can for the first time study the effect of age on the physical properties of the galaxy. Combining the results of spectroscopic surveys with our MSTO photometry also allows us to measure the age-metallicity relation in Sculptor dSph galaxy.
The chapter is structured as follows: in section 2.2 we present the observations and data reduction. In section 2.3 we describe how we obtained and calibrated the photometry and the resulting structural properties. Section 2.4 describes the analysis and interpretation of different evolutionary features in the CMDs. Finally, section 2.5 discusses the conclusions and their implications in terms of galaxy formation. In a subsequent chapter we will present the detailed Star Formation History analysis of the Sculptor dSph.

2.2 Observations & Data Reduction

Deep optical photometry of the Sculptor dSph in the B, V and I bands was obtained using the CTIO 4-m MOSAIC II camera over 10 nights in September 2008 and November 2009. In order to ensure accurate photometric calibration without using too much 4m telescope time we obtained service mode observations with the 0.9m CTIO telescope over 3 photometric nights. Observations were made of Landolt standard fields (Landolt, 1992, 2007) covering a range of different airmass and colour.
The positions of fields observed with the 4m (big black squares) and 0.9m (small blue squares) telescopes are shown in Figure 2.1, relative to the Sculptor centre. B,V and I photometry was obtained for the central 5 pointings (1,2,3,4,5), whereas the outer pointings (9,10,11,12) were only observed in V and I bands. The observation logs for Sculptor observations are given in Tables 2.1 and 2.2. The observation logs for standard star calibration fields with both the 4m and the 0.9m telescopes are given in Appendix 2.A.

2.2.1 CTIO 4m MOSAIC

The CTIO MOSAIC II camera has an array of eight 2048×4096 pixel CCDs, each of which can be read out through one or two amplifiers. The CCDs combine to form a 8192×8192 pixel image corresponding to a field of view of $36' \times 36'$ on the sky. For our observing runs, one amplifier on one CCD was found to be inoperable, such that we were forced to read out MOSAIC II with 8 amplifiers only. This resulted in a readout overhead of 2m40s per image. An observing strategy was chosen involving non-dithered long (600s) exposures to be stacked together. We chose not to dither images, in order to be able to directly co-add images to obtain the deepest photometry possible. Furthermore, not dithering allowed us to apply accurate position dependent aperture corrections for each pointing. The loss of area incurred by not dithering exposures is roughly 2 percent, which means it will not materially affect the conclusions in this chapter. However, the very inner part of Sculptor (r_{ell} <0.05 deg) does suffers from incomplete coverage due to the presence of CCD gaps there. Since the average saturation level of the CCDs is ≈43000 counts (corresponding to B≈18, V≈17.5 and I≈17.5 for 600s

integration) additional shorter exposures (90s + 10s) were taken to sample the bright stars in each field.
For the data reduction we used the IRAF[1] data reduction program, which includes the **MSCRED** package (Valdes, 1998), designed for working with mosaics of CCD's. The standard data reduction steps include correcting for bias and flatfield, removing bad pixels and obtaining precise astrometry. For wide-field images there are a number of extra steps which needed to be taken, as outlined in (Valdes, 2002).

Table 2.1: *List of fields observed in the Scl dSph with the 4m CTIO Blanco telescope.*

Date	Field	RA J2000	DEC J2000	Filter	exp time sec	seeing $''$	airmass
2009 Nov 19	Scl1	01:00:03.96	−33:41:30.48	B	1800, 90, 10	1.0-1.3	1.00-1.01
2009 Nov 19				V	1800, 90, 10	1.1-1.2	1.01-1.02
2009 Nov 19				I	2400, 90, 10	1.0-1.3	1.03-1.07
2008 Sep 05	Scl2	01:02:52.08	−33:41:24.00	B	1500, 60	1.6-2.2	1.00-1.06
2009 Nov 20				B	2400	1.6-2.2	1.00-1.06
2008 Sep 05				V	1500, 60, 30	1.0-1.1	1.00-1.01
2009 Nov 21				V	1800	1.0-1.1	1.00-1.01
2008 Sep 05				I	2400, 60,10	1.2-1.3	1.00-1.07
2009 Nov 23	Scl3	00:57:15.48	−33:41:22.92	B	900, 60	1.2-1.4	1.62-1.70
2009 Nov 23				B	600	1.2-1.4	1.62-1.70
2008 Sep 06				V	900, 60, 30	1.0-1.2	1.01-1.02
2009 Nov 21				V	1800	1.0-1.2	1.01-1.02
2008 Sep 06				I	1800, 60, 10	0.9-1.0	1.03-1.08
2009 Nov 21				I	2400	0.9-1.0	1.03-1.08
2008 Sep 06	Scl4	01:00:03.96	−33:06:30.60	B	1500, 60, 10	0.9-1.0	1.01-1.03
2008 Sep 06				V	900, 60, 10	1.0-1.5	1.10-1.30
2009 Nov 21				V	1800	1.0-1.5	1.10-1.30
2009 Nov 21				I	2400, 90, 10	1.0-1.3	1.20-1.30
2008 Sep 06	Scl5	01:00:03.96	−34:16:30.36	B	900, 60, 30	0.8-1.1	1.00-1.01
2008 Sep 06				V	900,60, 30	0.7-1.1	1.00-1.01
2009 Nov 22				V	1800	0.7-1.1	1.00-1.01
2009 Nov 22				I	2400, 90, 10	1.1-1.3	1.01-1.04
2009 Nov 22	Scl9	00:57:16.92	−33:06:23.40	V	1800, 90, 10	1.1-1.2	1.06-1.11
2009 Nov 22				I	2400, 90, 10	1.0-1.2	1.14-1.28
2009 Nov 23	Scl10	00:57:14.40	−34:16:22.80	V	1800, 90, 10	1.1-1.2	1.10-1.17
2009 Nov 23				I	2400, 90, 10	1.0-1.2	1.21-1.39
2009 Nov 23	Scl11	01:02:53.16	−34:16:23.52	V	1800, 90, 10	0.9-1.0	1.00-1.02
2009 Nov 23				I	2400, 90, 10	0.8-0.9	1.00-1.02
2009 Nov 22	Scl12	01:02:51.00	−33:06:24.12	V	1800, 90, 10	1.0-1.1	1.29-1.43
2009 Nov 23				I	2400, 90, 10	0.9-1.0	1.03-1.07

The 8 chips of each MOSAIC image suffer from electronic crosstalk which causes ghost images. Each pair of CCD's are controlled by one CTIO Arcon controller, which causes one CCD to show ghost images from stars in a different CCD that are saturated or nearly saturated. This crosstalk was removed using correction terms provided by NOAO.

[1] IRAF is distributed by the National Optical Astronomy Observatories,which are operated by the Association of Universities for Research in Astronomy, Inc., under cooperative agreement with the National Science Foundation.

Table 2.2: *List of fields observed in the Scl dSph with the 0.9m CTIO telescope.*

Date	Field	RA J2000	DEC J2000	Filter	exp time sec	seeing $''$	airmass
2008 Oct 31	Scl1 N	01:00:03.96	−33:32:30.48	B	300	1.5	1.02-1.05
2008 Oct 31				V	300	1.4	1.02-1.04
2008 Oct 31				I	600	1.3	1.00-1.03
2008 Nov 02	Scl1 S	01:00:03.96	−33:50:30.48	B	300	1.5	1.06-1.09
2008 Nov 02				V	300	1.3	1.05-1.08
2008 Nov 02				I	600	1.3	1.04-1.07
2008 Oct 31	Scl2 N	01:02:52.08	−33:32:24.00	B	300	1.7	1.01-1.03
2008 Oct 31				V	300	1.5	1.01-1.03
2008 Oct 31				I	600	1.5	1.02-1.04
2008 Nov 02	Scl2 S	01:02:52.08	−33:50:24.00	B	300	1.3	1.02-1.04
2008 Nov 02				V	300	1.3	1.02-1.03
2008 Nov 02				I	600	1.3	1.01-1.03
2008 Oct 31	Scl3 N	00:57:15.48	−33:32:22.92	B	300	1.5	1.13-1.18
2008 Oct 31				V	300	1.3	1.15-1.20
2008 Oct 31				I	600	1.3	1.16-1.22
2008 Nov 02	Scl3 S	00:57:15.48	−33:50:22.92	B	300	1.8	1.01-1.03
2008 Nov 02				V	300	2.0	1.02-1.04
2008 Nov 02				I	600	1.7	1.02-1.04
2008 Oct 31	Scl4 N	01:00:03.96	−32:57:30.60	B	300	1.5	1.25-1.35
2008 Oct 31				V	300	1.3	1.25-1.40
2008 Oct 31				I	600	1.5	1.30-1.42
2008 Nov 02	Scl4 S	01:00:03.96	−33:15:30.60	B	300	1.7	1.05-1.08
2008 Nov 02				V	300	1.9	1.06-1.09
2008 Nov 02				I	600	1.5	1.07-1.10
2008 Nov 02	Scl5 S	01:00:03.96	−34:25:30.36	B	300	1.5	1.17-1.23
2008 Nov 02				V	300	1.5	1.18-1.27
2008 Nov 02				I	600	1.4	1.21-1.29
2008 Nov 02	Scl6 S	01:05:40.20	−33:50:03.12	B	300	2.0	1.92-2.18
2008 Nov 02				V	300	1.8	1.97-2.30
2008 Nov 02				I	600	1.9	2.07-2.39
2008 Nov 01	Scl8 N	01:00:03.96	−33:22:31.08	B	300	1.5	1.05-1.08
2008 Nov 01				V	300	1.4	1.04-1.07
2008 Nov 01				I	600	1.4	1.03-1.06
2008 Nov 01	Scl9 N	00:57:16.92	−32:57:23.40	B	300	1.8	1.00-1.01
2008 Nov 01				V	300	1.7	1.00-1.01
2008 Nov 01				I	600	1.4	1.00-1.01
2008 Nov 01	Scl10 N	00:57:14.40	−34:07:22.80	B	300	1.6	1.01-1.03
2008 Nov 01				V	300	1.5	1.02-1.04
2008 Nov 01				I	600	1.4	1.02-1.04
2008 Nov 01	Scl11 N	01:02:53.16	−34:07:23.52	B	300	1.5	1.05-1.11
2008 Nov 01				V	300	1.5	1.07-1.12
2008 Nov 01				I	600	1.3	1.10-1.14
2008 Nov 01	Scl12 N	01:02:51.00	−32:57:24.12	B	300	1.3	1.26-1.33
2008 Nov 01				V	300	1.4	1.27-1.35
2008 Nov 01				I	600	1.4	1.30-1.38

The flat-field obtained for the MOSAIC camera is made up of different chips. Instead of normalizing each chip individually, all chips were normalized using the average mean

across the whole image. The normalization factor for each chip then depends on its exact gain, and can be used to correct the science images both for the variation of sensitivity across each chip and to normalise the gain between different chips to a common value, thus obtaining a final image which has one uniform average gain. The standard flat-field obtained using the dome lamp was improved with the use of sky flat-fields. Sky flat-fields better approximate uniform illumination than possible with the dome lamp, as light enters the telescope in the same way as during science observations. The sky flat-field provides a correction on the dome flat-field, creating a master flat-field which is used to correct the science images. The MOSAIC I-band images also suffer from fringing, caused by constructive and destructive interference of night sky lines reflected in the CCD substrate. These fringe patterns were removed using an archival I-band fringe frame.

We created a bad pixel mask to flag saturated and negative pixels, cosmic rays and any damaged areas on each CCD. Cosmic rays were detected with a moving 7×7 pixel block average filter with the central target pixel excluded. The average value of the block is a prediction for the value of the target pixel, and the median of a background annulus around the block is used to protect cores of stars from being flagged as bad pixels. If the difference between the average block value and the central pixel value was larger than a threshold, the target pixel was flagged as a cosmic ray and added to the bad pixel mask. Subsequently, we remove these bad pixels from the image by interpolating over them, preventing them from propagating into adjacent pixels during the resampling process.

Due to the radial distortion in the large field of view the pixel scale is not constant across the field-of-view. Therefore the images had to be resampled to a common uniform pixel scale before stacking different exposures that have been offset with respect to each other because of telescope pointing errors between multiple observations of the same field. This requires a precise World Coordinate System (WCS), which provides the rotation, scale and offsets for mapping pixel coordinates to sky coordinates. The WCS header assigned to each image by the CTIO 4m-Blanco telescope was not sufficient to accurately align the images. Therefore, we obtained a new WCS solution using stars from the 2MASS point source catalog (Skrutskie et al., 2006) that were found in our field-of-view. The solution uses a ZPN projection (Calabretta and Greisen, 2002), which was fitted on each chip individually, while taking into account it's position with respect to a reference point (the center of the mosaic).

From a comparison of the final calibrated positions with 2MASS positions we find that the WCS is accurate to $\pm 0.2''$ across the entire field of view. This level of accuracy (less than one pixel) is sufficient to align individual images. The images are resampled to a uniform pixel scale of $0.27''$ and then scaled to a common exposure time and sky level and stacked together to produce as deep a final image of each pointing as is possible.

2.2.2 CTIO 0.9m

The 0.9m telescope is equiped with a single 2048×2046 pixel CCD detector, which has a field of view of $13.5' \times 13.5'$ and a pixel scale of $0.396''$. We use standard bias and flat-field removal techniques in IRAF for the reduction. A predefined bad pixel mask

provided by NOAO is used to flag bad pixels, since the CCD's of the 0.9m telescope have stable defects. A precise WCS is obtained, in order to match all stars observed in the 0.9m images to the same stars observed in the 4m images. As for the 4m data the WCS solution is derived using stars from the 2MASS catalog, using a ZPN projection of sky coordinates to pixel coordinates. The final solution is also accurate to $\pm 0.2''$ across the image, which corresponds to roughly half a pixel. This is sufficiently accurate to cross-correlate the 0.9m source catalogues with those of the 4m.

2.3 Photometry

Photometry is performed on all reduced images using DoPHOT (Schechter et al., 1993), using a version optimized to carry out accurate photometry down to the faintest levels. The methodology used in this section is described in detail in Saha et al. (2010).
DoPHOT uses an analytical function as a model PSF for describing different object types. Each model is characterized by six different parameters (X position, Y position, total intensity and three shape parameters), used both for the detection of objects and for determining their brightness. The initial shape parameters for star-like objects are determined separately for each image using a sample of bright, isolated stars. These parameters are updated after each consecutive pass through the image.

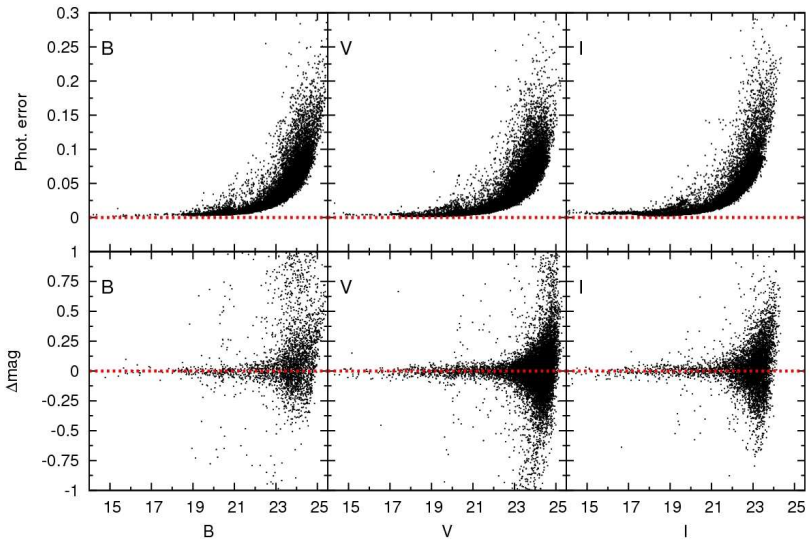

Figure 2.2: ***Top row:*** *Calibrated PSF magnitudes plotted against photometric errors for the central pointing for B, V & I filters.* ***Bottom row:*** *Magnitude difference between stars in overlapping regions of different pointings, for B,V & I filters.*

The model PSF is not allowed to vary with position on the image. Instead, a fixed PSF

is used on each chip, which is only allowed to vary from chip to chip. However, since the true PSF is expected to vary across the image (and also across each chip), we incorporate a position-dependency into the determination of the aperture corrections. Aperture magnitudes (which are independent of the PSF shape) are determined for bright isolated stars across each chip. The difference between the PSF and aperture magnitudes is mapped as a function of position over the field of view, and this provides the correction factors for DoPHOT PSF magnitudes.
The fitting function used to map the difference between aperture and PSF magnitudes is different for 4m and 0.9m images. In the case of the 0.9m images, a simple quadratic surface is used, to allow variations across the image. In the case of the MOSAIC images a more complex surface is used, to allow variations across each chip to be treated independently, in addition to a quadratic surface across the whole image to fit tilts or offsets between the individual chips (See Saha et al. (2010) for details).
The photometry of the short and long exposures is combined by first cross-correlating the stellar positions. Subsequently, for stars that have are found in both exposures the star with the smallest photometric error is used in the combined catalog. Stars with bright magnitudes that were found only in the short exposure are also added to the catalog.

2.3.1 Photometric Calibration

We use standard star observations of fields taken from Landolt (1992, 2007) with included Stetson standard stars (Stetson, 2000) to obtain photometric solutions for each night. The photometry is calibrated to the Johnson-Cousins-Glass photometric system using a photometric solution of the form:

$$mag_{obs} = mag_{true} + A_{mag} + \alpha * \chi + \beta * colour$$

where mag_{obs} is the observed magnitude, mag_{true} the true magnitude, χ the observed airmass, colour the observed colour index used, A_{mag} the zeropoint correction term, α the airmass coefficient and β the colour term.
We determined the photometric solutions automatically with a Bayesian approach, which provides a statistically robust method to separate reliable measurements from inaccurate ones. We used a Monte Carlo method to determine the most probable photometric solution, given the standard star measurements and taking into account the possibility of an unknown fraction of inaccurate measurements.
Using this method, we obtain likelihood distributions for the coefficients of the photometric calibration, the fraction of outliers and the parameters of the outlier distribution. Furthermore, the likelihood of being an outlier is given for each standard star measurement. The mean of the likelihood distribution is adopted as the photometric solution, with the uncertainty of each coefficient given by the standard deviation of the corresponding distribution. The resulting photometric coefficients, along with their uncertainties are given in Table. 2.3. A detailed description of the checks done to ensure a reliable photometric calibration is given in Appendix 2.B.
The resulting catalogs of different bands are matched together to create one full catalog containing 147456 stars in the V band down to 25.5 mag, 72577 in the B band

Table 2.3: *Photometric solution parameters and uncertainties.*

Band & colour	A_{mag}	α	β
	4m		
B,B-V	5.133±0.009	0.246±0.001	−0.077±0.001
I,V-I	5.501±0.001	0.062±0.001	0.031±0.001
V,B-V	4.917±0.001	0.127±0.001	0.049±0.001
V,V-I	4.924±0.002	0.129±0.001	0.030±0.001
	0.9m		
B,B-V	7.969±0.013	0.309±0.006	0.069±0.003
I,V-I	8.749±0.011	0.031±0.005	−0.028±0.002
V,B-V	7.936±0.013	0.084±0.007	−0.039±0.007
V,V-I	7.928±0.012	0.084±0.007	−0.046±0.006

going down to 25.7 mag and 116414 in the I band going down to 24.3. The top panels of Figure 2.2 show the DoPHOT internal errors of all these stars as a function of their magnitude for the central pointing only. The other pointings display similar profiles, with the exception of the outer B band observations, which have shorter integration times and thus go to different depths. At the bright end the best error is ≈0.002, while at the faint end the error is ≈0.2 for the faintest MSTO stars at the magnitude levels quoted above. The catalog contains only the stars for which all PSF parameters could be determined (type 1) and those that are found as mergers of two stars (type 3).
The photometry of the outer pointings is placed on the same system as the central pointing by using stars in the overlapping region. The multiple measurements are used to fit an offset and colour term which put the photometry on the same system as the central pointing. Comparison of the magnitudes of stars which have two or more measurements in the overlapping regions are shown in the bottom panels of Figure 2.2. The figure shows that the photometry of all pointings is calibrated to the same scale as the central pointing within the uncertainty of the photometric measurements. The photometric accuracy of the final catalog coming from random errors is ≈0.002 mag for the brightest stars, going down to ≈0.2 mag for the faint stars.

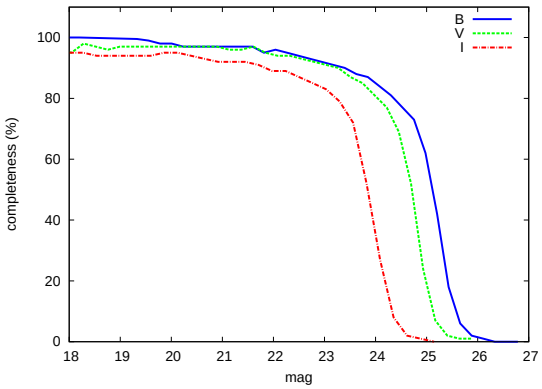

Figure 2.3: *Completenes fractions of the central Sculptor field as a function of magnitude for the B,V and I filter. For stars brighter then shown here the completeness factor is assumed to be 100%.*

2.3.2 Artificial star tests

Given that our photometry only just extends beyond the magnitude of the oldest MSTO it is important to quantify the completeness down to the faintest magnitudes. Incompleteness is caused by photometric errors, crowding effects and the detection limit of the images, and results in the loss of stars at faint magnitudes. In order to derive the completeness fraction at different magnitudes we have performed artificial star tests on the deep stacked images. Tests are done by inserting artificial stars in the images (a number of the order of 5% of the total) and re-doing the photometry in the same way. The resulting catalog is matched to the observed and artificial input catalogs to obtain the fraction of stars recovered (and their measurement errors) at different magnitudes and colours. The completeness fraction for different filters is plotted for the central Sculptor pointing in Figure 2.3 as a function of magnitude. For the other pointings the completeness profile looks similar in the V and I filters. Due to bad seeing conditions the B completeness profile in the outer pointings drops off faster than shown in Figure 2.3. For magnitudes brighter than shown in the figure the catalogs are assumed to be complete. Figure 2.3 shows that the 50% completeness level is located at B≈25.2, V≈24.8 and I≈24.0, which means our limiting magnitudes are about 1 magnitude deeper than the oldest MSTOs.

2.3.3 The Colour-Magnitude Diagrams

Using the full calibrated photometry catalog we can now produce Colour-Magnitude Diagrams (CMDs) to study different evolutionary features of the Sculptor dSph. Figure 2.4 shows an (I,V−I) CMD of the inner part of Sculptor, where we have identified the different evolutionary features that can be seen in all the CMDs.
Figures 2.5 and 2.6 show calibrated (I,V−I) and (V,B−V) CMDs for the Sculptor dSph for different annuli of elliptical radius (r_{ell}). A line indicating the 50% completeness levels of these stars is also included. The elliptical radius is defined as the major axis of the ellipse centred on Sculptor (RA=01:00:09, DEC=−33:42:30 with ellipticity e=0.32, see Mateo (1998)). We assume a tidal radius of 76.5 arcmin and core radius of 5.8 arcmin (Irwin and Hatzidimitriou, 1995). No de-reddening is applied to the CMDs in Figures 2.5 and 2.6; Instead, models and isochrones used to analyse the CMDs are reddened using the same extinction coefficient as obtained for the Sculptor dSph.
The CMDs show only the stars for which all PSF shape parameters are determined. Therefore, the CMDs do not go as deep as the limits determined from the completeness profile (Figure 2.3). If we consider the stars for which not all the shape parameters have been determined as 'lost', the 50% completeness levels for this subsample of stars are B≈23.9, V≈23.5 and I≈22.8. We stress that this does not mean that 50% of the stars at these levels are not observed, but only that these are not considered in the subsequent analysis. For the (I,V−I) CMDs full coverage is obtained for radii out to r_{ell}=0.8 deg and for the (V,B−V) CMDs out to r_{ell}=0.6 deg.
The CMDs display several features which remain clearly visible out to r_{ell}=1 deg (such as the RGB and BHB). The RHB, however, disappears around r_{ell}=0.6 deg where the number of foreground stars becomes comparable to the number of RHB stars. A pop-

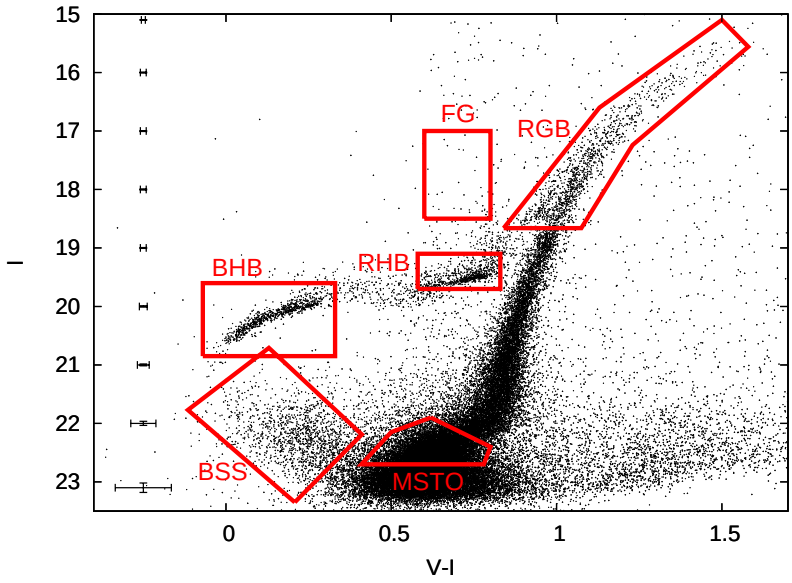

Figure 2.4: *Sculptor (I,V−I) colour magnitude diagram of the central region overlaid with regions identifying the different stellar populations. BHB: Blue Horizontal Branch, RHB: Red Horizontal Branch, RGB: Red Giant Branch, BSS: Blue Straggler Stars, MSTO: Main Sequence Turn-Off. In the RGB box numerous AGB stars can also be observed. A box is also included which provides an estimate of the contamination by foreground stars from the Milky Way (FG). Photometric errors are shown as the size of the errorbar at the corresponding magnitude level.*

ulation of potential Blue Straggler Stars (BSS) remains visible out to r_{ell}=1 deg. The old MSTO stars remain visible at all radii, but are strongly affected by Milky Way foreground contamination beyond r_{ell}=1 deg. The RGB has a spread in colour which is indicative of a spread in metallicity and/or age. A composite RGB bump is also present, for which a zoom in of the CMD is presented in Figure 2.7. This is consistent with the presence of an extended period of star formation.

To estimate the effect of foreground stars in the CMDs, we have used the Besançon models (Robin et al., 2003) to construct a model Galactic population in the direction of the Sculptor dSph. A comparison of the number of foreground stars in the CMD (FG, see Figure 2.4) with the predicted foreground stars of the same colours from the Besançon models agree to within 10%, validating the use of the Besançon models to accurately predict the number of foreground stars anywhere in the CMD.

Besides foreground stars a cloud of faint red stars is seen close to the detection limit in the (I,V−I) CMD, redward of V−I ≈1.0, which increases in number as we move out of the centre of Sculptor. These objects are consistent with the integrated colours of background spiral and irregular galaxies at a redshift z=0.5-0.8 (Fukugita et al., 1995) that remain unresolved due to a lack of spatial resolution and sensitivity.

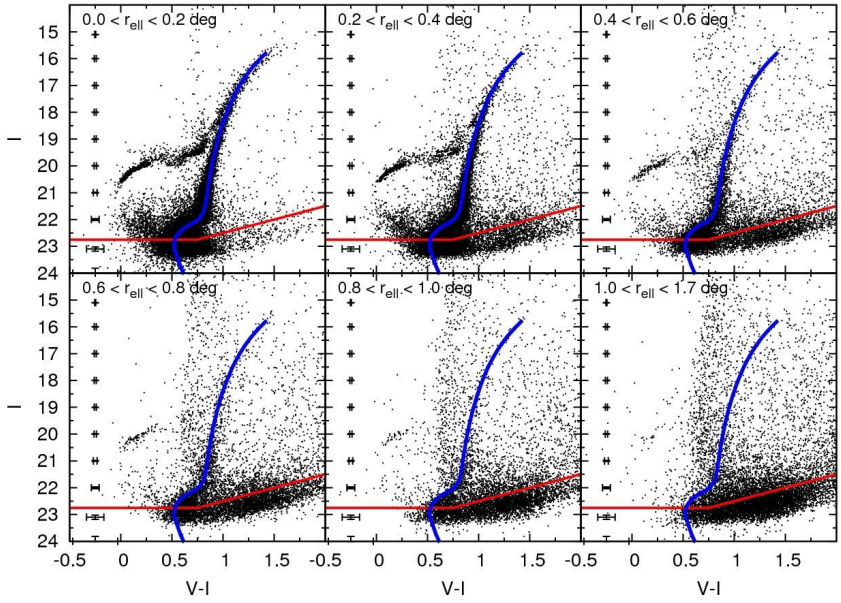

Figure 2.5: *(I,V−I) Colour-Magnitude Diagrams of the Sculptor dSph for increasing elliptical radius. Error bars show the average photometric error at that level. The 50% completeness level for this subsample is indicated by the grey line. The black line shows a reference isochrone ([Fe/H]=−1.80,[α/Fe]=0.2, age = 11 Gyr) which runs through the middle of the RGB in the centre.*

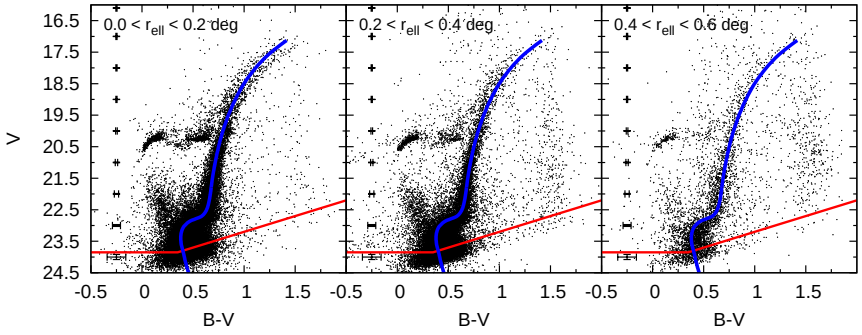

Figure 2.6: *(V,B−V) Colour-Magnitude Diagrams of the Sculptor dSph for increasing elliptical radius. Error bars showing the average photometric error and a 50% completeness line (in grey) are also included. A reference isochrone indicating the middle of the RGB in the centre is also shown as a black line.*

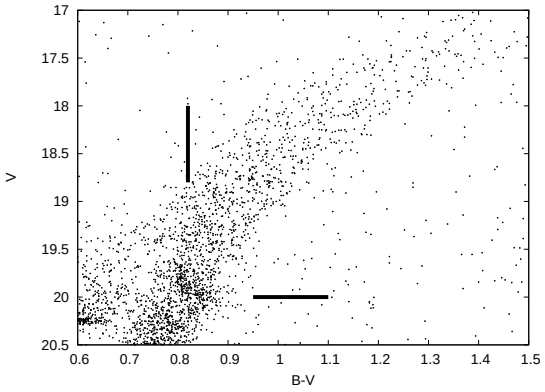

Figure 2.7: *Zoom in of the RGB bump region in the (V,B−V) CMD of the Sculptor dSph. A composite RGB bump is visible at 0.78<B-V<0.88 and 19.6<V<20.1.*

In order to disentangle the positions of the different contaminating populations present in our CMDs, we have constructed a Colour-Colour diagram (Figure 2.8c). The prominent evolutionary phases and foreground and background contamination have been colour-coded. The position of the same populations are shown in the (I, V−I) CMD (Figure 2.8b), and the (V, B−V) CMD (Figure 2.8a).

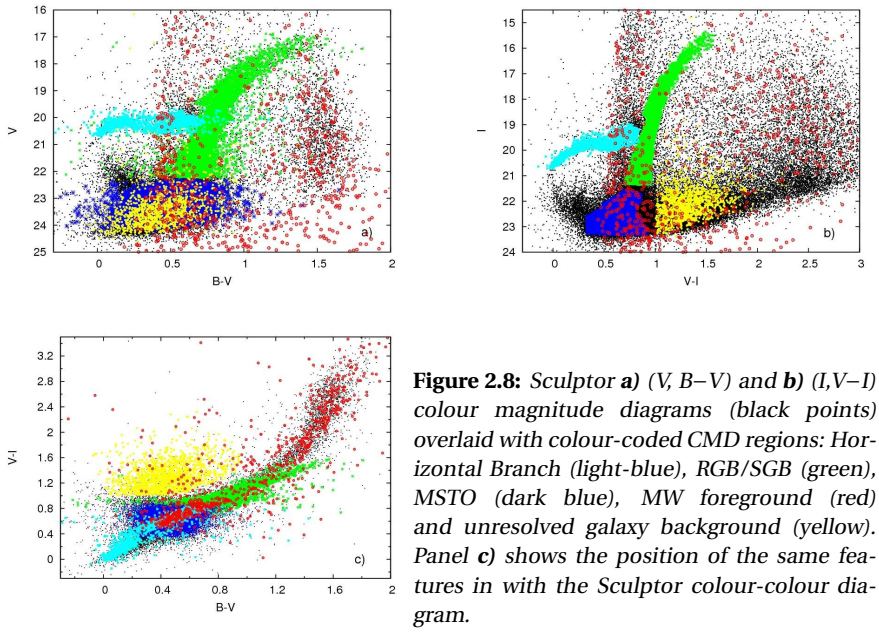

Figure 2.8: *Sculptor **a)** (V, B−V) and **b)** (I,V−I) colour magnitude diagrams (black points) overlaid with colour-coded CMD regions: Horizontal Branch (light-blue), RGB/SGB (green), MSTO (dark blue), MW foreground (red) and unresolved galaxy background (yellow). Panel **c)** shows the position of the same features in with the Sculptor colour-colour diagram.*

It is clear from Figure 2.8 that the Milky Way foreground contaminates several features in the Sculptor CMDs, including the MSTO. The foreground stars become distinct from the main Sculptor population in Colour-Colour space for the reddest colours, as can be seen from the distinct 'plume' of stars in Figure 2.8c at (V−I)≈1.6-3.4 and (B−V)≈1.2-

1.8. The unresolved background galaxies are most distinct from the Sculptor MSTO population in (V−I), making them show up as a separate 'cloud' of red stars, while in (B−V) they overlap with the MSTO. Therefore, having three filters helps in the interpretation of the CMDs. CMDs using different combinations of filters are also differently sensitive to age and metallicity effects (de Boer et al., 2011, in prep).

2.3.4 Structural Parameters

Having quantified the most prominent sources of foreground and background contamination in our CMDs we can now investigate the spatial distributions of the different CMD features using star counts in foreground/background corrected regions. We map the spatial distributions of different populations in the Sculptor dSph using 2D iso-density contour maps. The stars are convolved with a normalized Gaussian with a width of σ=0.05 deg to generate intensity distributions. These distributions are then used to construct iso-density contours. We obtain the intensity level of the foreground stars by applying the same procedure to the Besançon model predictions, spread homogeneously across the field.

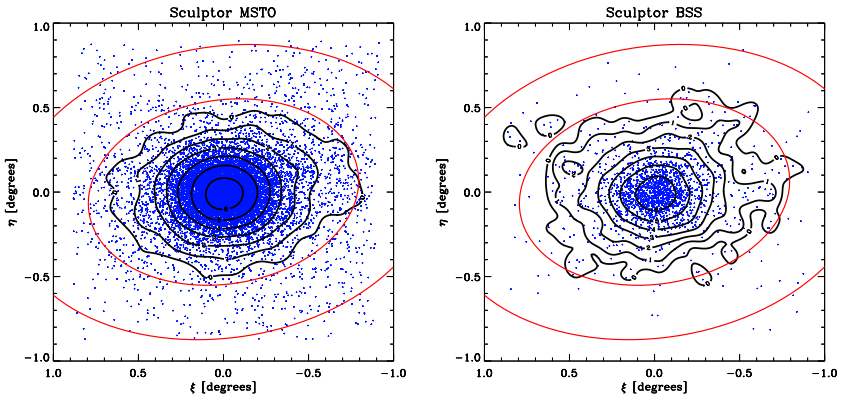

Figure 2.9: *Contour maps of the MSTO and BSS populations overlaid on the individual stars, shown as dots. The outer (red) ellipse is the tidal radius of the galaxy. The inner (red) ellipse is the largest ellipse not influenced by contour deformation caused by the proximity of the edge of observational coverage. The outermost contour in each plot is defined as 1% of the foreground corrected maximum intensity level. Subsequent contour levels increase by a factor 2 for each contour. North is up, and East is to the left.*

Since the centre of the resulting contour maps was found to be off-centre with respect to the published RA and DEC of the Sculptor centre we decided to re-derive the structural parameters of Sculptor using our current data set. Using 2D spatial Hess diagrams with a bin size of 0.02×0.02 deg we investigated the radial variation of the central position, eccentricity and position angle with the IRAF task **ELLIPSE**. The analysis reveals that the central position of Sculptor in our data set is located at RA=01:00:06.36,

DEC=−33:42:12.6, which is west ($-0.66' \pm 0.06'$) and north ($0.288' \pm 0.05'$) of the central coordinates listed by Mateo (1998). The eccentricity is found to be e=0.26±0.01 and the position angle PA=85.26±0.91, compared to the literature values of e=0.32 and PA=99 (Irwin and Hatzidimitriou, 1995). These parameters for our data set are adopted for the rest of the analysis in this chapter.

With these parameters the contour maps of the bright stars (down to the HB) confirm previous results, showing that the outer contours are more elliptical than the inner and that the spatial distribution of the RHB and BHB populations are different. We show for the first time the spatial distribution maps of the MSTO and BSS population in Figure 2.9. The BSS population looks similar in extent to the RGB and BHB. It shows the same change in ellipticity of the contours with different radii, as observed in the brighter features.

A small overdensity is visible around ξ=−0.5, η=0.1 in the MSTO stellar distribution in Figure 2.9, which is more prominent in the spatial Hess diagram (Figure 2.10). The photometric overdensity has about 30±5.5 stars per bin of 4.5×4.5 arcmin, compared to the mean number of stars of 13.6±3.7 per bin at the corresponding elliptical radius. The feature coincides spatially with the stars of a velocity substructure found in ESO/FLAMES spectroscopy (Battaglia, 2007), which are overlaid on the Hess diagram in Figure 2.10. The velocity substructure is made up of stars found in a cold structure at $0.2 < r_{ell} < 0.6$ deg, with heliocentric velocities between 128 and 142 km/s and a velocity dispersion of 2.4±0.7 km/s. The spectroscopic metallicities cover a range of −2.8<[Fe/H]<−1.6 dex. The substructure can be split up into two parts, one at $0.2 < r_{ell} < 0.3$ deg (crosses in Figure 2.10) with a narrow metallicity range of [Fe/H]=−1.96±0.05 and one at $0.3 < r_{ell} < 0.6$ deg (circles in Figure 2.10) with a broad metallicity range of −2.8<[Fe/H]<−1.6 dex. The photometric overdensity matches the spatial position of the velocity substructure at $0.3 < r_{ell} < 0.6$ deg. In terms of the CMD, the stars in the substructure match the same distribution as the main body of Sculptor stars, indicating that they are likely drawn from the same population, with a broad metallicity range.

In order to investigate asymmetries in the spatial distributions of the different CMD populations we performed starcounts within annuli centred on Sculptor. For different r_{ell} the fraction of stars West (ξ<0) of the centre versus East (ξ >0) of the centre is measured within an annulus. Figure 2.11 shows the fraction N_{West}/N_{East} for the full CMD (green circles), a selection of the CMD containing only Sculptor (black crosses), BSS population (blue asterisks), foreground stars (cyan filled boxes) and the unresolved background galaxies (red plusses).

The Sculptor populations (overall Sculptor, BSS) are almost symmetric for small elliptical radii, becoming more asymmetric further out. The foreground stars show a symmetric distribution at all radii, consistent with Galactic population models. The unresolved background galaxies (see Figure 2.8) display an anti-symmetric distribution with regards to the Sculptor features, which might be caused by obscuration of background galaxies by Sculptor stars, or a position-dependent morphological misclassification of galaxies and stars. The asymmetry difference of BSS stars with regards to the overall Sculptor population discussed by Mapelli et al. (2009) is not reproduced here and is likely due to the comparison with the full CMD at large radii instead of with

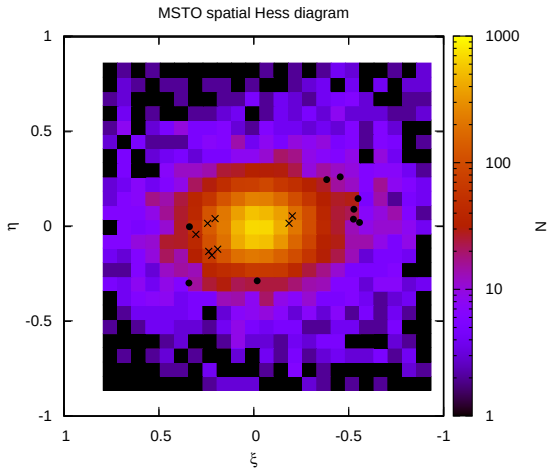

Figure 2.10: *Spatial Hess diagram of the MSTO population centred on Sculptor. Overlaid on the diagram are stars found in a velocity substructure (crosses indicate the substructure at 0.2 < r_{ell} < 0.3 deg and circles the one at 0.3 < r_{ell} < 0.6 deg.). A small photometric overdensity is visible at ξ=-0.5, η=0.1, which coincides with one of the velocity substructures.*

the overall Sculptor population. The figure shows that the overall Sculptor population displays a slight asymmetry, with ≈10% more stars in the West than in the East, in the same direction as observed earlier by Eskridge (1988d).

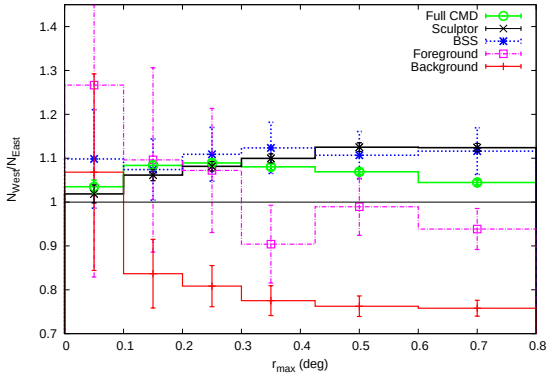

Figure 2.11: *Fraction of Sculptor stars in the West (ξ<0) vs East (ξ>0) for different annuli of elliptical radius. Different populations are indicated with different colors, full CMD (green circles), overall Sculptor (black crosses), BSS (blue asterisks), foreground (cyan filled boxes) and background galaxies (red plusses)*

2.4 Interpretation

Using the calibrated photometric catalog we can look at the behaviour of any stellar population over a large fraction of the galaxy. We can study the radial distributions of different CMD features and search for variations with elliptical radii. By analysing the CMDs of the MSTO region and combining this with information coming from spectroscopic surveys we can quantify the ages and metallicities of the different populations making up the Sculptor dSph.

2.4.1 The Horizontal Branch

We know from previous studies of the Sculptor dSph (Majewski et al., 1999; Hurley-Keller et al., 1999; Tolstoy et al., 2004) that two distinct HB populations are present, with different radial distributions. This can also be seen in our data in Figure 2.12, showing the foreground corrected number of stars in each bin of elliptical radius in the RHB and BHB populations. Since the number of foreground stars is not predicted to vary significantly with position across Sculptor the foreground correction is made by taking the predicted number of Galactic stars per unit area (as given by the Besançon models) within the same magnitude and colour range as the CMD feature. This number is then multiplying by the area of the ellipses of different r_{ell}, and subtracted from the observed star counts. The figure shows that the RHB population dominates in the central region, after which it falls off more rapidly than the BHB distribution. The BHB population is more uniformly distributed across the galaxy, and dominates only in the outer region.

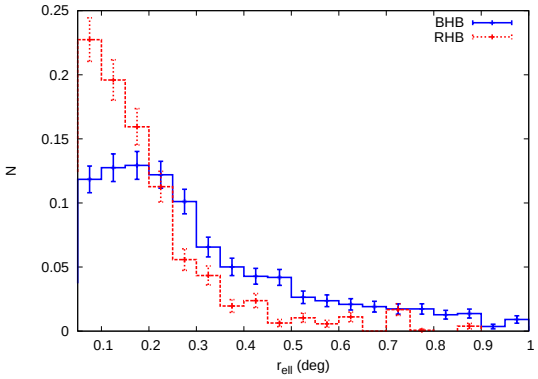

Figure 2.12: *Radial histograms of RHB (red, dashed) and BHB (blue, solid) populations in the Sculptor dSph.*

Besides the spatial distribution, the HB of Sculptor has also been extensively studied to look for variable stars. More than 90 RR Lyrae stars have been found in Sculptor, with an average [Fe/H]≈−1.7 dex or lower, along with 3 anomalous metal-poor Cepheids (Kaluzny et al., 1995). This confirms that the bulk of the stellar population in Sculptor is metal-poor. In addition, 2 more metal-rich short period variables (with [Fe/H]≤−0.7 dex) were found within the core radius, in accordance with the spatial distribution of the two HB populations.

2.4.2 The Red Giant Branch

The RGB of Sculptor is long known to have a larger colour spread than seen in Globular Clusters (Da Costa, 1984), consistent with it having experienced an extended period of star formation. However, no radial differences as clear as those on the HB have been found. This is because all populations overlap on the RGB, especially at low metallicity, and are thus not clearly distinguishable from each other.
In Figure 2.13 we show the RGB region in the (I,V−I) CMD for different elliptical radii.

Overlaid on the CMDs are two reference isochrones from the Dartmouth Stellar Evolution Database (Dotter et al., 2008). The isochrones are representative of the most metal-poor ([Fe/H]=−2.45 dex) and most metal-rich ([Fe/H]=−0.90 dex) stars making up the bulk of the population of Sculptor, as derived from RGB spectroscopy (Tolstoy et al., 2004; Battaglia, 2007). The most metal poor stars found in Sculptor with these surveys have a metallicity of [Fe/H]≤ −2.5 dex, which is not available in the Dartmouth Stellar Evolution Database. Instead, the most metal poor isochrone available in the library ([Fe/H]=−2.45 dex) is used. The ages of the isochrones have been selected to fit the colours of RGB stars of corresponding metallicity. For increasing elliptical radius it can be seen that the brightest and reddest part of the RGB diminishes, as does the blue side of the Subgiant Branch. From the overlaid isochrones it can be seen that this is broadly consistent with the disappearance of the metal-rich component, as expected from the HB distributions.

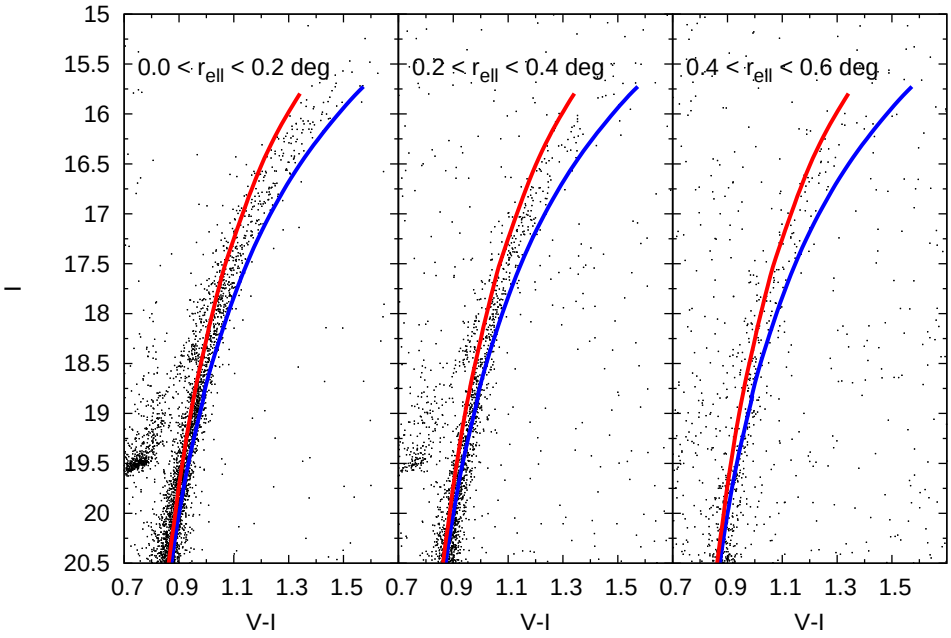

Figure 2.13: *The distribution of stars on the Red Giant Branch for different elliptical radii. A metal-rich isochrone ([Fe/H]≈−1.10 dex, [α/Fe]≈−0.10 dex, age=7Gyr, black) and metal-poor isochrone ([Fe/H]≈−2.45 dex, [α/Fe]≈0.40 dex, age=14Gyr, grey) from the Dartmouth Stellar Evolution Database have been overlaid in each panel.*

On the RGB, low resolution Ca II triplet (R~6500) spectroscopy is available for ≈630 individual stars using VLT/FLAMES (Tolstoy et al., 2004; Battaglia, 2007; Starkenburg et al., 2010). We correlated this information with our photometric catalogue to combine the colors, magnitudes and [Fe/H] for a sample of these stars. In Figure 2.14, we

show an (I,V−I) CMD of the RGB region for different radii overlaid with [Fe/H] metallicities for probable members stars to the Sculptor dSph where Ca II spectroscopy is available (Starkenburg et al., 2010). Besides member RGB stars, numerous AGB stars are visible as well, along with a number of possible foreground stars.

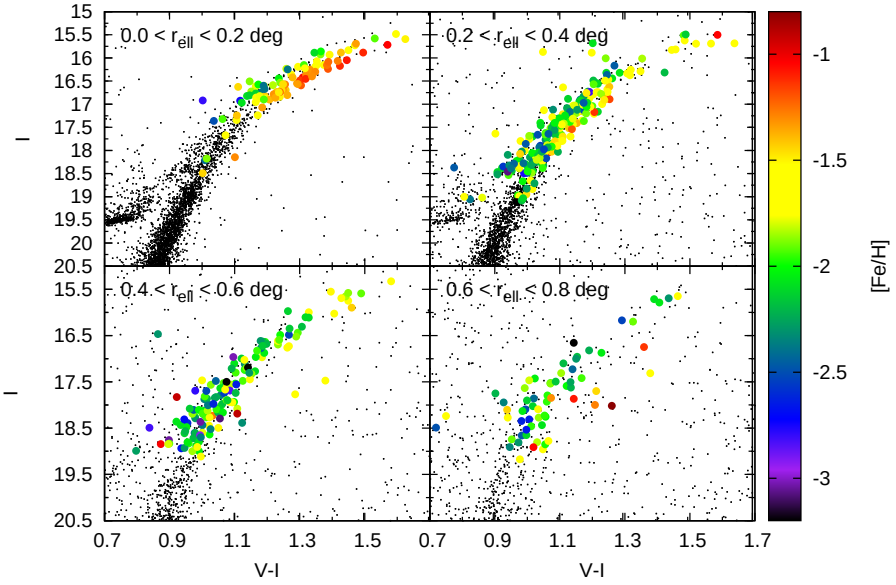

Figure 2.14: *Sculptor CMD in the RGB region at different elliptical radii, r_{ell} with Sculptor photometry as (black) dots, overlaid with larger (coloured) filled circles are stars for which spectroscopic metallicities are available. The colours indicate the [Fe/H] metallicities of individual RGB stars (Starkenburg et al., 2010), and the scale is given at the side of each CMD.*

In the central region low resolution targets were selected only from stars that also had high resolution abundances, which explains the brighter magnitude limit in the top left panel of Figure 2.14. Figure 2.14 shows that in the inner region stars are present with metallicities ranging from [Fe/H]=−1.0 to [Fe/H]>−3.0 dex. As we go outward in the galaxy the more metal rich components which are present on the bright, red part of the RGB in the inner 0.2 deg disappear. This is in agreement with the radial trend observed from the RGB photometry in Figure 2.13.

2.4.3 The Main Sequence Turn-Offs

The MSTO region of the Sculptor dSph has previously only been studied using small fields of view. These studies determined an age range of 13±2 Gyr (Da Costa, 1984; Dolphin, 2002). We present here the first wide-field study of the MSTO population using homogeneous photometry that covers a large fraction of the entire galaxy.
A close-up of the MSTO region in the (I,V−I) CMD for different elliptical radii is shown

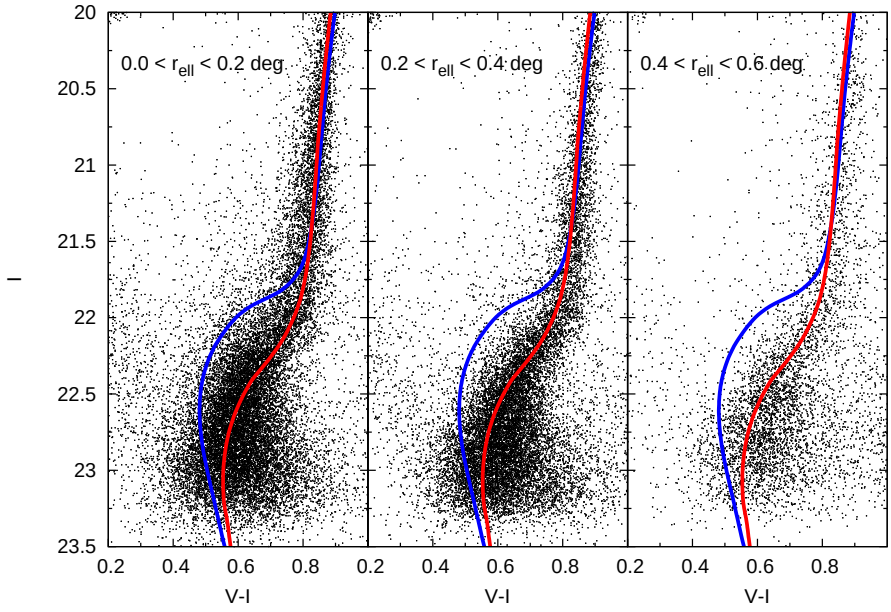

Figure 2.15: *The distribution of stars on the Main Sequence Turn-Off for different elliptical radii. Two isochrones representative of a metal-rich ([Fe/H]≈−1.10 dex, [α/Fe]≈−0.10 dex, age=7Gyr, black) and a metal-poor ([Fe/H]≈−2.45 dex, [α/Fe]≈0.40 dex, age=14Gyr, grey) population are overlaid in each panel.*

in Figure 2.15, overlaid with the same two isochrones used in Figure 2.13 (one relatively metal poor and old and one metal rich and younger). For increasing distance from the centre we see that the MSTO properties change. The inner regions display both young metal-rich stars and old metal-poor stars, while the outer regions lacks the young, metal-rich population.

Using isochrones which match the spectroscopic metallicities on the RGB, we selected regions of the MSTO corresponding to different metallicities and ages (see Figure 2.16). Regions were defined by selecting stars within a certain distance from each isochrone with the given age and metallicity. The range of [Fe/H] and [α/Fe] abundances of the isochrones were chosen to cover the spectroscopic abundance range (Tolstoy et al., 2009, Hill et al., in prep), with an equal spacing from metal-rich ([Fe/H]=−1.00 dex) to metal-poor ([Fe/H]=−2.20 dex). The ages of the isochrones were determined by comparing them in the CMD to stars with the same abundance range. Figure 2.16 shows the selected regions in the CMD as well as the resulting radial histograms along with the distributions of the RHB and BHB stars. From the MSTO radial distributions we see that the selected regions form a gradient from the metal-poor (BHB) to the metal-rich (RHB) distributions. This shows for the first time that this gradient is not only in metallicity, but also in age. The presence of an extended star formation history was

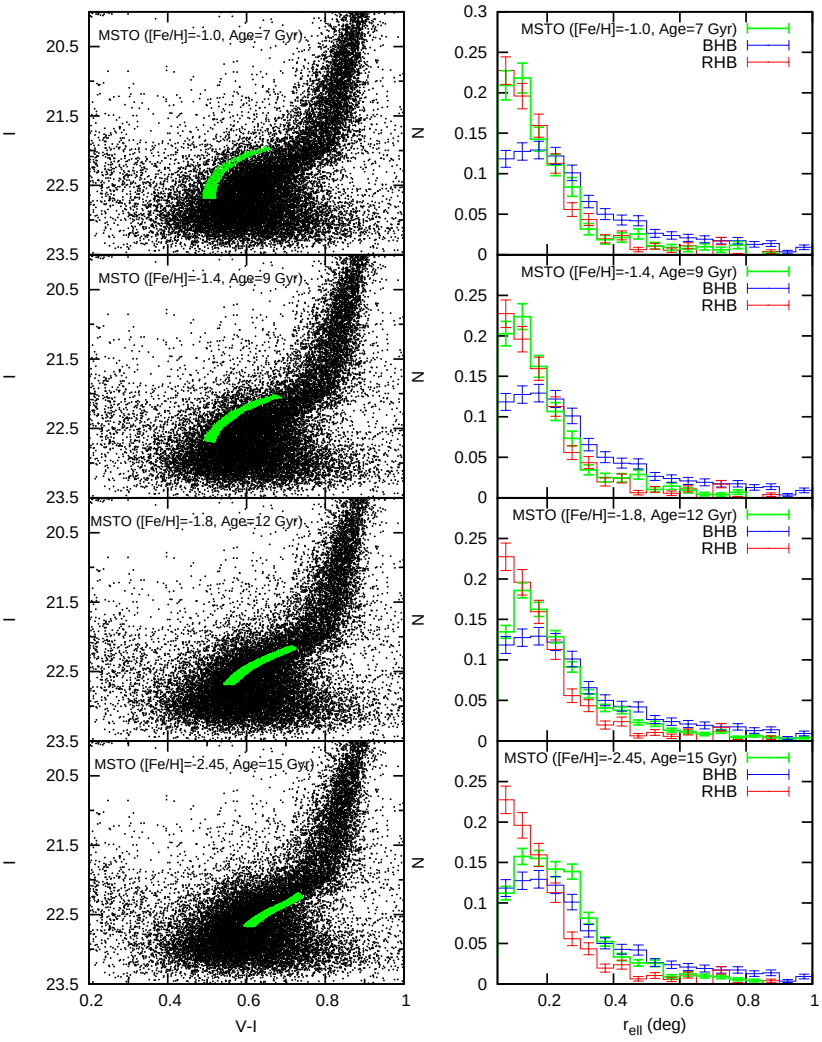

Figure 2.16: *On the left are selected regions on the MSTO in green for the labelled age and metallicity. The corresponding radial histograms are shown on the right (in green). Radial histograms of BHB (blue) and RHB (red) stars are also plotted. The radial distributions of the selected regions change from RHB-like for high metallicity to BHB-like for low metallicity.*

expected from studies of the brighter CMD features, but now for the first time the effects of the age gradient can be seen in the radial distribution. The oldest, most metal poor populations (with [Fe/H]≈−2.5 dex) were formed roughly 14 Gyr ago, while the youngest most metal rich populations (with [Fe/H]≈−1.0 dex) were formed approximately 7 Gyr ago.

2.4.4 Blue Straggler stars

In the Sculptor CMDs (Figure 2.5 and 2.6) a BSS population appears to lie above the MSTO region (see labels in Figure 2.4). In terms of understanding the evolutionary history of Sculptor it is important to understand what process produced these stars. Specifically, are they the result of star formation that continued until the much more recent times, after the main bulk of star formation 7-14 Gyr ago? There is a mechanism of creating BSS stars proposed for globular clusters resulting from mass transfer between low mass stars (McCrea, 1964), or collisional processes (Sigurdsson et al., 1994), which relates to an evolution of the old population in Sculptor.
The radial distribution of the BSS population is shown in Figure 2.17, along with the distributions of RGB and MSTO. The distributions of the other features have been scaled to same total number of stars as the BSS distribution. There is a good agreement between the distributions of BSS and RGB or MSTO, which represent the overall population in Sculptor. This seems to indicate that the BSS population is not linked to any distinct age or metallicity, but likely also has the same age and metallicity gradient as seen in the other CMD features.

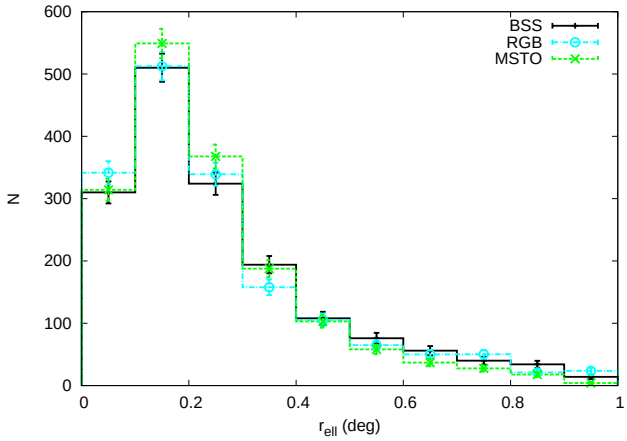

Figure 2.17: *Radial distributions of BSS stars (black crosses) compared to RGB (light blue filled circles), and MSTO (green filled squares).*

No obvious trend of a radial gradient in the BSS population is evident in the CMDs with increasing radius, indicating that the BSS population can not easily be separated in different components. In Figure 2.17 there is also no evidence of a central concentration of the BSS population with respect to the overall Sculptor population, and hence no indications of collisional BSS formation as seen in Globular Clusters (Ferraro et al., 1997). This is in agreement with the fact that the central luminosity density of dSph's (0.055

$L_\odot / pc^{-3}$ for Sculptor, see Mateo (1998)) is significantly lower than observed in globular clusters (3200 $L_\odot / pc^{-3}$ for M3, see Harris (1996)). This means the collision rates in dSph's must be much lower than in globular clusters, which makes the collisional BSS formation channel less likely to be dominant than the binary channel.
In order to test if the BSS population is made up of a "normal" young population we modelled the distribution of BSS stars in the CMDs using isochrones, covering the metallicity range observed from spectroscopy, assuming an age of 3 Gyr. Taking completeness effects into account the observed population of ≈1600 BSS stars should lead to ≈35 stars on the upper RGB. Thus, from the photometry alone it is not possible to rule out that the BSS are a "normal" young population. However, if the BSS stars were a young population they would be expected to be even more centrally concentrated than the older populations, if the trend of increasing central concentration with younger ages holds for these stars. Since this is not observed in Figure 2.17, BSS formation through mass transfer seems most likely, which results in a distribution similar to that of other populations. This is consistent with results found by Mapelli et al. (2007, 2009) for several nearby dwarf spheroidal galaxies, including Sculptor.

2.5 Discussion

We have shown that the two distinct stellar populations found in the Sculptor dSph by Tolstoy et al. (2004) using imaging of HB stars and spectroscopy of RGB stars are linked not only to a metallicity gradient but also to an age gradient going from roughly 7 to 14 Gyr ago. The Main Sequence Turn-Offs (Figures 2.15 and 2.16) show unequivocally that the outer regions of Sculptor lack significant numbers of young stars (<10 Gyr). This is supported by the spectroscopic Ca II triplet abundances (Figure 2.14), which show a decrease in metal-rich stars with increasing r_{ell}.
By using a combination of photometry and spectroscopic abundance distributions, we determine the age gradient using the MSTO (Figure 2.16). This shows that a radial gradient is present in age and metallicity, which is observed also as a bimodality in the HB distribution and as a spread on the RGB and MSTO. The importance of the MSTO is shown by the fact that only using this part of the CMD it is possible to constrain the age gradient accurately. Linking the age gradient to the existing metallicity gradient suggests that the observed change in HB morphology is due not only to a metallicity gradient (as suggested by Harbeck et al. (2001)), but that age is also an important parameter.
No obvious radial trend with age or metallicity is visible in the BSS population, but there are relatively few stars and there is no obvious way to separate them into distinct components. However, since its radial distribution does match the distribution seen in the overall Sculptor populations (Figure 2.17), it is possible that the gradient is also present there.
These results are consistent with the picture where the Sculptor dSph first formed an extended old metal-poor component, after which later generations of progressively more metal-rich stars were formed ever more concentrated towards the centre of the galaxy. It seems that about 7 Gyr ago the gas supply ran out and the galaxy continued

passively evolving up to the present time.
The fact that the population gradient is still visible today suggests that it is unlikely that the inner parts of Sculptor have suffered any significant tidal disruption, which could mix the different stellar populations together. Indeed, the spatial distributions (Figure 2.9) do not show any signs of obvious recent tidal interactions. This is in agreement with predictions of theoretical models of the Sculptor dSph (Sales et al., 2010). One aspect which remains unclear is what has caused the increasing ellipticity with radius (Battaglia, 2007). This may be due to a very early disruption, which would be visible only in the oldest outer parts of Sculptor, beyond radii studied here. Additionally, it could also be due to an encounter that only affected the outer regions of Sculptor.
In the next chapter, the CMDs we have presented here will be used to derive a detailed Star Formation History of the Sculptor dSph. This will be combined with high resolution spectroscopic information (Hill et al., in prep) to derive the enrichment timescales of various elements, and how this fits into the star formation history timescale.

acknowledgements

The authors thank ISSI (Bern) for support of the team "Defining the full life-cycle of dwarf galaxy evolution: the Local Universe as a template". T.d.B. would like to thank David Hogg and Dustin Lang for their help in creating a MCMC code to obtaining photometric solutions. T.d.B., E.T. and G.F. gratefully acknowledge the Netherlands Foundation for Scientific Research (NWO) for financial support.

Appendix 2.A List of standard field observations

To provide an accurate calibration of the science observations, observations of standard star fields were carried out during the observing runs in September 2008 and November 2009. Fields were selected from the Landolt standard fields (Landolt, 2007, 1992), to be used together with Stetson standard star photometry (Stetson, 2000). Using the CTIO 4m/Blanco telescope observations of standard star fields were taken during the night in between science observations, in order to monitor the photometric fidelity throughout the night. Standard fields were selected to cover a broad range of airmass and colour, to allow adequate determination of the airmass coefficient and colour term in the photometric solution. In order to ensure of the most accurate calibration possible additional observations of standard stars and Sculptor fields were taken using the CTIO 0.9m telescope during 3 nights in 2008 under photometric conditions. Using these observations the calibration of the 4m Sculptor fields using the 4m standards can be checked and adjusted to the photometric solution obtained under photometric conditions on the 0.9m telescope. Tables 2.4 and 2.5 list the observations of standard fields taken with the 0.9m and 4m Blanco telescopes respectively, taken during the runs in 2008 and 2009. The names of the standard fields are given, along with information on exposure times, seeing conditions (on image) and airmass.

Table 2.4: *List of observed standard star fields with the 0.9m CTIO telescope. Information is given about exposure time, airmass and seeing conditions as determined on image.*

Field	RA J2000	DEC J2000	Filter	exp time sec	seeing $''$	airmass
JL 163	00:10:42.6	−50:14:10	B	150	1.4, 1.8-2.0	1.16,2.31
			V	150	1.3, 1.8-2.1	1.15, 2.39
			I	300	1.2, 1.6-1.7	1.13, 2.53
T Phe	00:30:34.4	−46:28:08	B	150	1.4-1.7, 2.2-2.4	1.04-1.26, 1.57
			V	150	1.3-1.7, 2.0	1.04-1.28, 1.60
			I	300	1.3-1.7, 2.2-2.4	1.04-1.34, 1.65
MCT 0401-4017	04:03:01.2	−40:11:28	B	150	1.4-1.5, 2.1	1.04-1.24, 2.16
			V	150	1.3-1.6, 2.4	1.05-1.20, 2.08
			I	300	1.2-1.5, 2.0	1.04-1.18, 2.00
LB 1735	04:31:34.7	−53:37:13	B	150	1.3, 2.3	1.11-1.17, 1.38
			V	150	1.4, 1.9	1.11-1.18, 1.37
			I	300	1.2, 2.0	1.12-1.20, 1.34
LSE 259	16:53:45.1	−56:00:16	B	150	4.0	2.16
			V	150	2.2	2.21
			I	300	2.3	2.29
JL 82	21:36:01.0	−72:47:51	B	150	1.8	1.38-1.40
			V	150	1.5-1.7	1.39-1.41
			I	300	1.4	1.40-1.42
JL 117	22:54:55.5	−72:22:59	B	150	1.5	1.35
			V	150	1.4	1.35
			I	300	2.0	1.35

Table 2.5: *List of observed standard star fields with the 4m CTIO Blanco telescope during two observing runs. Information is given about exposure time, airmass and seeing conditions as determined on image.*

Field	RA J2000	DEC J2000	Filter	exp time sec	seeing $''$	airmass
			2008			
T Phe	00:30:34.4	−46:28:08	B	10, 8	0.9-1.1,1.9	1.05,1.08,1.20,2.66
			V	5, 4	0.8-1.0,1.9	1.05,1.08,1.17,2.62
			I	4, 3	0.8-1.0,1.8	1.05,1.08,1.17,2.55
MCT 0401-4017	04:03:01.2	−40:11:28	B	10, 8	0.9,1.3	1.02, 1.03
			V	5,4	1.0-1.1	1.02, 1.03
			I	4,3	1.0-1.1	1.02, 1.03
MCT 2019-4339	20:22:51.5	−43:29:24	B	10	1.3	1.1
			V	5	1.4	1.1
			I	4	1.1	1.1
JL 82	21:36:01.0	−72:47:51	B	10	1.6,1.8	1.57, 1.91
			V	5	1.5,1.8	1.56, 1.92
			I	4	1.2,1.5	1.55, 1.93
			2009			
T Phe	00:30:34.4	−46:28:08	B	30, 10	0.9-1.1	1.04,1.05
			V	30, 5	0.8-1.0	1.04,1.05
			I	30, 4	0.7-1.0	1.04,1.05
MCT 0401-4017	04:03:01.2	−40:11:28	B	10	0.9,1.7	1.42,1.44
			V	5	1.0,1.3	1.41,1.44
			I	4	0.9,1.3	1.40,1.45
MCT 0550-4911	05:51:53.9	−49:10:31	B	10	1.0,1.6	1.09,1.73
			V	5	0.9,1.2	1.10,1.72
			I	4	1.0,0.9	1.10,1.70
WD 0830-535	08:31:56.5	−53:40:52	B	10	1.5	1.13
			V	5	1.1	1.13
			I	4	0.9	1.12
LB 1735	04:31:34.7	−53:37:13	B	10	1.0	1.1
			V	5	0.9	1.1
			I	4	0.8	1.1
L92	00:55:38.0	+00:56:00.0	B	30, 5	1.5	1.18
			V	30, 5	1.2	1.17
			I	30, 5	1.3	1.17
L101	09:56:39.0	−00:19:53.0	B	30, 5	1.8	1.42
			V	30, 5	1.6	1.45
			I	30, 5	1.2	1.49
PG 2213-006	22:16:33.5	−00:23:34.7	B	30, 5	1.5	1.27
			V	30, 5	1.2	1.29
			I	30, 5	1.2	1.30
PG 0231+051	02:33:55.3	+05:14:22.9	B	30, 5	1.3	1.60
			V	30, 5	1.1	1.57
			I	30, 5	1.0	1.54
L95	03:53:58.0	+00:03:30.0	B	30, 5	1.5	2.10
			V	30, 5	1.4	2.00
			I	30, 5	1.4	1.90
L95	06:51:58.7	−00:24:18.7	B	30, 5	1.0	1.17
			V	30, 5	1.0	1.17
			I	30, 5	0.9	1.16

Appendix 2.B Photometric calibration

Obtaining an accurate photometric calibation is essential for a reliable interpretation of a CMD. For example the absolute luminosity of a Main Sequence Turn-off star correlates with age. The observing strategy was chosen in such a way as to combine deep 4m science images with 0.9m calibration images taken under photometric conditions. These images are used to ensure the most accurate photometric calibration possible for the science images.

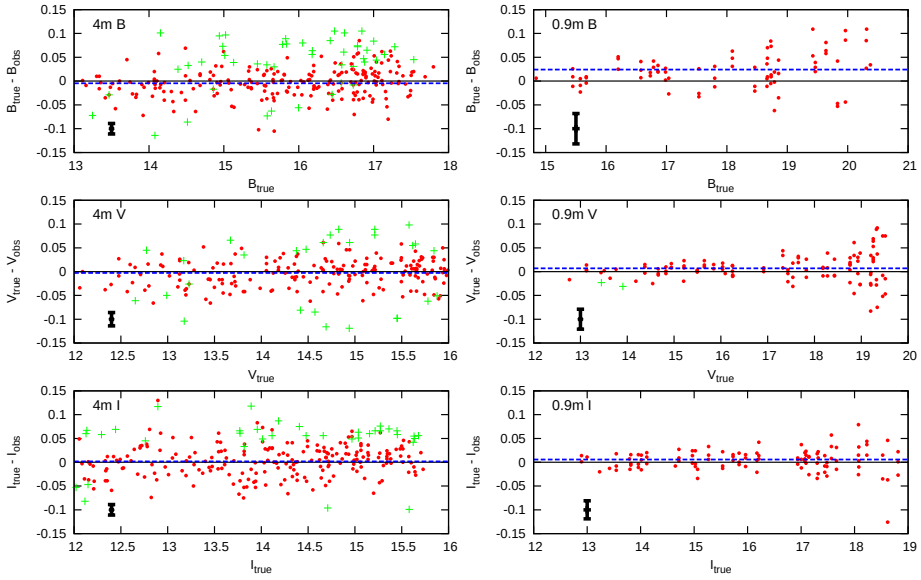

Figure 2.18: *Comparison between calibrated and true magnitudes for the standard stars used to obtain the photometric solution. Each plot shows magnitude residuals vs. true magnitude for different filters for the 4m data (left) and 0.9m data (right). Stars classified as outlyers when determining the photometric solution are marked as crosses. The average standard deviation of the residuals over all filters is ≈0.033 for the 4m data, and ≈0.03 for the 0.9m data. A line indicating the zero level residual (solid) and the mean of the residual (light, dashed) is also shown (visible only if there is an offset from zero), along with errorbars denoting the average photometric error. The zeropoint correction residuals are consistent with zero across all magnitudes, given the average photometric error. The mean of the residual in the 0.9m B (upper right) solution is most offset from zero (by 0.024) due to seeing conditions and large photometric error in B. However, the residuals are still within the average photometric error (±0.032), indicating an accurate calibration is achieved.*

A comparison of the calibrated magnitude and true magnitude of the standard stars used to obtain the photometric solution versus observed magnitude (for both the 4m and 0.9m data) is shown in Figure 2.18. Similar plots showing the magnitude difference versus airmass and colour are shown in Figures 2.19 and 2.20 respectively. A line indi-

cating the zero level residual (solid) and the mean of the residual (dashed) is shown, along with errorbars denoting the average photometric error. These plots show the accuracy of the calibration applied to the science data. The standard deviation of the residuals is $\sigma_B \approx 0.033$, $\sigma_V \approx 0.028$, $\sigma_I \approx 0.032$ for the 4m data and $\sigma_B \approx 0.038$, $\sigma_V \approx 0.028$, $\sigma_I \approx 0.029$ for the 0.9m data. Figure 2.18 shows that the zeropoint correction is consistent across all magnitudes used in the photometric solution, with the mean level of the residuals (dashed line) being less than the average photometric error. Figures 2.19 and 2.20 show that the effects of colour and airmass are well taken care of, with the mean level of the residuals (dashed line) being less than the average photometric error. Residuals in the B band observations of the 0.9m telescope are most offset from zero, due to the poorer seeing conditions and larger photometric errors in the B band. However, the B band residuals are consistent with zero in all plots, given the average photometric error in B, showing that an accurate calibration was obtained.

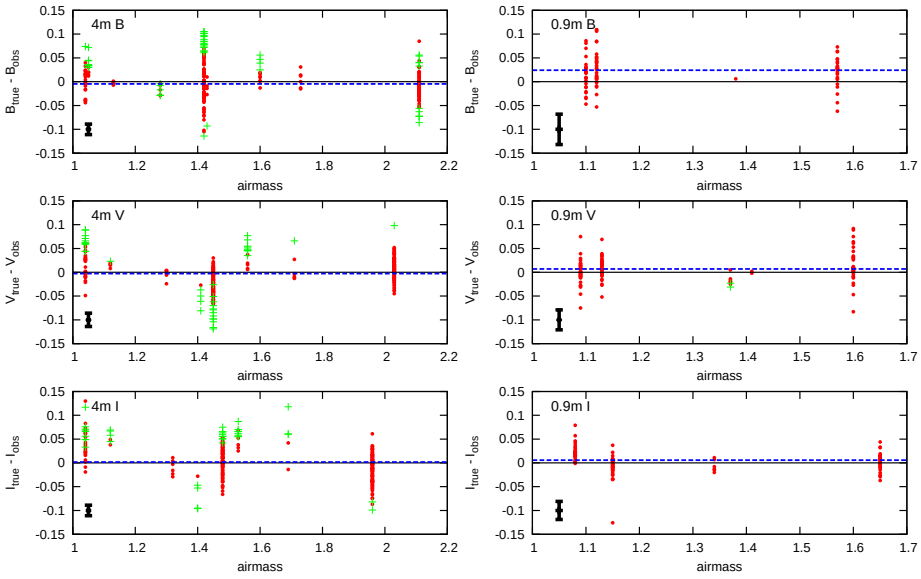

Figure 2.19: *Magnitude residuals vs. airmass for photometric standard stars for the 4m data (left) and 0.9m data (right). See Figure 2.18 for details. No trend with increasing airmass is visible, showing that the effects of airmass are well taken care of in the photometric calibration.*

A second check of the photometry is done by comparing aperture and PSF magnitudes.We determined aperture magnitudes for small samples of stars in standard fields and in the central Sculptor pointing. A photometric solution was obtained from the aperture photometry, and used to calibrate the aperture magnitudes in the Sculptor central field. Then, a comparison of the PSF and aperture magnitudes is made (shown in Figure 2.21) for both the 0.9m and 4m data. The standard deviation of the residuals is $\sigma_B \approx 0.101$, $\sigma_V \approx 0.040$, $\sigma_I \approx 0.033$ for the 4m data and $\sigma_B \approx 0.108$, $\sigma_V \approx 0.028$, $\sigma_I \approx 0.029$

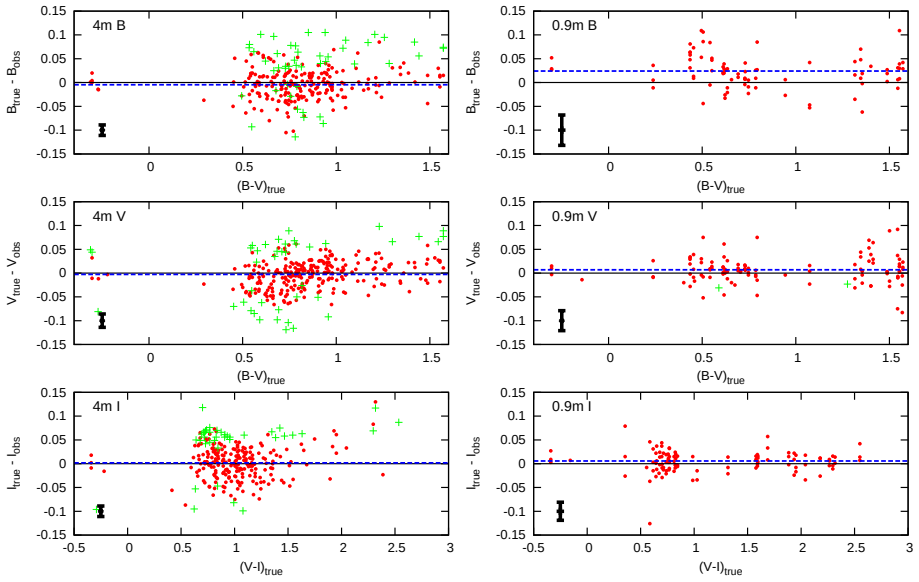

Figure 2.20: *Magnitude residuals vs. colour for 4m (left) and 0.9m (right).standard stars. See Figure 2.18 for details. No trend with colour is visible, showing that the photometric calibration correctly takes care of the effects of the colour term.*

for the 0.9m data. Figure 2.21 also shows that the differences between aperture and PSF magnitudes are negligible within the average photometric errors, giving confidence to the reliability of our PSF photometry. The B band residual is once again most offset from zero (by 0.05), but consistent with zero given the photometric errors (±0.061).
Next, the calibrated 4m and 0.9m PSF mags and aperture mags are compared to check whether the 4m data is consistently calibrated with the 0.9m data taken under photometric conditions. A comparison of both data sets for the central Sculptor field is shown in Figure 2.22 for PSF and aperture magnitudes respectively. Solid black errorbars have been overplotted for the PSF magnitudes, indicating the average error on the magnitude difference at bright, intermediate and faint magnitudes. For all three selections the mean of the residual is smaller than the error on the magnitude difference (from bright to faint: **B:** 0.0043<0.0617, 0.0079<0.0880, 0.0095<0.1546, **V:** 0.0099<0.0176, 0.0154<0.0484,
0.0187<0.0890, **I:** 0.0002<0.0125, 0.0072<0.0272, 0.0185<0.0844). For the aperture magnitudes the mean of the residuals (**B:** 0.0170 **V:** 0.0321 **I:** 0.0236) is comparable to the average error (**B:** 0.0759 **V:** 0.0292 **I:** 0.0191). The relatively high residuals are possibly due to the low number of stars with aperture magnitudes used in the determination of the photometric solution for the 0.9m data.
The above figures show that the 4m calibration properly takes into account zeropoint, airmass and colour effects. Furthermore, the calibration is consistent between aper-

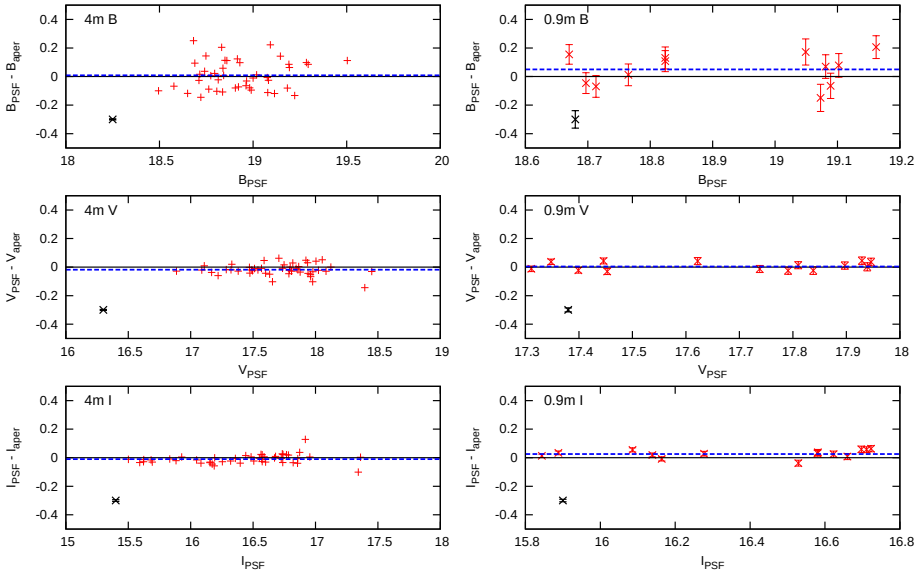

Figure 2.21: *Comparison of aperture and PSF magnitudes in the central Sculptor pointing for the 4m data (left) and 0.9m data (right). See Figure 2.18 for details. The residuals are consistent with zero, given the photometric errors, showing that the calibrations using aperture and PSF magnitudes agree.*

ture and PSF magnitudes, given the photometric errors. The absolute calibration of the 4m data is consistent with that of the 0.9m data for PSF magnitudes and to a lesser extent for aperture magnitudes. Thus, an accurate absolute calibration is achieved for the PSF magnitudes used in the final photometry catalog. The final catalog has an average accuracy due to random errors for all filters of $\approx \pm 0.002$ for the brightest stars, while at the faint end the accuracy is $\approx \pm 0.2$. The accuracy of the calibration varies for different magnitudes and filters, but the comparison of calibrated and true magnitudes shows an accuracy of ≈ 0.04 mag or better across the magnitude range used.

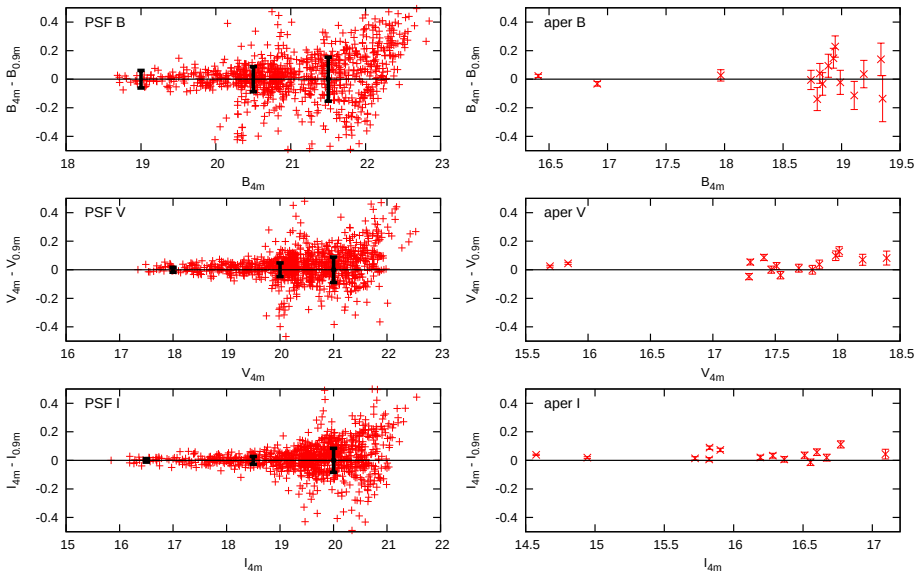

Figure 2.22: *Comparison between 4m and 0.9m photometry for the central Sculptor pointing for PSF (left) and aperture (right) magnitudes. A plume of short period RR Lyrae variable stars is visible in all bands in the PSF data at B~ 20.5−21; V~ 20−20.5; I~ 19.5−20.5. Solid black errorbars overplotted in the left-hand figures indicate the average error on the magnitude difference at the corresponding magnitude. The residuals of the PSF magnitudes are consistently smaller than the error on the magnitude difference, while for the aperture magnitudes the residuals are similar to the error.*

CHAPTER THREE

THE STAR FORMATION & CHEMICAL EVOLUTION HISTORY OF THE SCULPTOR DWARF SPHEROIDAL GALAXY

T.J.L. de Boer, E. Tolstoy, V. Hill, et al.

Based on: A&A, 2012, 539, A103

Abstract

We have combined deep photometry in the B,V and I bands from CTIO/MOSAIC of the Sculptor dwarf spheroidal galaxy, going down to the oldest Main Sequence Turn-Offs, with spectroscopic metallicity distributions of Red Giant Branch stars. This allows us to obtain the most detailed and complete Star Formation History to date, as well as an accurate timescale for chemical enrichment.

The Star Formation History shows that Sculptor is dominated by old (>10 Gyr), metal-poor stars, but that younger, more metal-rich populations are also present. Using Star Formation Histories determined at different radii from the centre we show that Sculptor formed stars with an increasing central concentration with time. The old, metal-poor populations are present at all radii, while more metal-rich, younger stars are more centrally concentrated. We find that within an elliptical radius of 1 degree, or 1.5 kpc from the centre, a total mass in stars of 7.8×10^6 $M_\odot$ was formed, between 14 and 7 Gyr ago, with a peak at 13−14 Gyr ago.

We use the detailed Star Formation History to determine age estimates for individual Red Giant Branch stars with high resolution spectroscopic abundances. Thus, for the first time, we can directly determine detailed timescales for the evolution of individual chemical elements. We find that the trends in alpha-elements match what is expected from an extended, relatively uninterrupted period of star formation continuing for 6−7 Gyr. The knee in the alpha-element distribution occurs at an age of

10.9±1Gyr, suggesting that SNe Ia enrichment began ≈2±1Gyr after the start of star formation in Sculptor.

3.1 Introduction

The Sculptor dwarf spheroidal galaxy (dSph) is a relatively faint ($M_V \approx -11.2$), well studied system in the Local Group. A distance of 86±5 kpc has been determined from RR Lyrae star measurements, in good agreement with other distance determinations, such as the tip of the RGB and horizontal branch level (Pietrzyński et al., 2008, and references therein). Sculptor is located at high galactic latitude (b=−83°) with relatively low reddening, E(B−V)=0.018 (Schlegel et al., 1998).

Past studies of the Star Formation History (SFH) of Sculptor have been made using colour-magnitude diagrams (CMDs) of varying depth, and spatial coverage. Using CMDs down to the Main Sequence Turn-Off (MSTO) in a field just outside the core radius Da Costa (1984) determined an age range for Sculptor of 13±2 Gyr. A small field of view (~2′), deep HST image of a field well outside the centre of Sculptor confirmed the ancient age (15±2 Gyr) of the bulk of the stars in Sculptor using synthesis CMD analysis, but also showed a small tail of star formation reaching down to more recent times (Monkiewicz et al., 1999; Dolphin, 2002). An effort was made to combine detailed spectroscopic abundances of 5 stars with photometric ages, which also suggested that Sculptor is predominantly old, with a small tail of intermediate age stars (Tolstoy et al., 2003).

In a previous qualitative study of wide-field CMDs, the Horizontal Branch (HB) morphology was found to change significantly with radius (Majewski et al., 1999; Hurley-Keller et al., 1999), which was later linked to a metallicity gradient (Tolstoy et al., 2004). From deep wide-field CMDs reaching the oldest MSTOs, covering a large fraction of Sculptor, this metallicity gradient was also found to be linked to an age gradient (de Boer et al., 2011).

In Sculptor, wide-field medium resolution Ca II triplet spectroscopy of a large number of RGB stars is available (Battaglia, 2007; Battaglia et al., 2008b; Starkenburg et al., 2010), giving a well defined spectroscopic Metallicity Distribution Function (MDF) for stars with ages ≥1.5 Gyr old. In the central 25′ diameter region of Sculptor high resolution (HR) spectroscopy (Hill et al., in prep, see Tolstoy et al., 2009; Tafelmeyer et al., 2010; Frebel et al., 2010) of stars on the upper RGB provides detailed abundances of α-elements (O, Mg, Ca, Si, Ti) as well as r- and s-process elements (Y, La, Ba, Eu, Nd). Furthermore, within the central 15′ diameter region stars have been observed using medium resolution spectroscopy going down to fainter magnitudes (Kirby et al., 2009, 2010), giving [Fe/H] as well as α-element abundances.

The presence of these gradients suggests that Sculptor has experienced an initial, spatially extended episode of metal-poor star formation at all radii, and stars of higher metallicity were subsequently formed more towards the centre. This picture explains the properties of the CMD, such as the different spatial distributions traced by the HB morphology and Red Giant Branch (RGB) metallicity gradient.

Sculptor is a galaxy that can be used as a benchmark for a simple galaxy with an ex-

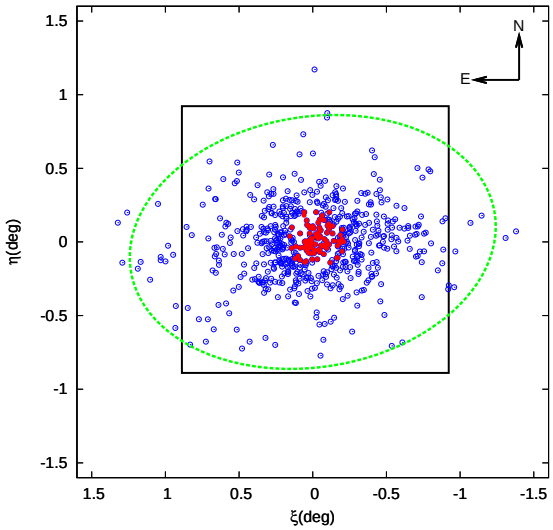

Figure 3.1: *Coverage of the photometric and spectroscopic observations across the Sculptor dwarf spheroidal galaxy. The solid (black) square denotes the full coverage of the CTIO 4m/MOSAIC fields. The (blue) open circles show the stars observed in the VLT/FLAMES low resolution Ca* II *triplet survey (Battaglia, 2007; Starkenburg et al., 2010). The (red) solid dots mark the RGB stars that also have high resolution abundance measurements (Hill et al., in prep, see Tolstoy et al., 2009) and the (green) dashed ellipse is the tidal radius of Sculptor, as given by Irwin and Hatzidimitriou (1995).*

tended episode of star formation in the early Universe. However, in order to quantify this picture and obtain accurate timescales for different stellar populations at different radii the detailed SFH needs to be determined over a large area of the galaxy.
The Sculptor dSph has been modelled several times in simulations using different techniques (e.g., Salvadori et al., 2008; Revaz et al., 2009; Lanfranchi and Matteucci, 2010; Kirby et al., 2011; Revaz and Jablonka, 2012). The cosmological semi-analitycal model of Salvadori et al. (2008) follows simultaneously the evolution of the Milky Way and its dwarf galaxy satellites, and reproduces the observed MDF and total mass content of the Sculptor dSph. Lanfranchi and Matteucci (2010) use chemical evolution modelling to reproduce the observed MDF of a variety of dwarf spheroidal galaxies, including Sculptor (see also Lanfranchi and Matteucci, 2004). Kirby et al. (2011) use a chemical evolution model to match the observed MDF and alpha-element distributions from a large sample of spectroscopic observations in Local Group dwarf spheroidal galaxies. Revaz and Jablonka (2012) use a chemo-dynamical Smoothed-particle Hydrodynamics (SPH) code to model the properties of Local Group dwarf spheroidal galaxies. Their model for the Sculptor dSph correctly matches the observed MDF and shows an extended SFH. Furthermore, the narrow [Mg/Fe] distribution in their Sculptor-like model matches well with observations from HR spectroscopy.
In this chapter the SFH of a large area of the Sculptor dSph will be determined using CMD synthesis methods (e.g., Tosi et al., 1991; Tolstoy and Saha, 1996; Gallart et al.,

1996a; Dolphin, 1997; Aparicio et al., 1997) to interpret the deep wide-field photometry presented in de Boer et al. (2011). The available spectroscopic information from Ca II triplet and HR spectroscopy will be directly used together with the photometry to provide additional constraints on the SFH. The spatial coverage of the photometric data (covering ≈80% of the tidal radius of Sculptor) allows us to determine the SFH at different radii and quantify the observed radial age and metallicity gradients.
Using the detailed SFH we also determine the probability distribution function for age for stars on the upper RGB, giving age estimates for individual stars. By linking these ages to the observed spectroscopic abundances we directly obtain, for the first time, the timescale of enrichment from different types of Supernovae (SNe).
The chapter is structured as follows: in section 3.2 we present our photometric and spectroscopic observations. In section 3.3 we describe our method of obtaining the SFH using the synthetic CMD method, adapted to include the MDF information. The detailed SFH analysis of the Sculptor dSph is given in section 3.4. The details of the age determination of individual stars are given in Section 3.4.4. Finally, the conclusions that can be drawn from the SFH are discussed in section 3.5.

3.2 Data

Deep optical images of the Sculptor dSph in the B, V and I bands were obtained using the CTIO 4-m MOSAIC II camera. The reduction and accurate calibration of this dataset is described in detail in a preceding paper (de Boer et al., 2011) (See also Chapter 2). The total coverage of the nine photometric fields observed is shown in Figure 3.1 as the solid black square. The spatial coverage of the B band photometry is complete for radii $r_{ell} \leq 0.5$ degrees, while the V and I bands are complete for $r_{ell} \leq 1$ degree.
By stacking together several images for each pointing the deepest photometry possible was obtained. Short exposures were also obtained, to be able to accurately photometer the bright stars that are saturated in the deep images. In order to ensure accurate photometric calibration, images were obtained with the 0.9m CTIO telescope under photometric conditions. Observations were also made of Landolt standard fields (Landolt, 1992, 2007). Photometry was carried out on these images using DoPHOT (Schechter et al., 1993). The different fields were placed on the same photometric scale and combined in order to create a single, carefully calibrated photometric catalog, as described in de Boer et al. (2011).
In addition, Ca II triplet spectroscopy is available for ≈630 individual RGB stars that are likely members of the Sculptor dSph, from medium resolution (R~6500) VLT/FLAMES observations (Battaglia, 2007; Battaglia et al., 2008b; Starkenburg et al., 2010). These observations measure [Fe/H] for a large sample of stars for which we also have photometry, out to a radius of 1.7 degrees from the centre of the Sculptor dSph (see Figure 3.1).
Furthermore, HR spectroscopy (VLT/FLAMES) is available for 89 individual RGB stars in the central part of the Sculptor dSph, for $r_{ell} \leq 0.2$ degrees (Hill et al., in prep, see Tolstoy et al., 2009). These observations provide [Fe/H] as well as [α/Fe] measurements. For [α/Fe] we assume [α/Fe] =([Mg/Fe] +[Ca/Fe] +[Ti/Fe])/3. The HR spectroscopy

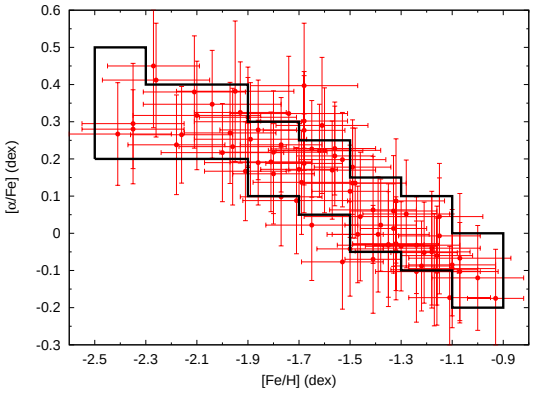

Figure 3.2: *Spectroscopic [Fe/H] and [α/Fe] measurements with their errors obtained from HR observations (Hill et al., in prep) in the central 25′ diameter of the Sculptor dSph. The solid (black) line shows the range of possible values of [α/Fe] assumed for each bin of [Fe/H] in the SFH determination.*

includes a range in metallicity from $-2.5<$[Fe/H]<-1.0 dex, with alpha-element abundances showing a clear correlation with [Fe/H] for the range $-0.3<[\alpha/\mathrm{Fe}]<0.5$ dex (See Figure 3.2).

3.3 Method

CMDs contain the signatures of numerous evolutionary parameters, such as age, chemical abundance, initial mass function, etc. The typical method of determining a SFH relies on comparing observed and synthetic CMDs of the individual stars that can be resolved. There have been many schemes proposed to quantify the SFH extracted from the CMD (e.g., Tosi et al., 1991; Tolstoy and Saha, 1996; Gallart et al., 1996a; Dolphin, 1997; Aparicio et al., 1997; Dolphin, 2002).

We have created our own routine, Talos, which uses an approach that compares observed CMDs with a grid of synthetic CMDs through the use of Hess diagrams (density plots of stars in the CMD) to determine the SFH (similar to Dolphin, 1997, 2002). The synthetic CMDs include observational effects in a statistical manner, which provides the most realistic way to include them.

We assume that a SFH can be built up from a linear combination of simple stellar populations. The advantage of this approach is that instead of synthesising a large number of artificial CMDs, each with their own complex Star Formation Rate (SFR(t)), the simple populations only need to be generated once. Then, the combination of simple stellar populations has to be found, which best represents the observed CMD.

Using the standard technique a number of different CMDs (e.g., V,B-V and I,V-I) can be independently used to obtain SFHs. A CMD is inherently two dimensional (colour and magnitude), whereas when photometric information is available in more than two filters, we can use 3D information to more precisely constrain the SFH.

To fully utilize all the available photometric information to constrain the SFH, Talos fits the measurements in all the available passbands at once. In this way all the advantages of the different CMDs (such as the more precise photometry in the I,V-I CMD and the larger colour range of the V,B-I CMD) are incorporated into a single, more accurate

SFH.
In addition to the photometric data we can also add spectroscopic observations of a large number of individual RGB stars. To take into account this extra information Talos also fits the observed MDF at the same time as the photometry, which allows us to put well motivated constraints on the metallicity range of the different stellar populations. The SFH determination technique consists of the following steps:

1. Construct synthetic CMD and MDF models
2. Find the combination of models that best match the data.
3. Determine the resolution and uncertainties of the final SFH.

These steps will be explained in more detail in the following sections.

3.3.1 Constructing synthetic CMD models

The synthetic stellar evolution library adopted in Talos is the Darthmouth Stellar Evolution Database (Dotter et al., 2008). The database contains isochrones distributed with a specific grid of age, metallicity and α-element abundance, among which are also those with [α/Fe]<0. These are of particular importance for our analysis, since Sculptor contains a substantial number of stars (33% of the total) with low α-element abundances (See Figure 3.2).
In order to allow greater flexibility in choosing the population domain and parameter resolution to use when modelling the SFH, we interpolate between the provided isochrones to produce a finer grid. A routine is provided by the Dartmouth group, to interpolate isochrones in [Fe/H]. Interpolation in age and [α/Fe] is done linearly, given that the grid of age points is sufficiently fine that there will only be small changes between isochrones of different age.
The isochrone library does not model the HB, Asymptotic Giant Branch (AGB) or Blue Straggler Star (BSS) phases, which means we cannot use these evolutionary features to constrain the SFH. The AGB is especially important, since it merges with the RGB in the CMD. The largest uncertainties in our final model may come from misidentifying the AGB using RGB models or the BSS as a young population. However, the Dartmouth isochrones have been shown to give a good simultaneous fit to all other evolutionary features within a CMD, justifying their use (e.g., Glatt et al., 2008a,b).
Synthetic CMDs are generated by drawing stars from the isochrones according to an initial mass function (IMF) and the mass range within each isochrone. The IMF used is the Kroupa IMF (Kroupa, 2001). An initial SFR for a stellar population (within a default mass range of 0.1−120 $M_{\odot}$) is assumed (resulting in several times more synthetic stars than in the observed CMD)„ which ensures that enough stars are generated in each part of the synthetic CMD, consistent with the time spent in each evolutionary phase. These synthetic stars are then placed at the distance of the Sculptor dSph, assuming a reddening of E(B-V)=0.018.
This gives us ideal CMDs for each stellar population that we consider in the SFH analysis. To create a synthetic CMD that can be compared directly to the observed photom-

etry we need to include observational effects in order to simulate our observational limitations.

Adding observational effects

The crucial aspect in comparing observed and synthetic CMDs is to determine the observational biases, such as photometric errors, incompleteness, etc.
This is done by carrying out a large number of simulations, in which a number of artificial stars (with known brightness) are placed on the observed images. These images are then re-reduced in exactly the same way as the original images, after which the artificial stars are recovered from the photometry. In this way we obtain a look-up table, which can be used to accurately model the effects of observational conditions (e.g., Stetson and Harris, 1988; Gallart et al., 1996b). The lookup-table is used in Talos to assign an individual artificial star (with similar colours and magnitudes) to each star in an ideal synthetic CMD and considering the manner in which this star is recovered to be representative of the effect of the observational biases.
Using individual artificial stars has the disadvantage that a huge number of stars need to be generated in order to correctly sample the effects in each CMD bin. This is because using the same artificial star in assigning offsets to several synthetic stars creates artificial clustering in the CMD. However, this approach is the only way to properly take into account the colour-dependence of the completeness level and the asymmetry of the offsets applied to model stars at faint magnitudes (e.g. Gallart et al., 1996b).
The set of artificial stars was generated with input parameters encompassing the range 5<Age<15 Gyr, $-2.5<$[Fe/H]<-0.80 dex, $-0.2<[\alpha/\mathrm{Fe}]<0.40$ dex. The stars were distributed randomly across the nine MOSAIC pointings in Sculptor, in 3 different filters. In each image no more than 5% of the total observed stars were ever injected as artificial stars at one time, so as not to change the crowding properties in the image. For each observed pointing 200−400 images containing artificial stars were created, in order to obtain a sufficient total number of artificial stars. This resulted in nearly 7000 images containing a total number of 3.5 million artificial stars spread across the full area of the Sculptor dSph. Each image was re-reduced using the same techniques and calibrations as the original image, after which the output catalog was matched to the input catalog (while taking care not to match artificial stars to observed real stars), to produce a lookup-table containing the recovered artificial stars (and the recovered photometric offsets) in 3 filters.
Figure 3.3 shows the result of the artificial star tests in the I,V-I CMD of Sculptor. The completeness level accounts for only those objects that DoPHOT unambiguously recognises as stars. DoPHOT actually detects more objects, but the faintest objects do not have high enough signal-to-noise to be confidently distinguished as stars as opposed to unresolved galaxies. Only the unambiguously detected stars are considered in the completeness level, since those are observed with sufficient accuracy to be useful in our analysis. Figure 3.3 shows the dependence of the completeness level on both colour and magnitude. The dependence on colour in particular has to be properly taken into account when generating realistic synthetic CMDs.
The need to carry out artificial star tests over the entire observed field of view is high-

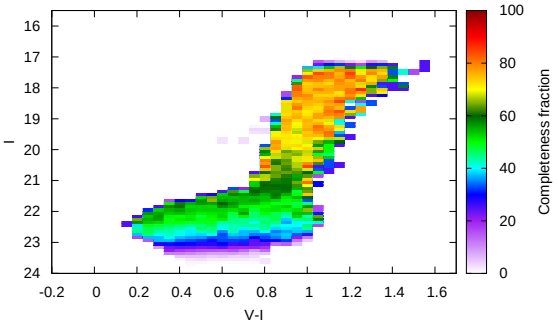

Figure 3.3: *The recovered I,V-I CMD of the artificial stars put into the observed images of Sculptor. The colours indicate the completeness fraction of artificial stars in each bin, with a scale on the right hand side of the plot.*

lighted in Figure 3.4. Here we show the variation of the 50% completeness level with distance from the centre of Sculptor, in the three different filters. The completeness level in the B filter is zero for $r_{ell} \geq 0.5$ degrees, because of the lack of B band observations in the outer parts of Sculptor. Figure 3.4 also shows that the centre of Sculptor is less complete at a fixed magnitude limit than the outer regions. This is due to the increased crowding in the central region, which means it is harder to determine the shape of the PSF of stars in the centre, causing fewer stars to be unambiguously detected at a given brightness level, and placing the 50% completeness at brighter magnitude levels.
However, the CMDs at different radii from the centre (see Figure 5 from de Boer et al., 2011) show that the photometry in the central part of Sculptor actually goes deeper than in the outskirts (due to longer exposure times), with a well defined shape of the MSTOs. Additionally, using the artificial star test results to simulate observational conditions makes sure that this changing completeness level is properly taken into account when determining the SFH.

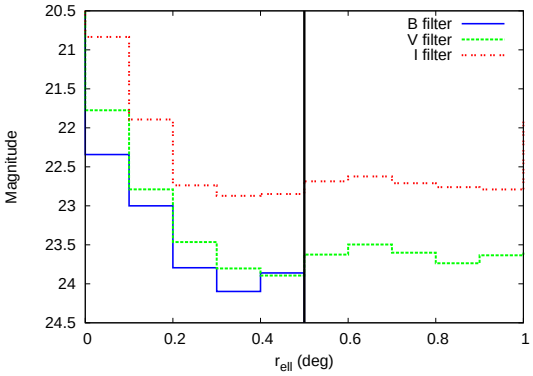

Figure 3.4: *The magnitude of the 50% completeness level with increasing elliptical radius (r_{ell}) from the centre of the Sculptor dSph, in B (solid blue line), V (green dashed line) and I (red dotted line) filters. The vertical (black) line indicates the elliptical radius up to which observations in the B filter are available.*

Artificial star tests have only been carried out on the long, stacked exposures. For those stars saturated in the long exposures, observational effects are modelled by giving them random offsets within the photometric error distribution of stars with similar instrumental magnitude and colour. This is justified because the recovery fraction for the

brightest stars is very close to 100%, and the offsets induced by crowding are insignificant and signal-to-noise is not an issue.
The process of including observational errors in synthetic CMDs in a statistical manner means that they can be directly compared to the observed CMDs, to obtain the best matching SFH.

3.3.2 Constructing MDF models

In order to include the spectroscopic MDF at the same time as the photometry in Talos we use the equivalent of a Hess diagram for [Fe/H]. This is done by generating synthetic CMDs of different stellar populations and binning the stars in metallicity. In this way it is possible to create synthetic MDF models for stellar populations of different [Fe/H], age and [α/Fe].
The spectroscopic observations only come from a fraction of the RGB, which are in turn a small fraction of stars present in the CMD. To make sure that the synthetic CMDs fully sample the RGB, synthetic MDF populations are generated with an artificially increased initial SFR, which is later corrected in the MDF models. To correctly reproduce observational limits we construct the synthetic MDFs using only stars within a similar magnitude range to those of the the observed spectroscopic sample. From the number of stars observed both photometrically and spectroscopically in the same magnitude range we then calculate the spectroscopic completeness fraction on the RGB. This fraction is used to scale down the synthetic MDF, and thus match the spectroscopic completeness.
The observed spectroscopic uncertainties on the metallicites are simulated by considering each individual synthetic star to have a Gaussian profile with a width determined by the average observational uncertainty on [Fe/H]. The metallicities of these individual stars are then combined to form a synthetic MDF which takes into account observed uncertainties, and can be directly compared to the observed MDF.

3.3.3 Determining the SFH

In Section 3.3.1 we described how Talos can be used to create accurate synthetic CMDs, which can be compared directly to the observed CMDs. We then described in Section 3.3.2 how model MDFs are created in Talos, which add additional information that can be used to restrict the SFH. Here we now put everything together to determine the SFH of a galaxy.
The technique used to determine the best SFH minimises the difference between observed and synthetic CMDs through Hess diagrams to produce the closest match to the observed data, as described in Dolphin (2002). Photometric Hess diagrams are constructed by binning CMDs in magnitude and colour space (or three magnitude space for Hess diagrams using B,V and I filters) and counting the number of stars in each bin. The synthetic Hess diagrams are scaled to contain a number of stars equal to the observed Hess diagrams, to make sure that no model is given preference during the SFH determination based on the total number of stars it contains.
In Talos, the synthetic MDFs are used in the fitting procedure in a similar manner as

the photometric Hess diagrams. The spectroscopic MDF is treated as an extra observed dimension, for which the difference between model and observations also needs to be taken into account. A different weight is applied to the photometric and spectroscopic components, in order to enhance the importance of the spectroscopic information, which contributes less to the overall goodness of fit than the photometry, but significantly restricts the possible solutions.
Since the observed data follows a Poisson distribution, the goodness of fit is expressed as a difference parameter between models and observations (a Poisson equivalent of χ^2), given by Dolphin (2002):

$$\chi^2_{Poisson} = 2\sum_i m_i - n_i + n_i ln\frac{n_i}{m_i}$$

In which m_i is the total number of stars in a synthetic Hess bin ($m_i = \sum_j \mathrm{SFR}_j \times \mathrm{CMD}_{i,j}$ in the photometric part, and $m_i = \sum_j \mathrm{SFR}_j \times \mathrm{MDF}_{i,j}$ in the spectroscopic part) and n_i the total number of stars in an observed Hess bin. By minimising the difference parameter we determine the SFH (given by SFR_j) that best matches both the observed CMD as well as the observed spectroscopic MDF.

SFH uncertainties

Equally as important as determining the best matching SFH is determining the uncertainties on this choice. The two main sources of statistical uncertainties on the determination of the SFH are related to data and parameter sampling of the SFH solution (Aparicio and Hidalgo, 2009).
Data sampling is related to how representative a model is of the underlying population. In the context of CMD analysis, constructing the same model twice, with different random samplings of the same isochrones will result in two slightly different synthetic CMDs. In order to quantify how this effect may impact the inferred SFH without synthesizing an entire new set of synthetic CMDs we use the approach used by Aparicio and Hidalgo (2009). A number of different representations of the observed CMD is generated, by generating a synthetic CMD from the SFH obtained in the first run-through of the code and randomly swapping a certain fraction (by default 20%) in the observed CMD. In this way we obtain a new “observed" CMD which is representative of a CMD with a different sampling of the underlying population. By generating a number of these CMDs and using them with the original models to find the SFH we can quantify the errors on the SFH caused by data sampling.
The other major source of error is parameter sampling. This means that the choice of CMD gridding, age bins and metallicity bins will affect the final SFH. In order to quantify the effect of this gridding on the recovered SFH, different bin sizes and distributions are used and then compared. In the parameter space of age and metallicity three different shifts are applied: a shift of half a bin size in age and in metallicity and also a shift in both age and metallicity simultaneously. For the photometric binning two different bin sizes are used, with the different shifts applied to each. For all these different griddings the SFH is determined, after which the results are returned to a common grid.

The average of all the different solutions is adopted as the final SFH, with errorbars determined as the standard deviation of the distribution of solutions. This technique has been shown to adequately take into account the major uncertainties on the recovered SFH, and give realistic errorbars on the final SFH (Aparicio and Hidalgo, 2009).

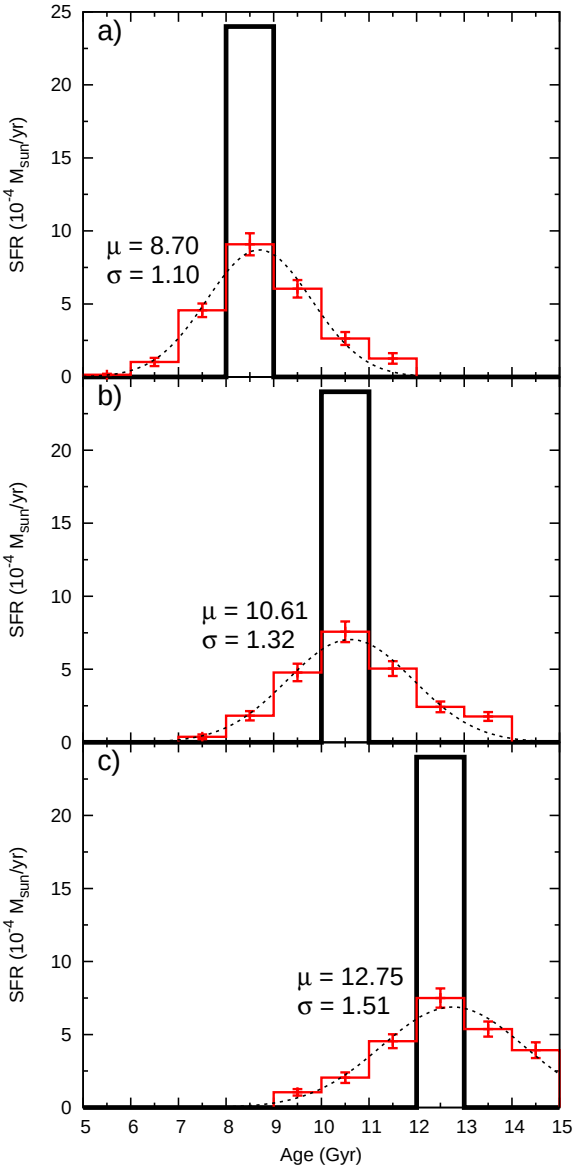

Figure 3.5: *The input and recovered SFHs of a series of short (10 Myr) bursts of star formation at different input age. The black, solid histogram shows the input SFH, given the binning adopted. The red histograms show the recovered SFH, along with the fit of a Gaussian distribution as the dashed line. The mean (μ) and variance (σ) of the fitted Gaussian distribution are also listed.*

3.3.4 General properties of Talos

In order to verify the basic operation of Talos, a number of tests have been performed, and the results are shown in Appendix 3.A. We checked our ability to correctly recover the age and metallicity of a simple synthetic stellar population. We also showed that we can accurately recover a synthetic SFH of a continuous period of star formation from the earliest times until now. Furthermore, we tested Talos on observations of the globular cluster NGC1904. The metallicity we determined is consistent with that obtained from spectroscopic observations, showing that Talos can accurately recover the age and metallicity of an observed simple stellar population. The main effect that makes the output solution different from the input is the depth of the photometric data, and the set of parameter griddings adopted to compute the final SFH. These result in limits to the age resolution of our final SFH.
In order to understand the limitations of the final SFH determined by Talos, it is important to obtain an accurate estimate of the age resolution of the solution. This is determined by recovering the SFH of a set of synthetic populations at different input ages, as described by (e.g., Hidalgo et al., 2011).
Three synthetic populations were generated at the distance of the Sculptor dSph, with single short bursts of star formation (with a duration of 10 Myr) at an age of 8.5, 10.5 and 12.5 Gyr. The metallicity of the bursts was distributed to match the observed MDF of the Sculptor dSph, as were the observational errors.
The recovered and input SFH for these bursts are shown in Figure 3.5. The recovered SFH is well fit by a Gaussian distribution, which shows that the mean of the central peak (μ) is recovered at the correct age, with a minor shift of $\approx$0.1$-$0.2 Gyr. The recovered SFH shows that typically $\approx$40% of the total input SFR is contained within the central bin, at all ages. The star formation is spread out over the Gaussian distribution, leading to uncertainties in the recovered SFH. However, in the case of constant star formation (see Section 3.A.1) the recovered star formation rates show a more accurate recovery of the input SFH.
From the Gaussian fits to the three bursts in Figure 3.5 we can derive the variance σ, which determines the resolution with which the burst is recovered. The three bursts are recovered with an age resolution of $\approx$1.5 Gyr at an age of 12.5 Gyr, $\approx$1.3 Gyr at an age of 10.5 Gyr and $\approx$1.1 Gyr at an age of 8.5 Gyr, which is consistent with a value of 12% of the adopted age.

3.3.5 Simulating the Sculptor dSph

To use Talos to determine the SFH of the Sculptor dSph the general method described in the preceding sections needs to be adapted to the specifics of this galaxy.

General setup

The observed CMD of Sculptor contains both stars that belong to Sculptor as well as Milky Way foreground and unresolved background galaxies. To avoid these objects influencing the SFH, the observed CMD is “cleaned" using the colour-colour diagram presented in de Boer et al. (2011) (see Figure 2.8 in Chapter 2). Foreground stars with

colours that coincide with those of Sculptor are assumed not to significantly alter the total number of stars in different evolutionary features, as determined by using the Besançon models to predict the number of Milky Way stars in the CMD (Robin et al., 2003).
Additionally, the observed CMDs (shown in Figure 5 from de Boer et al., 2011) show that Sculptor contains a significant number of BSS stars, which we do not attempt to include in the SFH determination as a younger population, since they are likely to be genuine BSS stars (Mapelli et al., 2009). To avoid the BSS stars influencing the SFH, we generate a mock BSS population which is used as a fixed background in the SFH determination. The mock BSS stars are constructed by using only the main sequence part of populations spanning a range in metallicity of $-2.5<$[Fe/H]<-1.0, with ages between $3-4$ Gyr. This background Hess diagram is subsequently scaled so the number of synthetic stars in the BSS region matches the observed number.
The SFH is determined using the CMD without including the RGB region. The number of stars on the RGB is low compared to that in the MSTO region, and therefore does not contribute strongly to the determination of the SFH. Furthermore, the RGB feature has been shown to substantially vary from one set to the other (e.g., Gallart et al., 2005b). Conversely, there is good agreement between the theoretical MSTO phase at old ages ($\geq$10 Gyr) in different isochrone sets. Instead, information from the RGB phase is taken into account through the inclusion of the MDF fitting.

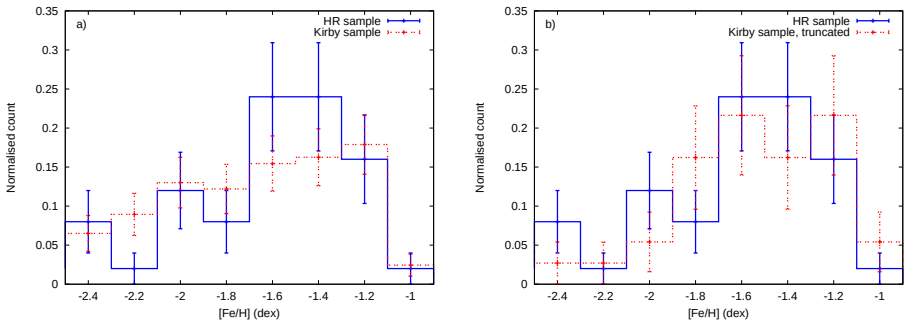

Figure 3.6: *The MDF of RGB stars in the Sculptor dSph from Hill et al., in prep (HR sample, solid histogram) and Kirby et al. (2010) (dashed histogram). Panel* ***a)*** *shows the complete samples for both MDFs (HR, going down to V≈18 and Kirby et al. going down to V≈20), while panel* ***b)*** *shows the Kirby MDF truncated at V≈18 along with the full HR sample. Poissonian errorbars are also shown.*

Determining the SFH without including the spectroscopic MDF shows similar overall trends as obtained when including the MDF. However, the addition of the MDF has a result of putting better constraints on less populated region of the CMD, such as the metal-rich stars, which would otherwise be fit using a lower metallicity and higher age, due to the mismatch between the RGB and MSTO in the isochrones.
A single, well defined distance is assumed for the Sculptor dSph in the SFH determination, as obtained by a number of reliable distance indicators (Pietrzyński et al., 2008).

The effect of adopting a different distance is shifting the main peak of star formation to younger ages for a larger distance and older ages for a smaller distance. However, the internal distribution of the presented SFHs does not change significantly when adopting a different distance, given the small observed uncertainties on the distance. Furthermore, the good agreement between different distance determination methods gives confidence to the single distance adopted in this work.

Taking into account the spectroscopic information

The spectroscopic information which is used to provide extra constraints on the SFH comes from two different sources. For $r_{ell} \leq 0.2$ degrees the metallicity information comes from HR spectroscopy on the upper RGB, while in the outer parts of Sculptor ($0.2 \leq r_{ell} \leq 1.7$ degrees) it comes only from Ca II triplet spectroscopy which also includes fainter stars. Ca II triplet spectroscopy is also available in the central region, which shows that metallicities from both samples are placed on the same scale, and consistent with each other (Battaglia et al., 2008b). However, because the spectroscopic sample in the central region encompasses only the brightest ≈1mag of the RGB, an intrinsic bias may be present in the observed central MDF due to the limited sampling of the stellar populations on the upper RGB.
To check for the presence of such a bias in our HR spectroscopic sample, a comparison is made with a different spectroscopic sample taken in the same region, going down to fainter magnitudes (Kirby et al., 2010). Figure 3.6a shows a comparison between the normalised MDFs of both samples. The MDF of the deeper sample clearly shows a larger fraction of metal-poor stars than the brighter sample. Figure 3.6b shows that the MDF of both samples look the same, when the sample of RGB stars is truncated at the same magnitude. Figure 3.6 shows that an MDF determined from only the upper RGB stars in Sculptor results in a lower relative fraction of metal-poor stars. This effect is due to the luminosity function bias on the upper RGB, causing an incomplete sampling of the metal-poor components for the brightest RGB stars.

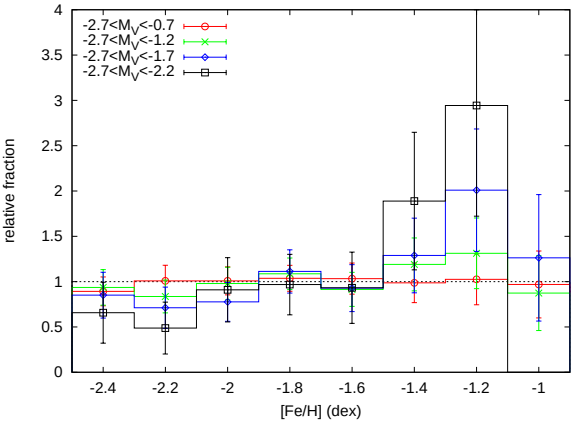

Figure 3.7: *The relative fractions of different metallicities present on the RGB at different photometric depths, with respect to an MDF going down to M_V=−3.2 (V=19.5) on the RGB. The relative fraction indicates by which factor a population is incorrectly sampled in the CMD. For comparison the level of the HB is V_{HB}=20.13 (M_V=0.43).*

In order to investigate the effects of the bias in more detail we consider the sampling

of the MDF at different photometric depths. Using a synthetic CMD of a Sculptor-like galaxy for which the metallicity is known for each star, we construct MDFs from RGB stars going down to different photometric depths. By comparing to the input parameters of the synthetic CMD we find that going down to M_V=−3.2 (V=19.5) fully samples the overall MDF. MDFs of different depths are compared to the overall MDF to produce the correct relative fraction of stars sampled at each metallicity. Figure 3.7 shows the relative fraction of stars sampled on the RGB at different metallicities in CMDs of different photometric depth. The effect of depth on the RGB is clearly seen, with shallower MDFs under-sampling populations with [Fe/H]<−1.9 dex and over-sampling more metal-rich components. A similar effect is also seen when applying the same approach to the observed, deep Ca II triplet data, with a more severe under-sampling of the populations with [Fe/H]<−1.9 dex compared to the synthetic CMD results.
It is important not to neglect the metal-poor component in Sculptor, which is well sampled by the MSTO region, but not on the RGB. Figure 3.7 shows that no bias is present in the MDF for [Fe/H]≥−1.9 dex. Therefore, we adopt this as a metallicity cut-off, below which the SFH is only constrained using photometry. In the outer parts of Sculptor (r_{ell}≥0.2 degrees) no metallicity cut-off is adopted, since the Ca II triplet spectroscopy extends to faint enough magnitudes to avoid this bias.

SFH parameter space

To set the limits in age and metallicity used in determining the SFH of the Sculptor dSph we consider all information currently available in the literature. We first consider the spectroscopic MDF from Ca II triplet and HR spectroscopy. The range in [Fe/H] is limited at the metal-poor end by the availability of the isochrones, which go down to only [Fe/H]≈−2.5 dex. This is not a problem, because the spectroscopic MDF shows that the majority of the stars in Sculptor (92% of the total) have [Fe/H]≥−2.5 dex (Starkenburg et al., 2010). The metal-rich is limited by the absence of stars with [Fe/H]≥−1.0 dex in the observed MDF (see Figure 3.2). A binsize of 0.2 dex is assumed for [Fe/H], similar to the average uncertainty on [Fe/H] in the spectroscopic sample.
To constrain [α/Fe] we use the 89 stars in the HR sample in the central 25′ diameter region of Sculptor. Figure 3.2 shows that a well-defined [α/Fe]−[Fe/H] relation from HR spectroscopy is present in the centre of Sculptor. We assume that there is no change in this relation with radius and directly use it to determine the range in [α/Fe] that corresponds to the [Fe/H] used in a particular stellar population (the region defined by the solid black lines in Figure 3.2). In this way we generate a set of populations that cover the full range of [Fe/H] and [α/Fe] in the spectroscopic observations.
To restrict our choice of possible ages we notice that the distribution of stars in the observed CMDs do not allow any stars ≤5 Gyr old to be present in Sculptor (de Boer et al., 2011). Assuming a maximum age of 14 Gyr, for the age of the Universe, the range of ages we consider is thus between 5 and 14 Gyr old, with a bin size of 1 Gyr.

3.4 Results

We have described our method and carried out tests to show that it works as expected using real and synthetic test data (see Section 3.3.4) Now we apply Talos to our photometric and spectroscopic data sets of the Sculptor Sph (de Boer et al., 2011; Starkenburg et al., 2010, Hill et al., in prep).
To derive the SFH of Sculptor the available photometry (excluding the RGB) is fit simultaneously with the spectroscopically determined MDF. Within $r_{ell} \leq 0.43$ degrees photometry in three filters (B,V and I) is used to determine the SFH, while further out only the V and I filters can be used. For radii $r_{ell} \leq 0.2$ degrees the spectroscopic MDF obtained from HR spectroscopy is used. This MDF is used in the SFH fitting for [Fe/H]≥ -1.9 dex, to avoid the luminosity function bias described in Section 3.3.5. Below this value only the photometry is used to constrain the MDF and SFH. For $r_{ell} \geq 0.2$ degrees the MDF obtained from Ca II triplet data is used, and no metallicity cut is applied.
We include a static background Hess diagram to account for the presence of a BSS population (as discussed in Section 3.3.5). Furthermore, the observed HB and AGB are ignored, since the isochrone set we use does not include these evolutionary features.

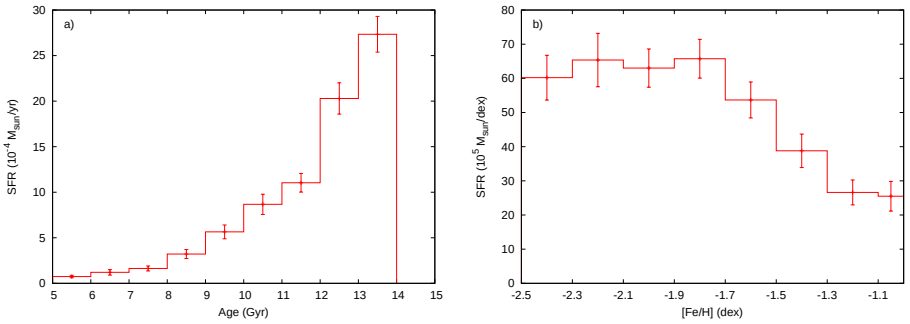

Figure 3.8: *The final (**a**) SFH and (**b**) Chemical Evolution History of Sculptor, out to a radius of r_{ell}=1 degree, obtained by fitting all available photometric and spectroscopic information simultaneously.*

The final Star Formation History and Chemical Evolution History (CEH) of the entire Sculptor dSph (out to $r_{ell} \approx 1$ degree) are presented in Figure 3.8. The SFH and CEH display the rate of star formation at different age and metallicity respectively, in units of solar mass per year or dex respectively, over the range of each bin. The total mass in stars formed in a bin can be obtained by multiplying the star formation rate by the age or metallicity range of that bin.
The overall SFH shows that the Sculptor dSph is dominated by an ancient (>10 Gyr old), metal poor stellar population. A tail of more metal-rich, younger stars is seen at a lower SFR down to an age of ≈6-7 Gyr. The shape of the SFH shows that the star formation rate declines with age, suggesting a single episode of star formation over an extended period of time (≈7 Gyr).

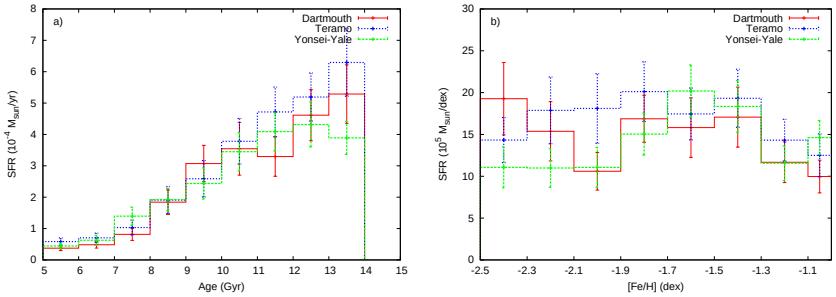

Figure 3.9: *The (**a**) SFH and (**b**) CEH of the centre of Sculptor, determined using three different isochrone sets. The obtained solution is shown for the Darthmouth Stellar Evolution Database as the (red) solid line, for the BaSTI/Teramo isochrones as the (blue) dotted line and for the Yonsei-Yale isochrones as the (green) dashed line.*

The SFH is determined using the Darthmouth Stellar Evolution Database (Dotter et al., 2008). To determine the effect of using different isochrones sets, the SFH of the central part of Sculptor (r_{ell}≤0.116 deg) was obtained using three different isochrone sets (Dotter et al., 2008; Pietrinferni et al., 2004, 2006; Yi et al., 2001; Kim et al., 2002). The obtained SFHs displayed in Figure 3.9 show that the obtained solution is very similar in all cases, due to the fact that the SFH determination is dominated by the MSTO region, for which the different isochrone agree at old ages. This gives confidence to adopting the Dartmouth isochrone library for the determination of the final SFH of Sculptor.
Using the SFH it is possible to simulate CMDs of the Sculptor dSph, which can be used to show the distribution of age across the CMD in detail. Figure 3.10 shows the synthetic V,B-V CMD of the Sculptor MSTOs colour coded with age as inferred from the SFH. The separation of different ages is clearly visible on the MSTO, which highlights the necessity of photometry going down to the oldest MSTOs to obtain accurate ages.

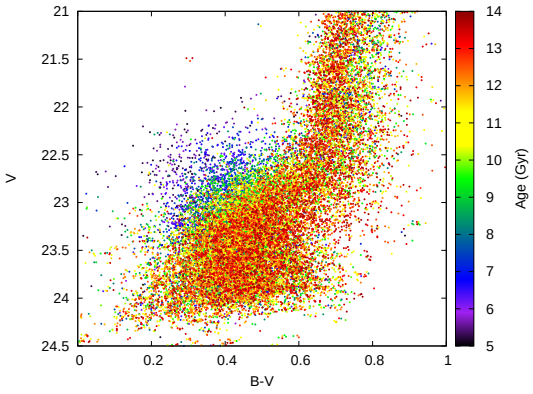

Figure 3.10: *Synthetic V,B-V CMD of the MSTO region of the Sculptor dSph, colour coded by age as inferred from the SFH.*

3.4.1 Reliability of the SFH

The most basic check of the reliability of the recovered SFH is to compare the synthetic and observed CMDs. Figure 3.11 shows the observed I,V-I CMD of the Sculptor dSph as well as the synthetic CMD corresponding to the best matching SFH. Furthermore, the difference between both CMDs is shown, expressed as a fraction of the observed star counts in each bin.

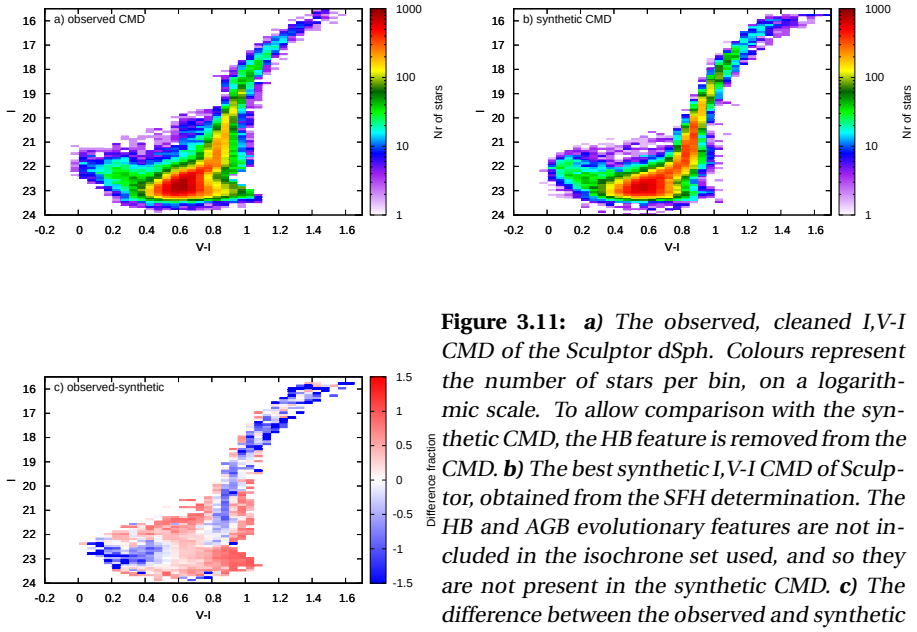

Figure 3.11: ***a)*** *The observed, cleaned I,V-I CMD of the Sculptor dSph. Colours represent the number of stars per bin, on a logarithmic scale. To allow comparison with the synthetic CMD, the HB feature is removed from the CMD.* ***b)*** *The best synthetic I,V-I CMD of Sculptor, obtained from the SFH determination. The HB and AGB evolutionary features are not included in the isochrone set used, and so they are not present in the synthetic CMD.* ***c)*** *The difference between the observed and synthetic I,V-I CMD of Sculptor, expressed as a fraction of the observed number of stars.*

The total number of stars in the synthetic CMD is consistent with the observed CMD to within a few percent, showing that the total mass in stars is well matched to the observations. The CMDs are in general a good match, over most of the MSTO region. The static background BSS is not reproduced with the same colour distribution as the observed stars, leading to an under-dense region at blue colours (V−I≈0.2) in Figure 3.11c. However, the transition from the BSS into the MSTO region is matched well, despite being modelled in a simple way (See Section 3.3.5). Figure 3.11c shows that the colours of the RGB extend to redder colours than observed in Sculptor. The RGB colours of the adopted isochrone set are slightly too red for the metallicity and age determined from the MSTO region and Ca II triplet spectroscopy, which is a known problem for theoretical isochrones (e.g., Gallart et al., 2005b). The HB and AGB are obviously not reproduced in the synthetic CMD, as they are not included in the Dartmouth isochrone set.

On the RGB a comparison can be made between the observed spectroscopic MDF and

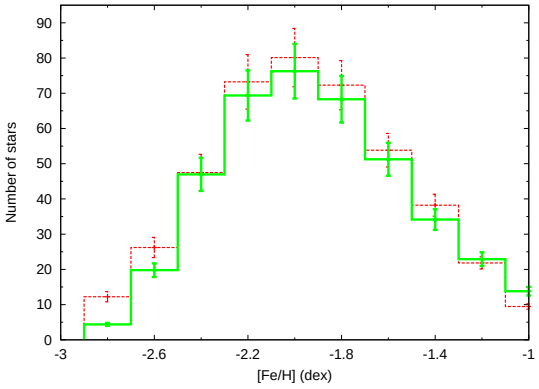

Figure 3.12: *The best matching simulated MDF (solid) histogram and observed MDF (dashed) histogram from spectroscopic observations.*

the MDF obtained from the SFH determination, as shown in Figure 3.12 for the full extent of the Sculptor dSph. We can see that the synthetic MDF is mostly consistent with the observed MDF within the errors, as expected, given that the MDF is used as an input in the SFH determination. A population which is not so well fit is the tail of metal-poor stars ([Fe/H]<-2.5 dex). From the spectroscopic observations it is known that these stars are present in Sculptor, although in small numbers (≈8%, see Starkenburg et al., 2010; Tafelmeyer et al., 2010). The models used to fit the SFH do not contain metallicities low enough to include these stars. Despite these uncertainties we feel confident that the differences between the observed and synthetic CMDs and MDFs are sufficiently low to conclude that the fitted SFH constitutes an accurate representation of the full range of ages of stellar populations present in Sculptor.

3.4.2 Spatial variations in the SFH

Due to the extensive spatial coverage of both the MSTO photometry and RGB spectroscopy we are able to determine the SFH over most of the area of the Sculptor dSph. Thus, it is possible to determine the radial variation in the SFH in 5 annuli (see Figure 3.13), each containing a similar number of stars observed in the V and I filters. For comparison, the Sculptor core radius is 0.1 degrees, just within the first annulus. The V and I filters were chosen, since they are offer the most complete spatial coverage further from the centre.

The SFH is determined independently in each of these annuli in the same way as for the full galaxy. The SFH and CEH of the five selected spatial regions are shown in Figure 3.13, using all photometric filters as well as the available spectroscopy. In the outermost annulus the SFH is determined only using the I,V-I CMD, together with the spectroscopic MDF. Figure 3.13 shows that the SFH changes significantly with distance from the centre of Sculptor. The metallicity and age gradient discussed by de Boer et al. (2011) is quantified here. The younger, metal-rich populations are found mostly in the central region and drop off towards the outer parts.

Figure 3.14 shows the observed and synthetic MDFs resulting from the SFH determination for all five annuli in Sculptor. The MDF shown in the upper two panels comes

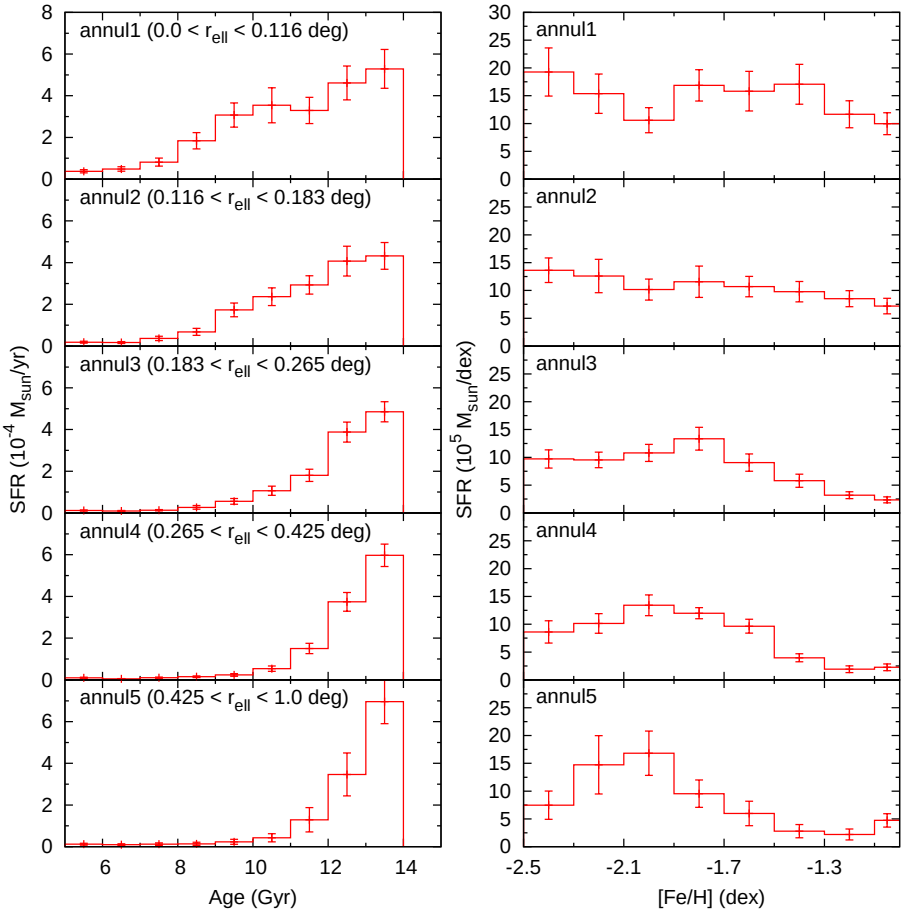

Figure 3.13: *The SFH and CEH (obtained by fitting all available photometry and spectroscopy) for each of the 5 annuli of Sculptor, with the corresponding radial extent indicated in the plot. For annulus 5 only the I,V-I CMD is used together with the spectroscopy to constrain the SFH.*

from HR spectroscopy, while the MDF in the lower three panels comes from Ca II triplet spectroscopy. Figure 3.14 shows that the synthetic MDFs resulting from the SFH determination are consistent with the observed MDFs within the errors. In the upper two panels the synthetic MDF lies above the observed MDF for metallicities lower than indicated by the black line and below the observed MDF for higher metallicities. This is similar to the effects of the luminosity function bias seen in Figure 3.7.

Using the SFH at different positions it is possible to determine the radial distribution of the total mass of stars in Sculptor. This is done by integrating the SFRs over the duration of star formation, at different radii from the centre. Figure 3.15 shows the radial distribution of the total stellar mass, obtained from the SFH modelling. The total

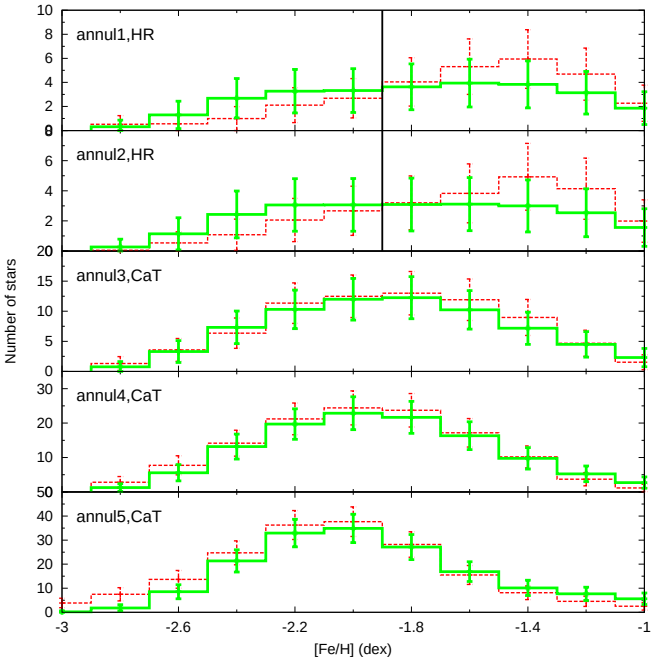

Figure 3.14: *The observed (dashed) histogram and the synthetic (solid) histogram MDFs from the SFH analysis in the five annuli. The solid (black) line in the upper two panels shows the [Fe/H] above which the HR spectroscopic MDF is unbiased, and can be used in the SFH determination.*

mass in stars formed is highest in the central parts of Sculptor ($r_{ell} \leq 0.2$ degrees) and drops off steeply towards the outskirts. The total mass in stars formed over all radii in Sculptor for our SFH is 7.8×10^6 $M_\odot$ within an elliptical radius of 1 degree or 1.5 kpc. To determine the core radius of the total mass distribution we use a Sersic profile to fit the distribution shown in Figure 3.15. The resulting core radius $r_c = 0.11 \pm 0.04$ degrees, is consistent within the errors with that derived from the observed density profile (Battaglia et al., 2008a).
It is also possible to quantify the radial distribution of populations with different ages. Figure 3.16 shows the cumulative radial distributions of stellar populations with different ages, as determined from SFH modelling. Figure 3.16 is another way of showing that the oldest population is the most extended component, while younger populations show an increasing central concentration, as qualitatively described in de Boer et al. (2011).

3.4.3 Resolving bursty star formation

One crucial aspect of the interpretation of our SFH is: can we distinguish between bursty and continuous star formation, given our SFH resolution and uncertainties?

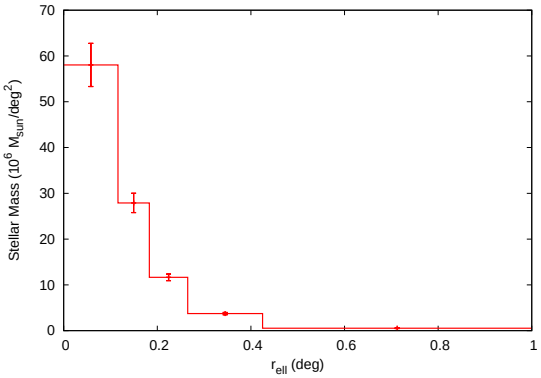

Figure 3.15: *The radial distribution of the total stellar mass per square degree in the Sculptor dSph, as determined from the SFH modelling. This provides the total mass of stars formed over the lifetime of Sculptor, 7.8×10^6 $M_\odot$.*

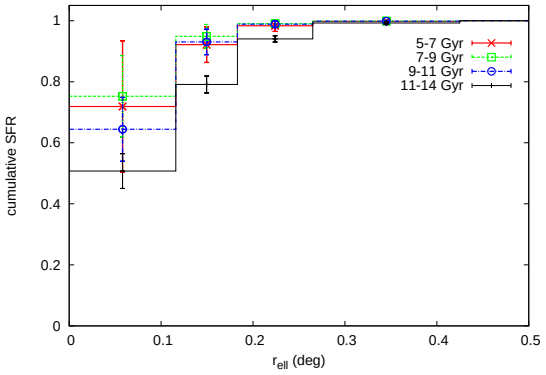

Figure 3.16: *The cumulative radial distributions of stellar populations with different ages.*

The intrinsic uncertainties on the SFH determination (as described in Section 3.3.3) result in a smoothing of the star formation rates, potentially hiding the presence of bursts of star formation.

To test our ability to distinguish a series of distinct bursts of star formation from continuous star formation in Sculptor, we carry out a series of experiments using the final SFH of the innermost and outermost annuli of Sculptor (anull1 and annul5 in Figure 3.13). The metallicities and star formation rates from the final SFH are adopted, and distributed over one or more short bursts of star formation.

For a single narrow (10 Myr) burst of star formation at an age of 13.5 Gyr and a metallicity range of $-2.2\leq$[Fe/H]≤-2.0 dex, the recovered and input SFH and CEH for annulus 5 are shown in Figure 3.17. The recovered SFH matches well with the final adopted SFH of the outermost annulus given in Section 3.4.2. This suggests that the star formation in the outermost part of Sculptor can be approximated with a single, short burst of star formation. However, the SFH and CEH shown in Figure 3.17 indicate that the spread in age and metallicity of the burst must be more extended than assumed here.

A similar analysis for annulus 1 of Sculptor shows that the recovered SFH using a single, short burst is clearly inconsistent with the adopted SFH of the inner annulus. A

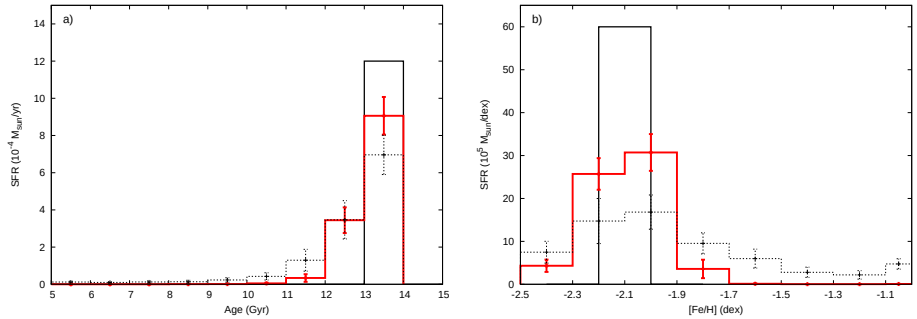

Figure 3.17: *The recovered and input (**a**) SFH and (**b**) CEH of a synthetic population with a single short (10 Myr) episode of star formation at an age of 13.5 Gyr. The solid black histogram shows the input population given the SFH binning, while the grey histogram shows the recovered SFH. For comparison, the adopted SFH of annulus 5 of Sculptor is shown as the black, dashed histogram.*

comparison of the synthetic CMD with the observed CMD of annulus 1 shows a bad fit to the data, with a value of χ^2=5.51 (compared to χ^2=2.94 for the adopted SFH of annul1), making it unlikely to be an accurate representation of the actual SFH in the centre of Sculptor. Additionally, it seems unphysical to assume that the large spread in metallicity observed in the centre of Sculptor (1.5 dex) can be built up during a single short episode of star formation.

We continue by adding a second burst of star formation to see if this can improve the match to the SFH of the innermost annulus of Sculptor. Figure 3.18 shows the recovered SFH of a synthetic population with two narrow 10Myr bursts of star formation at different age, with metallicities and star formation rates determined from the adopted SFH of annulus 1. In each test an old burst was assumed to take place at an age of 13.5 Gyr, with an additional burst at a younger age. Figures 3.18a,b show that the input SFH is not recovered as two individual bursts if the age separation between the two bursts is less than 4 Gyr. Only when the youngest burst is placed at an age of 8.5 Gyr, that a separation can be seen between the two bursts in the SFH, as shown in Figure 3.18c.

The SFHs shown in Figure 3.18 are in relatively good agreement with the final adopted SFH of annulus 1, especially when the youngest burst is placed at 9.5 Gyr (Figure 3.18b). The recovered SFH shows features consistent with the adopted SFH at similar strengths. However, a comparison of the synthetic CMD to the observed CMD of annulus 1 shows that the synthetic populations provide a bad fit to the observed CMD, with χ^2 values of 4.32, 4.10 and 4.28 respectively for the populations with the young burst at 10.5, 9.5 and 8.5 Gyr. The smooth SFH, as given in Section 3.4.2 provides a better representation of the observed CMD, which makes it unlikely that strong, short bursts of star formation dominated the SFH of the Sculptor dSph.

A synthetic population with three narrow 10Myr bursts of star formation, at 13.5, 10.5 and 8.5 Gyr, gives a better agreement with the observed SFH. Furthermore, the synthetic CMD provides a better fit to the observed CMD of annulus 1, with a χ^2 value of

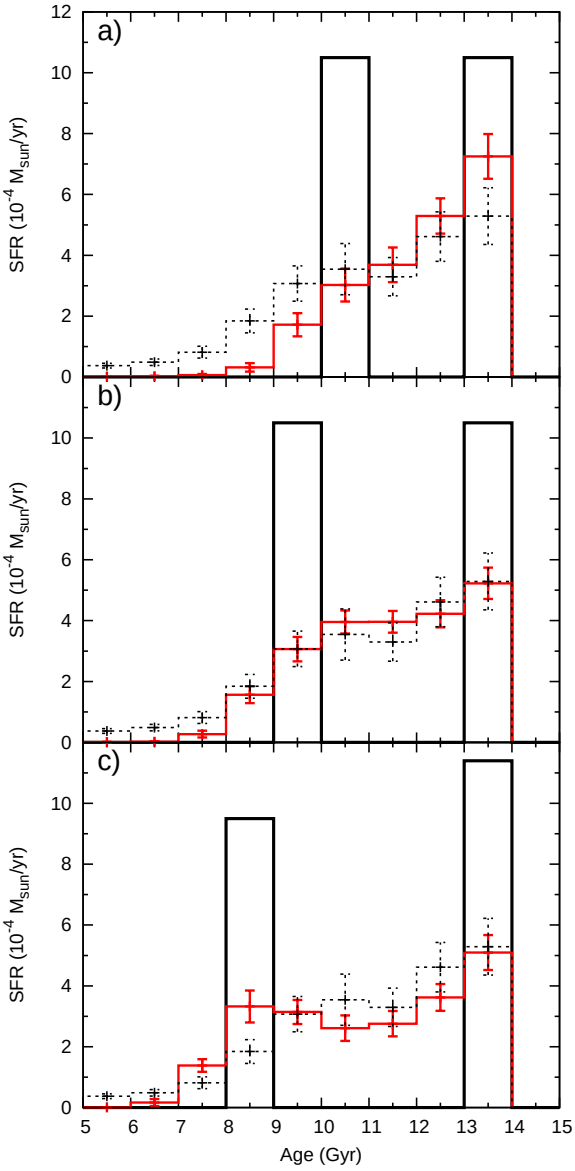

Figure 3.18: *The input and recovered SFH for a series of synthetic populations with two short (10 Myr) bursts of star formation. The oldest takes place at an age of 13.5 Gyr, with the second burst at an age of (**a**) 10.5 Gyr, (**b**) 9.5 Gyr and (**c**) 8.5 Gyr. The solid black histogram shows the input population, given the SFH binning adopted. The solid grey histogram shows the recovered SFH along with statistical errorbars. For comparison, the adopted SFH of annulus 1 of Sculptor (Figure 3.13) is shown as the black dashed histogram.*

3.96, although still not as good as the smooth SFH given in Section 3.4.2. Taking this approach further, adding ever more short bursts of star formation will provide a better representation of the observed CMD, to the point where we can not distinguish between bursty and continuous star formation. In the end, this is how our model builds up the SFH. The limits of the bursty nature of the Sculptor SFH cannot be tied down with CMD analysis at such old ages as these with better accuracy than shown in Fig-

ure 3.18. However, the form of the CMD and the metallicities of individual RGB stars would be markedly different if star formation had truly occurred in a few short bursts, and also other evidence such as the broad MDF makes it unlikely.

3.4.4 The timescale for chemical evolution

Determining ages of individual stars

Using the SFH determined for Sculptor it is possible to go back to the spectroscopic sample and determine the ages of the individual RGB stars. For each observed star with spectroscopic abundances we find all the stars in a synthetic CMD made with the SFH of Sculptor, with the same magnitude (in all filters) and metallicity within the observed uncertainties. These stars are considered to be representative of the age of the observed star. The mean age of the matched sample is adopted as the age of the observed star, with the corresponding standard deviation of the sample as an errorbar. In the case of Sculptor around 100 synthetic stars are typically available to compute the mean and standard deviation for each observed star, ensuring enough stars are present to determine a reasonable errorbar.
To demonstrate the advantage of using the SFH results to obtain ages for individual RGB stars a comparison is made to the standard simple isochrone fitting technique, which uses a fine grid of [Fe/H], age and [α/Fe] to obtain the age and uncertainty for an observed star along an isochrone. Figure 3.19a shows the Age-Metallicity Relation (AMR) obtained using simple isochrone fitting, and Figure 3.19b using our full SFH approach. The AMR determined using isochrone fitting has bigger age uncertainties and allows younger ages for each star, which are inconsistent with the SFH (see Fig 3.8). This is because the age for simple isochrone fitting is dependent only on the colour of the RGB and the measured [Fe/H], which allows a wide range in ages for each observed star. Conversely, the more constrained AMR coming from the SFH is because information from the entire CMD (and all modelled evolutionary phases) is used to constrain the age of a single observed star.

Chemical evolution of the Sculptor dSph

With accurate ages assigned to each RGB star in the HR spectroscopic sample it is possible to effectively measure the evolution of particular elements and, for the first time, directly determine timescales for chemical evolution. Figure 3.20a shows [Mg/Fe] for RGB stars in Sculptor measured from HR spectroscopy, with the age of the individual stars colour coded. Figure 3.20b shows that [Mg/Fe] follows a uniform trend with age, such that the oldest stars are more enhanced than the younger. We can also determine the age at which the “knee" (Tinsley, 1979; Gilmore and Wyse, 1991) occurs. This marks the time at which SNe Ia start to contribute to the [Fe/H] content of a galaxy (Matteucci and Brocato, 1990; Matteucci, 2003). In Sculptor, the turnover takes place between $-1.8<$[Fe/H]<-2.0 dex, from which we determine that the [Fe/H] from SNe Ia started to be produced 10.9 ± 1 Gyr ago. Therefore, the SNe Ia started contributing noticeably to the chemical evolution of Sculptor approximately 2 ± 1 Gyr after the beginning of star formation. This is the first direct measure of this timescale, although it has previously

been inferred from SNe Ia timescales and chemical evolution models (Mannucci et al., 2006, and references therein).

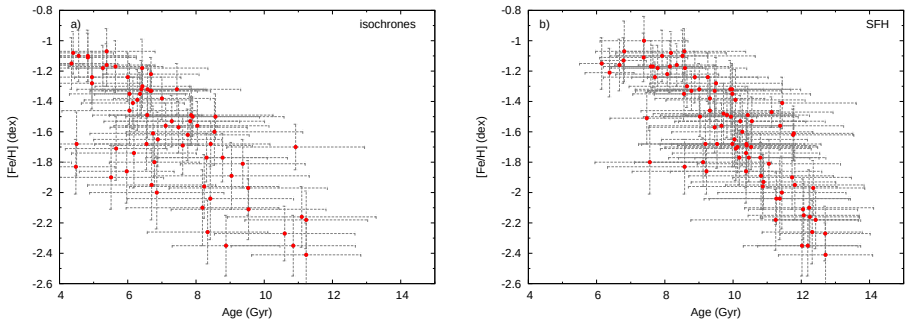

Figure 3.19: *The Age-Metallicity Relation of stars on the upper RGB in Sculptor, as determined using (**a**) simple isochrone fitting and (**b**) from our method incorporating the full SFH and MDF information.*

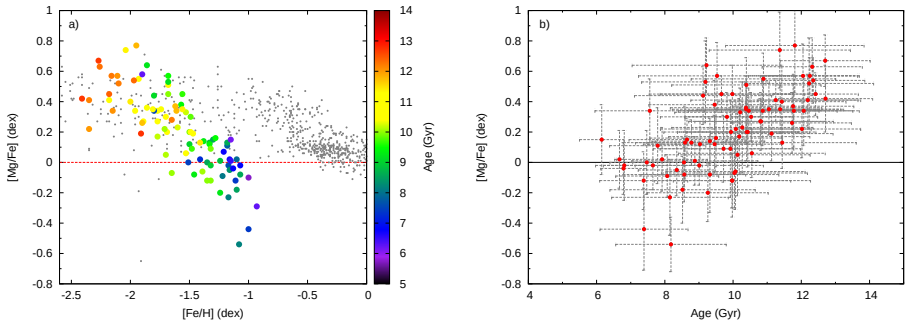

Figure 3.20: ***a)*** *[Mg/Fe] measurements for the HR spectroscopic sample of RGB stars in the Sculptor dSph (coloured filled circles). The colours represent the age in Gyr, derived from the SFH. Stars in the Milky Way are shown for comparison (small grey points).* ***b)*** *[Mg/Fe] is plotted directly against age for the same sample.*

3.5 Conclusions

We have presented the first detailed SFH of the Sculptor dSph, using a combination of deep, wide-field multi-colour photometry and spectroscopic metallicities and abundances. The method used to determine the SFH (described in Section 3.3) directly combines, for the first time, photometry with spectroscopic abundances.

The SFH (see Figure 3.8) shows features similar to previous rough SFHs (e.g. Da Costa, 1984; Hurley-Keller et al., 1999; Dolphin, 2002; Tolstoy et al., 2003), but resolves the

stellar ages with much greater accuracy. Additionally, the SFH quantifies the age and metallicity uncertainties and provides well motivated errors. The SFH and CEH have been determined over a large fraction of the Sculptor dSph (≈80% of the tidal radius), allowing us to quantify the radial age and metallicity gradients in Sculptor.

The SFH shows that star formation took place in Sculptor for an extended period of time, from 14 to 7 Gyr ago (see Figure 3.8) with a simple, steadily decreasing trend. The spatially resolved SFH over the whole galaxy (see Figure 3.13) shows that a radial gradient is present in age and metallicity. The MDF (right-hand panels of Figure 3.13) shows that the metal-poor, old populations are present at all radii while the more metal-rich, younger populations are found more toward the centre, consistent with previous qualitative results (de Boer et al., 2011).

We explored the temporal resolution of our final SFH for the innermost and outermost parts of Sculptor under study. We find that the outermost annulus is roughly consistent with a single episode of star formation. In the inner parts of Sculptor it is difficult to find a bursty SFH that matches all the available data. Therefore, we find no reason to assume bursty star formation episodes here and prefer the overall picture of a single, extended episode of star formation. Additionally, the spatially resolved SFH and CEH are more consistent with an age gradient than with two separate populations.

The SFH and CEH at different radii from the centre are consistent with the scenario where Sculptor first experienced a single sizeable burst of star formation at early times, with more metal-rich populations forming ever more concentrated towards the centre until about 6−7 Gyr ago, when the star formation activity ceased.

Likewise, the chemical evolution of the Sculptor dSph seems to be straightforward, according to Figure 3.20, which shows that [Mg/Fe] decreases steadily with time. The simple decline in the [Mg/Fe] distribution suggests that the chemical enrichment occurs uniformly over the SFH of the Sculptor dSph, with a change in slope when the SNe Ia start to contribute.

The timescale on which SNe Ia start to contribute significantly to the chemical evolution of Sculptor (approximately 2±1 Gyr after the beginning of star formation) is comparable within the errors to the timescale expected from the theory of SNe Ia timescales, although inconsistent with timescales of prompt SNe Ia explosions (see e.g. Raiteri et al., 1996; Matteucci and Recchi, 2001). The small number of stars and the large scatter on the knee position in Figure 3.20a means that the turnover age is not exactly defined. A larger sample of metal-poor stars is needed to obtain better statistics.

The formation of a well defined, narrow α-element vs. metallicity distribution and a tight Age-Metallicity relation (see Figure 3.19b) is consistent with the overall picture that the Sculptor dSph formed stars uninterrupted for an extended period of time. The temporal evolution of individual stars suggests a slow build up over several gigayears. A galaxy with a shorter period of star formation is unlikely to show such a well-defined extended AMR. If the SFH were more bursty, a greater spread in [α/Fe] would also be expected, instead of a smooth trend with age and [Fe/H].

As a result, Sculptor can be considered as a good benchmark for isolated star formation over an extended period of time at the earliest epochs.

acknowledgements

The authors thank ISSI (Bern) for support of the team “Defining the full life-cycle of dwarf galaxy evolution: the Local Universe as a template". T.d.B., E.T., E.S. and B.L. gratefully acknowledge the Netherlands Foundation for Scientific Research (NWO) for financial support through a VICI grant. The research leading to these results has received funding from the European Union Seventh Framework Programme (FP7/2007-2013) under grant agreement number PIEF-GA-2010-274151

Appendix 3.A Tests of the method

In order to test the ability of Talos to accurately recover a SFH, a number of tests were made on CMDs for which the properties are known, as well as on observed data for a well studied globular cluster.

3.A.1 Synthetic tests

First of all, a number of simple artificial stellar populations were generated. By recovering the SFH of these populations it is possible to test how accurate our method can recover an input SFH.

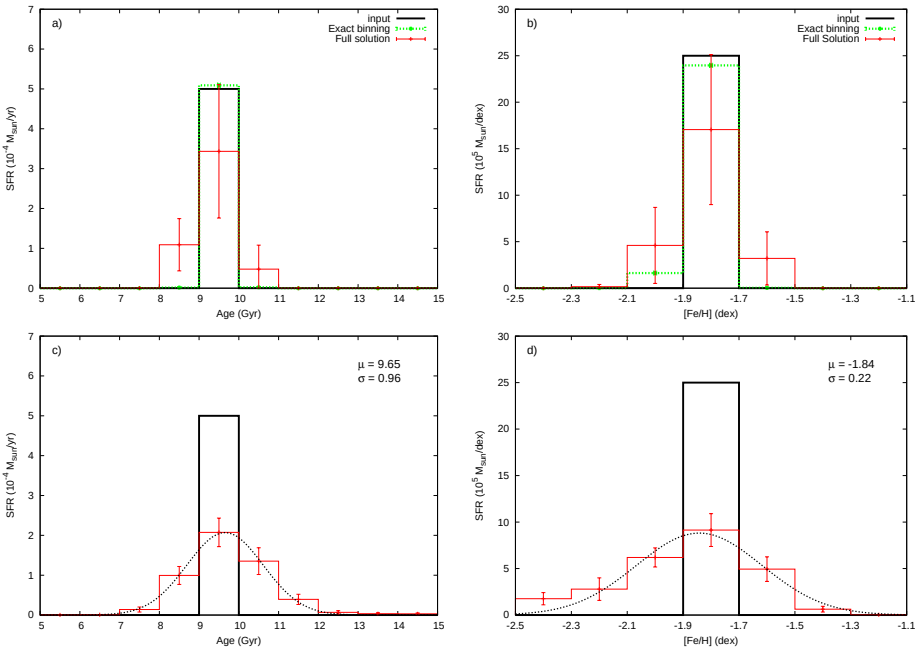

Figure 3.21: ***Upper row:*** *(**a**) Synthetic SFH and (**b**) CEH of a single burst of star formation without adding any photometric errors. The input SFH is the solid black histogram, while the recovered SFH is the green histogram when using the same parameter gridding as the input. The red histogram gives the solution when using a set of different parameter griddings.* ***Bottom row:*** *A burst of star formation with realistic errors from artificial star tests. The black histogram in (**c**) the SFH and (**d**) the ceh is the input SFH and the red histograms indicate the recovered SFH using a set of different population gridding schemes. A Gaussian fit to the recovered SFH is shown as a black line, with the mean (μ) and variance (σ) also listed.*

We determine the ability of Talos to recover the age, metallicity and SFR in a series of synthetic episodes of star formation. The stellar population was generated assuming the distance modulus and reddening of Sculptor, and using the artificial star tests to

obtain realistic photometric uncertainties. In this way realistic colour magnitude diagrams can be obtained, of the same quality as the observed CMD of the Sculptor dSph. As a first check, we apply the SFH fitting method to a single synthetic episode of star formation. The Dartmouth isochrones are used to generate a synthetic CMD with a continuous star formation between 9 and 10 Gyr and $-1.9<$[Fe/H]<-1.7 dex. First, the episode was generated without any photometric errors and the SFH determined using the exact parameter gridding of [Fe/H] and age as used to generate the population (green histogram). The SFH is also determined using a set of different parameter griddings (red histogram, see Figure 3.21a,b) in order to test the effect of using different griddings to obtain the uncertainties on the SFH (see Section 3.3.3).
Given exactly the same parameter gridding as the input population, the SFH is recovered at the right age and metallicity with the correct strength. A limited amount of "bleeding" is observed, due to the uncertainties induced by the quality of the data. The effect of using a set of different griddings is more substantial bleeding of the star formation rate into neighbouring bins in age and metallicity (as seen in the red histograms in Figure 3.21a,b). This bleeding is a direct consequence of the quality of the photometric data and the use of different parameter griddings, and determines the SFH resolution (see Section 3.3.3). Since we do not have a priori knowledge of the duration and metallicity of an episode of star formation in the observed data, the choice of adopting a single population gridding will lead to biases in the results. Therefore, we always consider a range of different parameter griddings in obtaining the final SFH.

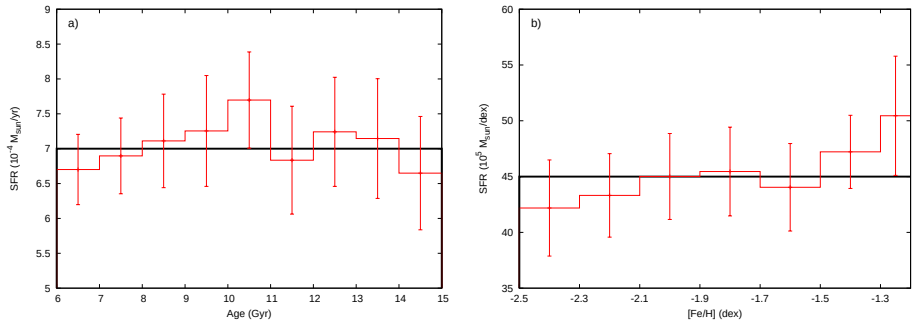

Figure 3.22: *(**a**) SFH and (**b**) CEH of a continuous episode of star formation including realistic errors. The black line indicates the input values and the red histogram the recovered values.*

When including realistic photometric errors determined from artificial star tests for the model of an episode of star formation, the same bleeding effect is seen. The parameters of the recovered SFH are determined by fitting a Gaussian profile, see Figures 3.21c,d. The peaks of the SFH and CEH are recovered well within the input values ([Fe/H]$_{mean}$=-1.84 dex, Age$_{mean}$=9.64 Gyr), but the star formation is distributed over more bins, spreading out the star formation episode in time. Figure 3.21 shows that ≈40% of the total star formation is typically recovered within the central peak. Due to the quality of the observed photometric data (which only just detects the oldest MSTOs) there remains some degeneracy between the burst strength and duration,

which could be removed by obtaining deeper CMDs that resolve the MSTO with more accuracy.
Next we consider a more realistic synthetic population which has experienced constant star formation (SFR=$10^{-4}M_{\odot}$/yr) over the metallicity range $-2.5<$[Fe/H]<-1.1 dex between 6 and 15 Gyr ago. To take into account the effect of constraints from spectroscopic observations, the solution was determined taking into account a synthetic MDF which samples 50% of the RGB stars. The results are given in Figure 3.22. It can be seen that the input values are correctly recovered for a synthetic population with constant star formation, within the SFH uncertainties.

3.A.2 Globular cluster NGC 1904

The final test we carry out is to apply our method to real observations of a Globular cluster, which is, within our errors, a simple stellar population. During our observing run Galactic globular cluster NGC 1904 was also observed in the B,V and I filters. For NGC1904 there have been several photometric and spectroscopic studies (see Table 3.1), making it a good test of our method. The reduction of these observations, as well as the artificial star tests were done in exactly the same way as for Sculptor.

Table 3.1: *Adopted properties of NGC1904*

Property	Value	Reference
$(m\text{-}M)_V$	15.45±0.02	(Ferraro et al., 1992)
E(B-V)	0.01	(Harris, 1996)
[Fe/H]	−1.579±0.069 dex	(Carretta et al., 2009)
[α/Fe]	0.31 dex	(Carretta et al., 2010)

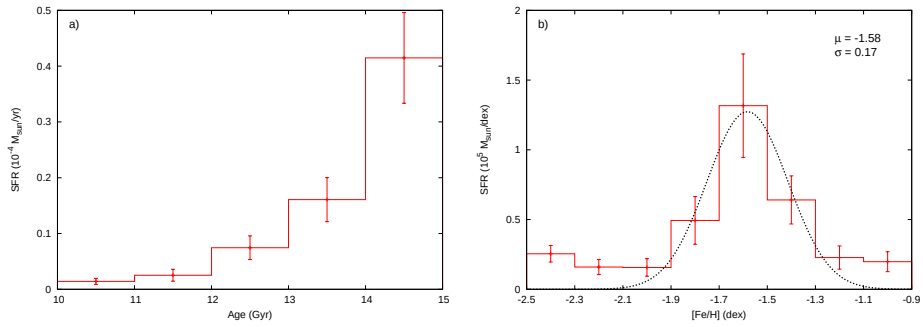

Figure 3.23: *(**a**) The SFH and (**b**) CEH obtained for NGC1904 from photometric information in the B,V and I filters. A Gaussian fit to the MDF is also shown as a black, dotted line, with parameters given in the plot.*

To obtain the SFH for NGC1904, [α/Fe] was chosen as a fixed value constrained by spectroscopic observations (see Table 3.1), while the age and metallicity were left as free parameters. The best solution, using only the available photometric data is given in Figure 3.23. The SFH and CEH show bleeding into neighbouring bins, due to measurement errors and the use of different parameter griddings used. This is similar to the bleeding effect seen in Figure 3.21. The SFH clearly indicates a very old population, in good agreement with typical globular ages. A Gaussian fit to the metallicity distribution gives a mean value (μ) at [Fe/H]=$-$1.58 dex, with a variance of σ=0.17 dex. This is in good agreement with the spectroscopic [Fe/H] given in Table 3.1. This shows that Talos is able to recover the age and metallicity of a real data set with all the errors and uncertainties that it implies.
These experiments show the capability of Talos to recover the age and metallicity of a stellar population, as well as the limit of our ability to unambiguously distinguish a burst of star formation from a more continuous SFR over a longer time.

CHAPTER FOUR

THE STAR FORMATION & CHEMICAL EVOLUTION HISTORY OF THE FORNAX DWARF SPHEROIDAL GALAXY

T.J.L. de Boer, E. Tolstoy, et al.

To be submitted to A&A

Abstract

We present deep photometry in the B,V and I filters from CTIO/MOSAIC for about 440.000 stars in the Fornax dwarf Spheroidal galaxy, out to a radius of $r_{ell} \approx 0.8$ degrees. By combining the carefully calibrated photometry with the spectroscopic metallicity distributions of individual Red Giant Branch stars we obtain the detailed star formation and chemical evolution history of Fornax, as well as its globular cluster system.

The star formation history shows that Fornax has had a complex past, which is dominated by intermediate age (1−10 Gyr) populations, but also includes ancient (10−14 Gyr), and young (≤1 Gyr) stellar populations. The Star Formation History at different radii from the centre shows that Fornax displays a radial age and metallicity gradient, with younger, more metal-rich populations dominating the centre. Within an elliptical radius of 0.8 degrees, or 1.9 kpc from the centre, a total mass in stars of 4.3×10^7 $M_\odot$ was formed, from the earliest times until 250 Myr ago.

Using the detailed star formation history, age estimates are determined for individual stars on the upper RGB, for which spectroscopic abundances are available. This gives the accurate age-metallicity relation of the Fornax dSph from individual stars, which suggests that the average metallicity of Fornax went up rapidly from [Fe/H]≤−2.5 dex to [Fe/H]=−1.5 dex between 8−12 Gyr ago, after which a gradual enrichment resulted in a narrow, well-defined sequence which reaches [Fe/H]≈−0.8

dex, ≈3 Gyr ago.
These age estimates also allow us to study the change of chemical elements directly as a function of time, and determine detailed timescales for the evolution of individual chemical elements. A rapid decrease in [Mg/Fe] is seen for the stars with [Fe/H]≥−1.5 dex, with a clear trend in age. The knee in the alpha-element distribution is not observed, but predicted to occur at [Fe/H]≈−1.5 dex, at an age of 7–10 Gyr.
The spatial distribution of young stars in Fornax reveals the presence of a new young substructure, located at 0.3 degrees, or 0.7 kpc from the centre of Fornax. This substructure is dominated by very young stars with a peak at 250 Myr, and contains a total mass in stars of 2.28×10^4 $M_\odot$ within ≈6 arcmin^2.
Analysis of the star formation history of the Fornax globular clusters shows that Fnx 1, 2,3 and 5 are consistent with old, metal-poor populations, consistent with observed spectroscopic metallicities. Conversely, Fnx 4 displays an extended star formation history, inconsistent with normal globular clusters, suggesting it might be the nucleus of theFornax dSph.

4.1 Introduction

Dwarf spheroidal galaxies (dSph) are good places to study the processes that drive galaxy evolution on small scales. Due to their close proximity to the Milky Way (MW) they can easily be resolved into individual stars, and studied in detail. Once thought to be the simplest systems in the Local Group (LG), the dSphs have been found to display complicated evolutionary histories (Tolstoy et al., 2009).
The Fornax dSph was discovered by Shapley in 1938, and is currently regarded as one of the most luminous and massive dSphs in the Local Group, second only to the Sagittarius dwarf (Mateo, 1998). It has an absolute magnitude of M_V=−13.3, and a total (dynamical) mass of $\approx1.6\times10^8$ $M_\odot$ (Walker et al., 2006; Klimentowski et al., 2007; Łokas, 2009). Fornax is located at a distance of 138 kpc ($(m\text{-}M)_V$=20.84±0.04), determined using RR Lyrae stars, in good agreement with other measurements using the infrared tip of the Red Giant Branch (RGB) method and the Horizontal Branch (HB) level (Greco et al., 2005; Rizzi et al., 2007; Pietrzyński et al., 2009). The estimated reddening toward Fornax, from extinction maps, is E(B−V)=0.03 (Schlegel et al., 1998).
Fornax can easily be resolved into individual stars, but given the substantial size on the sky (r_{tidal}=71±4 arcmin or 2.85±0.16 kpc), wide-field imaging is needed to study the spatial distribution of resolved stars (Irwin and Hatzidimitriou, 1995; Battaglia et al., 2006). The first structural study of Fornax was done with photographic plates by Hodge (1961b), revealing that the ellipticity of Fornax isophotes increased with distance from the centre. Furthermore, an asymmetry was found with a peak density offset from the adopted Fornax central position, confirmed by subsequent studies (de Vaucouleurs and Ables, 1968; Hodge and Smith, 1974). Several globular clusters (GC) were also found (Shapley, 1938b; Hodge, 1961a), making Fornax one of the few Local Group dwarf galaxies to have a globular cluster system.
Later, CCD studies were conducted in the Fornax dSph, down to ever fainter brightness levels (Eskridge, 1988a,b; Demers et al., 1994; Irwin and Hatzidimitriou, 1995; Walcher et al., 2003). Recent, deep photometric surveys of Fornax have found stel-

lar over-densities and “shells", some of which are believed to be the result of a recent encounter with a smaller system (Coleman et al., 2004, 2005b; Olszewski et al., 2006; Battaglia et al., 2006).
Photometric studies of the Fornax dSph have revealed a large number of carbon stars, indicating a substantial intermediate age (1−10 Gyr) population (Aaronson and Mould, 1980, 1985; Azzopardi et al., 1999). In the central regions of Fornax, young Main Sequence stars (≤1 Gyr) were first identified by Buonanno et al. (1985), which led to the discovery of a stellar population gradient of the young and intermediate age stars (Stetson et al., 1998). The presence of old stellar populations (≥10 Gyr) was revealed by the discovery of several RR Lyrae stars (Bersier and Wood, 2002), and confirmed by the presence of an extended HB (Saviane et al., 2000).
Detailed studies of the Star Formation History (SFH) of Fornax have been made, using deep Colour-Magnitude Diagrams (CMDs) (Stetson et al., 1998; Buonanno et al., 1999; Saviane et al., 2000; Gallart et al., 2005a). Using wide-field CMDs, Stetson et al. (1998) determined the age of the young MS population as 100−200 Myr, with similar results found by Saviane et al. (2000). Deep photometry in small fields close to the Fornax centre indicated that star formation started ≈12 Gyr ago, continuing almost to the present day, with a young burst of star formation at an age of 1−2 Gyr (Buonanno et al., 1999; Gallart et al., 2005a). Furthermore, hints were found of separate Sub-Giant Branches (SGB), indicating that star formation occurred in discrete bursts (Buonanno et al., 1999).
A deep photometric survey was done by Coleman and de Jong (2008), covering an area of 5.25 deg^2 centred on Fornax, down to a 50% completeness limit of B=23.0 and R=23.5. The SFH was determined at different radii from the centre, showing that Fornax experienced a complex evolutionary history with numerous epochs of star formation. A significant population gradient is found with radius, with ancient stars being present at all radii, but more recent star formation concentrated to the centre. The star formation is found to have gradually decreased from the earliest time, until a sudden burst of strong star formation occurred ≈4 Gyr ago.
Numerous spectroscopic studies have also been performed in Fornax, of individual stars on the upper RGB. Medium resolution Ca II triplet spectroscopy has provided [Fe/H] measurements for increasing numbers of stars (33 stars (Tolstoy et al., 2001), 117 stars (Pont et al., 2004), 870 stars (Battaglia et al., 2008b), 675 stars (Kirby et al., 2010)). These studies have accurately determined the Metallicity Distribution Function (MDF) of Fornax, which confirms that the dominant population is relatively metal-rich ([Fe/H]≈−0.9 dex), but that stars as metal-poor as [Fe/H]≤−2.8 dex are also present. The metal-rich stars ([Fe/H]≥−1.3 dex) have been shown to display colder kinematics and a greater central concentration, while the metal-poor stars ([Fe/H]≤−1.3 dex) are found in a spatially extended distribution.
High resolution (HR) spectroscopic studies of individual RGB stars in Fornax have been carried out within the central 0.3 degrees of Fornax, for 3 stars (Tolstoy et al., 2003; Shetrone et al., 2003), 9 stars in three globular clusters (Letarte et al., 2006) and more recently 81 stars (Letarte et al., 2010) using VLT/FLAMES. These studies have revealed the complex abundance pattern for individual stars in Fornax, including alpha, iron-peak and heavy-elements. Additionally, a recent HR follow-up study has discovered

the presence of an extremely metal-poor star (Fe/H]=-3.66±0.04 dex) in the Fornax dSph (Tafelmeyer et al., 2010).
Observed properties of the Fornax dSph have been modelled several times, in simulations using different techniques (e.g., Lanfranchi and Matteucci, 2003; Mashchenko et al., 2008; Revaz et al., 2009; Kirby et al., 2011; Revaz and Jablonka, 2012). The chemodynamical Smoothed-Particle Hydrodynamics (SPH) code used by Revaz and Jablonka (2012) correctly matches the observed metal-rich MDF of Fornax, and shows a narrow [Mg/Fe] distribution, consistent with trends derived from HR spectroscopy. Cosmological simulations have been performed by Mashchenko et al. (2008), reproducing stellar parameters of a model galaxy in good agreement with the Fornax dSph, including a globular cluster system. Furthermore, chemical evolution models of the Fornax dSph have been able to correctly reproduce the observed MDF and alpha-element distribution (Lanfranchi and Matteucci, 2003; Kirby et al., 2011).
In this work, we present accurately calibrated, wide-field photometry of the Fornax dSph, going down to the Main Sequence Turn-Off (MSTO), carried out with MOSAIC on the CTIO 4m/Blanco telescope. Using the accurate photometry, the SFH is determined over a large area of the Fornax dSph, using CMD synthesis methods (e.g., Tosi et al., 1991; Tolstoy and Saha, 1996; Gallart et al., 1996a; Dolphin, 1997; Aparicio et al., 1997). Spectroscopic metallicities (from Ca II triplet spectroscopy) are directly used in combination with the photometry, to provide additional constraints on the age of the stellar populations. The detailed SFH is used to determine the probability distribution function for age of individual stars, giving age estimates for stars on the upper RGB. These ages are linked to observed spectroscopic metallicities and abundances, giving an accurate Age-Metallicity Relation (AMR) and determining the timescale of chemical enrichment from different types of Supernovae (SNe) in the Fornax dSph.
The paper is structured as follows: in section 4.2 we present our photometric and spectroscopic observations. In section 4.3 we describe the specifics of the method used to obtain the SFH of Fornax. An analysis of the photometric and spectroscopic properties of resolved stars in Fornax is done in section 4.4. Subsequently, section 4.5 discusses the analysis of stellar over-densities in the Fornax dSph. The analysis of the detailed, spatially resolved SFH is given in section 4.6 and the chemical evolution timescales derived from individual RGB stars in section 4.7. Finally, section 4.8 discusses the results obtained from the SFH and chemical evolution timescales, and section 4.9 gives a summary.

4.2 Data

4.2.1 Photometry

Deep optical photometry of the Fornax dSph in the B, V and I filters was obtained using the CTIO 4-m MOSAIC II camera over 9 nights in October 2008 and November 2009. Our observing strategy was to obtain several non-dithered, long (600s) exposures for each pointing, which were stacked together to obtain the deepest photometry possible. Short (10s, 90s) exposures were also obtained, in order to sample the bright stars

that are saturated in the deep images.
In order to ensure accurate photometric calibration of the data set, several fields were observed in Fornax using the 0.9m CTIO telescope, under photometric conditions. Furthermore, observations were also made of Landolt standard fields (Landolt, 1992, 2007) covering a range of different airmass and colour.

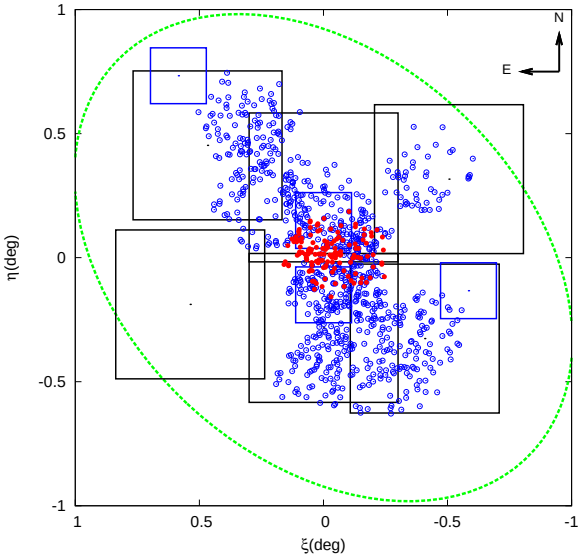

Figure 4.1: *Coverage of the photometric and spectroscopic observations across the Fornax dwarf spheroidal galaxy. The big squares denote the coverage of the CTIO 4m/MOSAIC fields, while the smaller squares show the CTIO 0.9m fields. The open circles show the stars observed in the VLT/FLAMES Ca* II *triplet survey (Battaglia et al., 2008b; Starkenburg et al., 2010), while the solid dots mark the stars observed using medium and high resolution spectroscopy (Letarte et al., 2010; Kirby et al., 2010). The dashed ellipse is the tidal radius of Fornax, as given by Battaglia et al. (2006).*

The reduction and accurate calibration of this dataset follows the steps described in detail in Chapter 2.2 (see also de Boer et al. (2011)). An accurate astrometric solution was determined for each pointing, after which the different exposures of each field were aligned and stacked together to obtain a single, deep image. Photometry was carried out on all images using DoPHOT (Schechter et al., 1993). An accurate photometric calibration solution was determined using the standard star observations, depending on airmass, colour and brightness. All fields were calibrated and subsequently placed on the same photometric scale using the overlapping regions between different fields. Finally, the different fields were combined to obtain a single, carefully calibrated photometric catalog.
The positions of the observed fields from the 4m telescope are shown in Figure 4.1. The spatial coverage of the B and V filters is complete for $r_{ell} \leq 0.8$ degrees, while the I filters is complete for $r_{ell} \leq 0.4$ degrees. The position, exposure time, airmass and seeing conditions of the Fornax fields are given in Appendix 4.A.

4.2.2 Spectroscopy

Medium and high resolution spectroscopic observations are available for individual stars on the RGB in Fornax, giving either measurements of [Fe/H] or detailed abundance patterns of individual stars.
Medium resolution (R~6500) Ca II triplet spectroscopy is available for 870 individual RGB stars in the Fornax dSph, from VLT/FLAMES observations (Battaglia et al., 2008b; Starkenburg et al., 2010). These observations provide [Fe/H] measurements for stars out to a radius of 1.3 degrees from the centre of the Fornax dSph, and include a range in metallicities from $-3.0<$[Fe/H]<-0.5 dex. Additionally, medium resolution spectroscopy by Kirby et al. (2010) provides [Fe/H] and α-element abundances for 675 stars within the central 0.3 degrees of Fornax, with a metallicity range of $-2.8<$[Fe/H]<-0.1 dex.
Furthermore, HR spectroscopy (VLT/FLAMES) is also available for $r_{ell} \leq 0.3$ degrees, for 81 individual RGB stars in the Fornax dSph (Letarte et al., 2010), providing [Fe/H] as well as α-elements (O, Mg, Ca, Si, Ti) and r- and s-process elements (Y, La, Ba, Eu, Nd). For [α/Fe] obtained from these observations, we assume [α/Fe] =([Mg/Fe] +[Ca/Fe] +[Ti/Fe])/3. The HR spectroscopy covers a range in metallicity from $-2.6<$[Fe/H]<-0.6 dex, for stars on the upper RGB.
The spatial coverage of the spectroscopic observations is shown in Figure 4.1, for both the HR and Ca II triplet spectroscopy.

4.3 SFH Method

To determine the SFH of the Fornax dSph, we compare the observed CMDs with a grid of synthetic CMDs using Hess diagrams (plots of the density of observed stars) of stars in the CMD. We use our own code, Talos, which is based on the synthetic CMD method (e.g., Tosi et al., 1991; Tolstoy and Saha, 1996; Gallart et al., 1996a; Dolphin, 1997; Aparicio et al., 1997). However, Talos simultaneously takes into account observations in all available photometric filters as well as the spectroscopic MDF, to obtain the most accurate SFH, as discussed in detail in Chapter 3.3 (see also de Boer et al. (2012)).
First, a set of synthetic ideal CMDs and MDFs is generated using the Dartmouth Stellar Evolution Database (Dotter et al., 2008), for population bins covering the range in age, metallicity and α-element abundances. Results from artificial star tests are used to add observational effects to the synthetic CMDs in a statistical manner, to obtain models that can be compared directly to the observed CMD. Using the synthetic CMDs, model MDFs are generated by extracted only the stars corresponding to the same magnitude range as the spectroscopic sample. The stars are binned in metallicity and convolved with a Gaussian profile to simulate observational errors.
The difference between model and observed CMD and MDF is minimized according to a Poisson equivalent of χ^2 (Dolphin, 2002). The uncertainties on the SFH are obtained by determining the SFH using a series of different CMD and parameter griddings, as described by Aparicio and Hidalgo (2009). The average of all solutions is adopted as the final SFH, with the standard deviation as errorbars. In this way, the best matching star formation rate is obtained for each population bin (with age and metallicity)

considered in the SFH. These values are then projected onto one axis to obtain the star formation rate as a function of age (Star Formation History) or metallicity (Chemical Evolution History).
Talos has been extensively tested, and has been shown to accurately reproduce the properties of both real and synthetic test data (de Boer et al., 2012). Before applying Talos to our photometric and spectroscopic data sets of the Fornax dSph, we need to take into account the specifics of the SFH determination of this galaxy.

4.3.1 Artificial star tests

To simulate observational conditions in the synthetic CMDs used to determine the Fornax SFH, a large number of artificial star test simulations have been carried out, similar to the method described in de Boer et al. (2012). This approach is the only way to take into account the complex effects that go into the simulation of observational biases, such as colour-dependence of the completeness level and the asymmetry of the photometric errors of stars at faint magnitudes (e.g. Gallart et al., 1996b).

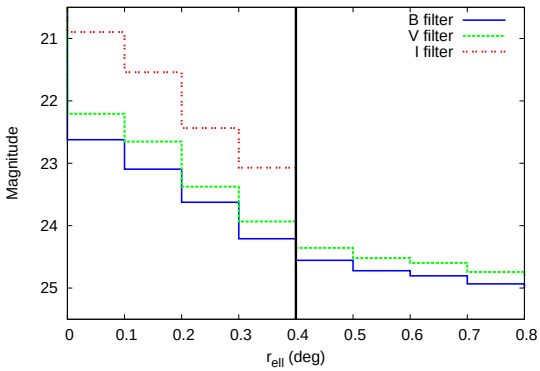

Figure 4.2: *The 50% completeness level in the B (solid blue line), V (green dashed line) and I (red dotted line) filters for increasing elliptical radius (r_{ell}) from the centre of the Fornax dSph. The vertical (black) line indicates the radius up to which observations in the I filter are completely sampled.*

A set of artificial stars was generated with parameters within the range 0.25<age<15 Gyr, $-2.5<$[Fe/H]<-0.30 dex, $-0.2<[\alpha/\mathrm{Fe}]<0.60$ dex. Stars were distributed randomly across the six MOSAIC pointings in Fornax, in 3 different filters. To avoid changing the crowding properties in the images no more than 5% of the total observed stars were ever injected as artificial stars at one time. A total of 400 images in each of the two inner fields, and 200 images in each of the four outer fields were created, containing 5000 artificial stars each. This resulted in 4000 images, containing a total of 8 million artificial stars spread across the full area of the Fornax dSph.
Figure 4.2 shows the variation of the 50% completeness level with distance from the centre of Fornax, in the three different filters. The completeness level in the I filter is shown only for $r_{ell} \leq 0.4$ degrees, due to the lack of I band observations in the outer parts of Fornax. The centre of Fornax is less complete at a fixed magnitude limit than the outer regions, due to the large amount of crowding in the central region, which means fewer stars are unambiguously detected, and placing the 50% completeness at brighter magnitude levels.

The results from the artificial star tests are used to include observational errors in synthetic CMDs in a statistical manner, so they can be compared directly to the observed CMDs, to obtain the best matching SFH.

4.3.2 Parameter space

The limits of populations adopted in the SFH are determined by considering all available information from the current data sets (see Section 4.2) as well as the literature.
For the limits on metallicitiy, we consider the spectroscopic MDF from Ca II triplet and HR spectroscopy. On the metal-poor end, the [Fe/H] is limited to [Fe/H]=−2.5 dex, by the availability of metallicity in the Dartmouth Stellar Evolution Database (Dotter et al., 2008). However, this is not a problem, since the spectroscopic MDF shows that almost no stars in Fornax have [Fe/H]≤−2.5 dex (Starkenburg et al., 2010). On the metal-rich end, the spectroscopic MDF shows that no stars with [Fe/H]≥−0.5 dex are present on the RGB. However, higher metallicities may be present in young Main Sequence stars, which have no corresponding RGB. From previous derivations of the SFH, no stars have been found more metal-rich than [Fe/H]=−0.1 dex (Coleman and de Jong, 2008), which we adopt as the metallicity limit in our SFH. A binsize of 0.2 dex is assumed for [Fe/H], which is similar to the average observed uncertainty on [Fe/H].
In order to take into account the α−element abundances, we adopt a linear [Fe/H] vs [α/Fe] relation, based on the HR spectroscopic abundances (Letarte et al., 2010). A range in [α/Fe] is assumed for each bin in [Fe/H], which reproduces the trends in the HR data.
The choice of possible ages to adopt in the SFH solution is motivated by previous derivations of the SFH of the Fornax dSph. Previous work has shown that Fornax contains stars covering all ages, from ancient (≥10 Gyr) to very young (≤1 Gyr) ages (Buonanno et al., 1999; Gallart et al., 2005a; Coleman and de Jong, 2008). This is also consistent with the observed CMDs, which show a prominent blue plume, caused by stars with ages less than 1 Gyr. The lower limit in age is set by the adopted isochrone set, which does not contain isochrones with ages≤0.25 Gyr. Assuming a maximum age of 14 Gyr, for the age of the Universe, we consider therefore a range of ages between 0.25 and 14 Gyr old. A binsize of 1 Gyr is used for ages ≥5 Gyr, 0.5 Gyr for ages between 1−5 Gyr and 0.25 Gyr for ages ≤1 Gyr, to take into account the different age sensitivity of young MSTOs (Hidalgo et al., 2011).

4.3.3 Age resolution

The age resolution of the SFH solution determined by Talos is important to understand the limitations of the final SFH of Fornax. The ability to resolve episodes of star formation at different ages depends mainly on the photometric depth of the observed photometry. Furthermore, the method of determining the uncertainties of the solution (see Section 4.3) results in a smoothing of the SFH, which gives limits to the resolution of the SFH at different ages. The age resolution of the SFH solutions is determined by the ability to recover the SFH of a set of synthetic populations at different input ages (e.g., Hidalgo et al., 2011).

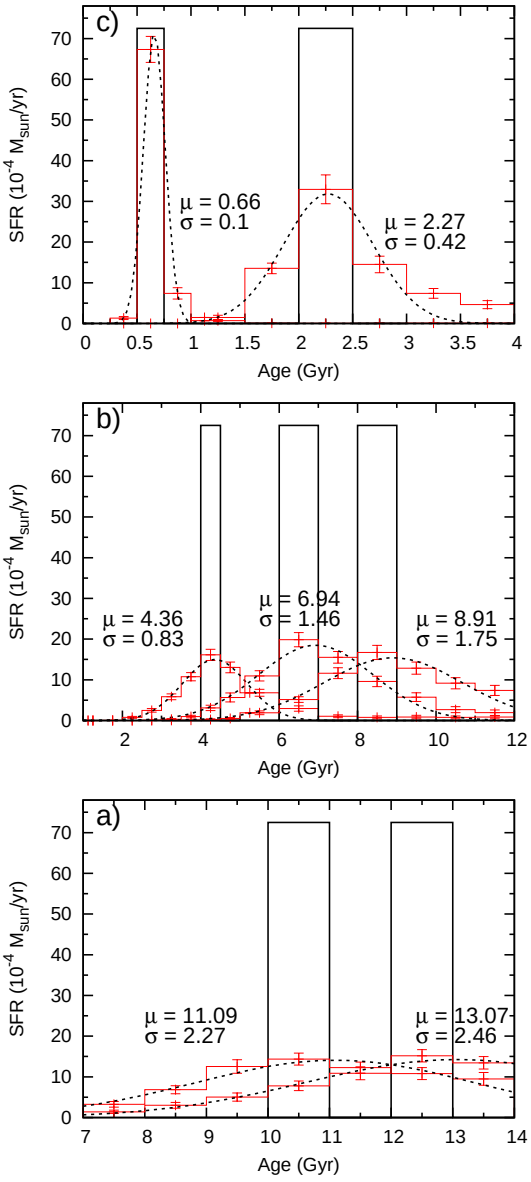

Figure 4.3: *Input and recovered SFHs of a series of synthetic short (10 Myr) bursts of star formation at young (a), intermediate (b) and old (c) ages. The black, solid histogram shows the input SFH, given the adopted binning of the solution. The red histograms show the recovered SFH, as well as the fit of a Gaussian distribution as the dashed line. The mean (μ) and variance (σ) of the fitted Gaussian distribution are also listed.*

A set of seven synthetic short bursts of star formation (with a duration of 10 Myr) was generated, with different input ages covering the age range adopted for Fornax (0.6, 2.2, 4.2, 6.5, 8.5,10.5 and 12.5 Gyr). The metallicity distribution of the synthetic bursts is chosen to match the observed MDF of Fornax. Using artificial star test results, observational conditions were simulated corresponding to the central region of Fornax.

Given that the crowding is highest in this part of the galaxy (and the resulting photometry the least deep), this will result in upper limits to the age resolution. The SFH for the synthetic bursts is recovered by fitting the photometry in three filters (B,V and I), simultaneously with a synthetic 50% complete MDF with similar photometric depth as the Ca II triplet spectroscopy.

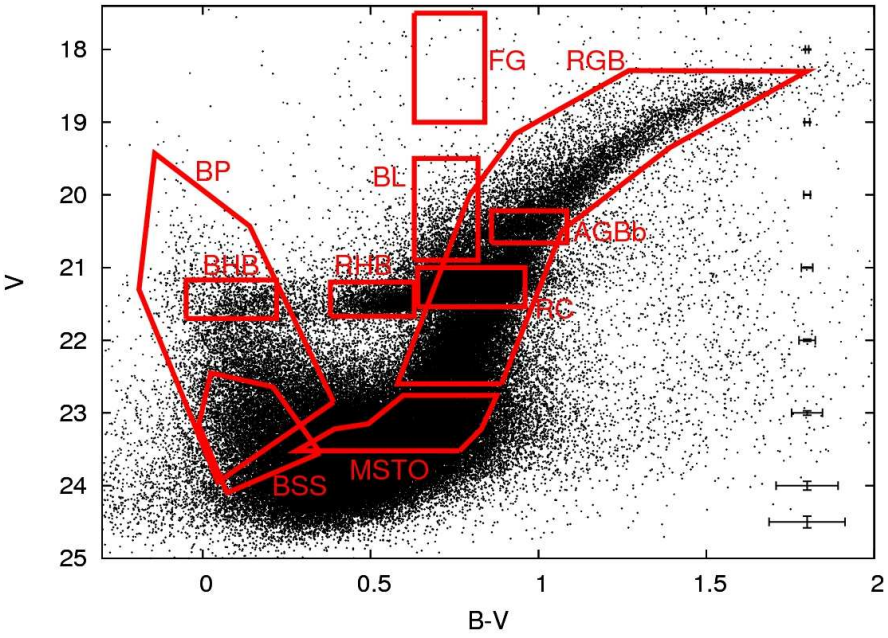

Figure 4.4: *Fornax (V, B−V) CMD of the central r_{ell}≤0.4 degrees with boxes identifying the different stellar populations. BHB: Blue Horizontal Branch, RHB: Red Horizontal Branch, RGB: Red Giant Branch, BSS: Blue Straggler Stars, MSTO: Main Sequence Turn-Off, BP: Blue Plume, BL: Blue Loop, RC: Red Clump, AGBb: AGB bump. A box providing an estimate of the Milky Way foreground contamination is also shown (FG). Errorbars represent the photometric errors at each magnitude level.*

The recovered and input SFH for the synthetic bursts is shown in Figure 4.3, for young (a), intermediate (b) and old (c) star formation episodes. The recovered SFH is fit by a Gaussian distribution, from which we determine the age of the central peak (μ) as well as the variance σ, which determines the resolution of the recovered burst. Figure 4.3 shows that the central peak is recovered at the correct age for young ages (≤7 Gyr), given the binning adopted for the solutions. For older ages the peak of the synthetic burst is recovered at slightly too old ages.
The Gaussian fits to the bursts show that the age resolution of the recovered bursts is significantly better at young ages than at old ages. For the bursts at young ages with small age resolution, the star formation is confined mostly to the central bin, while

for the older bursts the star formation is spread out over multiple bins. The bursts are recovered with a resolution of ≈0.1 Gyr at an age of 0.6 Gyr, ≈0.4 Gyr at an age of 2.2 Gyr, ≈0.8 Gyr at an age of 4.2 Gyr ≈1.5 Gyr at an age of 6.5 Gyr, ≈1.8 Gyr at an age of 8.5 Gyr, ≈2.3 Gyr at an age of 10.5 Gyr and ≈2.5 Gyr at an age of 12.5 Gyr, which is consistent with values between 17 and 22% of the adopted age.

4.4 The Colour-Magnitude Diagrams

The full, calibrated photometry catalog discussed in Section 4.2.1 contains photometry in the Fornax dSph in the B,V and I filters for radii out to r_{ell}≈1.5 degrees. The B and V filters are fully complete for radii r_{ell}≤0.8 degrees, while the I filter is complete only for r_{ell}≤0.4 degrees. Figure 4.4 shows a (V, B−V) CMD of the inner r_{ell}≤0.4 degrees of the Fornax dSph, marked with the different evolutionary features that can be seen in the CMD. Using the full catalog we can construct CMDs at different radii from the centre of the Fornax dSph, which can be used to study the radial behaviour of different evolutionary features.

Figures 4.5 and 4.6 show carefully calibrated (V, B−V) and (I, V−I) CMDs for the Fornax dSph at different elliptical radii (r_{ell}). Errorbars show the photometric errors at each magnitude level, and the (grey) line indicates the 50% completeness level at each elliptical radius. A reference isochrone tracing the dominant RGB of Fornax is also shown, in black. No de-reddening has been applied to the CMDs in Figures 4.5 and 4.6; Instead, models and isochrones used in the CMD analysis are reddened using the extinction coefficient adopted for Fornax (Schlegel et al., 1998).

The CMDs in Figures 4.5 and 4.6 display a wide variety of evolutionary features, consistent with an extended period of star formation (Gallart et al., 2005a; Coleman and de Jong, 2008). The presence of blue RGB stars and an old MSTO at all radii indicate the presence of ancient stars (≥10 Gyr). Additionally, Blue Horizontal Branch (BHB) stars are also present, as becomes clear from the CMDs of the outskirts of Fornax. In the inner parts of Fornax the BHB is heavily contaminated by the presence of young stars, which occupy the same position in the CMD.

A well populated Red Horizontal Branch (RHB) and Red Clump (RC) indicate that the main population of stars in Fornax has intermediate age (1−10 Gyr), further supported by the presence of a strong red RGB population. These features disappear from the CMDs with increasing elliptical radius, which is a clear sign that the intermediate age stars are more centrally concentrated than the old stars.

Clear signs of recent star formation (≤2 Gyr) are found only in the central parts of Fornax, such as the presence of Blue Loop (BL) stars and a strong Blue Plume (BP) population. These evolutionary features disappear rapidly at larger distances from the centre, which is a clear sign of radially changing age and/or metallicity of stars in Fornax.

This is also seen in the radial distribution of the BP, RGB and MSTO populations, as given in Figure 4.7. The young (BP) population is most centrally concentrated, while the stars on the RGB (which traces both the intermediate and old populations) is more extended. Finally, the old MSTO stars show an extended radial distribution, with stars present at all radii.

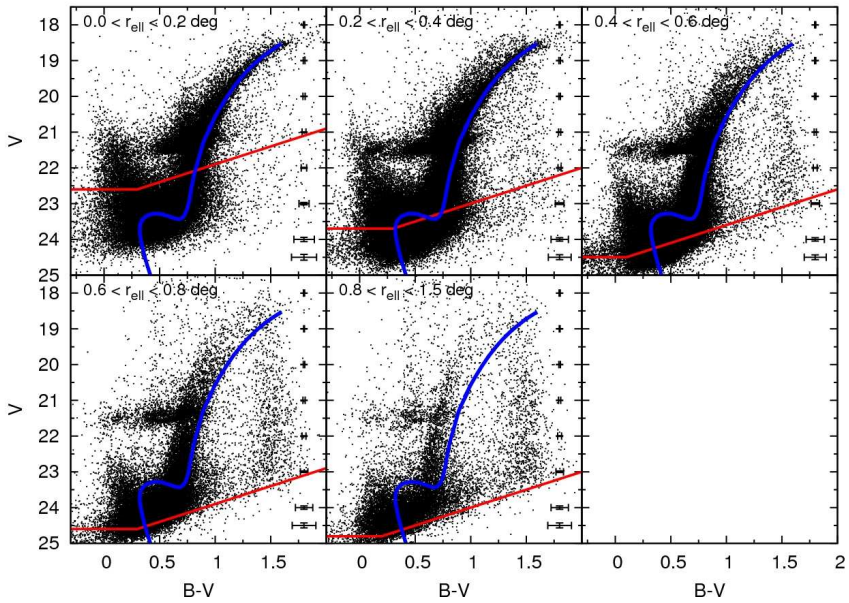

Figure 4.5: *(V, B−V) Colour-Magnitude Diagrams of the Fornax dwarf spheroidal, shown for increasing elliptical radius. Error bars showing the average photometric error and a 50% completeness line (grey) are also included. The solid black line shows a reference isochrone corresponding to the RGB of the dominant population ([Fe/H]=-1.00 dex, [α/Fe]=0.00 dex, Age=4 Gyr).*

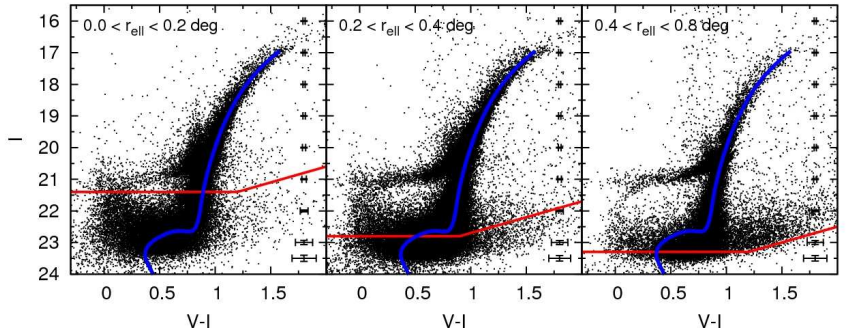

Figure 4.6: *(I, V−I) Colour-Magnitude Diagrams of the Fornax dSph for increasing elliptical radius. The error bars show the average photometric error at each magnitude level, and the grey line indicates the 50% completeness level. The solid black line shows a reference isochrone corresponding to the dominant RGB population in Fornax.*

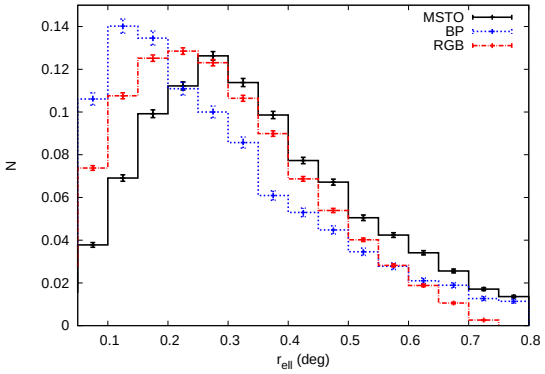

Figure 4.7: *Normalised radial distribution of the BP, RGB and MSTO populations (shown in Figure 4.4) of the Fornax dSph.*

Besides these features, the outskirts of Fornax also show a population of blue stars extending from the old MSTO with a different slope than observed in the central region. This feature could be due to the presence of young stars, but is also consistent with the position of possible Blue Straggler Stars (BSS) (Mapelli et al., 2009). To study the stellar populations of Fornax, and their trends, in more detail we analyse the different CMD features and search for variations with elliptical radius.

4.4.1 The Red Giant Branch

The RGB of Fornax displays a wide spread in colour, as seen in Figures 4.5 and 4.6. This is indicative of a spread in metallicity and/or age, as first found by (Stetson et al., 1998). Figure 4.8 shows a zoom-in off the RGB region of the Fornax dSph, at different elliptical radii. Two reference isochrones are overlaid on the CMD, representative of the metal-poor ([Fe/H]=−2.5 dex, Age=14 Gyr, grey) and metal-rich ([Fe/H]=−1.0 dex, Age=4 Gyr, black) populations present in Fornax (Battaglia et al., 2008b; Starkenburg et al., 2010; Letarte et al., 2010). The ages of both isochrones have been selected to fit the colours of RGB stars of the corresponding metallicity.

The innermost region of Fornax displays a strong red RGB component, which is well traced by a population with an age of 4 Gyr. For increasing elliptical radius this population diminishes rapidly, while the old, blue RGB component remains present at all radii. The observed effect with distance from the centre is consistent with the presence of a radial metallicity gradient in Fornax. We have checked if this effect could be due to the decreased total number of stars at different elliptical radii, and found that the same effect is still visible after randomly selecting the same number of stars in each panel of Figure 4.8.

To investigate this gradient in more detail we use the medium resolution Ca II triplet spectroscopy of individual RGB stars from Starkenburg et al. (2010) (see Section 4.2.2). Figure 4.9 shows the RGB of Fornax overlaid with the [Fe/H] metallicities of individual RGB stars where Ca II spectroscopy is available. Due to the higher crowding in the central region a brighter magnitude limit was adopted for the spectroscopic observations in the innermost radial bin in Figure 4.9.

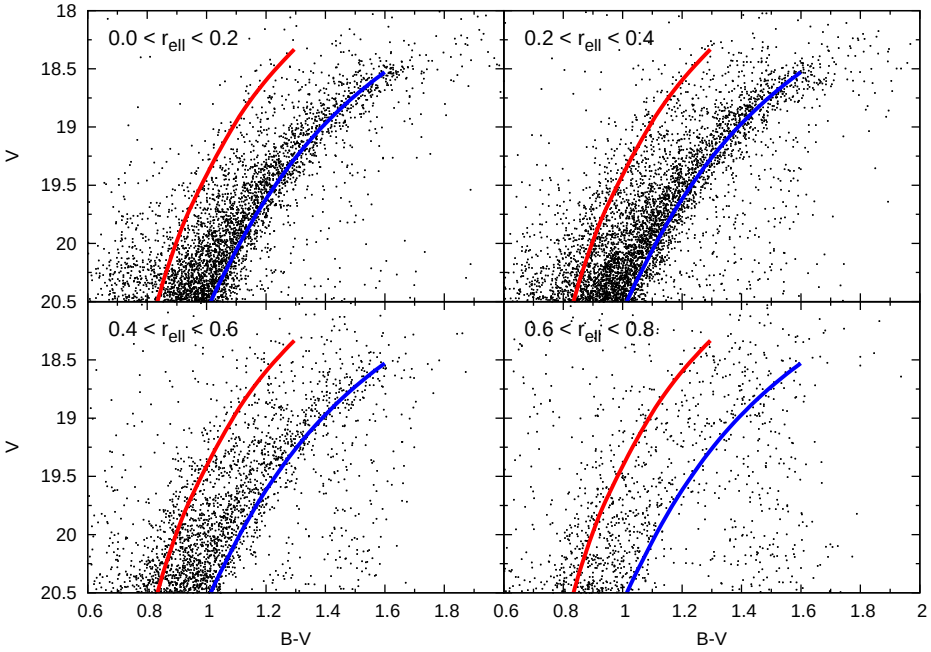

Figure 4.8: *The distribution of stars on the Red Giant Branch in the Fornax dSph, for different elliptical radii. Overlaid isochrones from the Dartmouth Stellar Evolution Database trace the metal-rich ([Fe/H]=−1.00 dex, [α/Fe]=0.00 dex, age=4 Gyr, black) and metal-poor populations ([Fe/H]=−2.45 dex, [α/Fe]=0.40 dex, age=14 Gyr, grey) present on the RGB.*

The inner regions of Fornax show stars with metallicities ranging from −2.8≤[Fe/H] ≤−0.2 dex. For increasing radius, the spectroscopic abundances show that the most metal-rich populations ([Fe/H]≥−0.7 dex) rapidly disappear. The dominant RGB population (with [Fe/H]≈−1.0 dex) also diminishes with radius from the centre, albeit at a slower pace. Conversely, the metal-poor, old populations ([Fe/H]≤−1.7 dex) are present at all radii. This is in agreement with the radial trend observed from the RGB photometry in Figure 4.8, and indicates the presence of a metallicity gradient with radius.

4.4.2 The Main Sequence Turn-Offs

The MSTO region of the Fornax dSph (see Figure 4.5) shows the presence of stellar populations with a wide range of ages, from very young (BP) to very old (red MSTO). Previous studies of this region have found clear evidence of a population gradient with radius in the Fornax dSph (Stetson et al., 1998; Buonanno et al., 1999; Gallart et al., 2005a). Here, we present deep homogeneous photometry of the MSTO region covering a large fraction of the galaxy out to r_{ell}=0.8 degrees.
Figure 4.10 shows the MSTO region of the Fornax dSph at different radii from the cen-

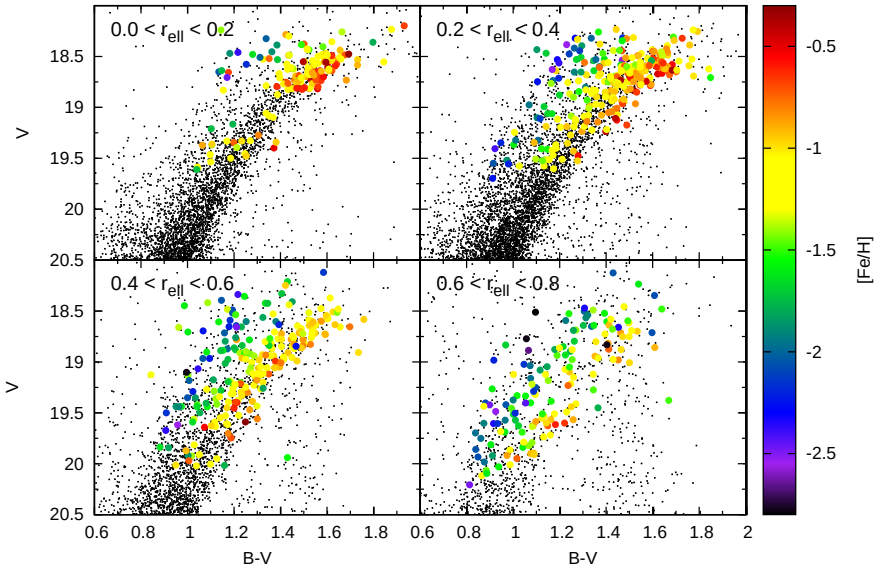

Figure 4.9: *The RGB region of the Fornax dSph at different elliptical radii, r_{ell}. The (black) dots show the photometry, while the larger (coloured) filled circles indicate the [Fe/H] metallicities of individual RGB stars for which spectroscopic metallicities are available (Starkenburg et al., 2010),.*

tre. Reference isochrones have once again been overlaid on the CMDs, representative of the old, intermediate and young populations. Figure 4.10 clearly shows that the youngest populations are confined to the centre of Fornax, while the older populations are more extended. The youngest BP populations disappear rapidly as we go outward from the Fornax centre. The stars corresponding to the young population seen at $0.6 \leq r_{ell} \leq 0.8$ degrees display a different slope in the CMD than the young populations in the centre, and could also be consistent with a BSS population (Mapelli et al., 2009). For increasing elliptical radius the dominant intermediate population also diminishes, as becomes clear when comparing the area underneath the (black) metal-rich reference isochrone at different distance from the centre. Conversely, the oldest populations traced by the (grey) metal-poor isochrone remain present at each elliptical radius. A random selection of equal numbers of stars in each panel shows that this effect is not due to the decreased total number of stars at different elliptical radii. These trends are consistent with a radial gradient in both metallicity and age in the Fornax dSph, spanning a wide range in age.

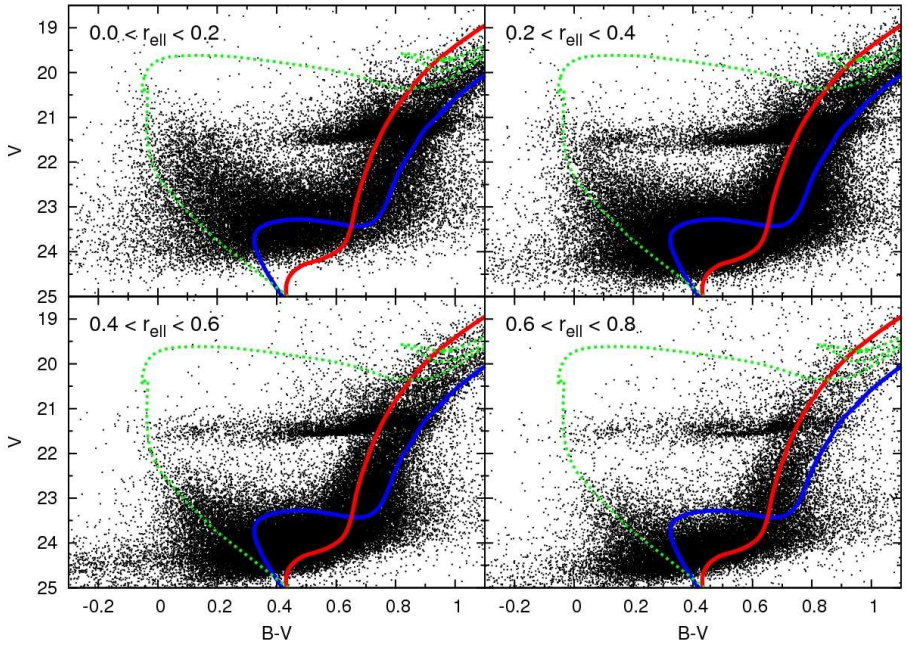

Figure 4.10: *The distribution of stars in the MSTO region of the Fornax dSph, for different elliptical radii. Three isochrones are overlaid, representative of the metal-rich ([Fe/H]=−1.00 dex, [α/Fe]=0.00 dex, age=4 Gyr, black) and metal-poor populations ([Fe/H]=−2.45 dex, [α/Fe]=0.40 dex, age=14 Gyr, grey) on the RGB, as well as the young population of the Fornax dSph ([Fe/H]=−0.30 dex, [α/Fe]=−0.20 dex, age=0.3 Gyr, dotted).*

4.5 Stellar over-densities

Analysis of the spatial distribution of stars in the Fornax dSph has revealed the presence of several stellar over-densities. Among those, five globular clusters (GC) were found (Shapley, 1938b; Hodge, 1961a), which have been investigated in great detail (Buonanno et al., 1985, 1998, 1999; Greco et al., 2007; Letarte et al., 2010). In particular, Fnx 1,2,3 and 5 have been found to be metal-poor and representative of the old population of Fornax, while Fnx 4 is found to contain more metal-rich and younger stars with respect to the other GCs (Strader et al., 2003).
From accurate HR spectroscopic observations of nine stars in the Fornax GCs the mean metallicity of Fnx 1,2 and 3 are determined as $\langle$[Fe/H]$\rangle$ =−2.5, −2.1 and −2.4 dex respectively (Letarte et al., 2006). Furthermore, Ca II triplet spectroscopic metallicities have been obtained for 4 stars in Fnx 1 ([Fe/H]=−2.81, −2.71, −2.54 and −2.16 dex), 1 star in Fnx 2 ([Fe/H]=−1.76 dex), 2 stars in Fnx 3 ([Fe/H]=−2.38 and −1.25 dex) and 1 star in Fnx 4 ([Fe/H]=−0.99 dex). However, some of these stars are expected to belong to the Fornax field populations instead of the GCs.

Furthermore, two substructures were found in Fornax, located at distances of ≈17 arcmin and 1.3 degrees from the centre (Coleman et al., 2004, 2005b; Olszewski et al., 2006), interpreted as shell features. Both of these shell features have been associated with young star formation, with approximate ages of ≤2 Gyr.

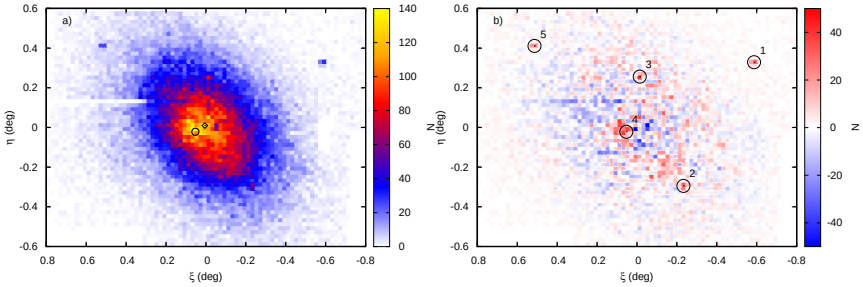

Figure 4.11: *Spatial Hess diagram of the RGB population of Fornax,* ***a)*** *before and* ***b)*** *after subtraction of the average RGB spatial distribution. The central position of the RGB population is shown as the (black) diamond. In the right panel, the circles indicates the position of the known GCs in the Fornax dSph, with position according to Mackey and Gilmore (2003).*

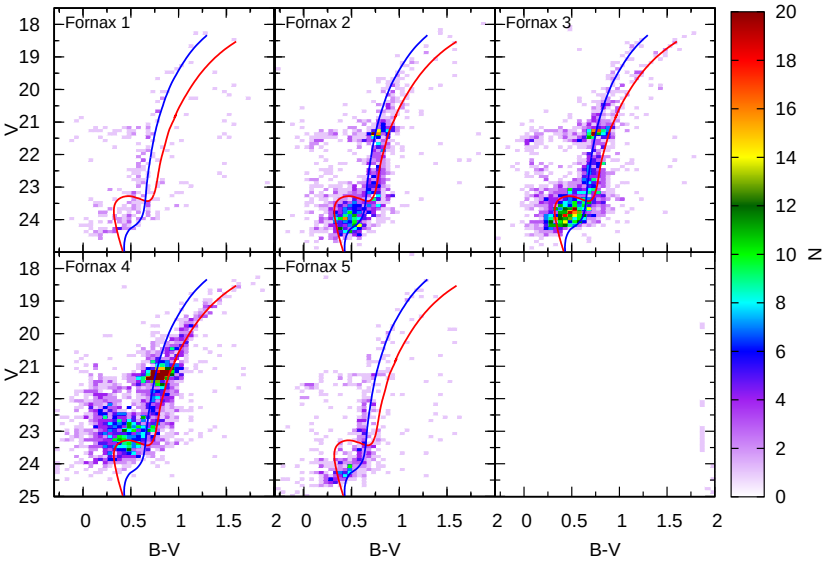

Figure 4.12: *Hess diagrams of the Globular Cluster in the Fornax dSph. Overlaid isochrones represent the metal-rich and metal-poor populations of the Fornax field stars (see Section 4.4.1).*

4.5.1 Globular Clusters

The presence of the Fornax GCs in our dataset is investigated by analysing the spatial distribution of old (RGB) stars. Figure 4.11a shows a spatial Hess diagram of RGB stars in Fornax. The outermost GCs of Fornax are easily identified in the spatial distribution, but the inner GCs are not easily distinguished due to the presence of the Fornax field population. Therefore, a mock average spatial distribution of RGB stars is generated, and subtracted from the observed Hess diagram. Figure 4.11b shows the field star subtracted Hess diagram, in which all five Fornax GCs (marked by circles in Figure 4.11b) clearly stand out.
A selection of all stars within two tidal radii is adopted for the GCs, as obtained from the literature (Mackey and Gilmore, 2003). Figure 4.12 shows the observed Hess diagrams of the GCs in the Fornax dSph, overlaid with two isochrones representative of the intermediate and old populations in the Fornax field. Fnx 1,2,3 and 5 are all consistent with the oldest, metal-poor populations present in the Fornax field stars. The CMD of Fnx 3 shows a clear double RGB population within 2 tidal radii, which is due to Fornax field contamination. Conversely, the Hess diagram of Fnx 4 shows no hints of the old, metal-poor populations traced by the (blue) reference isochrone, but instead a strong population of intermediate age stars. Additionally, Fnx 4 also shows large numbers of young stars, which might be the result of the substantial Fornax field stars contamination.
In order to test the association of Fnx 4 to the youngest populations, we re-derive the position of the centre of Fornax for young stars. The spatial Hess diagram is fit with ellipses at different radii using the IRAF ELLIPSE routine, to determine the central position, ellipticity and position angle, similar to Battaglia et al. (2006). We find that the resulting mean central position of the young stars is slightly offset with regards to the adopted values from Battaglia et al. (2006) by ξ =1.01±1.14 arcmin, η=0.84±0.84 arcmin, giving a central position of RA=02^h:39^m:56.9^s, DEC=-34°:29′:58.6″. With respect to Fnx 4 the central position of the BP population is within the tidal radius of the GC given the errorbars.
Additionally, the spatial Hess diagram of the BP population in Figure 4.13 shows that the position of Fnx 4 (as indicated by the circle) coincides with the highest density region of the young populations of Fornax. Therefore, Fnx 4 is likely to be associated with the young populations, making it perhaps more likely to be the nucleus of the Fornax dSph instead of a GC (Hardy, 2002; Strader et al., 2003). This is consistent with its central position, and would also explain why the properties of Fnx 4 are so different from others GCs in Fornax and the MW.

4.5.2 Substructure

The observed shell features have been associated with young star formation, and should therefore show up in the spatial distribution of young stars. Figure 4.13 shows the observed spatial Hess diagram of the BP stars (with the area corresponding to the BHB removed) in the Fornax dSph. It is clear from Figure 4.13 that the spatial distribution of the young populations of Fornax is different than that of the intermediate and old

populations shown in Figure 4.11 (Stetson et al., 1998; Saviane et al., 2000; Battaglia et al., 2006).

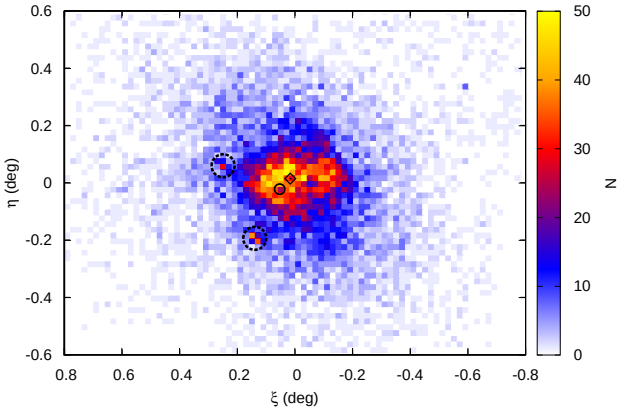

Figure 4.13: *The spatial Hess diagram of the BP stars in the Fornax dSph. The central position of the RGB population is shown as the (black) diamond. Furthermore, the (solid) circle indicates the position of Fnx 4, with a radius corresponding to its tidal radius (Mackey and Gilmore, 2003). The two dashed circles indicate the position of the two other over-densities.*

The coverage of our deep photometry is not enough to be able to see the outermost shell feature. However, the inner shell feature shows up clearly in the BP spatial distribution. The position and alignment of the detected feature is consistent with the parameters of the inner shell feature (Coleman et al., 2004). Surprisingly, another feature stands out clearly in the spatial distribution of young stars, East of the Fornax centre, at RA=02^h:41^m:02.2^s, DEC=-34°:27′:17.6″. This feature is located at a distance of 0.3 degrees, or 0.7 kpc from the centre of Fornax.

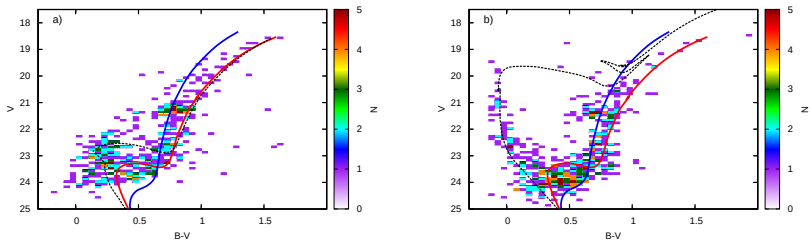

Figure 4.14: *The Hess diagram of* ***a)*** *the inner shell feature found by Coleman et al. (2004) and* ***b)*** *the new over-density. Three isochrones are overlaid, representative of the populations traced by the Fornax field RGB (blue and red), as well as the overdense population in the both features (black, dashed). Parameters of the overlaid isochrone of the overdense population are [Fe/H]=−0.70 dex, [α/Fe]=0.00 dex, age=2.0Gyr and [Fe/H]=−0.50 dex, [α/Fe]=−0.20 dex, age=0.3Gyr respectively for panels* ***a)*** *and* ***b)*** *.*

The reason why the new substructure was not found earlier in previous surveys of Fornax is due to the photometric depth. Most surveys, (including Eskridge, 1988a,b; Irwin and Hatzidimitriou, 1995; Walcher et al., 2003; Coleman et al., 2005b) did not go

deep enough or were not able to make a colour selection. This did not allow them to select only young stars, which make up the bulk of the substructure. The small field-of-view ($2.3' \times 2.3'$) observations by Olszewski et al. (2006) did go deep enough to detect the young BP stars, but did not cover the region of the new substructure.
The observed Hess diagrams for the substructures are shown in Figure 4.14, overlaid with isochrones representative of the intermediate and old Fornax field populations and the main population in the feature. The Hess diagram of the previously observed inner shell feature is consistent with previous CMDs (Coleman et al., 2004; Olszewski et al., 2006). The Hess diagram of the new substructure (Figure 4.14b) shows clearly that a very young population is responsible for the over-density, consistent with an age of 0.3 Gyr. This is substantially younger than the populations found in the inner and outer shell features.

4.6 The Star Formation History of the Fornax dSph

Having described our method for determining the SFH of the Fornax dSph in Section 4.3 (see also Chapter 3.3), we now apply Talos to our photometric and spectroscopic data sets of the Fornax dSph (Battaglia et al., 2008b; Starkenburg et al., 2010; Letarte et al., 2010).
The SFH is derived using the photometric CMDs in combination with the spectroscopic MDF, to put most constraints on the final SFH. Within the central 0.4 degrees, photometric information in three filters (B,V and I) is combined with the available HR and Ca II triplet spectroscopy. For radii $r_{ell} \geq 0.4$ degrees, the SFH is determined using just the (V, B−V) CMD combined with Ca II triplet spectroscopy. The spectroscopic MDF is used to constrain the SFH solution for $-2.5 \leq [Fe/H] \leq -0.6$ dex. CMD analysis shows that stars with greater metallicity are too young to appear on the RGB. For these stars the ages and metallicity are constrained only from the photometry. An investigation of the MDF at different photometric depth has shown that no luminosity function bias is present in the spectroscopic sample of Fornax stars, as was observed in Sculptor (de Boer et al., 2012).
Figure 4.15 presents the final SFH and Chemical Evolution History (CEH) of the Fornax dSph out to a radius of r_{ell}=0.8 degrees. The SFH and CEH display the rate of star formation at different ages and metallicities over the range of each bin, in units of solar mass per year or dex respectively. The total mass in stars formed in each bin can be determined by multiplying the star formation rates by the range in age or metallicity of the bin.
The SFH shows that star formation is present with significant levels at all ages, from as old as 14 Gyr to as young as 0.25 Gyr. Most of the star formation takes place at intermediate ages, between 1−10 Gyr, consistent with earlier determinations of the Fornax SFH (Gallart et al., 2005a; Coleman and de Jong, 2008). The CEH in Figure 4.15b shows that the dominant population displays metallicities between $-1.5 \leq [Fe/H] \leq -0.7$ dex, but that significant levels of star formation are also present at $[Fe/H] \approx -2.4$ dex and $[Fe/H] \approx -0.2$ dex.
Figure 4.16 shows the overall SFH of Fornax, divided into different age ranges, with the

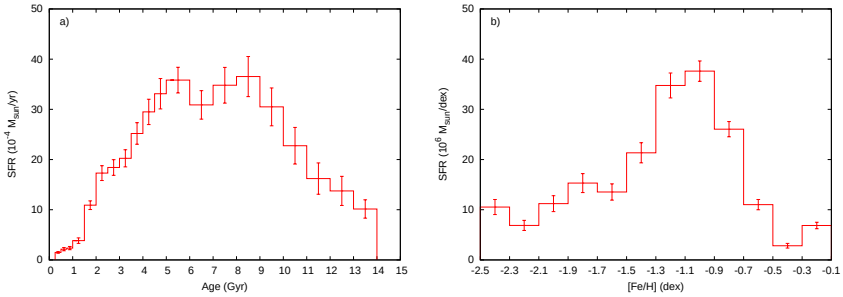

Figure 4.15: *The overall **a)** Star Formation History and **b)** Chemical Evolution History (CEH) of the Fornax dSph, out to an elliptical radius of r_{ell}=0.8 degrees. The SFH and CEH have been determined using all available photometric information, incombination with observed spectroscopic metallicities.*

corresponding CEH. The youngest star formation in Fornax (≤1 Gyr) displays declining star formation rates for younger ages, with a metal-rich CEH showing a peak at [Fe/H]≈−0.2 dex. The intermediate age star formation shows metallicities between −1.5≤[Fe/H]≤−0.5 dex with a peak at [Fe/H]≈−1.0 dex, for ages between 2−5 Gyr. The slightly older intermediate age star formation (5−10 Gyr) displays an age peak at ≈8 Gyr, and is dominated by more metal-poor stars with a distribution between −2.1≤[Fe/H]≤−0.7 dex, showing two peaks at [Fe/H]≈−1.8 and −1.2 dex. Finally, at the oldest ages (10−14 Gyr) the star formation rates become lower for increasing age, with a metal-poor CEH displaying a similar range as observed in the Sculptor dSph (de Boer et al., 2012).

To check the distribution of stars in the CMD we compare the best matching observed and synthetic CMDs of the Fornax dSph in Figure 4.17. The overall distribution of stars in the observed CMD is well matched in the synthetic CMD. Stars on the BP and MSTO occupy the same range in colour and brightness as in the observed CMD. Furthermore, the colour range and slope of the RGB is a good match to the observations, as shown by comparison to the reference lines.

The total number of stars in the synthetic CMD is consistent with the observations to within a few percent. Additionally, the relative fraction of stars occupying the RGB and BP phase is similar to that of the observed stars. This shows that the total mass in stars in the Fornax dSph is well matched, and distributed across the CMD with the right numbers. Therefore, we feel confident that the SFH constitutes an accurate representation of the overall behaviour of the stellar populations in the Fornax dSph.

Using the best matching SFH we can show the age and metallicity corresponding to different CMD features. Figure 4.18 shows the synthetic (V, B−V) CMD of Fornax, colour coded with age and metallicity for each individual star. The effect of different stellar populations on the MSTO region of the CMD is clearly seen from Figure 4.18, with younger Main Sequence stars occupying bluer and brighter positions on the BP. The CMD shows that the majority of stars is of intermediate age, but that lower levels of old star formation are also present. The position of different stellar populations on the

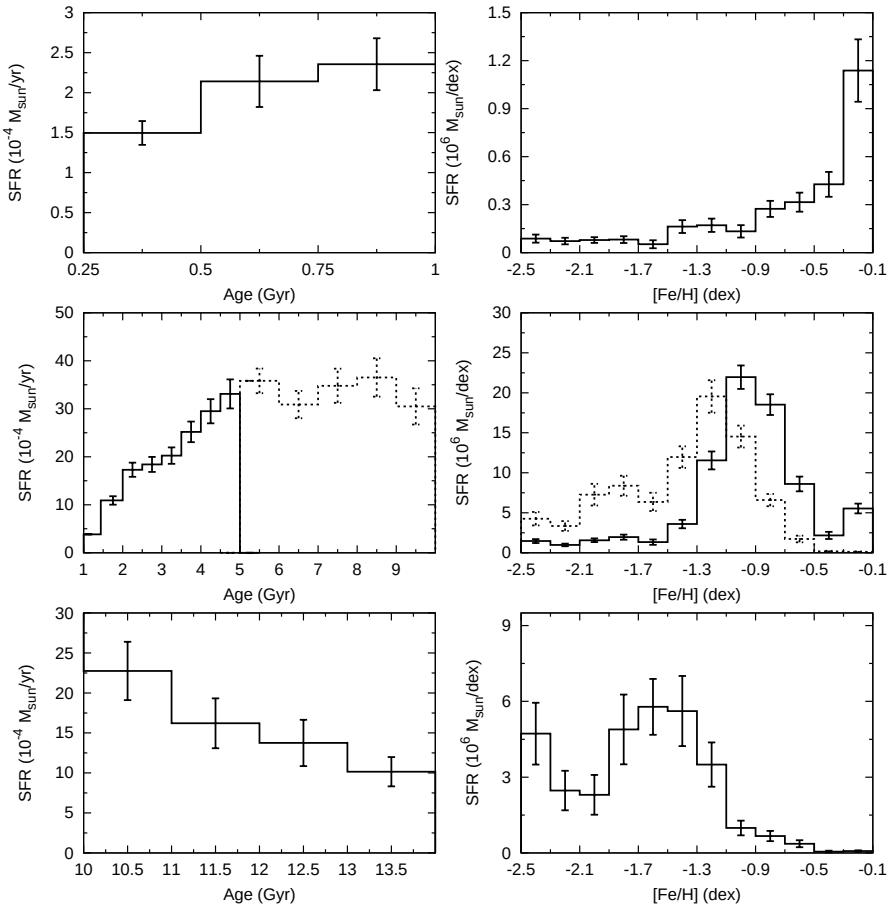

Figure 4.16: *The overall Star Formation History of the Fornax dSph, divided into different age ranges. The corresponding CEH is also shown for each age range.*

RGB shows that the oldest stars occupy the blue side of the RGB, while progressively younger stars are found toward the red side of the RGB. However, small numbers of young (≤4 Gyr) stars are also found on the blue side of the RGB, after evolving off the young MS.

The effect of metallicity on the positions of stellar populations is shown in Figure 4.18b. The RGB is sensitive to [Fe/H] rather than age, and shows a clear metallicity pattern across the RGB, which provides a good match to the observed metallicity pattern seen in Figure 4.9. Stars on the BP are mostly metal-rich, although metal-poor stars are also present. This could be due to the presence of BSS stars, which are fit as young populations. Additionally, the lack of spectroscopy of BP stars means the metallicity of these populations is not constrained from the MDF fitting.

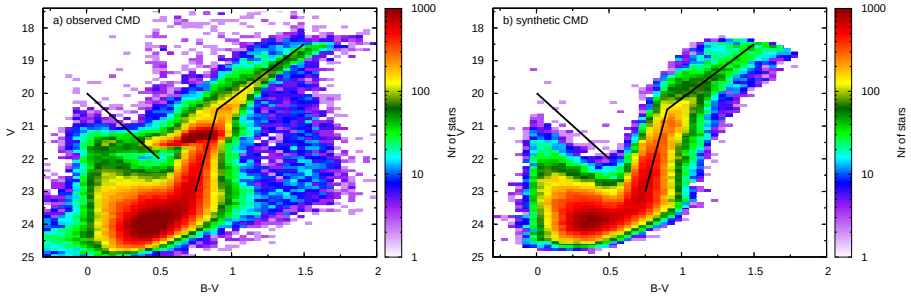

Figure 4.17: *The **a)** observed and **b)** synthetic Hess diagrams for the Fornax dSph, out to r_{ell}=0.8 degrees. The colours represent the number of stars in each bin, on a logarithmic scale. To allow a better comparison between both Hess diagrams, (black) reference lines are also shown. The BHB, RHB and RC are not present in the synthetic Hess diagram, since they are not modelled in the isochrone set used.*

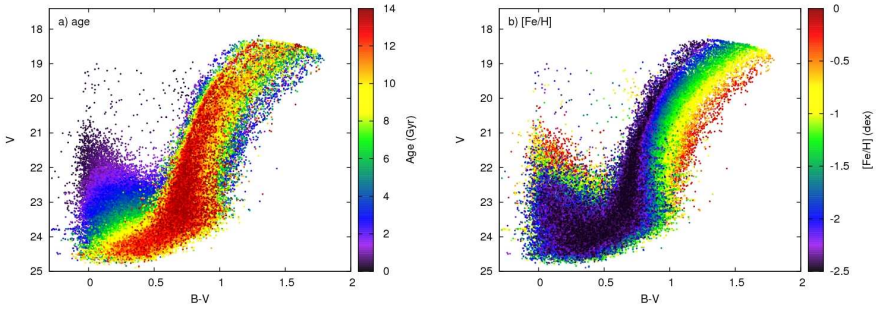

Figure 4.18: *The synthetic Hess diagram of the Fornax dSph, as inferred from the best matching SFH. The colours represent **a)** age and **b)** [Fe/H] for each individual synthetic star.*

4.6.1 Spatial variations in the SFH

The coverage of the photometric and spectroscopic information extends to a radius of r_{ell}=0.8 degrees. Therefore, it is possible to derive the SFH at different radii from the centre, which allows us to determine the variation of the SFH with radius in the Fornax dSph.

The total radial extent of the photometry and spectroscopy is divided into 5 annuli, each containing a similar number of stars observed in the B and V filters, since these filters are fully complete out to greater radii from the centre. For each of the annuli, the SFH and CEH are determined by fitting all available photometric and spectroscopic information, in the same way as discussed in Section 4.6. For the inner three annuli, photometric information in all three available filters (B, V and I) is used, together with the spectroscopic MDF. The SFH in the outer two annuli is determined using just the (V, B−V) CMD, together with the spectroscopic MDF from Ca II triplet spectroscopy.

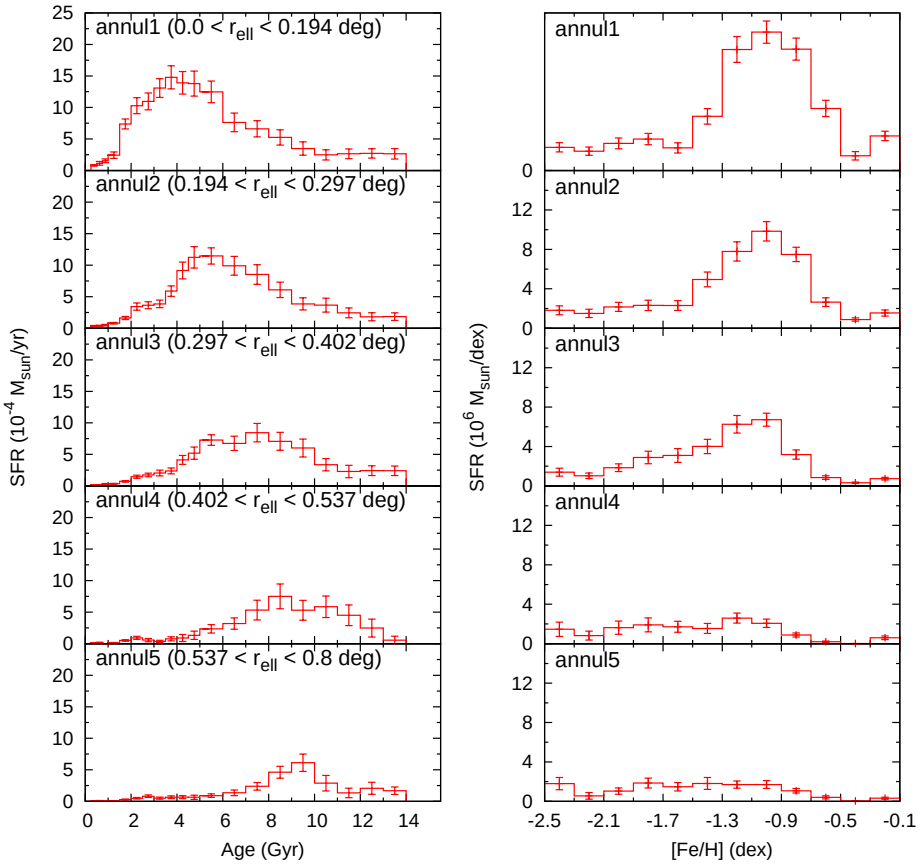

Figure 4.19: *The SFH and CEH for 5 annuli of Fornax containing roughly equal number of stars, with the radial extent indicated in each panel. For comparison, the core radius of the Fornax dSph is 0.23 degrees (Irwin and Hatzidimitriou, 1995). The SFH for annuli 1–3 is obtained by fitting all available photometry (in the B, V and I filters) and spectroscopy. For annuli 4 and 5 only the V,B-V CMD is used together with the spectroscopy to constrain the SFH.*

Figure 4.19 shows the best matching SFH and CEH in each of the five annuli of the Fornax dSph. Figure 4.19a shows that a clear gradient with age is present in Fornax, with the peak of star formation shifting to progressively older ages for increasing radius. The CEH shown in Figure 4.19b shows that the distribution of metallicities changes from peaked in the inner parts to a broad distribution in the outermost bin.
The young star formation (age≤1 Gyr) is present only within the centre of Fornax, consistent with the observed CMDs. This is also seen in the CEH, where significant star formation at high metallicities ([Fe/H]≥-0.5 dex) is found only in the central part of Fornax. Very low levels of young star formation are seen in the outer parts, which are

likely due to fitting the probable BSS population in the outer parts as a young stellar population.
The dominant population in Fornax has intermediate ages (between 1−10 Gyr), with a peak at age≈4 Gyr and [Fe/H]≈-1.0 dex in the central bin, shifting to older ages for increasing radii. This is in good agreement with the dominant RGB population seen in Figures 4.5 and 4.6.
Old star formation (age≥10 Gyr) is present at all radii in Fornax, with a relatively flat distribution at the oldest ages. The star formation rate starts to increase gradually in all regions at an age of ≈10 Gyr, consistent with previous studies (Buonanno et al., 1999; Gallart et al., 2005a).

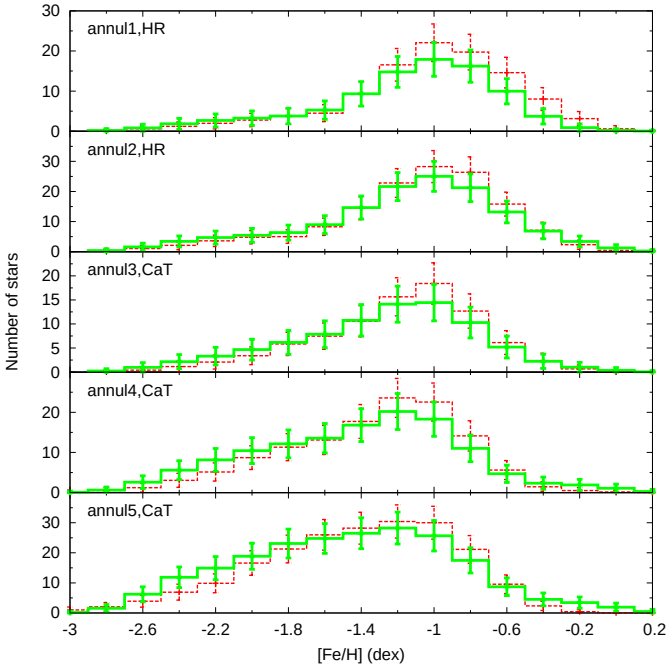

Figure 4.20: *Observed (red, dashed) and synthetic (green, solid) histogram MDFs from the SFH analysis in each of the five annuli in Fornax.*

The observed and synthetic MDFs inferred from the SFH are shown in Figure 4.20, for all five radial annuli. The synthetic MDFs are consistent with the observed spectroscopic MDFs within the errors, as expected, given that the MDF is used as an input in the SFH determination. In the outer parts of Fornax, the metal-poor component is slightly over-estimated in the synthetic MDF, while the inner parts show that the metal-rich populations are slightly under-estimated. The MDF on the upper RGB shows the same trend with radius as the CEH in Figure 4.19b, changing from a peaked distribution in the innermost bin to a more broad distribution in annulus 5, consistent with the diminishing strength of the dominant intermediate age component.

The total mass in stars formed in our SFH of the Fornax dSph is 4.3×10^7 $M_\odot$ within 0.8 degree or 1.9 kpc. The core radius of the mass distribution is r_c=0.29±0.03 degrees, determined using a Sersic profile fit. This is consistent within the errors with the core radius derived from the observed density profile (Battaglia et al., 2006).

4.6.2 The SFH of Fornax GCs and substructures

The SFH of the Fornax GCs and substructures described in Section 4.5 is determined on the basis of the (V,B−V) CMD. No spectroscopic MDF is used in the SFH determination, due to the limited sample of spectroscopic observations. Contamination from the Fornax field stars is taken into account by adopting a background Hess diagram in the SFH fitting. This Fornax field background is determined by assuming that all stars within a sufficiently big aperture around the GC or substructure are representative of the Fornax field population. The CMD of this region is scaled to the same spatial area as the observed CMD and used as a static background in Talos. The SFH is determined by finding the combination of static Fornax field background and model CMD that best matches the observed CMD.
Figure 4.21 shows the SFH and CEH of the five globular clusters of the Fornax dSph, determined from the (V,B−V) CMD. All five GCs show signs of an ancient (12−14 Gyr) population, and sometimes lower levels of intermediate age star formation. The CEH of Fnx 1 is peaked at [Fe/H]≈−2.5 dex, consistent with a very metal-poor GC. However, the CMD indicates that Fnx 1 may be more metal-poor than this value, which is the limit of the adopted isochrone set. This would result in a best matching SFH with a slightly younger age, to fit the blue RGB. The CEH of Fnx 2 shows a wider metallicity distribution, and a peak at 11 Gyr, consistent with its higher metallicity. Fnx 3 and Fnx 5 display a SFH and CEH consist with a metal-poor, old GC, although low levels of Fornax field stars contamination are seen in the SFH of Fnx 3. Conversely, the SFH and CEH of Fnx 4 shows a variety of different populations, after taking into account the Fornax field contribution. Peaks are visible in the SFH at ancient (≈14 Gyr), intermediate (5 and 9 Gyr) and young (≈0.5 Gyr) ages. Therefore, the stellar populations of Fnx 4 are clearly different from those of a normal GC.
Figure 4.22 shows the SFH and CEH of the stellar substructures discussed in Section 4.5. The SFH is determined using the (V,B−V) CMD without taking into account spectroscopic data. Furthermore, the Fornax field star population is used as a static background during the SFH determination. The SFH of the inner shell structure discovered by Coleman et al. (2004) shows a clear peak at an age of 1.0−1.5 Gyr, consistent with the Hess diagram in Figure 4.14. The CEH peaks at [Fe/H]≈−0.2 dex, which is more metal-rich than the parameters of the shell structure adopted in Coleman et al. (2004). The SFH of the new substructure displays a peak at 0.25 Gyr, which is the youngest age possible in our adopted isochrone set. Star formation at older ages is also present, but consistent with very low levels given the errorbars, indicating that the population responsible for the over-density is clear extremely young. The CEH indicates that the metallicity of this populations is metal-rich ([Fe/H]≈−0.5 dex), but more metal-poor than the inner shell structure.
The total mass in stars in the over-denisties is calculated from the SFH as 1.78×10^4 $M_\odot$

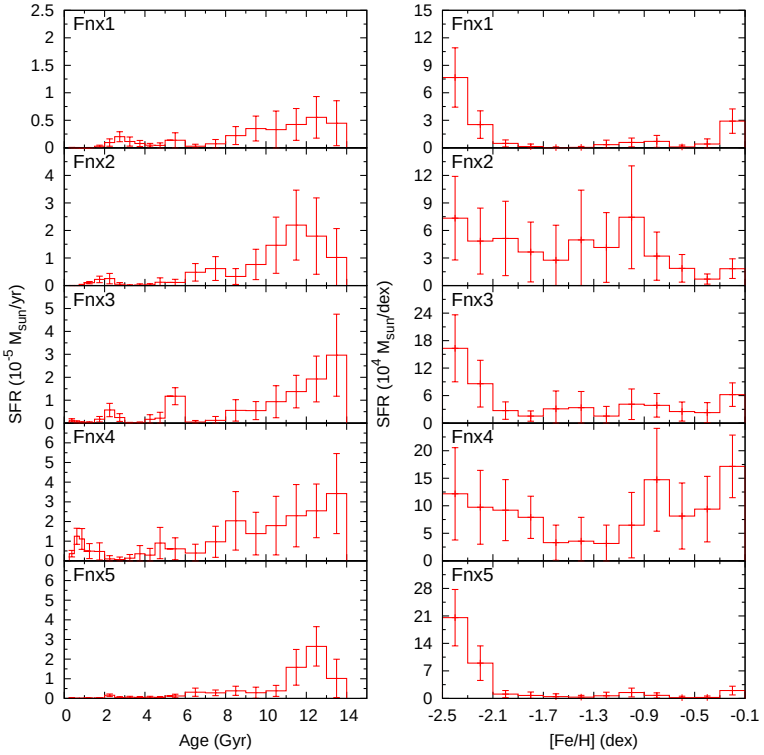

Figure 4.21: *The SFH and CEH for the 5 GCs of the Fornax dSph, as obtained from the V,B-V CMD. A static background Hess diagram has been used to model the Fornax field contamination during the SFH determination.*

for the inner shell structure and 2.28×10^4 $M_\odot$ for the new substructure, without the Fornax field star contribution.

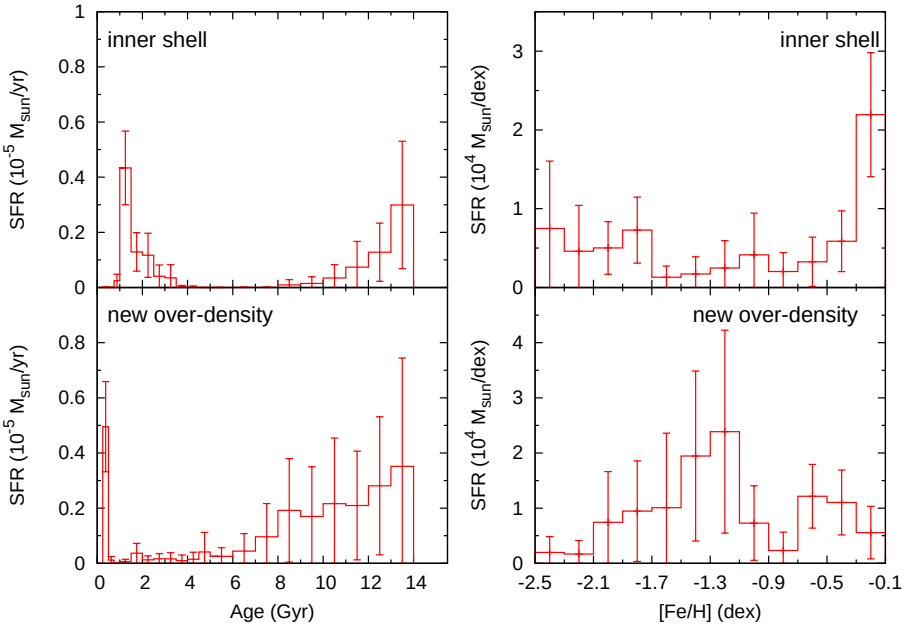

Figure 4.22: *The SFH and CEH for the two substructures discussed in Section 4.5, as obtained from the V,B-V CMD.*

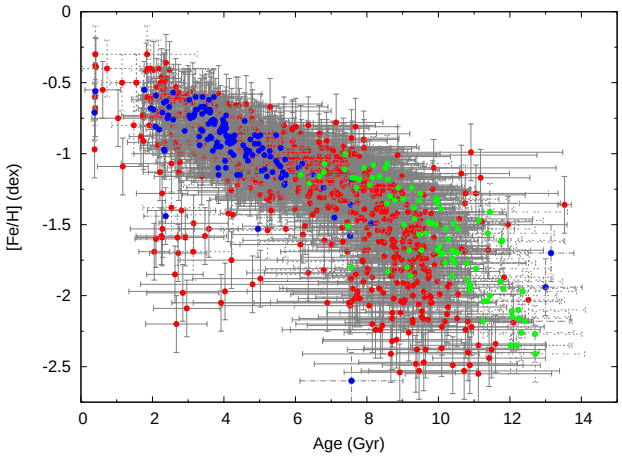

Figure 4.23: *The Age-Metallicity Relation of stars on the upper RGB in the Fornax dSph, incorporating the full SFH and MDF information. Medium and high resolution spectroscopy from Letarte et al. (2010); Kirby et al. (2010) is shown as blue points, while Ca II triplet spectroscopy from Pont et al. (2004) and Battaglia et al. (2008b) is shown in red. The AMR of the Sculptor dSph, from HR spectroscopy, is shown as green points (de Boer et al., 2012).*

4.7 The timescale for chemical evolution of the Fornax dSph

Using the SFH presented in Figure 4.19 it is possible to determine the age probability function of individual stars on the RGB. For each observed star, all stars in the synthetic CMD (generated using the SFH) with the same magnitude (in all filters) and metallicity within the observed uncertainties are considered to be representative of the age of the observed star, as described in detail in de Boer et al. (2012) (see also Chapter 3.4.4). Using this method, we determine accurate age estimates (and age uncertainties) for all available samples of spectroscopic stars in Fornax (Battaglia et al., 2008b; Pont et al., 2004; Starkenburg et al., 2010; Letarte et al., 2010; Kirby et al., 2010). From the spectroscopic sample of Kirby et al. (2010), only those stars with an uncertainty in [Fe/H] and [Mg/Fe] lower than 0.2 dex are considered.

Using the accurate ages for stars with spectroscopic metallicities, we determine the detailed AMR of the Fornax dSph. Figure 4.23 shows the AMR obtained using individual RGB stars in Fornax, as determined from the SFH. The AMR shows that the metallicity in Fornax rapidly went up from [Fe/H]≤ -2.5 dex to [Fe/H]$=-1.5$ dex between 8−12 Gyr. Subsequently, the Inter-Stellar Medium (ISM) is gradually enriched over several gigayears, resulting in a narrow, well-defined AMR which reaches [Fe/H]≈ -0.8 dex at $\approx$3 Gyr. Furthermore, from Figure 4.23, hints are seen that the slope of the AMR becomes steeper at even younger ages ($\leq$3 Gyr), corresponding to a phase of rapid enrichment (Pont et al., 2004). However, more spectroscopic observations, in particular of young BP stars, are needed to unambiguously detect this change in slope. The young, metal-poor stars in the lower left of Figure 4.23 correspond to AGB stars which are fit as if they were RGB stars (due to the absence of the AGB phase in the adopted isochrone set), leading to a too young age estimate.

Figure 4.23 suggests that Fornax underwent an initial episode of star formation at old ages, leading to a rapid metallicity enrichment. This first episode does not need to be very strong to enrich the ISM to values of [Fe/H]≈ -1.5 dex. The subsequent gradual increase of [Fe/H] is caused by intermediate age star formation between 5−10 Gyr, after which the strong burst occurred at $\approx$4 Gyr. This scenario is consistent with the SFH in Figures 4.15 and 4.19. A comparison to the AMR of the Sculptor dSph shows that the slope of the AMR in Fornax at the oldest ages is steeper than in Sculptor, which indicates that metal enrichment occurred with a different pace. After the initial phase of metal enrichment, the slope of the AMR is comparable in both galaxies.

Figure 4.24 shows the spatially resolved AMR of Fornax, in each of the five annuli described in Section 4.6.1. The shape of the AMR is consistent in all annuli, with a similar slope at intermediate ages. At the oldest ages, more scatter is seen in the inner two annuli than in the outer three annuli. The presence of the age gradient is visible in Figure 4.24 as a longer continuation of the AMR for more centrally concentrated regions.

The accurate age estimates can also be coupled to the stars for which HR observations are available, to determine for the first time, the evolution of particular elements as a function of time. In this way, we can measure directly the detailed timescale for chemical evolution of particular elements. Figure 4.25a shows the [Mg/Fe] abundance of

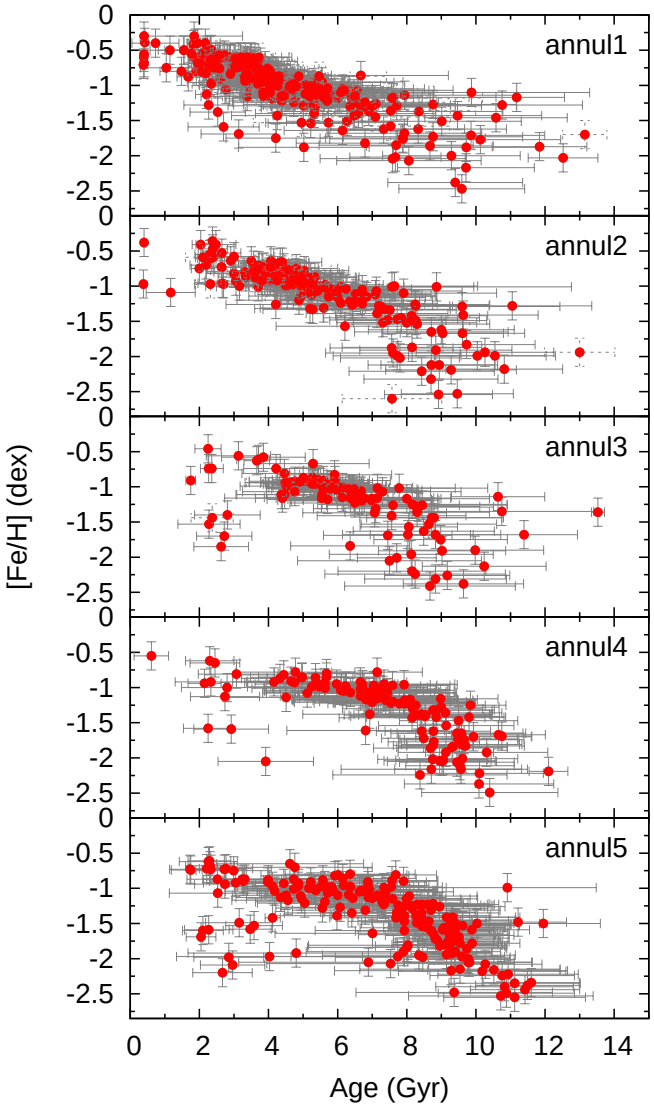

Figure 4.24: *The Age-Metallicity Relation of stars on the upper RGB in Fornax, in each of the five annuli, from medium and high resolution spectroscopy (Letarte et al., 2010; Kirby et al., 2010), as well as Ca* II *triplet spectroscopy (Pont et al., 2004; Battaglia et al., 2008b).*

individual RGB stars as a function of [Fe/H], with the age of the individual stars colour coded, while Figure 4.25b shows [Mg/Fe] directly as a function of age.
Figure 4.25 shows directly the effect of different stellar populations on the magnesium abundance of Fornax, and can be used to determine the rate with which this abun-

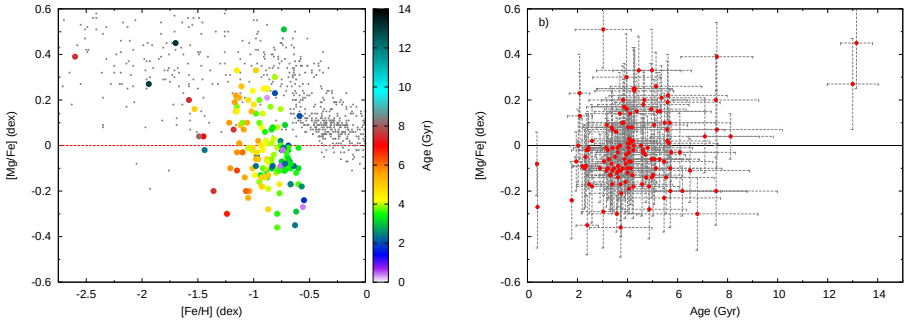

Figure 4.25: ***a)*** *[Mg/Fe] measurements for the medium and high resolution spectroscopic samples of RGB stars from (Letarte et al., 2010; Kirby et al., 2010) (coloured filled circles). The colours represent the age in Gyr, derived from the SFH. Stars in the Milky Way are shown for comparison (small grey points).* ***b)*** *[Mg/Fe] is plotted directly against age for the same sample.*

dance changes at different times. The most metal-poor stars in Figure 4.25a are consistent with the abundances observed for the MW. Conversely, on the metal-rich end the abundances of the Fornax stars are different from those of the MW. This indicates that Fornax followed a separate evolutionary path after the oldest times, as seen in other Local Group dwarf galaxies (Tolstoy et al., 2009).
The more metal-rich stars in Figure 4.25a display rapidly decreasing [Mg/Fe] abundances, with a clear trend with age. Hints are seen of a changing slope in the [Mg/Fe] distribution for populations of different ages. Furthermore, there are no signs from Figure 4.25 that younger populations start with a lower [Mg/Fe] abundance than the older populations. Connecting the metal-poor and metal-rich populations observed in the [Mg/Fe] distribution in Figure 4.23, a “knee" is expected to occur at [Fe/H]≈ -1.5 dex, at an age of 7−10 Gyr. The “knee" in [Mg/Fe] marks the time at which SNe Ia start to contribute to the [Fe/H] content of a galaxy (Matteucci and Brocato, 1990; Matteucci, 2003). However, due to the limited sampling of intermediate metallicity stars in Fornax, the “knee" (Tinsley, 1979; Gilmore and Wyse, 1991) is not visible in the data presented in Figure 4.25.

4.8 Discussion

We have presented the detailed SFH and CEH of the Fornax dSph out to r_{ell}=0.8 degrees, obtained using a combination of deep, multi-colour photometry and spectroscopic metallicities. The obtained, spatially resolved SFH (see Figures 4.15 and 4.19) shows features similar to previous SFHs (e.g. Gallart et al., 2005a; Coleman and de Jong, 2008). However, the SFH presented here resolves the stellar ages with greater accuracy, due to the direct inclusion of the spectroscopic MDF. In particular, the age of the dominant burst of star formation is determined with great accuracy, consistent with the position of the RGB in the observed CMD (see Section 4.4.1).

The spatially resolved SFH (see Figure 4.19) shows that a radial population gradient is present in Fornax, with more metal-rich, younger populations dominating the central region. The old star formation (≥10 Gyr) is found at all radii, while the dominant population of Fornax (ages 2−8 Gyr) is found more toward the centre. Finally, very young star formation (age≤1 Gyr) is found in the very centre (r_{ell}≤0.2 degrees) of Fornax, continuing almost until the present day. Traces of young star formation is also found in the outer parts of Fornax, which could be due to the presence of BSS stars, which are incorrectly fit as young populations.
Using the accurate SFH, the age of individual RGB stars is estimated, as described in Section 4.7. This allows us to measure the evolution of metallicity and particular chemical elements with time, and study the chemical evolution of the different populations in Fornax.

4.8.1 Old stars

A comparison between the AMR of Fornax and Sculptor (de Boer et al., 2012) suggests that the initial metal enrichment in Fornax occurred on a shorter timescale than in Sculptor, leading to a steeper slope in Figure 4.23. A possible explanation for this could be the greater mass of Fornax, which allows it to retain more of its gas after a SNe explosion, leading to more rapid enrichment, similar to what is predicted by simulations (e.g., Revaz and Jablonka, 2012).
The distribution of [Mg/Fe] with respect to [Fe/H] and age (see Figure 4.25) shows that the abundance pattern at the oldest ages was similar to that seen in the MW. A rapid decrease of [Mg/Fe] is seen at younger ages, with a clear gradient with age. Connecting both features suggests a “knee" in [Mg/Fe] should be present at [Fe/H]≈−1.5 dex, and age=7−10 Gyr. No “knee" is visible in Figure 4.25, due to the limited number of stars at intermediate metallicities ([Fe/H]≤−1.5 dex) in the HR spectroscopy. More HR spectroscopic observations are needed to define the position of the [Mg/Fe] “knee" in Fornax.
The position of the [Mg/Fe] “knee" is expected to occur at a different metallicity in Fornax than the observed “knee" in Sculptor (de Boer et al., 2012), due to the different SFH and more rapid metal enrichment. Furthermore, the large range in [Fe/H] covered by the metal-rich stars in Figure 4.25a indicates that the “knee" will also be spread over a large metallicity range. The changing slope of the [Mg/Fe] trends for different ages in Figure 4.25a could be linked to the different strength of previous stellar populations, leading to a different contribution of SN Ia to the chemical abundance pattern at different times.

4.8.2 Intermediate age stars

The dominant stellar component of the Fornax dSph is a strong, intermediate age population. The strength and duration of this intermediate age episode is far greater than that of the old star formation episode. Continuous star formation activity is seen over a large range in age, at increased spatial concentrations. A strong burst of star formation occurred at ≈4 Gyr, leading to a dominant, centrally concentrated, red RGB popula-

tion. This is very different to Sculptor, which lacks intermediate age stars, as it formed the bulk of its stars before age≈10 Gyr.
The strong burst of star formation in Fornax at ≈4 Gyr is expected to lead to another change in slope in the AMR (Pont et al., 2004). However, the limited number of stars in spectroscopic samples at high metallicity ([Fe/H]≥-0.6 dex) prevents the detection of any change at young ages.
The reason for the occurrence, and strength, of the intermediate star formation episode in Fornax is not clear. One possibility is a merger with a gas-rich companion, which triggered a strong burst of star formation. However, this gas would need to be pre-enriched to high metallicity ([Fe/H]≈−1.5 dex), which makes this scenario unlikely. Furthermore, no signs of an encounter are seen in the stellar distribution corresponding to this age range (Coleman and de Jong, 2008).
Another scenario is that initially expelled gas fell back onto the galaxy, leading to a burst of star formation similar to what is predicted by simulations (Revaz et al., 2009). It is possible that the expelled gas in the outer regions of Fornax remained bound to the system for an extended period of time, after which an interaction with the MW triggered the onset of a burst of star formation (Piatek et al., 2007), similar to models proposed for the Carina dSph (Pasetto et al., 2011). The lack of intermediate age star formation in Sculptor could then be due to its lower (dynamical) mass, which did not allow it to retain as much of its gas as Fornax.

4.8.3 Young stars

Star formation was taking place in the very centre of Fornax a few 100 Myr ago, leading to a clear young BP population (see Figure 4.5). The young population ranges in age between ≈2 Gyr and 0.25 Gyr, which is the lower limit of our age sampling. The age of the youngest stars may be younger than can be fit using the adopted isochrone set (Coleman and de Jong, 2008), which would lead to an incorrect estimate of the star formation rate in the youngest bin (0.25−0.50 Gyr). However, the level of star formation is expected to be low, not significantly influencing the results at young ages in Figure 4.19.
The young stars of Fornax display a different spatial distribution with respect to the old stars (see Section 4.5). Furthermore, several over-densities have been discovered in the Fornax dSph, consisting of young stars (Coleman et al., 2004, 2005a). The SFH of the previously discovered shell structure (see Figure 4.22) is consistent with stars of a young age (≈1.5 Gyr) being responsible for the over-density, similar to Coleman et al. (2004). The newly discovered over-density is created by very young stars with ages ≤0.5 Gyr.
Given that the ages of stars in the substructures overlap with ages of the Fornax field stars, a link may be present between both over-densities, and the Fornax centre, as suggested by Coleman et al. (2005a). The infall of a smaller system or of gas may be responsible for all three substructures, and may have triggered centrally concentrated star formation with a different spatial distribution.

4.8.4 Globular Clusters

The globular cluster system of Fornax has been investigated in detail in Section 4.5. The SFH of the GCs shows that Fnx 1,2,3 and 5 are old and metal-poor, consistent with HR and Ca II triplet spectroscopy. Fnx 1 is found to be the most metal-poor ([Fe/H]≈ -2.7 dex), consistent with Letarte et al. (2006). As a result, the RGB is more metal-poor and bluer than can be fit by our isochrone set, which results in a younger age in the SFH of Fnx 1. Fnx 4 is found to be more metal-rich than the other GCs, with multiple populations covering a substantial age range. Furthermore, Fnx 4 is found to contain significant amounts of young star formation, even after taking into account the Fornax field star contribution. Previous analysis of the age of Fnx 4 determined it to have an age only ≈3 Gyr younger than the other Fornax GCs (Buonanno et al., 1999). However, this might a result of using a single stellar population CMD ridge-line for Fnx 4, which determines only an average age for the cluster.
The multiple stellar populations of Fnx 4 could be the result of incorrectly taking into account the Fornax field contribution, or could be inherent to the GC. However, this is not likely to be responsible for all peaks displayed in the SFH (see Figure 4.21). Given the central location (consistent with the centre of Fornax within the errors), and the unusual populations of Fnx 4, it is more likely to be the nucleus of the Fornax dSph, as proposed by Hardy (2002); Strader et al. (2003).

4.9 Summary

We have presented deep B, V and I CMDs of the Fornax dSph, out to an elliptical radius of 0.8 degrees, containing a total number of 440000 stars. The CMDs show that Fornax displays a radial gradient with age and metallicity, with more metal-rich, younger stars forming more toward the centre. Fornax is dominated by intermediate age (1−10 Gyr) star formation, and shows a strong dominant RGB linked to a stellar population with an age of ≈4 Gyr, at [Fe/H]≈ -1.0 dex.
The coverage of our photometric data allows us to study the Globular Cluster system of Fornax, as well as the inner shell structure discovered by Coleman et al. (2004). Furthermore, the spatial distribution of young stars has revealed the presence of a new stellar over-density, dominated by very young stars (≈0.25 Gyr).
Combining the deep CMDs with the spectroscopic MDF of individual RGB stars we have derived the detailed SFH of Fornax, at different radii from the centre. Furthermore, we have also derived the SFH of the five GCs as well as the two young substructures. The spatially resolved SFH confirms and quantifies the radial age and metallicity gradient, with a peak of star formation that shifts to older ages for increasing radius. From the SFH we determine that the total mass in stars formed in Fornax is 4.3×10^7 $M_\odot$ within an elliptical radius of 0.8 degrees, or 1.9 kpc.
Using the SFH, we determined age estimates for individual RGB stars, for which spectroscopic abundances are available. This allows us to study, for the first time, the evolution of different elements in Fornax, directly as a function of time. Using the individual age estimates, we determined the detailed AMR of individual stars and timescale for evolution of α-elements of the Fornax dSph. The AMR shows that Fornax experienced

an initial period of star formation, which enriched the metallicity from [Fe/H]≤−2.5 dex to [Fe/H]=−1.5 dex from ≈12 to 8 Gyr ago. Subsequent gradual metal enrichment resulted in a narrow, well-defined AMR during the next 5 Gyr that reaches [Fe/H]≈−0.8 dex at ≈3 Gyr. Hints are seen in the AMR of a second change in slope at young ages (1−3 Gyr).
The detailed timescale of chemical enrichment (see Figure 4.25) shows that the abundances of old, metal-poor stars are consistent with the MW, while the abundances of more metal-rich stars show a departure from MW abundances. Metal-rich ([Fe/H]≈−1.3 dex) stars show a rapid decrease of [Mg/Fe], with a clear trend with age. Connecting both features predicts the presence of a knee in the alpha-element distribution at [Fe/H]≈−1.5 dex, at 7−10 Gyr. Hints are seen of a different slope in the [Mg/Fe] distribution for different populations, which could be a result of the different strength of previous stellar populations, leading to a different rate of chemical enrichment.
The SFH of the five GCs of the Fornax dSph (see Figure 4.21) shows that Fnx 1, 2,3 and 5 are all old, metal-poor GCs, consistent with available spectroscopic data. The SFH of Fnx 4 displays a range of ages and metallicities, inconsistent with normal GCs, making it more likely to be the nucleus of Fornax than a GC. The SFH of the inner shell structure is consistent with an age of 1.0−1.5 Gyr, consistent with Coleman et al. (2004). The SFH of the new substructure displays a peak at 0.25 Gyr, showing that the over-density is formed by extremely young stars. The total mass in stars in both over-denisties, as determined from the SFH as 1.78×10^4 $M_\odot$ for the inner shell structure and 2.28×10^4 $M_\odot$ for the new substructure.

acknowledgements

The authors thank ISSI (Bern) for support of the team “Defining the full life-cycle of dwarf galaxy evolution: the Local Universe as a template". T.d.B., E.S. and E.T. gratefully acknowledge the Netherlands Foundation for Scientific Research (NWO) for financial support through a VICI grant. T.d.B. would like to acknowledge valuable contributions to the chapter, made by V. Hill, A. Saha, E. Olszewski, M. Mateo, G. Battaglia, E. Starkenburg and M. Walker.

Appendix 4.A Observing log

Table 4.1: *List of observed fields in the Fornax dSph, with the 4m CTIO Blanco telescope during two observing runs. Information is given about exposure time, airmass and seeing conditions as determined on image.*

Date	Field	RA J2000	DEC J2000	Filter	exp time sec	seeing $''$	airmass
2009 Nov 19	Fnxc1	02:39:51.84	−34:47:48.96	B	3600, 90, 10	1.2	1.08-1.25
2009 Nov 19				V	3600, 90, 10	1.2-1.4	1.30-1.70
2009 Nov 22				I	4800, 90, 10	1.0-1.5	1.25-1.70
2009 Nov 21	Fnxc2	02:39:51.84	−34:13:48.96	B	3600, 90, 10	0.9-1.2	1.08-1.26
2009 Nov 21				V	3600, 90, 10	1.1-1.5	1.30-1.70
2009 Nov 23				I	4800, 90, 10	1.0-1.3	1.20-1.68
2008 Oct 4	FnxNE	02:42:07.28	−34:03:34.90	B	6600, 90, 10	0.9-1.7	1.07-1.55
2008 Oct 4				V	9000, 90, 10	1.0-1.5	1.09-1.74
2008 Oct 6	FnxNW	02:37:25.24	−34:11:44.40	B	4200, 90, 10	1.3-1.6	1.00-1.21
2008 Oct 6				V	7800, 90, 10	1.3-1.6	1.00-1.15
2008 Oct 5-6	FnxSE	02:42:28.77	−34:42:00.10	B	5400, 90, 10	1.1-1.7	1.00-1.70
2008 Oct 5-6				V	7200, 90, 10	0.9-1.6	1.00-1.80
2008 Oct 4-5	FnxSW	02:37:52.57	−34:50:12.30	B	4200, 90, 10	1.0-1.4	1.08-1.43
2008 Oct 4-5				V	7200, 90, 10	0.9-1.3	1.06-1.60
2008 Oct 5-6	FnxIW	02:39:51.84	−34:47:48.96	B	1800	1.2-1.4	1.09-1.20
2008 Oct 5-6				V	6000	1.3-1.6	1.06-1.30

CHAPTER FIVE

COMPARING MODELS OF THE SCULPTOR DWARF SPHEROIDAL GALAXY

T.J.L. de Boer, et al.

5.1 Introduction and motivation

The Star Formation History (SFH), Metallicity Distribution Function (MDF) and detailed abundance pattern of individual galaxies define the properties of stellar populations, as traced by the Colour-Magnitude Diagrams (CMD) and spectroscopic observations. Therefore, the ability to reproduce the observed SFH, CMD, MDF and chemical abundance patterns of the stars in a galaxy provides an excellent test of numerical simulations and chemical evolution models.
The Sculptor dSph is dominated by star formation in the early Universe (10−14 Gyr, which is redshift z≥2) As shown in Chapters 2 and 3, Sculptor experienced star formation over an extended period of time, without any obvious interruption. The result is a stellar population with a well defined α-element vs. metallicity distribution and a tight Age-Metallicity relation (AMR), that built up slowly over several gigayears. Therefore, it provides a good test-case of the early formation processes of small galaxies. Therefore, it can be used to put well motivated constraints on simulations which follow the formation and evolution of small galaxies that must have dominated the early Universe.
The Sculptor dSph has been modelled several times by different groups. The chemical evolution has been modelled directly (e.g., Kirby et al., 2011, Romano & Starkenburg, in prep), and also Sculptor-like galaxies have been picked out of global simulations of large numbers of dwarf galaxies (e.g., Salvadori et al., 2008; Revaz et al., 2009; Revaz and Jablonka, 2012). The new SFH determined in Chapter 3 puts new, more robust constraints on the age and metallicity of the stellar populations of Sculptor. Therefore, it is now useful to make a very detailed comparison with several types of models.

As part of the ISSI[1] team “Defining the full life-cycle of dwarf galaxy evolution: the Local Universe as a template", four different groups came together, to compare different modelling approaches. The four groups use different approaches, including hydrodynamical simulations, semi-analytic cosmological models and purely chemical evolution models. They either directly modelled a Sculptor-like galaxy, or more often picked a Sculptor-like galaxy from a more general set of simulations. The aim of the chapter is to compare how these different approaches and individual “best" models of the Sculptor dSph reproduce the observed properties, and investigate any differences.
A careful comparison of the CMD and MDF predicted by the models, shows if the right combination of age and metallicity and the relative strength of the different populations reproduces the properties of Sculptor as observed. A comparison between the SFH and Chemical Evolution History (CEH, the star formation as a function of metallicity) as well as the distribution of age and metallicity across the CMD will reveal in detail if the properties of the Sculptor dSph are reproduced, and will provide feedback to constrain the physical assumptions used in each model.

5.2 modelling description

Below, a short description is given of each modelling approach that we compare.

5.2.1 Model A (GEAR, a hydrodynamic code)

Model A is obtained from a chemo-dynamical Tree/Smoothed-Particle Hydrodynamics (SPH) code, GEAR, which models a large number of dwarf galaxies over a range of mass. For each galaxy, a large number of individual gas particles are used, for which the physical prescriptions are solved over the history of the Universe (Revaz and Jablonka, 2012).
GEAR is based on Gadget-2 (Springel, 2005), but also includes the treatment of baryonic physics, such as star formation, cooling and feedback. The gas cooling inside a simulated galaxy is taken into account by treating the gas as an ideal, non-viscuous gas, and assuming a cooling function dependant on temperature and metallicity. Star formation is initiated in a gas particle when it collapses and also fulfils requirements set by density and temperature. The chemical evolution inside each stellar particle is determined by nucleosynthesis and stellar feedback through supernovae (SNe) type II and type Ia explosions. The chemical elements released by SNe are modelled by taking into account mass dependent yields for SNe type II from Tsujimoto et al. (1995) and the model for SNe type Ia of Kobayashi et al. (2000). The chemical abundance patterns are traced at each timestep, which results in the detailed distribution of metallicity and α-element abundances.
A large number of simulations have been performed, varying most of the parameters at play, such as the star formation efficiency, total mass, central density and SNe feedback efficiency. From these simulations, the model that best fits the parameters of

[1] International Space Science Institute, Bern, Switzerland

the Sculptor dSph (total stellar mass, luminosity, SFH and metallicity distribution) was chosen and is called model A.

5.2.2 Model B (GAMETE, a cosmological semi-analytic code)

Model B comes from a semi-analytic, chemical evolution code, GAMETE, which reconstructs the gradual build-up of a stellar population history and chemical enrichment along hierarchical dark-matter merger trees (Salvadori et al., 2007, 2008). The code follows at the same time the evolution of both the host halo and all possible satellite systems.
First, the merger history of the Milky Way is constructed through a Monte Carlo algorithm based on the extended Press-Schechter theory. Subsequently, the evolution of gas and stars in the resulting haloes is followed by assuming a series of physically based recipes defining star formation and chemical enrichment. Stars are only allowed to form in haloes above a certain mass, which gradually increases at decreasing redshifts to account for radiative feedback effects, such as the reionization of the inter galactic medium (Salvadori and Ferrara, 2009). The rate of star formation is proportional to the mass of cold gas in each halo, with a prescription taking into account normal star formation as well as massive Population III stars. The star formation efficiency, assumed to be the same for all the star-forming haloes, is fixed to reproduce the observed global properties of the Milky Way at z = 0. The chemical enrichment of gas is based on mass-dependant stellar evolutionary timescales, and traced in both Galactic haloes and the intergalactic medium through a mechanical SNe feedback mechanism. The chemical elements released into the ISM from SNe type II are modelled through a series of yields at different stellar mass (Heger and Woosley (2002) for 140 < m < 260 $M_{\odot}$, Woosley and Weaver (1995) for 8 < m < 40 $M_{\odot}$ and van den Hoek and Groenewegen (1997) for 0.9 < m < 8 $M_{\odot}$). The metals are instantly mixed with the gas asuming the instantaneous recycling approximation. Furthermore, no SNe type Ia are taken into account in this model.
In this way, the build up of stellar populations in a galaxy is followed along its past hierarchical evolution. Among the different star-forming haloes, dwarf spheroidal galaxies are selected as haloes corresponding to density fluctuations $\leq 2\sigma$, based on N-body cosmological simulations. At each redshift step, likely dSph candidates are selected, and subsequently followed in isolation, leading to a statistically significant sample of dSph candidates.
From this set of candidate dSph galaxies, a single halo is chosen as Model B, which best fits the properties of Sculptor (total mass, luminosity, metallicity distribution).

5.2.3 Model C (cosmological N-body simulation with semi-analytic chemical evolution)

Model C is obtained from the Aquarius cosmological N-body simulations (Springel et al., 2008), with the addition of a semi-analytical code to simulate the baryonic properties of galaxies inside each dark-matter halo (Starkenburg et al, 2012, in prep). The Aquarius simulations contain six examples of an isolated halo similar in mass to that

of the Milky Way in which also the history and kinematics of smaller surrounding (sub) haloes can be followed. The baryonic properties of each (sub) halo are simulated by applying a series of relatively simple, but well motivated, physical prescriptions to the dark-matter haloes. In this way information can be obtained on the baryonic content of the very large number of dark matter haloes within the high-resolution simulations at a relatively low computational cost.
The semi-analytic recipes account for the change in baryonic fraction due to reionization, as well as the cooling of the gas within the dark-matter haloes, which depends on both metallicity and temperature. Star formation is started when the cold gas reaches a density threshold, with the star formation rate proportional to the mass of cold gas. The stars subsequently cause heating and ejection of gas, which is determined by a prescription for the feedback of SNe type II. No SNe type Ia are taken into account in this model. Finally, the simulations also take into account whether a galaxy becomes a satellite of a bigger system, and the effects of (ram-pressure) stripping.
The Aquarius simulations provide a good opportunity to study the predicted properties of Local Group dwarf galaxies, both satellites and isolated galaxies, and compare them to observations in a statistical way. From the modeled dwarf satellite galaxies one example was chosen (out of ≈30 that correspond to the luminosity of Sculptor), which approximates the observable global properties for Scl (luminosity, average metallicity and SFH). Although no one dwarf galaxy in the simulations matches exactly Sculptor, several models could be chosen, based on which properties were given priority. In this work just one of them has been explored in detail, which is adopted as model C.

5.2.4 Model D (a chemical evolution model)

Model D is the only case in which the Sculptor dSph is specifically modelled. The model is an extension of a chemical evolution model developed for the dSph precursor of the globular cluster Omega Centauri (Romano et al., 2007, Romano & Starkenburg, in prep). The approach traces the evolution of a wide variety of chemical elements, through a one zone treatment model with an instantaneous mixing of chemical elements within the galaxy. However, the code takes into account the actual lifetime of stars, before enriching the Inter-Stellar Medium (ISM) with the products of stellar evolution.
For the formation of dSph galaxies, an initial infall of a large amount of pristine gas is assumed (much higher than the final mass in stars in each galaxy), according to an exponentially decreasing law with a very short time scale (0.05 Gyr). From this gas, stars are formed according to a Schmidt law (with exponent 1 and efficiency 0.023 Gyr^{-1}), with resulting supernovae releasing chemical elements, as prescribed by SNe II and Ia yields (Woosley and Weaver (1995) for $8 < m < 40$ $M_{\odot}$ stars, van den Hoek and Groenewegen (1997) for $1 < m < 8$ $M_{\odot}$ stars and Iwamoto et al. (1999) for Sne type Ia). Furthermore, the effect of AGB stars on the chemical evolution is also taken into account, by including yields of AGB stars in the model. When the thermal energy of the ISM equates its binding energy, a galactic wind develops that removes SNe ejecta from the galaxy, as well as a fraction of the ISM.
The properties of each model galaxy are determined by the choice of parameters such

as gas accretion, star formation efficiency and the properties of the galactic winds. In this way a variety of different dSph galaxies can be simulated, for which the evolution of chemical elements is followed in detail over the duration of the SFH.
To simulate a Sculptor-like galaxy, model parameters are chosen in such a way to lead to a final SFH that closely resembles the observed SFH (see Chapter 3). In this way, a simulation of the Sculptor dSph is obtained, giving an accurate MDF and a detailed chemical abundance pattern. This is model D.

5.3 Comparing Sculptor models to observations

The models described in Section 5.2 for a Sculptor-like galaxy will be compared to the observed properties of the Sculptor dSph, as described in de Boer et al. (2011, 2012) (see chapters 2 and 3). Furthermore, a comparison will also be made to the observed spectroscopic abundances and metallicities from high resolution (HR) and Ca II triplet spectroscopy (Battaglia et al., 2008b; Starkenburg et al., 2010, Hill et al, in prep). For the different models of Sculptor we will compare the predicted and observed SFH, spectroscopic MDF, photometric CMDs as well as the chemical abundance patterns (if available).
Due to the extremely detailed, error-free information provided by the modelling groups, the models are all re-binned to the same age and metallicity range and resolution as used to determine the SFH of the Sculptor dSph (ages between 1 and 14 Gyr with 1 Gyr bins, metallicities between −2.5 and −1.0 dex with 0.2 dex bins). This makes the direct comparison between individual models and the observed data straightforward.
Each model is scaled to produce a total mass in stars of 7.8×10^6 $M_\odot$, equal to the total mass of stars obtained from the SFH of Sculptor (see Chapter 3). In this way, a comparison can be made between the total number of stars generated in each evolutionary feature in the different models.

5.3.1 Colour Magnitude Diagrams

Comparing the observed and synthetic CMDs reveals the ability of a model to reproduce the general observed features and the ability of the observations to be able to determine if subtle effects (such as very short bursts of star formation) are resolvable. This comes from observational details, such as the position and colour range of the Red Giant Branch (RGB) and the morphology of the Main Sequence Turn-Offs (MSTO). The synthetic CMDs generated for each model contain information about the age and metallicity of each individual star, which can be used to distinguish regions of the CMD by age and metallicity, as described in chapter 3. This distribution can be compared to the distribution obtained from the SFH as well as observed spectroscopic metallicities from Ca II triplet spectroscopy. This comparison shows if populations occupy positions in the CMD as would be expected from the observations, with the correct relative number of stars.

5.3.2 MDFs and abundances

The synthetic CMDs of the models also allow us to derive the MDF that would be observed from these simulations, which can be compared to the true spectroscopic MDF. To correctly reproduce the observational limits, the synthetic MDFs are constructed using only those stars that correspond to the same selection criteria as the observed spectroscopic samples. The uncertainties are simulated by convolving each star with a Gaussian profile with a width determined by the average observational uncertainty on [Fe/H]. The metallicities of individual stars are then combined to create an MDF for each model. Comparing the observed and model MDF determines if the relative number of stars at different metallicities are correctly and self-consistently reproduced.
Furthermore, for those models that trace the chemical evolution of the simulated galaxy, a comparison can be made between the chemical abundance pattern inferred from the models and the observed abundance pattern from HR spectroscopy (Hill et al., in prep, see Tolstoy et al., 2009). This will allow us to determine if the observed trends of α-elements are reproduced, and allow us to constrain the SNe yields adopted in each model.

5.3.3 Star Formation Histories

The SFH and Chemical Evolution History (CEH) of each model tells us the star formation rate at different age and metallicity. The ability to reproduce the SFH as derived from observations is an important test for the different models, and will tell us if the star formation is reproduced with the correct strength at each age. Furthermore, comparing the observed and predicted CEH will determine if the timescale of metal enrichment is reproduced in each model.

5.4 Comparing CMDs for different models

The observed (V, B−V) and (I, V−I) CMDs of the Sculptor dSph (see Figures 2.5 and 2.6 in Chapter 2) display a relatively wide RGB, which indicates the presence of a significant spread in metallicity and/or age. This is confirmed by spectroscopic measurements of the metallicity of several hundreds RGB stars (Battaglia et al., 2008b). The presence of both a blue and red HB indicates the presence of old (≥10 Gyr) and intermediate (6-10 Gyr) age stars. The MSTO region is consistent with a dominant old population, although the presence of bright turn-offs (V≤23) indicates the presence of low levels of younger (≤10 Gyr) star formation.
Using the star formation rates (at different age and metallicity) provided by the different modelling groups, synthetic (V, B−V) and (I, V−I) CMDs have been generated using the method described in Section 5.3. Stars with [Fe/H]≤−2.5 dex or [α/Fe]≤−0.2 dex are not included in the predicted CMDs, due to the lack of these isochrones in the isochrone library (Dotter et al., 2008). Furthermore, the Horizontal Branch (HB) and Asymptotic Giant Branch (AGB) phases are also not included in the isochrone set, and will therefore not be used in this comparison between models and observations. Additionally, the HB and AGB are sensitive to numerous parameters (such as age, metal-

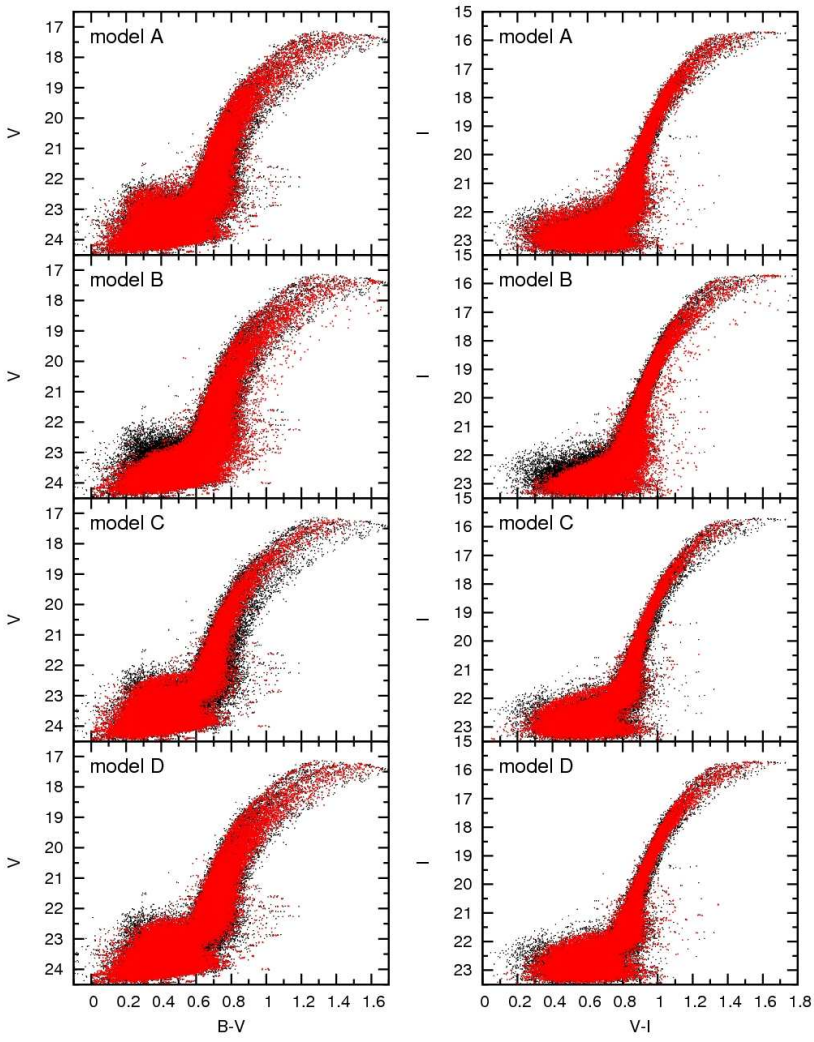

Figure 5.1: *Synthetic (V, B−V) and (I, V−I) CMDs for the four different Sculptor models (red), overlaid on top of the synthetic CMD determined from the best matching SFH of Sculptor (black).*

licity α-element abundance and mass-loss efficiency), making it very hard to model these features even if they were included.
The synthetic CMDs of each model can be compared to the results obtained from the Sculptor SFH determined from observations. Figure 5.1 shows the CMDs generated for all four models of Sculptor that we are comparing, overlaid on top of the synthetic CMD obtained from the best-matching SFH. Some models match the best-matching SFH CMD better than others, although all models provide a reasonable to good match to the observations. It is clear that the exact combination of age and metallicity in each model does not always agree with the observations. Furthermore, the relative number of stars in each population can also lead to differences between the observed and synthetic CMDs.
Therefore, Figure 5.2 shows the difference between the synthetic CMD of each model and the CMD determined from the best-matching SFH. The difference is expressed as a fraction of the counts in each bin of the CMD derived from the best-matching SFH (N_{SFH}-N_{model})/N_{SFH}. In that way, a difference fraction of +1 (red) indicates that the CMD of the best-matching SFH displays more stars than the model CMD, with a difference equal to the number of stars in the CMD derived from the SFH. Conversely, a difference fraction of -1 (purple) indicates that the model CMD displays more stars than the CMD derived from the SFH, with a difference equal to the number of stars in the CMD of the best-matching SFH of Sculptor.

5.4.1 Model A:

The synthetic CMD of model A displays similar features to the observed CMD, such as a wide RGB, and bright turn-offs in the MSTO region. The colour range of the observed and model RGB is similar, which indicates that the range in metallicities in model A is similar to that in Sculptor. Furthermore, the predicted MSTO of model A indicates the presence of stars with intermediate age (6-10 Gyr) populating the brightest part of the MSTO region, in very good agreement with the observed CMD.
The difference Hess diagram shows that the predicted number of stars across most of the MSTO are consistent with the observations to well within ≈25%. However, the number of metal-rich stars ([Fe/H]≥−1.2 dex) in model A is slightly under-predicted, giving a ≈30% difference on the bright MSTO, compared with the observations. This also leads to an RGB that is too thin, causing negative difference fractions in the B−V difference Hess diagram (see Figure 5.2), off the order of 50%.

5.4.2 Model B:

A comparison between the observed and synthetic CMDs of model B shows that the bulk of the stars form a RGB with colours consistent with the observations. However, the red part of the RGB is too red in comparison to the observed CMD, which could be due to the contribution of stars of high metallicity or old ages. This is also seen in the difference Hess diagram in Figure 5.2, which shows that the number of stars on the red RGB is significantly (≥100%) over-predicted, while the predicted number of stars on the blue RGB is ≈50% less than observed.

The MSTO region in Figure 5.1 is consistent with the oldest (≥12 Gyr) populations, but the fainter magnitude of the oldest MSTO in the model CMD indicates that stars of intermediate age (7−10 Gyr) are not present. This is consistent with the difference Hess diagram, which shows large (≥75%) positive residuals on the bright MSTO and negative residuals across the oldest MSTO.

5.4.3 Model C:

The synthetic (V, B−V) and (I, V−I) CMDs for model C display an overall width of the RGB which is too thin, compared to that observed in Sculptor. This indicates that metal-poor stars on the blue side of the RGB and metal-rich stars on the red side of the RGB are not present in the model, leading to large under-predictions of more than 100% on the blue and red sides of the RGB in Figure 5.2. The MSTO region of model C shows that both old and intermediate age stars are present, leading to a bright MSTO, consistent with the age range in the observed CMD of Sculptor. However, a gap between different stellar populations is seen on the bright MSTO in Figure 5.2, indicating the presence of distinct episodes of star formation. The number of stars on the MSTO is in good agreement with the observations, with residuals across the MSTO within ≈30%.

5.4.4 Model D:

The bottom panels of Figure 5.1 show the (V, B−V) and (I, V−I) CMDs of model D, overlaid on the CMD derived from the best-matching SFH of Sculptor. The model CMD shows that the colour range of the RGB is a good match to the observations of Sculptor, indicating that the range in metallicities is consistent with the observations. Furthermore, the synthetic MSTO of model D provides a good match to the observations, showing the presence of both intermediate age and old stars. However, Figure 5.2 shows that the number of stars on the red RGB and bright MSTO regions is much greater (≥50%) than observed, indicating that the number of metal-rich stars in model D is significantly over-predicted. Furthermore, residuals on the blue RGB show that the number of metal-poor stars is under-predicted by ≈30% compared to the observations.

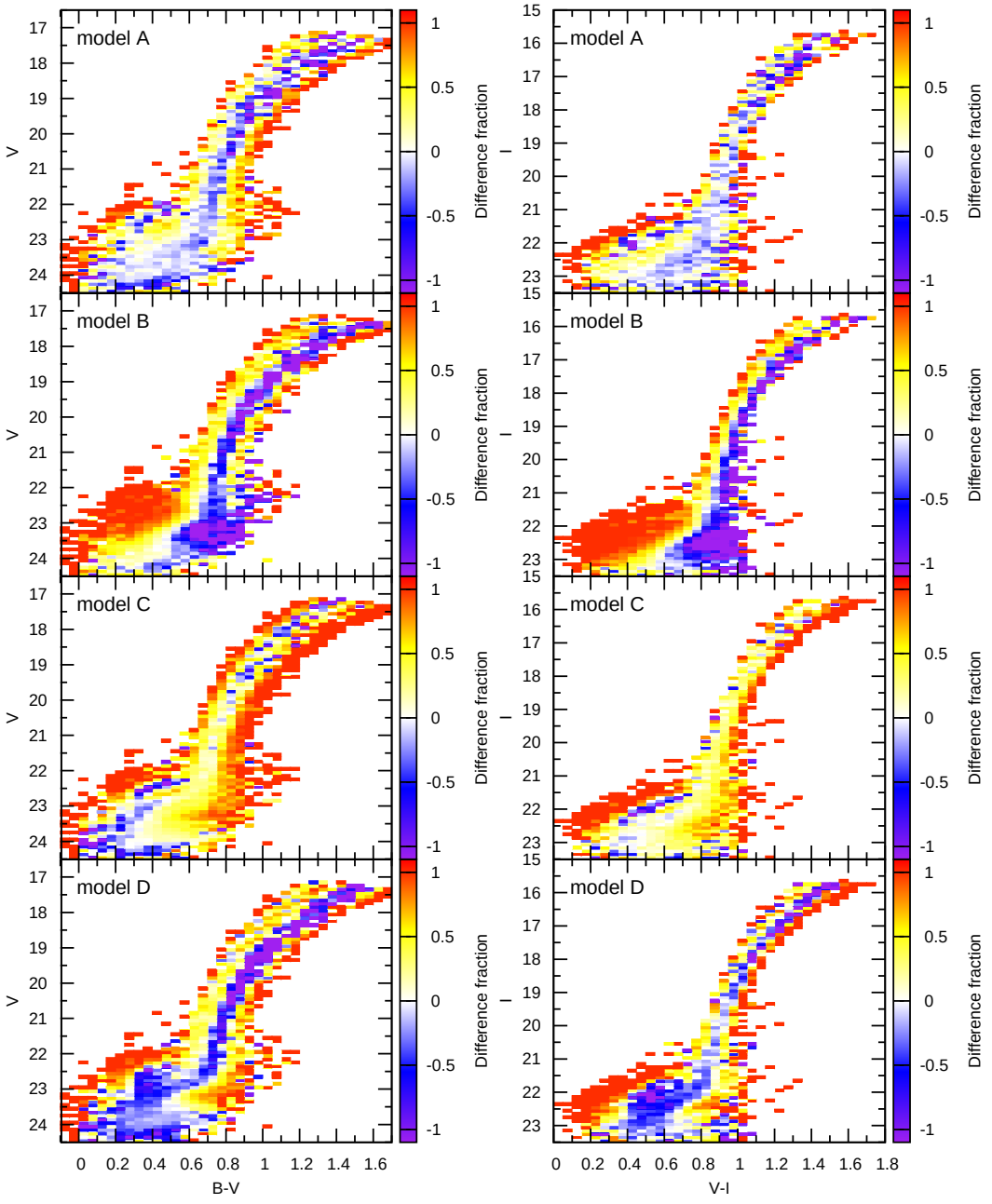

Figure 5.2: *Difference Hess diagrams for (V, B−V) and (I, V−I) CMDs for each Sculptor model, expressed as a fraction of the counts in each bin of the synthetic CMD derived from the best-matching SFH.*

5.5 Population distributions across the CMD

Using the synthetic stars generated for each model, it is possible to create CMDs for which the age and metallicity of each star is known. This allows us to compare the age and metallicity distribution of stellar populations across the CMD in more detail, to determine if different populations occupy the correct place in the CMDs.
The distribution of metallicity across the upper RGB can be compared to the observed metallicity distribution from Ca II triplet spectroscopy (Battaglia, 2007; Battaglia et al., 2008b; Starkenburg et al., 2010), as well as to the SFH results. To directly compare the models and observations, only those stars are selected which correspond to the same magnitude range as the spectroscopic sample. The spectroscopic completeness is taken into account by randomly selecting the same number of stars as observed in the Ca II triplet spectroscopy. Figure 5.3 shows the RGB region of the synthetic CMD of each Sculptor model, as would be obtained from spectroscopic observations similar to the available Ca II triplet spectroscopy. Each panel has the same total number of stars, equal to that obtained from Ca II triplet spectroscopy. A clear trend in metallicity is visible on the observed RGB from the observed metallicities, with blue colours corresponding to metal-poor stars, and red colours to metal-rich stars. This trend is matched to a greater or lesser degree by all models.
Figures 5.4 and 5.5 show the entire synthetic (V, B−V) CMD of each model, with colours representing respectively the [Fe/H] and age of individual stars. The CMD of the best matching SFH from de Boer et al. (2012) is also shown for comparison. The population distribution obtained from the SFH shows that the blue RGB corresponds to older (13-14 Gyr), metal-poor stars ([Fe/H]≈ -2.5 dex), while the red RGB is populated by relatively young (7-10 Gyr), metal-rich stars ([Fe/H]≈ -1.1 dex).
The comparison between the detailed age and metallicity distributions on the CMD show which parameter (age or metallicity) is responsible for some of the observed CMD differences. In general, the discrepancy between the models and observations is mainly due to a too narrow or too wide total range in either metallicity or age or both.

5.5.1 Model A:

Comparing the metallicity distribution of model A with the observations (see Figures 5.3 and 5.4) shows that the model metallicity distribution on the RGB matches the observed distribution in the spectroscopic sample and the SFH results. The blue side of the RGB is populated by metal-poor stars, while the red side corresponds to metal-rich stars, consistent with the observations. However, the total number of metal-rich stars ([Fe/H]≥ -1.2 dex) is under-estimated with respect to the results from the SFH. The distribution of age and metallicity on the MSTO reveals that the age of the stellar populations in model A is consistent with the ages derived from the SFH, with the bright MSTO being formed from the youngest stars. However, the bright MSTO is populated by stars of intermediat metallicity ([Fe/H]≈ -1.4 dex), which is not seen in the SFH results.

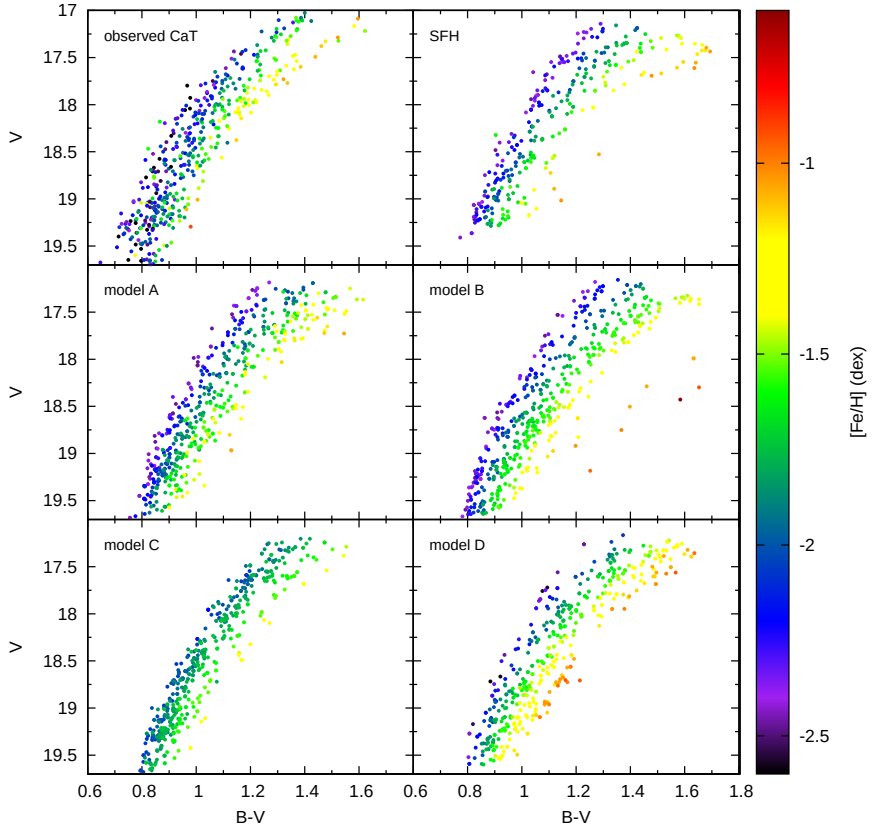

Figure 5.3: *(V, B−V) CMD of the RGB region of each Sculptor model as would be obtained from spectroscopic observations, coloured with [Fe/H] of individual stars. The upper panels display the observed RGB region of Sculptor, coloured with [Fe/H] measurements from Ca* II *triplet spectroscopic observations and from the best matching SFH.*

5.5.2 Model B:

The population distribution across the RGB region of model B indicates that the overall range in metallicity is consistent with the results from the SFH. However, the colours of the different populations are redder than observed in the spectroscopic sample. The age distribution on the MSTO reveals that the ages of the stellar populations are much older than in the Sculptor SFH derived from observations, and that stars younger than ≈11 Gyr are missing. As a result, for stars with [Fe/H]≥−2.0 dex, the colours of stars on the RGB are too red in comparison to the observed stars in the spectroscopic sample

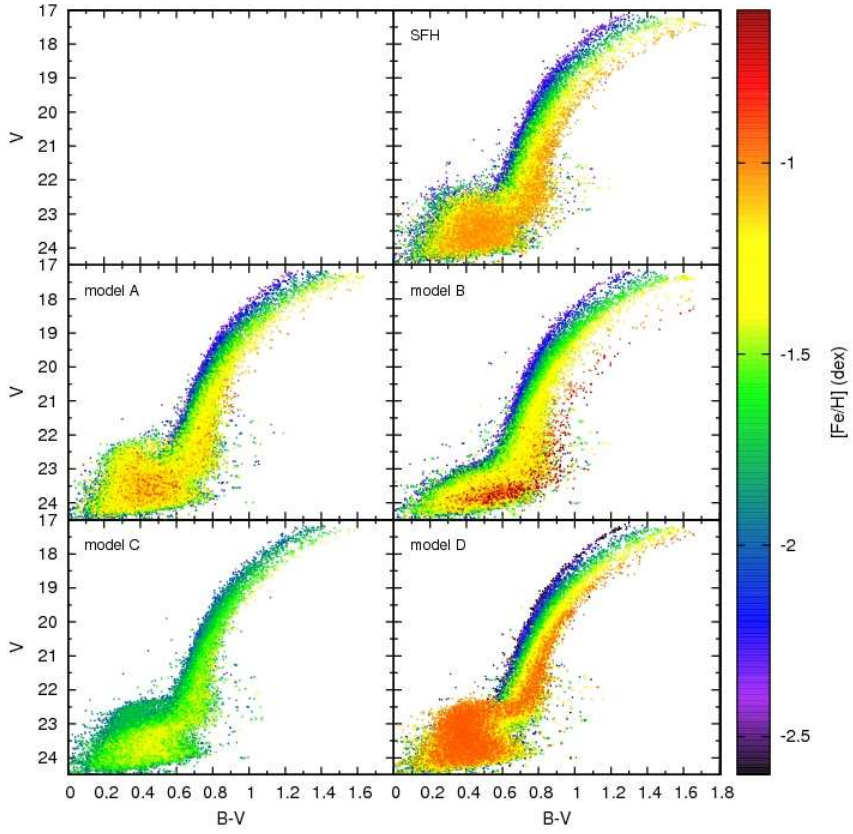

Figure 5.4: *Synthetic (V, B−V) CMDs obtained for the different models, coloured with [Fe/H] of individual stars. The synthetic (V, B−V) CMD obtained for the best matching SFH model is also shown, for comparison.*

in Figure 5.3.

5.5.3 Model C:

The metallicity distribution of model C shows that the position of the present stellar populations on the RGB is consistent with the observed Ca II triplet spectroscopy, indicating that the predicted combination of age and metallicity qualitatively matches the observations. However, no stars more metal-rich than [Fe/H]≥−1.3 dex or more metal-poor than [Fe/H]≤−2.3 dex are present in Figure 5.3, inconsistent with the spec-

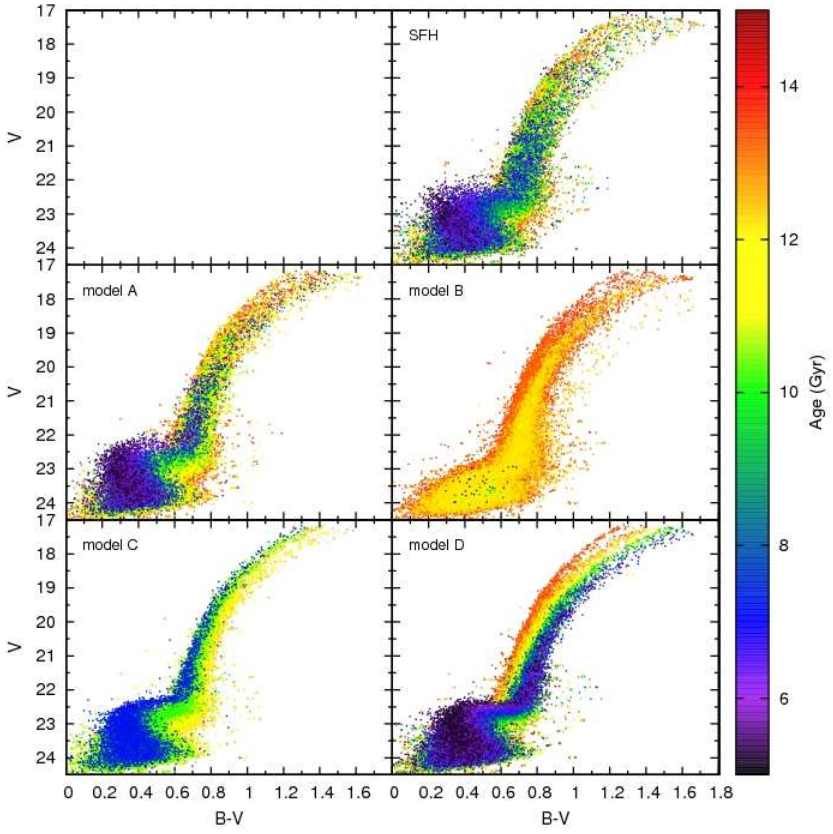

Figure 5.5: *Synthetic (V, B−V) CMDs obtained for the different models, coloured with the age of individual stars. For comparison, the upper panel shows the synthetic CMD of the best matching SFH, coloured with age.*

troscopic observations.

A comparison with the MSTO region also shows that no ancient stars (≥13 Gyr) are present, which contributes to the lack of stars on the blue side of the RGB. There are also no stars with ages ≤7 Gyr, but instead, stars with [Fe/H]≈−1.7 dex are predicted to be younger than the SFH derived from observations would suggest. These stars populate the bright part of the MSTO, leading to a good match to the overall CMD, but not to the age and metallicity distribution.

5.5.4 Model D:

The age and metallicity distribution in the synthetic CMD of model D reproduces the overall trends observed in the spectroscopic sample. The position of the stellar populations on the RGB is a good match to the SFH results in Figure 5.3. However, the number of metal-rich stars ([Fe/H]≥−1.5 dex) is over-estimated with respect to the best-matching SFH derived from observations (see Figure 5.3). Conversely, the number of metal-poor stars is under-estimated in model D, leading to a sparsely populated blue RGB in Figure 5.3. The age distribution of stars in model D reproduces the same trends as seen in the results obtained from the SFH, indicating that the right combination of age and metallicity is reproduced, but not with the same relative strength in different stellar populations. The age distribution across the predicted MSTO of model D in Figure 5.5 is a good match to the SFH derived from observations. Both intermediate and old stars are observed on the MSTO, indicating that the correct range of ages are reproduced in model D.

5.6 The SFH and MDF of each model

Using the synthetic SFH and MDF that are predicted by the different models we can compare the relative number of stars at different ages and metallicities. The synthetic SFH and Chemical Evolution History (CEH) of each model is determined from the models provided by each modelling group, and compared to the best matching SFH and CEH for Sculptor (de Boer et al., 2012). Figure 5.6 shows the SFH and CEH for all four models, in comparison to the SFH and CEH taken from the observations.
Furthermore, reproducing the MDF is an important constraint on the models, since it can be directly measured using spectroscopic observations. Therefore, the synthetic CMDs of each model are used to determine the MDF with the same magnitude limits and completeness as the Ca II triplet spectroscopy. This synthetic MDF is determined by selecting all synthetic stars within the same magnitude as the Ca II triplet spectroscopic sample. These stars are then convolved with a Gaussian profile to take into account observational uncertainties and binned in metallicity. Finally, the MDFs are scaled down according to the completeness level of the spectroscopic observations. The resulting MDFs are shown in Figure 5.7, directly compared to the observed MDF from Ca II triplet spectroscopy.

5.6.1 Model A:

The SFH and CEH predicted for model A (see Figure 5.6) show that the relative strength of most populations matches the SFH and CEH derived from observations. The peak of star formation is predicted to be at the oldest ages, consistent with the observations. However, the star formation rate in the oldest bin is about ≈25% higher than observed, and the rate drops too fast with respect to the observations, resulting in too few young, metal-rich stars in the CMD. The CEH of model A agrees well with the SFH derived from the observations, and shows differences of at most ≈10% for [Fe/H]≤−1.1 dex. However, the CEH peaks at [Fe/H]≈−1.8 dex, which is slightly more metal-rich than

the observed values.
The MDF of model A, as would be obtained from Ca II triplet spectroscopy (Figure 5.7), shows that the strength of most populations matches the observed spectroscopic MDF. However, the peak of the model MDF is slightly shifted towards more metal-rich values than the observed MDF, consistent with the shift observed in Figure 5.6. Therefore, the number of stars at intermediate metallicities is too high with respect to the observed MDF, consistent with the difference Hess diagram in Figure 5.2.

5.6.2 Model B:

The predicted SFH and CEH of model B show that all significant star formation takes place within the first two gigayears, clearly inconsistent with the SFH derived from the observations. The burst at the oldest ages is over-predicted by a factor ≈2 compared to the observations, which causes the very red RGB in Figure 5.1, and the high negative residuals in Figure 5.2. Furthermore, the absence of young stars in the SFH leads to a lack of bright MSTO stars in the CMD, as seen in Figure 5.1.
The CEH and MDF of model B are peaked at [Fe/H]≈−1.6 dex, which is at significantly more metal-rich values than observed in Sculptor. As a result, model B predicts too many metal-rich stars, and too few metal-poor stars on the upper RGB. However, the total range in metallicity is consistent with the observations.

5.6.3 Model C:

The SFH of model C shows that most stars are formed between 10−13 Gyr, with a significant drop in the star formation rate at younger ages, leading to lesser degrees of star formation at 7−9 Gyr. The CEH predicted for model C in Figure 5.6 shows little or no star formation at [Fe/H]≤−2.1 dex and [Fe/H]≥−1.3 dex, leading to a narrow peak in the MDF, ≈2 times higher than the observed star formation rate. This leads to too low numbers of metal-poor and metal-rich stars, and the absence of the blue edge of the RGB. Furthermore, the peak of the MDF predicted by model C is also shifted toward more metal-rich values than is observed in the spectroscopic sample.

5.6.4 Model D:

In the case of model D, the SFH shows a very good agreement with the SFH derived from the observations of Sculptor, especially at the youngest ages. The SFH in Figure 5.6 is consistent with the SFH derived from the observations within the errorbars, except at the oldest age, where star formation is underestimated by ≈20 %. The predicted CEH of model D is shifted toward higher metallicities with respect to the observation, leading to a significant under-prediction of metal-poor stars (by a factor of ≈4 at [Fe/H]≤−2.1 dex) and too many metal-rich stars. This is also evident from the spectroscopic MDF of model D (see Figure 5.7) which is shifted toward metal-rich stars. Therefore, the number of metal-rich stars is overestimated in the synthetic CMD in Figure 5.1.

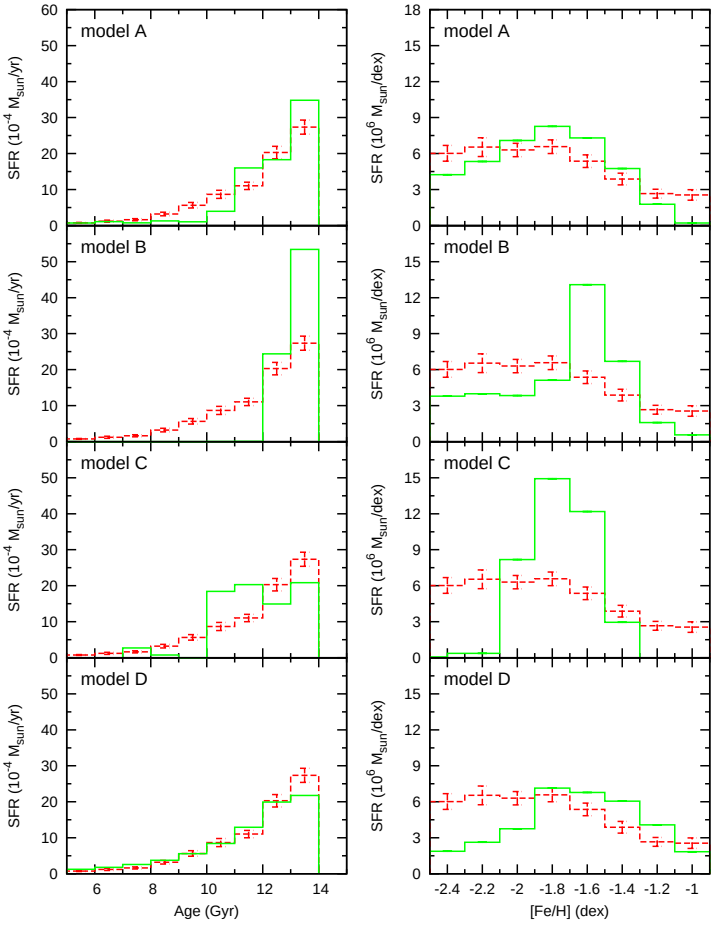

Figure 5.6: *The SFH and Chemical Evolution History (CEH) predicted by the model Sculptor galaxies (solid, green), in comparison to the best matching SFH and MDF taken from observations of the Sculptor dSph (dashed, red).*

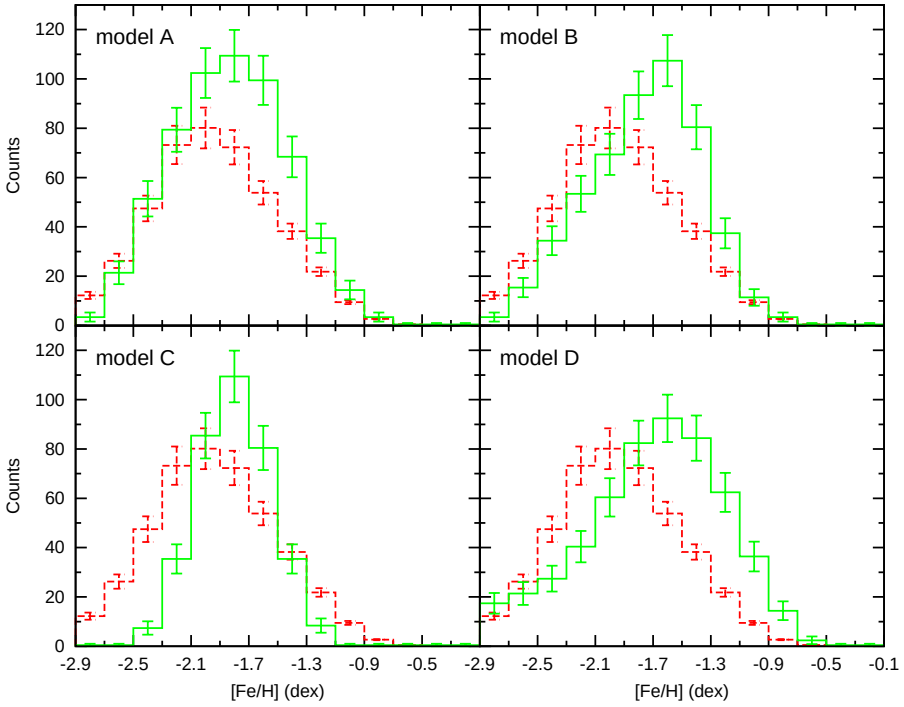

Figure 5.7: *The predicted MDF as would be obtained from Ca II triplet spectroscopy for each Sculptor model (solid, green), in comparison to the observed MDF of the Sculptor dSph (dashed, red).*

5.7 Chemical Evolution

For the models of Sculptor that include detailed predictions of the chemical abundance evolution (models A, B and D), it is possible to compare these to the HR spectroscopic observations of Sculptor (Hill et al., in prep, see Tolstoy et al., 2009). The chemical evolution modelling of model D is the most advanced, and traces the evolution of a variety of chemical elements, including the α-elements. Furthermore, models A and B also traces the evolution of α-elements over the SFH of the simulation, although Model B only includes only prescriptions for SNe type II.
The [Mg/Fe] abundance is dependant on the yields produced by SN II and SN Ia and the relative strength of both SNe types over the SFH of each model. Therefore, the predicted α-element distribution provides a good test of the timescales and yields used for SN II and SN Ia in each of the models. Furthermore, the [Mg/H] abundance is dependant mostly on SNe type II, and will therefore provide a good way to study the enrichment produced by these SNe.

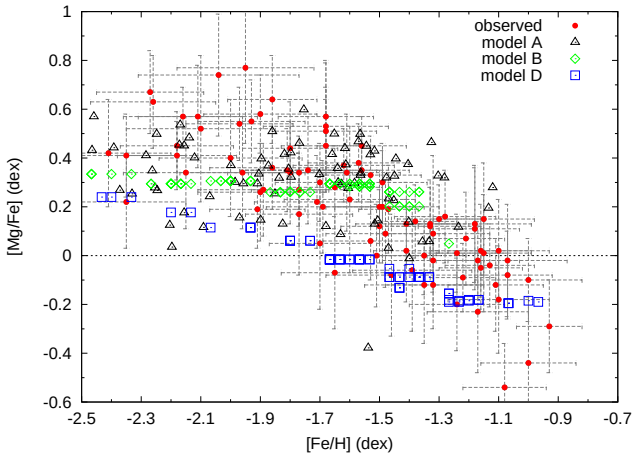

Figure 5.8: *The predicted evolution of [Mg/Fe] as a function of metallicity for models A (triangles), B (diamonds) and D (squares), in comparison to the observed [α/Fe] distribution from HR spectroscopy (circles).*

Figure 5.8 shows the distribution of [Mg/Fe] as a function of metallicity, for models A, B and D. Furthermore, Figure 5.9 shows the number of stars at each value of (**a**) [Mg/Fe] and (**b**) [Mg/H], for each model. The observed α-element distribution of Sculptor is also shown, obtained from HR spectroscopy.

5.7.1 Model A:

The [Mg/Fe] abundance pattern as a function of metallicity predicted for model A excellently reproduce the observed [Mg/Fe] distribution of the Sculptor dSph, especially at high metallicities ([Fe/H]≥ -1.5 dex). The overall trend of decreasing [Mg/Fe] abundances with increasing [Fe/H] is correctly reproduced in Figure 5.8. However, the numbers of stars at low [Mg/Fe] abundances ([Mg/Fe]$\leq$0.1 dex) are under-predicted in model A, compared to the observations, while the numbers of stars at high [Mg/Fe] ($\geq$0.3 dex) is over-predicted, causing a shift in the peak to higher abundances in the [Mg/Fe]

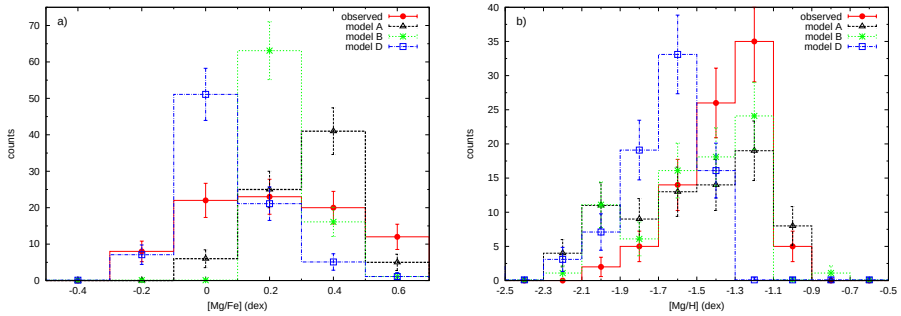

Figure 5.9: ***a)*** *The number of stars as a function of [Mg/Fe] abundance for each Sculptor model, compared to observed values from HR spectroscopy. Poissonian errorbars are also given for each model prediction.* ***b)*** *The histogram of number of stars at different [Mg/H] abundances for each Sculptor model, along with Poissonian errorbars. Observed values from HR spectroscopy are also shown.*

and [Mg/H] distributions.
Figure 5.9b shows that the overall trend in [Mg/H], as produced by SNE type II, is correctly reproduced in model A. Similar to Figure 5.9a, the number of metal-poor (and hence low [Mg/H]) stars are slightly over-predicted in model A, while the number of [Mg/H]-rich stars is under-predicted. These differences are likely due to the under-prediction of the star formation rate at young ages (and therefore low metallicity and α-element abundances), as seen in Figure 5.6. Therefore, the correct abundance pattern is predicted, but not with exactly the right strength at different age and/or metallicity.

5.7.2 Model B:

Figure 5.8 shows that model B predicts high [Mg/Fe] abundances for the majority of stars, inconsistent with the observed abundance pattern for Sculptor. Model B predicts a relatively flat distribution in [Mg/Fe], which is similar to the observed distribution abundances for [Fe/H] ≤-1.7 dex. However, no decrease is predicted in the [Mg/Fe] distribution of model B, due to the absence of SNe type Ia in the simulation, leading to a flat distribution in Figure 5.8 and a narrow peak in Figure 5.9a.
The predicted [Mg/H] abundances for model B (Figure 5.9b) show a good match to the observations, although the number of stars at low [Mg/H] is slightly over-predicted due to slightly too low [Mg/Fe] abundances at low metallicity. Furthermore, the number of stars at high [Mg/H] is under-predicted compared to the observations, due to the under-prediction of metal-rich ([Fe/H]≥−1.3 dex) in model B (see Figure 5.6).

5.7.3 Model D:

The predicted α-element abundances of model D follow the same trend as observed in Sculptor, but with lower [Mg/Fe] abundances for more metal-poor stars ([Fe/H]≤ -2.0 dex). Therefore, the slope of the model distribution is slightly shallower than observed in Sculptor.
The predicted [Mg/Fe] distribution for model D in Figure 5.9a is peaked at lower [Mg/Fe] abundances than the observed distribution, under-predicting the number of stars with high [Mg/Fe] and over-predicting the number of stars with low [Mg/Fe]. This is caused by the fast enrichment in model D, leading to a significant under-prediction of stars at low metallicity in the SFH (see Figure 5.6).
The predicted [Mg/H] abundances for model D in Figure 5.9b is inconsistent with the observed distribution for Sculptor. Too many stars are formed with low [Mg/H] abundances, while the number of stars at high [Mg/H] is under-predicted. This may be the result of the fast enrichment in model D, shifting the peak of the [Mg/H] distribution to lower abundances.

5.8 Summary

Overall, all four models we looked at are able to reproduce the major features in the CMD of Sculptor (see Figure 5.1). All models show a RGB and an old MSTO broadly consistent with a large range in metallicities, and dominated by old populations.
Model A results in a very good match to the observed CMD of Sculptor, as shown in Figure 5.1. The position and spread of the MSTO region and RGB are well matched to the observations. The predicted SFH and MDF of model A (see Figure 5.6) show small differences with the results derived from the observed CMD of Sculptor. The star formation rates at younger ages are slightly lower than the observations suggest, which indicates that the evolutionary rate of the model galaxy is faster than the observations show. This leads to a slight over-prediction of stars at intermediate metallicities ($-2.0 <$ [Fe/H] < -1.3 dex), giving negative values in the difference Hess diagram in Figure 5.2. Furthermore, the faster evolutionary rate also explains the under-prediction of stars with low α-element abundances, and the shift of the peak in Figure 5.9a with respect to Sculptor. A model with a slightly lower star formation efficiency might result in a better match to the observed properties of the Sculptor dSph.
Model B is able to reproduce the general features seen in the CMD of Sculptor (Figure 5.1). However, the distribution of age and metallicity across the RGB and MSTO regions (see Figures 5.3, 5.4 and 5.5) shows that the stellar populations are clearly too old with respect to what is observed in Sculptor. This is consistent with the SFH and MDF comparison (Figure 5.6), which shows that model B predicts a very old SFH and a metallicity distribution peaked at high metallicities ([Fe/H]≈ -1.50 dex). The predicted distribution of [Mg/H] (see Figure 5.9b) in model B shows a good match to the observations, while the lack of SNe type Ia in the simulations is responsible for the flat distribution in [Mg/Fe] abundances.
The very old model SFH of model B may be the result of assuming a star formation efficiency that is too high, which causes the galaxy to form and evolve on a very short

timescale. Physical processes such as a metallicity-dependent infall or the inclusion of gas heating due to supernovae energy deposition could be used to reduce the star formation efficiency in the model galaxies.
Model C is dominated by stars with intermediate metallicities ([Fe/H]≈ -1.75 dex). The SFH (in Figure 5.6) shows that the star formation in model C occurred in a dominant episode between 10−14 Gyr with a later smaller burst between 7−9 Gyr. This leads to a CMD which can be ruled out based on the observed CMD (with negligible errors on the RGB). For instance, the lack of metal-poor stars in the CEH (see Figure 5.6) results in a noticeable lack of stars on the blue side of the RGB in Figure 5.1. There is also a lack of younger, more metal-rich stars, which produces an MDF which is too narrow with respect to Sculptor (see Figure 5.7).
In general, the metallicity range in the simulated galaxies of model C are narrower than observed, which could be due to lack of a detailed prescription of the chemical evolution such as the use of the instantaneous recycling approximation (Starkenburg et al, 2012, in prep). A more continuous SFH would result in a better match with the observed CMD and SFH of the Sculptor dSph. Therefore, we intend to investigate in future work if a model from the same set of simulations, which displays a more continuous SFH, will provide a better match to the observed properties.
The synthetic CMD of model D shows that the model stellar populations distribute themselves very closely to the observed RGB and MSTO, as shown in Figure 5.1. A clear trend is visible with metallicity on the RGB and age on the MSTO in Figures 5.3 and 5.4. The SFH predicted by model D is a close approximation to the best matching SFH derived from the observations, except at the oldest ages. However, the chemical enrichment proceeded too fast in model D, with respect to that observed in Sculptor. The relative strengths of the populations are different from those in Sculptor, resulting in a shift of the peak of the MDF (see Figures 5.6 and 5.7). Furthermore, the α-element distribution shows that the [Mg/Fe] abundances predicted by model D are in general too low (at a given metallicity) compared to observations (see Figures 5.8 and 5.9), possibly driven by the enrichment timescale. The fast enrichment in model D could be a result of the timescale assumed for SNe explosions, or the timescale for the build-up of the reservoir of gas available to form stars.

5.9 Conclusions

In all models, the combination between age and metallicity is broadly similar to the observations (the differences with the observed CMD are often attributable to the lack or excess of certain populations). This shows that the models are able to correctly account for the major processes involved in the evolution of Sculptor.
For some models, the differences between the predicted and observed properties may be linked to the limited sample of available simulations in the parameter range of Sculptor. Therefore, not enough model galaxies were available to allow the selection of an “average" model corresponding to the overall properties of Sculptor. Furthermore, it is clear that missing physics can have a measurable effect on the predicted properties of the model, such as the absence of SNe type Ia in model B (see Figure 5.8). The

inability to maintain continuous star formation can also explain differences with the observations of the Sculptor dSph, particularly in model C. This could be linked to the pace of star formation, which is influenced by a variety of different physical processes, both internal and external to the galaxy. Including the timescale of chemical evolution as determined by de Boer et al. (2012) could help to produce a more exact match of the models and observations of the Sculptor dSph.
A comparison between all models shows that model A provides the closest fit to the observed CMD, as well as the MDF and SFH. However, the detailed modelling of the chemical evolution in model D allows the best comparison to the abundance pattern of the individual stars observed in Sculptor, making it the most sensitive to the timescale of chemical evolution. The differences between individual models could be due not only to the different physics, but also to the starting conditions of each simulations, which are not well constrained from observations. A set of simulations with identical starting conditions could be used to better compare the effects of model ingredients on the simulated galaxy .
All four models compared in this chapter are able to reproduce the evolution of stellar populations in a dwarf galaxy. Therefore, all models successfully form a Sculptor-like galaxy, but not all models result in an exact analogue of the Sculptor dSph. The best simulation of the Sculptor dSph would be a combination of the strengths of each simulation, such as the detailed chemical evolution modelling of model D, the full treatment of individual gas particles from model A and the cosmological approach of models B and C. In this way, the simulations would be able to incorporate detailed internal and external processes that influence the evolution of a dwarf galaxy. Finally, the observed properties and timescales of stellar populations can be used to find the best combination of model ingredients to reproduce this benchmark galaxy for isolated star formation.

acknowledgements

The authors would like to thank the International Space Science Institute (ISSI) in Bern for support of the team “Defining the full life-cycle of dwarf galaxy evolution: the Local Universe as a template", which made this project possible. T.d.B. would like to acknowledge valuable contributions to the chapter, made by Y. Revaz, P. Jablonka, D. Romano, S. Salvadori, E. Starkenburg, M. Tosi, V. Hill, G. Battaglia and E. Tolstoy.

Bibliography

Aaronson, M. and Mould, J.: 1980, ApJ **240**, 804

Aaronson, M. and Mould, J.: 1985, ApJ **290**, 191

Aparicio, A. and Gallart, C.: 2004, AJ **128**, 1465

Aparicio, A., Gallart, C., and Bertelli, G.: 1997, AJ **114**, 669

Aparicio, A. and Hidalgo, S. L.: 2009, AJ **138**, 558

Arp, H. C., Baum, W. A., and Sandage, A. R.: 1952, AJ **57**, 4

Azzopardi, M., Muratorio, G., Breysacher, J., and Westerlund, B. E.: 1999, in P. Whitelock & R. Cannon (ed.), *The Stellar Content of Local Group Galaxies*, Vol. 192 of *IAU Symposium*, p. 144

Baade, W.: 1944, ApJ **100**, 137

Baade, W. and Hubble, E.: 1939, PASP **51**, 40

Battaglia, G.: 2007, *PhD thesis, University of Groningen*

Battaglia, G., Helmi, A., Tolstoy, E., Irwin, M., Hill, V., and Jablonka, P.: 2008a, ApJ **681**, L13

Battaglia, G., Irwin, M., Tolstoy, E., Hill, V., Helmi, A., Letarte, B., and Jablonka, P.: 2008b, MNRAS **383**, 183

Battaglia, G., Tolstoy, E., Helmi, A., Irwin, M., Parisi, P., Hill, V., and Jablonka, P.: 2011, MNRAS **411**, 1013

Battaglia, G., Tolstoy, E., Helmi, A., Irwin, M. J., Letarte, B., Jablonka, P., Hill, V., Venn, K. A., Shetrone, M. D., Arimoto, N., Primas, F., Kaufer, A., Francois, P., Szeifert, T., Abel, T., and Sadakane, K.: 2006, A&A **459**, 423

Baugh, C. M.: 2006, *Reports on Progress in Physics* **69**, 3101

Belokurov, V., Zucker, D. B., Evans, N. W., Kleyna, J. T., Koposov, S., Hodgkin, S. T., Irwin, M. J., Gilmore, G., Wilkinson, M. I., Fellhauer, M., Bramich, D. M., Hewett, P. C., Vidrih, S., De Jong, J. T. A., Smith, J. A., Rix, H.-W., Bell, E. F., Wyse, R. F. G., Newberg, H. J., Mayeur, P. A., Yanny, B., Rockosi, C. M., Gnedin, O. Y., Schneider, D. P., Beers, T. C., Barentine, J. C., Brewington, H., Brinkmann, J., Harvanek, M., Kleinman, S. J., Krzesinski, J., Long, D., Nitta, A., and Snedden, S. A.: 2007, ApJ **654**, 897

Belokurov, V., Zucker, D. B., Evans, N. W., Wilkinson, M. I., Irwin, M. J., Hodgkin, S., Bramich, D. M., Irwin, J. M., Gilmore, G., Willman, B., Vidrih, S., Newberg, H. J., Wyse, R. F. G., Fellhauer, M., Hewett, P. C., Cole, N., Bell, E. F., Beers, T. C., Rockosi, C. M., Yanny, B., Grebel, E. K., Schneider, D. P., Lupton, R., Barentine, J. C., Brewington, H., Brinkmann, J., Harvanek, M., Kleinman, S. J., Krzesinski, J., Long, D., Nitta, A., Smith, J. A., and Snedden, S. A.: 2006, ApJ **647**, L111

Benson, A. J.: 2010, Phys. Rep. **495**, 33

Bersier, D. and Wood, P. R.: 2002, AJ **123**, 840

Besla, G., Kallivayalil, N., Hernquist, L., van der Marel, R. P., Cox, T. J., and Keres, D.: 2012, *ArXiv e-prints*

Bonifacio, P., Spite, M., Cayrel, R., Hill, V., Spite, F., François, P., Plez, B., Ludwig, H.-G., Caffau, E., Molaro, P., Depagne, E., Andersen, J., Barbuy, B., Beers, T. C., Nordström, B., and Primas, F.: 2009, A&A **501**, 519

Bono, G., Stetson, P. B., Walker, A. R., Monelli, M., Fabrizio, M., Pietrinferni, A., Brocato, E., Buonanno, R., Caputo, F., Cassisi, S., Castellani, M., Cignoni, M., Corsi, C. E., Dall'Ora, M., Degl'Innocenti, S., François, P., Ferraro, I., Iannicola, G., Nonino, M., Moroni, P. G. P., Pulone, L., Smith, H. A., and Thevenin, F.: 2010, PASP **122**, 651

Boylan-Kolchin, M., Springel, V., White, S. D. M., Jenkins, A., and Lemson, G.: 2009, MNRAS **398**, 1150

Buonanno, R., Corsi, C. E., Buzzoni, A., Cacciari, C., Ferraro, F. R., and Fusi Pecci, F.: 1994, A&A **290**, 69

Buonanno, R., Corsi, C. E., Castellani, M., Marconi, G., Fusi Pecci, F., and Zinn, R.: 1999, AJ **118**, 1671

Buonanno, R., Corsi, C. E., Fusi Pecci, F., Hardy, E., and Zinn, R.: 1985, A&A **152**, 65

Buonanno, R., Corsi, C. E., Zinn, R., Fusi Pecci, F., Hardy, E., and Suntzeff, N. B.: 1998, ApJ **501**, L33

Calabretta, M. R. and Greisen, E. W.: 2002, A&A **395**, 1077

Carrera, R., Gallart, C., Aparicio, A., and Hardy, E.: 2011, AJ **142**, 61

Carretta, E., Bragaglia, A., Gratton, R., and Lucatello, S.: 2009, A&A **505**, 139

Carretta, E., Bragaglia, A., Gratton, R. G., Recio-Blanco, A., Lucatello, S., D'Orazi, V., and Cassisi, S.: 2010, A&A **516**, A55+

Coleman, M., Da Costa, G. S., Bland-Hawthorn, J., Martínez-Delgado, D., Freeman, K. C., and Malin, D.: 2004, AJ **127**, 832

Coleman, M. G., Da Costa, G. S., and Bland-Hawthorn, J.: 2005a, AJ **130**, 1065

Coleman, M. G., Da Costa, G. S., Bland-Hawthorn, J., and Freeman, K. C.: 2005b, AJ

129, 1443

Coleman, M. G. and de Jong, J. T. A.: 2008, ApJ **685**, 933

Da Costa, G. S.: 1984, ApJ **285**, 483

Dalcanton, J. J., Williams, B. F., Melbourne, J. L., Girardi, L., Dolphin, A., Rosenfield, P. A., Boyer, M. L., de Jong, R. S., Gilbert, K., Marigo, P., Olsen, K., Seth, A. C., and Skillman, E.: 2012, ApJS **198**, 6

de Boer, T. J. L., Tolstoy, E., Hill, V., Saha, A., Olsen, K., Starkenburg, E., Lemasle, B., Irwin, M. J., and Battaglia, G.: 2012, A&A **539**, A103

de Boer, T. J. L., Tolstoy, E., Saha, A., Olsen, K., Irwin, M. J., Battaglia, G., Hill, V., Shetrone, M. D., Fiorentino, G., and Cole, A.: 2011, A&A **528**, A119+

De Lucia, G. and Helmi, A.: 2008, MNRAS **391**, 14

de Vaucouleurs, G. and Ables, H. D.: 1968, ApJ **151**, 105

Demers, S., Irwin, M. J., and Kunkel, W. E.: 1994, AJ **108**, 1648

Demers, S., Krautter, A., and Kunkel, W. E.: 1980, AJ **85**, 1587

Dolphin, A.: 1997, *New Astronomy* **2**, 397

Dolphin, A. E.: 2002, MNRAS **332**, 91

Dotter, A., Chaboyer, B., Jevremović, D., Kostov, V., Baron, E., and Ferguson, J. W.: 2008, ApJS **178**, 89

Eskridge, P. B.: 1988a, AJ **96**, 1352

Eskridge, P. B.: 1988b, AJ **96**, 1614

Eskridge, P. B.: 1988c, AJ **95**, 1706

Eskridge, P. B.: 1988d, AJ **96**, 1336

Ferraro, F. R., Clementini, G., Fusi Pecci, F., Sortino, R., and Buonanno, R.: 1992, MNRAS **256**, 391

Ferraro, F. R., Paltrinieri, B., Fusi Pecci, F., Cacciari, C., Dorman, B., Rood, R. T., Buonanno, R., Corsi, C. E., Burgarella, D., and Laget, M.: 1997, A&A **324**, 915

Frebel, A., Kirby, E. N., and Simon, J. D.: 2010, Nature **464**, 72

Fukugita, M., Shimasaku, K., and Ichikawa, T.: 1995, PASP **107**, 945

Gallart, C., Aparicio, A., Bertelli, G., and Chiosi, C.: 1996a, AJ **112**, 1950

Gallart, C., Aparicio, A., and Vilchez, J. M.: 1996b, AJ **112**, 1928

Gallart, C., Aparicio, A., Zinn, R., Buonanno, R., Hardy, E., and Marconi, G.: 2005a, in H. Jerjen & B. Binggeli (ed.), *IAU Colloq. 198: Near-fields cosmology with dwarf*

elliptical galaxies, pp 25–29

Gallart, C., Freedman, W. L., Aparicio, A., Bertelli, G., and Chiosi, C.: 1999, AJ **118**, 2245

Gallart, C., Zoccali, M., and Aparicio, A.: 2005b, ARA&A **43**, 387

Geisler, D., Smith, V. V., Wallerstein, G., Gonzalez, G., and Charbonnel, C.: 2005, AJ **129**, 1428

Gilmore, G. and Wyse, R. F. G.: 1991, ApJ **367**, L55

Glatt, K., Gallagher, III, J. S., Grebel, E. K., Nota, A., Sabbi, E., Sirianni, M., Clementini, G., Tosi, M., Harbeck, D., Koch, A., and Cracraft, M.: 2008a, AJ **135**, 1106

Glatt, K., Grebel, E. K., Sabbi, E., Gallagher, III, J. S., Nota, A., Sirianni, M., Clementini, G., Tosi, M., Harbeck, D., Koch, A., Kayser, A., and Da Costa, G.: 2008b, AJ **136**, 1703

Governato, F., Brook, C., Mayer, L., Brooks, A., Rhee, G., Wadsley, J., Jonsson, P., Willman, B., Stinson, G., Quinn, T., and Madau, P.: 2010, Nature **463**, 203

Greco, C., Clementini, G., Catelan, M., Held, E. V., Poretti, E., Gullieuszik, M., Maio, M., Rest, A., De Lee, N., Smith, H. A., and Pritzl, B. J.: 2007, ApJ **670**, 332

Greco, C., Clementini, G., Held, E. V., Poretti, E., Catelan, M., Dell'Arciprete, L., Gullieuszik, M., Maio, M., Rizzi, L., Smith, H. A., Pritzl, B. J., Rest, A., and De Lee, N.: 2005, *ArXiv Astrophysics e-prints*

Harbeck, D., Grebel, E. K., Holtzman, J., Guhathakurta, P., Brandner, W., Geisler, D., Sarajedini, A., Dolphin, A., Hurley-Keller, D., and Mateo, M.: 2001, AJ **122**, 3092

Hardy, E.: 2002, in D. P. Geisler, E. K. Grebel, & D. Minniti (ed.), *Extragalactic Star Clusters*, Vol. 207 of *IAU Symposium*, p. 62

Harris, J. and Zaritsky, D.: 2001, ApJS **136**, 25

Harris, W. E.: 1996, AJ **112**, 1487

Harris, W. E., Hesser, J. E., and Atwood, B.: 1983, ApJ **268**, L111

Heger, A. and Woosley, S. E.: 2002, ApJ **567**, 532

Hidalgo, S. L., Aparicio, A., Skillman, E., Monelli, M., Gallart, C., Cole, A., Dolphin, A., Weisz, D., Bernard, E. J., Cassisi, S., Mayer, L., Stetson, P., Tolstoy, E., and Ferguson, H.: 2011, ApJ **730**, 14

Hodge, P. W.: 1961a, AJ **66**, 83

Hodge, P. W.: 1961b, AJ **66**, 249

Hodge, P. W.: 1965, ApJ **142**, 1390

Hodge, P. W. and Smith, D. W.: 1974, ApJ **188**, 19

Hubble, E. P.: 1926, ApJ **64**, 321

Hubble, E. P.: 1936, *Realm of the Nebulae*, Yale University Press

Hurley-Keller, D., Mateo, M., and Grebel, E. K.: 1999, ApJ **523**, L25

Ibata, R. A., Gilmore, G., and Irwin, M. J.: 1994, Nature **370**, 194

Irwin, M. and Hatzidimitriou, D.: 1995, MNRAS **277**, 1354

Iwamoto, K., Brachwitz, F., Nomoto, K., Kishimoto, N., Umeda, H., Hix, W. R., and Thielemann, F.-K.: 1999, ApJS **125**, 439

Kaluzny, J., Kubiak, M., Szymanski, M., Udalski, A., Krzeminski, W., and Mateo, M.: 1995, A&AS **112**, 407

Kim, Y., Demarque, P., Yi, S. K., and Alexander, D. R.: 2002, ApJS **143**, 499

Kirby, E. N., Cohen, J. G., Smith, G. H., Majewski, S. R., Sohn, S. T., and Guhathakurta, P.: 2011, ApJ **727**, 79

Kirby, E. N., Guhathakurta, P., Bolte, M., Sneden, C., and Geha, M. C.: 2009, ApJ **705**, 328

Kirby, E. N., Guhathakurta, P., Simon, J. D., Geha, M. C., Rockosi, C. M., Sneden, C., Cohen, J. G., Sohn, S. T., Majewski, S. R., and Siegel, M.: 2010, ApJS **191**, 352

Klimentowski, J., Łokas, E. L., Kazantzidis, S., Prada, F., Mayer, L., and Mamon, G. A.: 2007, MNRAS **378**, 353

Kobayashi, C., Tsujimoto, T., and Nomoto, K.: 2000, ApJ **539**, 26

Koch, A., Grebel, E. K., Gilmore, G. F., Wyse, R. F. G., Kleyna, J. T., Harbeck, D. R., Wilkinson, M. I., and Wyn Evans, N.: 2008, AJ **135**, 1580

Koch, A., Grebel, E. K., Wyse, R. F. G., Kleyna, J. T., Wilkinson, M. I., Harbeck, D. R., Gilmore, G. F., and Evans, N. W.: 2006, AJ **131**, 895

Kravtsov, V., Ipatov, A., Samus, N., Smirnov, O., Alcaino, G., Liller, W., and Alvarado, F.: 1997, A&AS **125**, 1

Kroupa, P.: 2001, MNRAS **322**, 231

Kunkel, W. E. and Demers, S.: 1977, ApJ **214**, 21

Landolt, A. U.: 1992, AJ **104**, 340

Landolt, A. U.: 2007, AJ **133**, 2502

Lanfranchi, G. A. and Matteucci, F.: 2003, MNRAS **345**, 71

Lanfranchi, G. A. and Matteucci, F.: 2004, MNRAS **351**, 1338

Lanfranchi, G. A. and Matteucci, F.: 2010, in G. Bruzual & S. Charlot (ed.), *IAU Symposium*, Vol. 262 of *IAU Symposium*, pp 370–371

Lemasle, B., Hill, V., Tolstoy, E., Venn, K. A., Shetrone, M. D., Irwin, M. J., de Boer, T. J. L.,

Starkenburg, E., and Salvadori, S.: 2011, *ArXiv e-prints*

Letarte, B., Hill, V., Jablonka, P., Tolstoy, E., François, P., and Meylan, G.: 2006, A&A **453**, 547

Letarte, B., Hill, V., Tolstoy, E., Jablonka, P., Shetrone, M., Venn, K. A., Spite, M., Irwin, M. J., Battaglia, G., Helmi, A., Primas, F., François, P., Kaufer, A., Szeifert, T., Arimoto, N., and Sadakane, K.: 2010, A&A **523**, A17

Li, Y.-S., De Lucia, G., and Helmi, A.: 2010, MNRAS **401**, 2036

Łokas, E. L.: 2009, MNRAS **394**, L102

Mackey, A. D. and Gilmore, G. F.: 2003, MNRAS **340**, 175

Majewski, S. R., Siegel, M. H., Patterson, R. J., and Rood, R. T.: 1999, ApJ **520**, L33

Majewski, S. R., Skrutskie, M. F., Weinberg, M. D., and Ostheimer, J. C.: 2003, ApJ **599**, 1082

Mannucci, F., Della Valle, M., and Panagia, N.: 2006, MNRAS **370**, 773

Mapelli, M., Ripamonti, E., Battaglia, G., Tolstoy, E., Irwin, M. J., Moore, B., and Sigurdsson, S.: 2009, MNRAS **396**, 1771

Mapelli, M., Ripamonti, E., Tolstoy, E., Sigurdsson, S., Irwin, M. J., and Battaglia, G.: 2007, MNRAS **380**, 1127

Martin, N. F., de Jong, J. T. A., and Rix, H.-W.: 2008, ApJ **684**, 1075

Mashchenko, S., Wadsley, J., and Couchman, H. M. P.: 2008, *Science* **319**, 174

Mateo, M. L.: 1998, ARA&A **36**, 435

Matteucci, F.: 2003, Ap&SS **284**, 539

Matteucci, F. and Brocato, E.: 1990, ApJ **365**, 539

Matteucci, F. and Recchi, S.: 2001, ApJ **558**, 351

McCrea, W. H.: 1964, MNRAS **128**, 147

Monelli, M., Gallart, C., Hidalgo, S. L., Aparicio, A., Skillman, E. D., Cole, A. A., Weisz, D. R., Mayer, L., Bernard, E. J., Cassisi, S., Dolphin, A. E., Drozdovsky, I., and Stetson, P. B.: 2010, ApJ **722**, 1864

Monkiewicz, J., Mould, J. R., Gallagher, III, J. S., Clarke, J. T., Trauger, J. T., Grillmair, C., Ballester, G. E., Burrows, C. J., Crisp, D., Evans, R., Griffiths, R., Hester, J. J., Hoessel, J. G., Holtzman, J. A., Krist, J. E., Meadows, V., Scowen, P. A., Stapelfeldt, K. R., Sahai, R., and Watson, A.: 1999, PASP **111**, 1392

Norris, J. and Bessell, M. S.: 1978, ApJ **225**, L49

Olszewski, E. W. and Aaronson, M.: 1985, AJ **90**, 2221

Olszewski, E. W., Mateo, M., Harris, J., Walker, M. G., Coleman, M. G., and Da Costa, G. S.: 2006, AJ **131**, 912

Pasetto, S., Grebel, E. K., Berczik, P., Chiosi, C., and Spurzem, R.: 2011, A&A **525**, A99

Piatek, S., Pryor, C., Bristow, P., Olszewski, E. W., Harris, H. C., Mateo, M., Minniti, D., and Tinney, C. G.: 2007, AJ **133**, 818

Pietrinferni, A., Cassisi, S., Salaris, M., and Castelli, F.: 2004, ApJ **612**, 168

Pietrinferni, A., Cassisi, S., Salaris, M., and Castelli, F.: 2006, ApJ **642**, 797

Pietrzyński, G., Gieren, W., Szewczyk, O., Walker, A., Rizzi, L., Bresolin, F., Kudritzki, R., Nalewajko, K., Storm, J., Dall'Ora, M., and Ivanov, V.: 2008, AJ **135**, 1993

Pietrzyński, G., Górski, M., Gieren, W., Ivanov, V. D., Bresolin, F., and Kudritzki, R.: 2009, AJ **138**, 459

Pont, F., Zinn, R., Gallart, C., Hardy, E., and Winnick, R.: 2004, AJ **127**, 840

Raiteri, C. M., Villata, M., and Navarro, J. F.: 1996, A&A **315**, 105

Revaz, Y. and Jablonka, P.: 2012, A&A **538**, A82

Revaz, Y., Jablonka, P., Sawala, T., Hill, V., Letarte, B., Irwin, M., Battaglia, G., Helmi, A., Shetrone, M. D., Tolstoy, E., and Venn, K. A.: 2009, A&A **501**, 189

Rizzi, L., Held, E. V., Saviane, I., Tully, R. B., and Gullieuszik, M.: 2007, MNRAS **380**, 1255

Robin, A. C., Reylé, C., Derrière, S., and Picaud, S.: 2003, A&A **409**, 523

Romano, D., Matteucci, F., Tosi, M., Pancino, E., Bellazzini, M., Ferraro, F. R., Limongi, M., and Sollima, A.: 2007, MNRAS **376**, 405

Saha, A., Olszewski, E. W., Brondel, B., Olsen, K., Knezek, P., Harris, J., Smith, C., Subramaniam, A., Claver, J., Rest, A., Seitzer, P., Cook, K. H., Minniti, D., and Suntzeff, N. B.: 2010, AJ **140**, 1719

Salaris, M. and Girardi, L.: 2002, MNRAS **337**, 332

Sales, L. V., Helmi, A., and Battaglia, G.: 2010, *Advances in Astronomy* 2010

Salvadori, S. and Ferrara, A.: 2009, MNRAS **395**, L6

Salvadori, S., Ferrara, A., and Schneider, R.: 2008, MNRAS **386**, 348

Salvadori, S., Schneider, R., and Ferrara, A.: 2007, MNRAS **381**, 647

Sandage, A.: 1957, ApJ **126**, 326

Sandage, A.: 1982, ApJ **252**, 553

Sandage, A.: 1986, ARA&A **24**, 421

Saviane, I., Held, E. V., and Bertelli, G.: 2000, A&A **355**, 56

Schechter, P. L., Mateo, M., and Saha, A.: 1993, PASP **105**, 1342

Schlegel, D. J., Finkbeiner, D. P., and Davis, M.: 1998, ApJ **500**, 525

Shapley, H.: 1938a, *Harvard College Observatory Bulletin* **908**, 1

Shapley, H.: 1938b, Nature **142**, 715

Shetrone, M., Venn, K. A., Tolstoy, E., Primas, F., Hill, V., and Kaufer, A.: 2003, AJ **125**, 684

Sigurdsson, S., Davies, M. B., and Bolte, M.: 1994, ApJ **431**, L115

Simon, J. D. and Geha, M.: 2007, ApJ **670**, 313

Skrutskie, M. F., Cutri, R. M., Stiening, R., Weinberg, M. D., Schneider, S., Carpenter, J. M., Beichman, C., Capps, R., Chester, T., Elias, J., Huchra, J., Liebert, J., Lonsdale, C., Monet, D. G., Price, S., Seitzer, P., Jarrett, T., Kirkpatrick, J. D., Gizis, J. E., Howard, E., Evans, T., Fowler, J., Fullmer, L., Hurt, R., Light, R., Kopan, E. L., Marsh, K. A., McCallon, H. L., Tam, R., Van Dyk, S., and Wheelock, S.: 2006, AJ **131**, 1163

Springel, V.: 2005, MNRAS **364**, 1105

Springel, V., Wang, J., Vogelsberger, M., Ludlow, A., Jenkins, A., Helmi, A., Navarro, J. F., Frenk, C. S., and White, S. D. M.: 2008, MNRAS **391**, 1685

Springel, V., White, S. D. M., Jenkins, A., Frenk, C. S., Yoshida, N., Gao, L., Navarro, J., Thacker, R., Croton, D., Helly, J., Peacock, J. A., Cole, S., Thomas, P., Couchman, H., Evrard, A., Colberg, J., and Pearce, F.: 2005, Nature **435**, 629

Starkenburg, E., Hill, V., Tolstoy, E., González Hernández, J. I., Irwin, M., Helmi, A., Battaglia, G., Jablonka, P., Tafelmeyer, M., Shetrone, M., Venn, K., and de Boer, T.: 2010, A&A **513**, A34+

Stetson, P. B.: 2000, PASP **112**, 925

Stetson, P. B. and Harris, W. E.: 1988, AJ **96**, 909

Stetson, P. B., Hesser, J. E., and Smecker-Hane, T. A.: 1998, PASP **110**, 533

Stinson, G. S., Dalcanton, J. J., Quinn, T., Kaufmann, T., and Wadsley, J.: 2007, ApJ **667**, 170

Strader, J., Brodie, J. P., Forbes, D. A., Beasley, M. A., and Huchra, J. P.: 2003, AJ **125**, 1291

Suntzeff, N. B., Mateo, M., Terndrup, D. M., Olszewski, E. W., Geisler, D., and Weller, W.: 1993, ApJ **418**, 208

Tafelmeyer, M., Jablonka, P., Hill, V., Shetrone, M., Tolstoy, E., Irwin, M. J., Battaglia, G., Helmi, A., Starkenburg, E., Venn, K. A., Abel, T., Francois, P., Kaufer, A., North, P.,

Primas, F., and Szeifert, T.: 2010, A&A **524**, A58

Tinsley, B. M.: 1979, ApJ **229**, 1046

Tolstoy, E., Hill, V., and Tosi, M.: 2009, ARA&A **47**, 371

Tolstoy, E., Irwin, M. J., Cole, A. A., Pasquini, L., Gilmozzi, R., and Gallagher, J. S.: 2001, MNRAS **327**, 918

Tolstoy, E., Irwin, M. J., Helmi, A., Battaglia, G., Jablonka, P., Hill, V., Venn, K. A., Shetrone, M. D., Letarte, B., Cole, A. A., Primas, F., Francois, P., Arimoto, N., Sadakane, K., Kaufer, A., Szeifert, T., and Abel, T.: 2004, ApJ **617**, L119

Tolstoy, E. and Saha, A.: 1996, ApJ **462**, 672

Tolstoy, E., Venn, K. A., Shetrone, M., Primas, F., Hill, V., Kaufer, A., and Szeifert, T.: 2003, AJ **125**, 707

Tosi, M., Greggio, L., Marconi, G., and Focardi, P.: 1991, AJ **102**, 951

Tsujimoto, T., Nomoto, K., Yoshii, Y., Hashimoto, M., Yanagida, S., and Thielemann, F.-K.: 1995, MNRAS **277**, 945

Valdes, F. G.: 1998, in R. Albrecht, R. N. Hook, & H. A. Bushouse (ed.), *Astronomical Data Analysis Software and Systems VII*, Vol. 145 of *Astronomical Society of the Pacific Conference Series*, pp 53–+

Valdes, F. G.: 2002, in R. Gupta, H. P. Singh, and C. A. L. Bailer-Jones (eds.), *Automated Data Analysis in Astronomy*, pp 309–+

van den Hoek, L. B. and Groenewegen, M. A. T.: 1997, A&AS **123**, 305

Vandenberg, D. A.: 1983, ApJS **51**, 29

Venn, K. A., Irwin, M., Shetrone, M. D., Tout, C. A., Hill, V., and Tolstoy, E.: 2004, AJ **128**, 1177

Walcher, C. J., Fried, J. W., Burkert, A., and Klessen, R. S.: 2003, A&A **406**, 847

Walker, M. G., Mateo, M., and Olszewski, E. W.: 2009, AJ **137**, 3100

Walker, M. G., Mateo, M., Olszewski, E. W., Bernstein, R., Wang, X., and Woodroofe, M.: 2006, AJ **131**, 2114

Westfall, K. B., Majewski, S. R., Ostheimer, J. C., Frinchaboy, P. M., Kunkel, W. E., Patterson, R. J., and Link, R.: 2006, AJ **131**, 375

Woosley, S. E. and Weaver, T. A.: 1995, ApJS **101**, 181

Yi, S., Demarque, P., Kim, Y., Lee, Y., Ree, C. H., Lejeune, T., and Barnes, S.: 2001, ApJS **136**, 417

Nederlandse Samenvating

Sinds astronomen ontdekt hebben dat er andere sterrenstelsels bestaan naast het onze, vragen ze zich al af hoe de verschillende types sterrenstelsels gevormd worden, en welke processen verantwoordelijk zijn voor hun diversiteit aan eigenschappen.
De evolutie van sterrenstelsels wordt gewoonlijk bestudeerd door te kijken naar het gas en de sterren in deze stelsels. De levensduur van sterren met een lage massa is heel lang, en kan zelfs langer zijn dan de huidige leeftijd van het heelal. Dit betekent dat sommige sterren die gevormd zijn toen het heelal heel jong was, nu nog in leven zijn. Tijdens hun leven produceren sterren “metalenïn hun kern, door de fusie van lichtere elementen (Astronomen noemen alle elementen zwaarder dan helium “metalen"). Deze metalen worden de ruimte in geslingerd doordat sterren een wind produceren die gas en metalen uitzendt, en aan het eind van hun levensduur meestal een supernova explosie ondergaan. De metalen worden gemixt met het interstellaire gas in een sterrenstelsel, en verhogen daardoor het metaalgehalte van dit gas. Latere generaties sterren worden gevormd uit het verrijkte gas, en bevatten in hun atmosfeer een vingerafdruk van de chemische eigenschappen van het sterrenstelsel, ten tijde van de vorming van de ster. Door de chemische vingerafdruk van verschillende generaties sterren te onderzoeken kunnen astronomen een beeld opbouwen van hoe het gehalte aan chemische elementen veranderd is over kosmische tijd.
Voor sterrenstelsels die ver van ons verwijderd zijn is het alleen mogelijk hun eigenschappen te bestuderen door te kijken naar het geïntegreerde licht van het hele stelsel (het licht van alle sterren tezamen). Op die manier kunnen de algemene eigenschappen van sterrenstelsels onderzocht worden, zoals de gemiddelde leeftijd en metalliciteit (de hoeveelheid metalen ten opzichte van Waterstof, vergeleken met de hoeveelheid in de Zon).
In nabije sterrenstelsels is het echter mogelijk om met telescopen individuele sterren te onderscheiden. Daardoor kunnen eigenschappen van afzonderlijke sterren onderzocht worden, met behulp van photometrische en spectroscopische waarnemingen, die de helderheid, kleur, metalliciteit, radiële snelheid (naar ons toe of van ons af) en de hoeveelheden van diverse chemische elementen bepalen. Door metingen aan een groot aantal individuele sterren te doen, is het mogelijk verschillende sterpopulaties (verschillende generaties van sterren) te onderscheiden, en hun karakteristieken te bepalen in termen van leeftijd, metalliciteit en/of positie in het stelsel.
Photometrische waarnemingen geven ons de helderheid en kleur van sterren, die we vervolgens kunnen plotten in een kleur-helderheid diagram (CMD). Door modellen te maken van het geobserveerde CMD kunnen we de stervormingsgeschiedenis van het sterrenstelsel bepalen, wat aangeeft hoeveel sterren er gevormd zijn van verschillende

leeftijd en metalliciteit. Daardoor kunnen we bestuderen hoe de stervormingsactiviteit veranderd is over tijd, en wanneer de meerderheid van de sterren in het stelsel is gevormd. Door de stervormingsgeschiedenis te bepalen op verschillende posities binnen het stelsel is het ook mogelijk om te bepalen wat de verschillen in sterpopulaties zijn als een functie van de afstand tot het centrum van het stelsel.
Met behulp van spectroscopische waarnemingen kunnen we voor individuele sterren direct bepalen wat de hoeveelheden zijn van vele chemische elementen. Op die manier kunnen we de evolutie van chemische elementen onderzoeken, als een functie van metalliciteit. Door deze informatie te bepalen voor een groot aantal sterren is het ook mogelijk om effecten van verschillende sterpopulaties op het abundantie patroon te onderzoeken.
In dit proefschrift beschrijf ik de ontwikkeling van een nieuwe methode om de stervormingsgeschiedenis te bepalen, die gebruik maakt van alle beschikbare photometrische en spectroscopische informatie. Met behulp van deze methode wordt de evolutie van stervorming in twee sterrenstelsels in detail onderzocht. Ook wordt de tijdschaal van chemische evolutie bepaald in beide stelsels, door de nauwkeurige stervormingsgeschiedenis te combineren met nauwkeurige spectroscopische waarnemingen.

De satellieten van de Melkweg

De Lokale Groep van sterrenstelsels wordt gedomineerd door de Melkweg en het Andromedastelsel, twee grote spiraalstelsels. Daarnaast bevat de Lokale Groep ook nog een heleboel kleinere sterrenstelsels (dwergstelsels), die satellieten zijn van de grotere spiraalstelsels. Door de nabijheid van deze kleine sterrenstelsels is het mogelijk om hun individuele sterren te onderscheiden. Daarnaast zijn ze ook klein genoeg aan de sterrenhemel om de distributie van hun sterren redelijk makkelijk in kaart te brengen.
De dwergstelsels in de Lokale Groep vertonen een grote verscheidenheid aan eigenschappen. Sommige stelsels hebben gedurende lange tijd continue stervorming ondergaan, terwijl andere stervorming vertonen in verschillende, discrete episodes. Ook zijn sterrenstelsels gevonden die dezelfde globale eigenschappen hebben (zoals totale massa en helderheid), maar een compleet andere evolutie hebben ondergaan.
Gedetailleerd onderzoek aan de distributie van sterren binnen de sterrenstelsels heeft geleid tot de ontdekking van ruimtelijke substructuren, zoals sterren die uit stelsels worden getrokken door interacties met de grote spiraalstelsels. Ook zijn bewijzen gevonden dat kleinere sterrenstelsels worden “opgegeten"door grotere stelsels. Een goed voorbeeld is het Sagittarius-dwergstelsel, dat momenteel opgeslokt wordt door de Melkweg, en daardoor uitgerekt wordt als een lange sliert over de hemel.
Om te ontdekken welk mechanisme ten grondslag ligt aan deze verscheidenheid aan sterrenstelsels, is het nodig hun eigenschappen in detail te onderzoeken. Door de gedetailleerde stervormingsgeschiedenis te bepalen van een groep dwergstelsels is het mogelijk om te onderzoeken wat het effect is van verschillende parameters (zoals de totale massa, nabijheid tot de Melkweg, etc.) op de evolutie van een sterrenstelsel.

Het analyseren van CMDs

In het begin van de vorige eeuw ontdekten Ejnar Hertzsprung en Henry Norris Russell onafhankelijk van elkaar dat sterren bepaalde plekken innemen als je ze plot in een temperatuur-helderheid diagram (dat later Hertzsprung-Russell diagram is genoemd). De plek van een ster in het diagram is gerelateerd aan zijn massa, en de evolutionaire staat waarin de ster verkeert. Tegenwoordig wordt meestal een CMD gebruikt, omdat temperatuur moeilijk rechtstreeks te meten is.

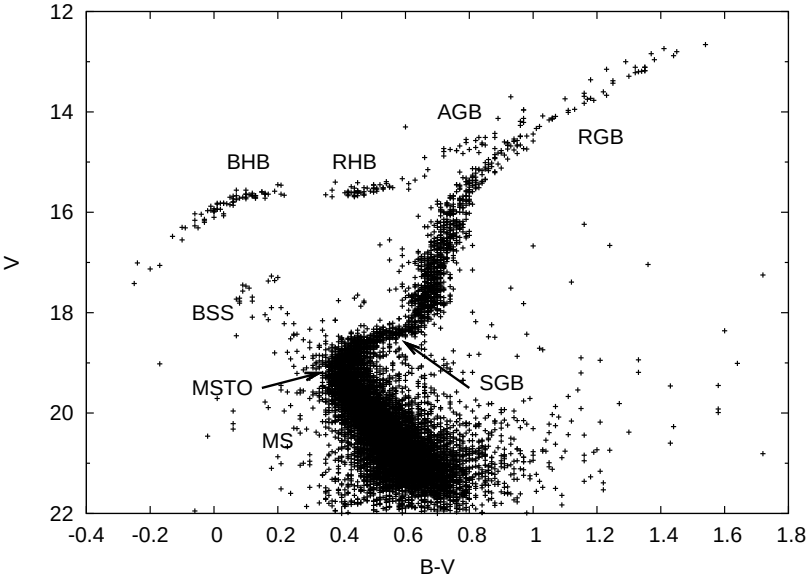

Figuur 1: *Een kleur-helderheid diagram (CMD) van de bolvormige sterrenhoop M3. De labels geven aan wat de verschillende evolutionaire toestanden zijn van sterren in het diagram. Met name de positie waar sterren de hoofdreeks verlaten (aangegeven met MSTO) is een gevoelige indicator voor de leeftijd van een sterpopulatie.*

Als een diagram gemaakt wordt van sterren die allemaal dezelfde afstand hebben (zoals in een stercluster of sterrenstelsel) geeft de vorm van het diagram ons inzicht in de leeftijd en metalliciteit van de sterpopulaties in het systeem. Sinds de ontdekking door Hertzsprung en Russell zijn een groot aantal sterrenstelsels en clusters onderzocht door te kijken naar de posities van hun sterren in het diagram. Er werd al snel ontdekt dat de sterren van bolvormige sterrenhopen een heel dunne reeks vormen in het diagram, wat aangeeft dat hun sterren allemaal dezelfde leeftijd hebben. Een voorbeeld van een CMD is te zien in Figuur 1, gemaakt voor sterren in de bolvormige sterrenhoop M3. De positie waar sterren de hoofdreeks verlaten (aangegeven met MSTO in Figuur 1) is een goede indicator van de leeftijd van de sterren, terwijl de positie van de reuzentak (aangegeven met RGB) meer gevoelig is voor de metalliciteit. De CMDs

van sterrenstelsels vertonen verschillende kenmerken, die aangeven dat ze een meer complexe stervormingsgeschiedenis hebben ondergaan. Zo laat het CMD van sommige stelsels een brede distributie van sterren zien, die aangeeft dat sterren gevormd zijn met een grote verscheidenheid aan leeftijden. Andere stelsels laten duidelijk verschillende reeksen zien, een indicatie van verschillende afzonderlijke fasen van stervorming.

Hoe bepaal je nauwkeurig de stervormingsgeschiedenis?

Door een geobserveerd CMD te vergelijken met theoretische modellen kunnen we de eigenschappen van de sterren bepalen. Een theoretische “isochroon"geeft de posities aan van een populatie sterren die allemaal dezelfde leeftijd en metalliciteit hebben. Door de isochroon te vinden die het best de vorm van het diagram reproduceert worden de mogelijke leeftijden van de sterren gevonden. Dit werkt heel goed in bolvormige sterrenhopen, aangezien hun sterren een dunne reeks vertonen in het diagram. In het geval van sterrenstelsels is het echter een stuk moeilijker om individuele, overlappende populaties te onderscheiden van elkaar, waardoor een andere techniek gebruikt moet worden, de synthetische CMD methode.
Een schematisch overzicht van de verschillende stappen die gebruikt worden in deze methode is te zien in Figuur 2. Om de stervormingsgeschiedenis van een systeem te achterhalen wordt eerst een grote set synthetische CMDs gemaakt, met behulp van theoretische isochronen. Voor elk van deze model CMDs weten we wat de leeftijd en metalliciteit van hun sterren is. Deze modellen kunnen vervolgens vergeleken worden met het geobserveerde CMD, om zo te vinden welke combinatie van afzonderlijke modellen het best het geobserveerde diagram reproduceert. De combinatie van modellen die gebruikt is vertelt ons wat de meest waarschijnlijke leeftijd en metalliciteit van de sterren in het diagram is, en geeft ons de stervormingsgeschiedenis van het sterrenstelsel.
De nauwkeurigheid waarmee de leeftijd van sterren bepaald kan worden hangt af van een aantal verschillende dingen. Hoe nauwkeuriger we de kleur en helderheid kunnen bepalen van sterren die de hoofdreeks verlaten, des te nauwkeuriger kunnen we de stervormingsgeschiedenis bepalen. Echter, de sterren die de hoofdreeks verlaten zijn relatief zwak, wat het moeilijk maakt om hun helderheid met grote precisie te bepalen. Het is ook mogelijk om de leeftijd van sterren te bepalen door alleen de reuzentak te gebruiken, maar de positie hiervan hangt af van zowel leeftijd als metalliciteit. Daardoor is het moeilijk om de ene parameter te bepalen als je de andere niet weet.
De nauwkeurigheid van de stervormingsgeschiedenis hangt ook af van de leeftijd van de sterren in het geobserveerde stelsel. Het is makkelijker om de leeftijd te bepalen van jonge sterren dan van oude sterren, omdat de vorm van een CMD gevoeliger is voor veranderingen in jonge sterren. Daarnaast is het punt waar jonge sterren de hoofdreeks verlaten meestal helderder dan voor oudere sterren, waardoor hun helderheid beter bepaald kan worden, wat weer leidt tot een betere precisie van de leeftijd.
Als gevolg van deze intrinsieke eigenschappen wordt de leeftijd van oude sterren meest-

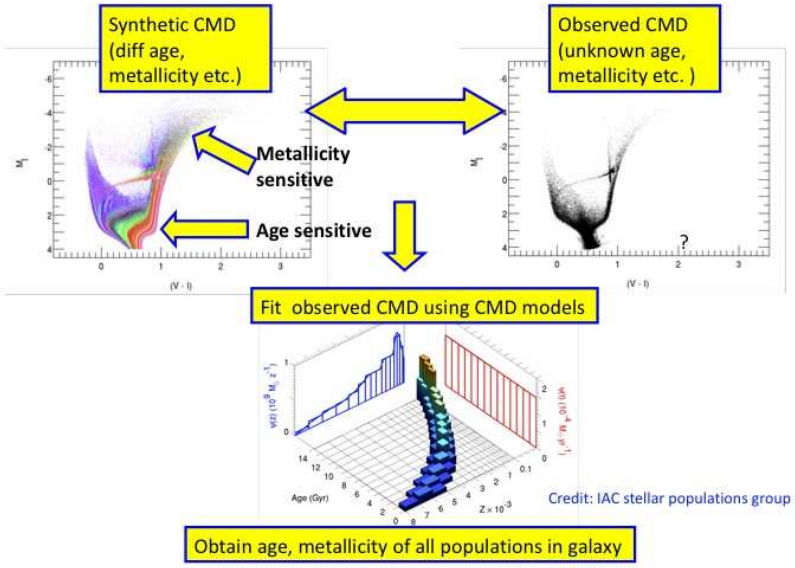

Figuur 2: *Een schematisch overzicht van de verschillende stappen die nodig zijn om de stervormingsgeschiedenis te bepalen. Eerst wordt een grote set van synthetische CMDs gemaakt, waarvan de leeftijd en metalliciteit bekend zijn (linksboven). Daarna worden deze CMDs vergeleken met het geobserveerde CMD (rechtsboven). Door de combinatie van verschillende modellen te vinden die het geobserveerde CMD reproduceert, is het mogelijk de stervormingsgeschiedenis van het stelsel te achterhalen (te zien in het onderste paneel).*

al bepaald met een zeer beperkte nauwkeurigheid. Helaas zijn de oudste leeftijden ook meestal de meest interessante, vooral in de context van het bestuderen van de vorming van sterrenstelsels. Astronomen willen bijvoorbeeld achterhalen hoe de hoeveelheid chemische elementen verandert als gevolg van de evolutie van de eerste generaties sterren in een sterrenstelsel. Daarvoor is het nodig om de oudste sterren in het systeem te vinden. Verder is het ook mogelijk dat de reïonizatie van het heelal (tussen 12.7 en 13.6 miljard jaar geleden) een effect gehad kan hebben op de vorming van sterrenstelsels, wat mogelijk te zien is in de stervormingsgeschiedenis. Echter, om effecten op deze schaal te kunnen onderscheiden is het noodzakelijk om de leeftijd van oude sterren te bepalen met een grotere nauwkeurigheid.

Dit proefschrift

In dit proefschrift presenteer ik een nieuwe methode om de stervormingsgeschiedenis van sterrenstelsels te bepalen, door resultaten van photometrische en spectroscopische waarnemingen direct te combineren. Op die manier kan de leeftijd van ster-

ren bepaald worden met grotere precisie, wat resulteert in een nauwkeurigere stervormingsgeschiedenis. De nauwkeurige stervormingsgeschiedenis van twee dwergstelsels in de Lokale Groep wordt berekend, waarmee de evolutie van chemische elementen en stervorming in detail onderzocht wordt. Door de stervormingsgeschiedenis te koppelen aan de nauwkeurige metingen van het gehalte aan verschillende chemische elementen, is het ook mogelijk om de evolutie van verschillende chemische elementen te bestuderen als een functie van tijd, en de tijdschaal voor chemische evolutie van deze dwergstelsels te bepalen.
Het eerste stelsel dat ik bestudeerd heb is het relatief simpele Sculptor dwergstelsel, waarvan een opname te zien is in Figuur 3. Uit eerdere studies weten we dat Sculptor hoofdzakelijk bestaat uit heel oude sterren, die meer dan 10 miljard jaar oud zijn. Dit betekent dat we door het bestuderen van Sculptor direct informatie verkrijgen over de alleroudste sterren. Ik heb met behulp van de CTIO/MOSAIC camera (geïnstalleerd op de 4m-Blanco telescoop in Cerro Tololo, Chile) nieuwe waarnemingen gedaan aan de sterren in dit stelsel. De verkregen nieuwe, nauwkeurige photometrische catalogus presenteer ik in hoofdstuk 2. De waarnemingen produceren een CMD dat diep genoeg gaat om nauwkeurig de helderheid en kleur te bepalen van zelfs de oudste sterren die de hoofdreeks verlaten, zodat nauwkeurige leeftijden bepaald kunnen worden. Ook beslaan de waarnemingen een groot gedeelte van het stelsel (ongeveer 80% van de oppervlakte), waardoor het mogelijk is om te kijken naar verschillen in de eigenschappen van sterren op verschillende afstanden van het centrum.

Figuur 3: *Een opname van het centrale deel van het Sculptor dwergstelsel, zoals waargenomen met de CTIO/MOSAIC camera. Een kleurenversie van deze opname is te zien als Figuur 1.4 in hoofdstuk 1.7.*

Hoofdstuk 2 beschrijft de photometrische en structurele eigenschappen van Sculptor, en analyseert de veranderingen in het CMD met positie in het stelsel. Ik laat zien dat de al bekende gradiënten in radiële snelheid en metalliciteit gekoppeld zijn aan een gradiënt in de leeftijd van de sterren. Sculptor bevat overal oude, metaalarme sterren, maar jongere, meer metaalrijke sterren zijn meer en meer geconcentreerd in het centrum, naarmate ze jonger zijn.

In hoofdstuk 3 presenteer ik een nieuwe methode voor het bepalen van de stervor-

mingsgeschiedenis. De methode, genaamd Talos, combineert de directe spectroscopische metingen van de metalliciteit van sterren met een klassieke analyse van het CMD zoals eerder beschreven. Door de directe metalliciteitsmetingen te gebruiken wordt de leeftijd van sterpopulaties met meer zekerheid bepaald, vooral voor oude sterren. Met behulp van Talos wordt de gedetailleerde stervormingsgeschiedenis van Sculptor bepaald. Dezelfde radiële gradiënten als beschreven in hoofdstuk 2 worden ook hier weer gevonden en gekwantificeerd.
Het is ook mogelijk om de mogelijke leeftijden van individuele sterren nauwkeuriger te bepalen dan met de standaard methode, door de stervormingsgeschiedenis direct te koppelen aan de sterren waarvoor spectroscopische waarnemingen zijn gemaakt. Op die manier is het voor het eerst mogelijk om de evolutie van diverse chemische elementen te volgen als een functie van tijd. De verandering van metalliciteit als een functie van leeftijd laat een duidelijke relatie zien, waarbij de oudste sterren het meest metaalarm zijn, en de jongere sterren meer metaalrijk. Ook bepaal ik in hoofdstuk 3 de evolutie van de hoeveelheid van het chemische element magnesium in een ster, als een functie van tijd. Daardoor kan ik de leeftijd bepalen van de zogeheten knie in de magnesium distributie, welke een indicatie geeft van de leeftijd waarop supernova-explosies van verschillende types een invloed beginnen te hebben op de hoeveelheid metalen in het stelsel.

In hoofdstuk 4 pas ik Talos toe op nieuwe waarnemingen van het Fornax dwergstelsel, dat een meer complexe evolutionaire geschiedenis heeft ondergaan. De nieuwe, gedetailleerde stervormingsgeschiedenis laat zien dat Fornax sterren heeft gevormd gedurende bijna zijn gehele levensduur, van 14 miljard jaar geleden tot minder dan 1 miljard jaar geleden. De evolutie van metalliciteit met leeftijd laat duidelijk zien dat de stervormingsactiviteit sterk veranderd is gedurende de levensduur van dit stelsel. De evolutie van magnesium met de tijd laat duidelijk zien dat de jonge sterren meer metalen bevatten dan de oudere sterren. Helaas is het niet mogelijk om de leeftijd van de knie in de magnesium distributie van Fornax te bepalen, aangezien er niet genoeg spectroscopische waarnemingen zijn om de locatie goed vast te stellen. Een vergelijking tussen beide stelsels laat zien dat ze een vergelijkbare evolutie hebben ondergaan, al verliep de metaalverrijking in Fornax sneller dan in Sculptor, en is de stervorming langer doorgegaan.

In hoofdstuk 5 maak ik een vergelijking tussen de gedetailleerde stervormingsgeschiedenis van Sculptor en de uitkomsten van vier verschillende simulaties van sterrenstelsels. Door de voorspelde en gemeten eigenschappen te vergelijken is het mogelijk om de simulaties te testen. De vergelijking wordt gedaan door een synthetisch CMD en stervormingsgeschiedenis te genereren voor iedere simulatie, en die te vergelijken met de gemeten waardes. De meeste simulaties slagen er in om in meer of mindere mate de globale eigenschappen van Sculptor te reproduceren. De details van de vergelijking worden gebruikt om te bepalen welke parameters van de modellen verantwoordelijk zijn voor de verschillen en overeenkomsten met de waarnemingen, en beter te begrijpen hoe een dwergstelsel als Sculptor gemodelleerd kan worden.

Ideeën voor de toekomst

De gedetailleerde analyse van Sculptor en Fornax heeft de kracht laten zien van de gecombineerde analyse van photometrische en spectroscopische waarnemingen. Echter, om een duidelijker beeld te krijgen van de effecten van verschillende globale parameters (zoals totale massa, nabijheid van de Melkweg, etc.) op de stervormingsgeschiedenis is het nodig om de stervormingsgeschiedenis van meer dwergstelsels te bepalen. Voor meerdere andere dwergstelsels zijn al nauwkeurige photometrische en spectroscopische waarnemingen gedaan, waarmee ik met behulp van mijn nieuwe methode de evolutie van stervorming kan bepalen. Op die manier kunnen we een beter inzicht krijgen in de processen die verantwoordelijk zijn voor de ongelofelijke diversiteit van de sterrenstelsels in onze nabijheid. Verder is het ook mogelijk om de vergelijking van modellen met waarnemingen uit te breiden naar meer stelsels, waardoor de ingrediënten van simulaties nog beter getest kunnen worden.

In conclusie: Gedetailleerd, zorgvuldig onderzoek aan de eigenschappen van individuele sterrenstelsels levert waardevolle inzichten op in de vorming en evolutie van sterrenstelsels.

Acknowledgements

These few pages of the thesis are always special. Being the acknowledgements, they are read most often, yet contain the least science. However, the acknowledgements are the most personal part of any thesis, and reflect the thoughts and experiences of the writer, as well as how doing the research for each chapter has affected that writer.
For the current writer, it has been a great experience to work on the projects discussed in this thesis, and learn so much about the fascinating world of resolved stellar populations. Being able to work out the details of star formation in both galaxies I studied has felt at times like an investigation akin to Sherlock Holmes. Trying to piece together exactly what happened in a particular region of a galaxy, many billions of years ago, makes one feel humble and aware of how special our own place in the Universe really is. Being able to produce a consistent, well-rounded picture for each galaxy has been immensely satisfying, and gives me hope that we are actually able to understand quite a lot about how galaxies form.
I have been very fortunate to have a great supervisor for my PhD project. It seems no matter where I went, everyone had always heard of Eline Tolstoy and the work she does, which made it very easy to introduce myself and explain my research. Eline, thank you very much for sharing your extensive knowledge and experiences with me, and offering valuable guidance throughout these four years. I have always enjoyed our meetings, talking about science, the life of an astronomer and many other subjects. I will never forget our snowed out observing trip to Cerro Tololo.
And then there is the co-promotor of my research, Abi. It feels more like I am lucky enough to have a grandsupervisor (the supervisor of my supervisor), instead of a co-promotor. Thank you very much for sharing with me your extensive knowledge on all things photometry and CMDs, and guiding me along the path of photometric data reduction. I have learned an incredible amount through our talks and emails, and going to Tucson. Thank you very much for your warmth and hospitality during my visits.
Then there are the fellow members of the DART collaboration. Vanessa, Mike, Giuseppina, Pascale, Giuliana, Amina, Else, Bertrand, Yves, Martin, Stefania, Kim, Matthew, Ryan and all the others. It has been great to be part of such a wonderful team, with incredible expertise on every subject needed to study dwarf galaxies. The work visits to Bern to meet the DART and greater ISSI collaborators were always both enjoyable and fruitful. Bertrand and Else, I will never forget, nor reveal, the secret fondue-place in the heart of Bern. Ryan, we never did manage to swap jobs for a few months unnoticed, but we can always try during our respective postdocs.
There were also many people outside the DART collaboration that I have had the privilege of working with. Knut, Edo, Monica, Donatella and Michele. Thank you all for

your contributions to my research and the resulting thesis. Knut, thank you for taking me on a trip through La Serena, after our very succesful observing run. The Pisco Sours were excellent! Donatella, it has been a pleasure to try to find the best set of ingredients for the Sculptor modelling.
I would like to take the opportunity to thank the ISSI in Bern for hosting the yearly meetings of our ISSI team. NWO, NOVA en natuurlijk ook het LKBF, bedankt voor alle financiële ondersteuning.
I also have to thank all the people at Kapteyn, for making the institute a great place to work and enjoy our time during coffee breaks, lunches and borrels. Stefania, Niels en Nynke, Esra and Dave, Giuliana, Guobao and Yanping, Guido, Yunhee, Edo en Alicia, Eline, Scott, Reynier, Koshy, Mark, Jakob, Antonela, Beike, Marjolein, Christian, Tjitske, Maarten and all the others I forgot to mention. All of you are the heart of the institute, and the driving force behind its international reputation of being a very nice place to be, socially and scientifically.
The supporting groups that actually keep the institute running, Wim, Eite, Martin, Hennie, Gineke, Jackie en Lucia. Bedankt voor alle ondersteuning en hulp bij kleine, grote en domme computerproblemen, en voor de hulp met alle bureaucratische en logistieke regelingen, waar wij wetenschappers niet al te bekend mee zijn.
The working group at Kapteyn, with whom I have shared my research over the course of these four years. Else, Bertrand, Stefania, Giuliana, Maarten, Eva, Casper, Leon and Asa, thank you for making the working atmosphere such a pleasurable one. I fondly remember the times we had to close the office door not to disturb other people with our laughter.
My roommates, Esra, Jakob and later Tjitske, thank you for sharing the daily struggles and breakthroughs, highs and lows of hands-on research. All of you have helped to make my PhD experience a very enjoyable one.
Equally as important as the people inside the institute are the friends outside the institute. Bertrand, my most direct colleague, and good friend. Our frequent wii and xbox battles are the stuff of legends. Yan, Tessa, Hennie, Michiel, Jolanda en Beike, mijn Alma Mater jaargenoten. Nancy, Oscar and Olmo, I always enjoy going out for drinks and meeting together for dinner and games. Paul en Pjotr, ook al waren de bezoeken aan Volendam, en aan jullie, minder vaak, ze waren altijd gezellig en ontspannend. Martin, bedankt voor alle bezoekjes aan Groningen. Ik ben blij dat je iemand hebt gevonden om samen gelukkig mee te zijn. En natuurlijk mijn ouders, bedankt dat jullie er altijd voor me waren. Jullie advies, goede moed en goede sfeer hebben me ontzettend bijgestaan tijdens mijn onderzoek in het verre Groningen.
And, sticking to Dutch tradition, I save the best for last. Sofia, my wife, I can honestly say that I never would have made it without you. It will not be a surprise to many readers that the best thing that came from doing my PhD at Kapteyn was meeting you. Thank you being there so many times for me, and sharing all my hopes and dreams and frustrations and struggles. You are the brightest star, and the light of my life.

Thank you all!

Thomas